Tuning Cation and Anion Redox Chemistry in Transition Metal Oxide Positive Electrode Materials for Lithium and Sodium-Ion Batteries

by

Se Young Kim

A thesis

presented to the University of Waterloo

in fulfillment of the

thesis requirement for the degree of

Doctor of Philosophy

in

Chemistry

Waterloo, Ontario, Canada, 2021

Examining Committee Membership

The following served on the Examining Committee for this thesis. The decision of the Examining Committee is by majority vote.

External Examiner	Steen B. Schougaard Professor
Supervisor(s)	Linda F. Nazar Professor
Internal Member	Holger Kleinke Professor
	Eric Prouzet Professor
Internal-external Member	ZhongWei Chen Professor
Other Member(s)	Dmitriy V. Soldatov Professor

Author's Declaration

This thesis consists of material all of which I authored or co-authored: see Statement of Contributions included in the thesis. This is a true copy of the thesis, including any required final revisions, as accepted by my examiners.

I understand that my thesis may be made electronically available to the public.

Statement of Contributions

Se Young Kim was the sole author for Chapters 1, 2, and 8 which were written under the supervision of Prof. Linda F. Nazar and were not written for publication. This thesis consists in part of four manuscripts written for publication. Exceptions to sole authorship of material are as follows:

Research presented in Chapters 3:

This research was conducted at the University of Waterloo by Se Young Kim under the supervision of Prof. Linda F. Nazar. Se Young Kim and Dr. Chansun Park performed the polydopamine coating for Li-rich NMC oxide. Dr. Shahrzad Hosseini contributed to this study by transmission electron microscopy characterization. Se Young Kim conducted all the electrochemical measurements, X-ray diffraction measurements, SEM characterization, X-ray photoelectron spectroscopy, time-of-flight secondary ion mass spectroscopy, and Raman spectroscopy analysis. Se Young Kim wrote the draft manuscripts, to which all co-authors contributed intellectual input. This chapter consists of the following manuscript submitted to *Adv. Energy Mater*.

> Se Young Kim, Chan Sun Park, Shahrzad Hosseinia, Jordan Lampert, Young Jin Kim, and Linda F. Nazar*, Inhibiting Oxygen Release from Li-rich, Mn-rich Layered Oxides at the Surface with a Solution Processable Oxygen Scavenger Polymer.

Research presented in Chapters 4 and 5:

The research in Chapter 4 and 5 were conducted under the supervision of Prof. Linda F. Nazar at University of Waterloo in collaboration with Prof. William C. Chueh, Prof. Thomas P. Devereaux, and Prof. Michael F. Toney at Stanford University.

For Chapter 4, Se Young Kim designed the research with consultation from Prof. Linda F. Nazar. Se Young Kim performed the materials syntheses, electrochemical measurements, and PDF analysis. Iwenetim Abate (Stanford University) performed RIXS and XANES measurements. Se Young Kim and Iwenetim Abate worked together in analyzing RIXS and XANES spectra. Iwenetim

Abate and Dr. C. Das Pemmaraju (Stanford University) conducted density-functional theory (DFT) calculations. Se Young Kim drafted the manuscript and each author provided intellectual input on successive manuscript drafts. This work have been published and adopted here with permission:

> Iwnetim Abate[+], Se Young Kim[+], C. Das Pemmaraju, Michael F. Toney, Wanli Yang, Thomas P. Devereaux, William C. Chueh*, Linda F. Nazar*, The role of metal substitution in tuning anion redox in sodium metal layered oxides revealed by X-ray spectroscopy and theory, *Angew. Chem. Int. Ed.* 2020, DOI: 10.1002/anie.202012205, Copyright 2020: WILEY-VCH GmbH.

For Chapter 5, Iwenetim Abate and Se Young Kim designed the experiments together with the other co-authors. Se Young Kim conducted syntheses of materials, electrochemical measurements, and XRD measurements. Iwenetim Abate performed RIXS and XANES measurements. Se Young Kim and Iwenetim Abate collaborated in analyzing and interpreting XRD, RIXS, XAS, and EXAFS data. The first-principle simulations were carried out by Dr. C. Das Pemmaraju, and Kuan H. Hsu. (Stanford University). These results have been posted on arXiv.org and currently submitted to *Energy and Environ. Sci*.:

> Iwnetim I. Abate, C. Das Pemmaraju, Se Young Kim, Kuan H. Hsu, Sami Sainio, Brian Moritz, John Vinson, Michael F. Toney, Wanli Yang, William E. Gent, Thomas P. Devereaux1,2*, Linda F. Nazar*, William C. Chueh*, "Coulombically-stabilized oxygen hole polarons enable fully reversible oxygen redox", Posted in arXiv: 2010.13107 (2020).

Research presented in Chapters 6:

This research was conducted at the University of Waterloo by Se Young Kim under the supervision of Prof. Linda F. Nazar. Se Young Kim and Dr. Dipan Kundu designed the experiments. Se Young Kim conducted materials synthesis, electrochemical measurements, ex-situ and in-situ X-ray diffraction measurements, Rietveld refinements, SEM characterization, EDX spectroscopy, and X-ray photoelectron spectroscopy. Dr. Dipan Kundu largely contributed to the SQUID analysis. Se Young Kim wrote the draft manuscripts, to which all co-authors contributed intellectual input. The results have been published and adopted here with permission:

Se Young Kim, Dipan Kundu, and Linda F. Nazar, A 4 V Na^+ Intercalation Material in a New Na-Ion Cathode Family, Adv. Energy Mater. 2017, 1701729. DOI: 10.1002/aenm.201701729, Copyright 2017: WILEY-VCH Verlag GmbH & Co. KGaA, Weinheim.

Research presented in Chapters 7:

This research was conducted at the University of Waterloo by Se Young Kim under the supervision of Prof. Linda F. Nazar. Se Young Kim designed the experiments together with Dr. Kern-Ho Park and Kavish Kaup. Se Young Kim conducted materials synthesis, electrochemical measurements, X-ray diffraction measurements, X-ray photoelectron spectroscopy measurement and bond valence site energy calculation. Kavish Kaup measured neutron powder diffraction and largely contributed to the Rietveld refinement. Dr. Abdeljalil Assoud performed single-crystal XRD measurement and structure refinement. Dr. Kern-Ho Park and Laidong Zhou assisted with electrochemical measurements. Se Young Kim wrote the draft manuscripts, to which all co-authors contributed intellectual input. This chapter consists of the following manuscript submitted to *ACS Mater. Lett.*

Se Young Kim, Kavish Kaup, Kern-Ho Park, Abdeljalil Assoud, Laidong Zhou, Jue Liu, Xiaohan Wu, and Linda F. Nazar*, Lithium Ytterbium Zirconium Halide Solid Electrolytes for High Voltage All-Solid-State Li-Ion Batteries.

Abstract

The surging demand for electrified transportation (both ground and air), robots, and other battery-powered devices has driven the development of electrochemical energy storage systems that can provide high gravimetric/volumetric energy density and cost-effectiveness.

Li-ion batteries (LIBs) have been highlighted as the most promising electrochemical energy storage system among the various options. They are the key component for electric vehicles. However, although LIBs have been intensively developed and commercialized, their energy density still needs to be improved to achieve goals in cost and energy efficiency. To improve the energy density of lithium layered transition metal oxide (Li_xTMO_2) positive electrodes for LIBs, oxygen redox in the high-valent state of the lithium-rich layered oxide (LRLO, $Li_{1+x}TM_{1-x}O_2$) materials has been extensively explored because it enables the high reversible capacity that exceeds the material's theoretical capacity (if one only accounts for transition metal redox). However, the local structural distortion and reactive oxygen release accompanied by anion redox have hindered the harnessing of oxygen redox for commercialized LIBs.

In addition to LIBs, sodium ion batteries (NIBs) have emerged as an alternative to LIBs owing to earth-abundant, low cost and environmentally-safe sodium. Although sodium is heavier and exhibits ~ 0.3 V higher redox potential than lithium, the energy penalty of NIBs is small enough to compete with LIBs. To improve the structural stability and energy density of sodium layered transition metal oxides (Na_xTMO_2, $0 \leq x \leq 1$), substituting transition metals with different types of metals (e.g. Li, Mg, and Sn) has been suggested as one of the effective strategies. Meanwhile, oxygen redox in sodium layered oxides has also been actively explored, especially for earth abundant Mn and Fe containing sodium layered metal oxides. However, the local structural environment for triggering oxygen redox in Na_xTMO_2 still requires further investigation.

Along with increasing capacity and raising the redox potential of positive electrode materials to improve the energy density of LIBs and NIBs, developing safe non-flammable electrolytes has become a critical issue due to thermal runaway of batteries caused by high operation voltage. In this regard, all-solid-sate Li-ion batteries (ASSBs) employing non-flammable solid electrolytes are emerged as a safe and sustainable energy storage system. While high Li-ion conductive sulfide solid electrolytes have been widely explored as a solid electrolyte for ASSBs, their poor electrochemical stability (S^{2-} oxidation at ~ 2.5 V vs. Li/Li^{+}) requires a protective coating layer on 4 V-class positive electrode materials. Therefore, developing solid electrolyte which can provide high ionic conductivity together with wide electrochemical stability window and chemical stability to the positive electrodes is necessary to fully utilize cation redox, and possibly anion redox together, of the high voltage positive electrode materials in ASSBs.

This thesis presents various approaches for improving energy density of LIBs, NIBs and ASSBs with respect to harnessing the cation and anion redox. In Chapter 3 a strategy to enhance the cycle performance of a LRLO cathode is demonstrated by scavenging the evolved reactive oxygen species with a polydopamine (PDA) surface coating. PDA, a well-known oxygen radical scavenger, provides a chemically protective layer that diminishes not only the growth of the undesirable cathode electrolyte interphase (CEI), but also results in less oxygen gas release compared to an unprotected surface, and significantly suppressed phase transformation at the surface. These factors lead to improved rate capability and diminished capacity fading on cycling; namely a capacity fade of 82% over 200 cycles at a C rate for the PDA-coated LRLO, compared to 70% for the bare LRLO material.

Chapter 4 reports the control of high-valent oxygen redox in the Na-ion positive electrode P2-$Na_{0.67-x}[Fe_{0.5}Mn_{0.5}]O_2$ (NMF), where Fe is partially substituted with Cu (P2-$Na_{0.67-x}[Mn_{0.66}Fe_{0.20}Cu_{0.14}]O_2$, NMFC) or Ni (P2-$Na_{0.67-x}[Mn_{0.65}Fe_{0.20}Ni_{0.15}]O_2$, NMFN). The combined study of electrochemistry, local structural evolution, and synchrotron radiation spectroscopies demonstrates

the correlation between the degree of structural disorder and the emergence of oxygen redox in charged NMF, NMFC, and NMFN electrodes. Importantly, we show that the presence of significant anion redox from charged NMF and NMFC, but with different extent, without the widely accepted requirement of an A-O-A' (where A= Na and A'= Li, Mg, vacancy) local configuration in the pristine materials. The density of states calculations demonstrate that the extent of oxygen redox is more favored when oxygen 2p band dominates the band near the Fermi level in the TM-O bond. This study further suggests that the amount of Jahn-Teller active Fe^{4+} ion and the oxygen redox mechanism are additional related factors to be considered to establish the correlation between the degree of structural disorder and the extent of anion redox in the materials.

In Chapter 5, layered $Na_{2-x}Mn_3O_7$ is synthesized in its hexagonal phase, and its local structural evolution that stabilizes oxygen redox is investigated. In $Na_2Mn_3O_7$, ordered Mn site vacancies in the MnO_2 layer generate a Na-O-Vacancy configuration which provides an environment for oxygen redox. By combining experimental (electrochemistry and synchrotron radiation spectroscopies) and theoretical (first principle calculation) studies for the partially desodiated $Na_{2-x}Mn_3O_7$ electrode, we demonstrate that coulombic interactions between oxidized oxide and the negatively charged Na vacancy can stabilize hole polarons on lattice oxygen and disfavor O-O dimerization at 4.2 V vs. Na/Na^+ which are commonly known as an evidence of oxygen redox. This study highlights the role of coulombic interactions for stabilizing highly oxidized oxygen for developing high energy density layered oxide materials.

Chapter 6 introduces a new class of polyanion-type Na^+ insertion materials for Na-ion batteries. By virtue of its moderately inductive polyanionic framework, the air and moisture stable sodium cobalt selenite, $Na_2Co_2(SeO_3)_3$, shows a redox potential of ~ 4 V vs. Na/Na^+ that utilizes the $Co^{2+/3+}$ redox couple, rendering it compatible with conventional liquid organic electrolytes. A microwave hydrothermal synthesis route is developed for the rapid synthesis of nanostructured $Na_2Co_2(SeO_3)_3$ and

its conductive graphene oxide composite. These studies reveal good structural and electrochemical reversibility of the $Na_2Co_2(SeO_3)_3$ positive electrode.

Chapter 7 reports a new metastable trigonal phase of Li_3YbCl_6 with an ionic conductivity of 1.0×10^{-4} $S\cdot cm^{-1}$, and mixed-metal halide solid electrolytes, $Li_{3-x}Yb_{1-x}Zr_xCl_6$ with conductivities up to 1.1 $mS\cdot cm^{-1}$ at room temperature. Combined neutron, single-crystal, and powder X-ray diffraction methods reveal that Zr-substitution for Yb in Li_3YbCl_6 triggers a trigonal-to-orthorhombic phase transition and forms new, lower energy pathways for Li-ion migration. All-solid-state cell cycling with uncoated >4 V-class cathodes is enabled by the high electrochemical oxidation stability of the mixed-metal halide solid electrolyte.

Acknowledgements

I would like to extend my utmost gratitude to my supervisor, Professor Linda F. Nazar, for giving me the great opportunity to learn how to think scientifically, propose ideas, and work thoughtfully during my doctoral studies. Her continuous support and guidance throughout the course of my research projects encouraged me to explore the science in Li/Na ion batteries and accomplish the work presented in my Ph.D. thesis. I would also like to extend my gratitude to my Ph.D. committee: Professor Holger Kleinke, Professor Eric Prouzet, and Professor Dmitriy Soldatov (University of Guelph) for their time and suggestions about my research. Furthermore, I would like to give a special thanks to Professor Steen B. Schougaard and Professor ZhongWei Chen for being my external examiner and internal-external examiner, respectively, and their time to participate in my thesis defence.

I would like to thank all the research collaborators for providing me with their expertise and wonderful contribution to this research (Chapter 4 and 5). Iwnetim I. Abate from Professor William Chueh (Stanford University) and Dr. C. Das Pemmaraju (SLAC National Accelerator Laboratory) carried out synchrotron experiments and theoretical calculations for sodium layered oxide materials. Dr. Wanli Yang (Advanced Light Source, Lawrence Berkeley National Laboratory) supervised the resonant inelastic x-ray scattering experiment, and Professor Thomas P. Devereaux (Stanford University) supervised the theoretical calculations. In addition, I appreciate BASF SE for their financial support and providing battery materials for the Li-rich NMC project.

I have been very fortunate to have great lab mates who are incredibly supportive and warmhearted. I would like to thank all the past and present lab members in Nazar's group. I am very thankful to Professor Dipan Kundu and Dr. Elahe Talaie-Pashiri for their help and guidance at the beginning of my Ph.D. studies. I also appreciate Dr. Hosseini's significant contribution to the high-resolution transmission electron microscopy study in chapter 3. Without their support and advice, I

might have lost direction to my goal for the projects. I would like to give my further thanks to Dr. Kernho, Dr. Xia, Dr. Erika, Abhi, Kavish, Laidong, Ivan, Chen Yuen, Lauren, and Nate for providing me with their expertise and experience for my research and sharing beautiful moments. I would also thank my dear friends Professor Wook Ahn, Professor Tae-Jung Kwon, Dr. Min Ho Seo, Dr. Yun-Seok Jun, Dr. Jun Geun Um, Dr. Sung Ho Park, Dr. Dong Un Lee, Dr. Joo Hyung Ryu, Dr. Moon Gyu Park, and Dr. YongWook Kim for making my Waterloo life so enjoyable.

Lastly, I would like to give my deepest gratitude to my parents and my siblings. I know how much you love me and how hard it was to support me while pursuing a Ph.D. Under your unconditional supports, I could finish this thesis. To my wife, your unconditional love and sacrifice made all of this possible. I also thank my son, Logan, who makes my life more meaningful.

Dedication

This thesis is dedicated to my parents, Nam Ho Kim and Kyung Hee park,

my sisters, Na Kyung Kim, Kyung Min Kim,

my parents-in-law, Heung Yeol Oh and Kyung Sook Kim,

my wife, Chae Hyeon Oh,

and my son, Logan Kim

Table of Contents

List of Figures

List of Tables

List of Abbreviations

ABF	Annular Bright-Field
AC	Alternating Current
ACN	Acetonitrile
AE	Auger Electron
ASSB	All Solid State Batteries
AVDF	Antisite Vacancy Defect
BSE	BackScattering Electron
BVSE	Bond Valence Site Energy
CDEM	Continuous Dynode Electron Multiplier
CEI	Cathode Electrolyte Interphase
CL	Cathodoluminescence
CPE	Constant Phase Element
CV	Cyclic Voltammetry
DEC	Diethyl Carbonate
DF	Dark-Field
DFT	Density Functional Theory
DMC	Dimethyl Carbonate
DOS	Density of State
DSC	Differential Scanning Calorimetry
EC	Ethylene Carbonate
EDX	Energy Dispersive X-ray Spectroscopy
EELS	Electron Energy Loss Spectroscopy
EES	Energy Storage System
EIS	Electrochemical Impedance Spectroscopy
EPR	Electron Paramagnetic Resonance
EV	Electrical Vehicle
EXAFS	Extended X-ray Absorption Fine Structure
FEC	Fluorothylene Carbonate
FFT	Fast Fourier Transform
FIB	Focused Ion Beam

HAADF	High-Angle Annular Dark-Field
HRTEM	High Resolution Transmission Electron Microscopy
ICE	Internal Combustion Engines
LCO	$LiCoO_2$
LHB	Lower-Hubbard Bands
LIB	Lithium Ion Battery
LiPF6	Lithium Hexafluorophosphate
LMCT	Ligand to Metal Charge Transfer
LRLO	xLi_2MnO_3 - (1-x)$LiMO_2$, M=Ni, Mn, Co
MS	Mass Spectroscopy
NCO	$NaCoO_2$
NIB	Sodium Ion Battery
NMC	$LiNi_xMn_yCo_zO_2$ (x + y + z = 1)
NMF	$Na_{0.67-x}[Fe_{0.5}Mn_{0.5}]O_2$
NMFC	$Na_{0.67-x}[Mn_{0.66}Fe_{0.20}Cu_{0.14}]O_2$
NMFN	$Na_{0.67-x}[Mn_{0.65}Fe_{0.20}Ni_{0.15}]O_2$
NMP	N-methyl-2-pyrrolidinone
NMR	Nuclear Magnetic Resonance
OEMS	Online Electrochemical Mass Spectroscopy
PC	Polyethylene
PDA	Polydopamine
PDF	Pair Distribution Function
PEEK	poly(aryl-ether-ether-ketone)
PES	Photoelectron Spectroscopy
PND	Powder Neutron Diffraction
PVDF	Polyvinylidene-fluoride
PXRD	Powder X-Ray Diffraction
RIXS	Resonant Inelastic X-ray Scattering
ROS	Reactive Oxygen Species
SE	Solid Electrolyte
SEI	Solid Electrolyte Interphase
SEM	Scanning Electron Microscopy

SNS	Spallation Neutron Source
SQUID	Superconducting Quantum Interference Device
STEM	Scanning Transmission Electron Microscopy
SXAS	Soft X-ray Absorption Spectroscopy
SXRD	Synchrotron X-Ray Diffraction
TEM	Transmission Electron Microscopy
TGA	Thermogravimetric Analysis
TM	Transition Metal
TOF-SIMS	Time of Flight Secondary Ion Mass Spectroscopy
UHB	Upper-Hubbard Bands
XANES	X-ray Absorption Near-Edge Structure
XAS	X-ray Absorption Spectroscopy
XPS	X-ray Photoelectron Spectroscopy

Chapter 1

Introduction

1.1 Overview

Global energy consumption has surged, along with a rapid development of electrical devices and their power-supplying infrastructures that enrich our lives with convenient and automated systems.[1, 2] To meet this increased energy demand, producing and supplying energy to our society in a sustainable and eco-friendly way has emerged as a crucial issue for our and future generations. Since the invention of the steam engine by Thomas Newcomen in 1712, fossil fuels have played a key role as a major energy source for the combustion engines to convert mechanical power to electrical energy, and it seems to continue to play an essential role for the next 10 years (**Figure 1.1**).[3]

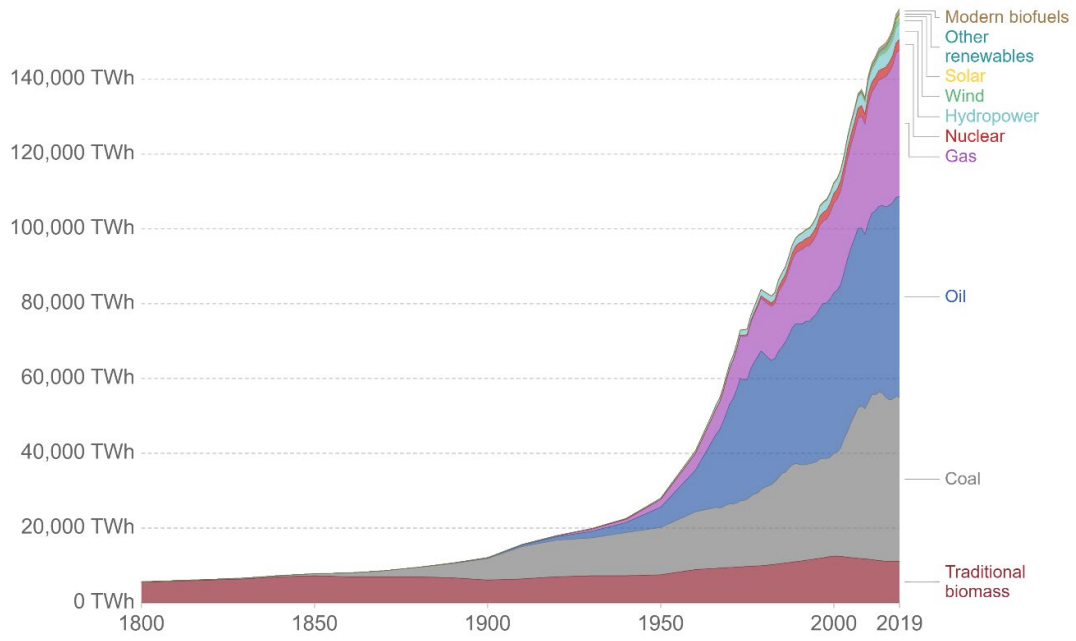

Figure 1.1 Global net energy consumption by energy source, 1800 – 2019.[3]

However, the inevitable environmental consequences of using fossil fuels, such as greenhouse gas emissions, air pollution and wastewater, are threatening the ecosystem and humans by accelerating climate change. In an effort to reverse or slow down climate change, a portion of the total energy produced from fossil fuels has been taken over by clean and renewable energy sources, such as solar photovoltaic cells, and wind turbine generators. However, geometric dependency for installation and the low persistency of most renewable energy systems are hindering them from replacing fossil fuels and being utilized as a sustainable, large-scale energy supply system. Therefore, along with continued progress in renewable energy generating systems, developing large-scale and sustainable energy storage systems is needed in order to save the generated energy during low demand periods and then use it efficiently to supplement the energy supply without burning fossil fuels during high demand periods. In the same context, transportation industries are implementing revolutionary changes and developments in their power supply systems to convert them from internal combustion engines (ICE) to electrochemical energy storage systems, such as rechargeable batteries and fuel cells, in order to reduce air pollution.

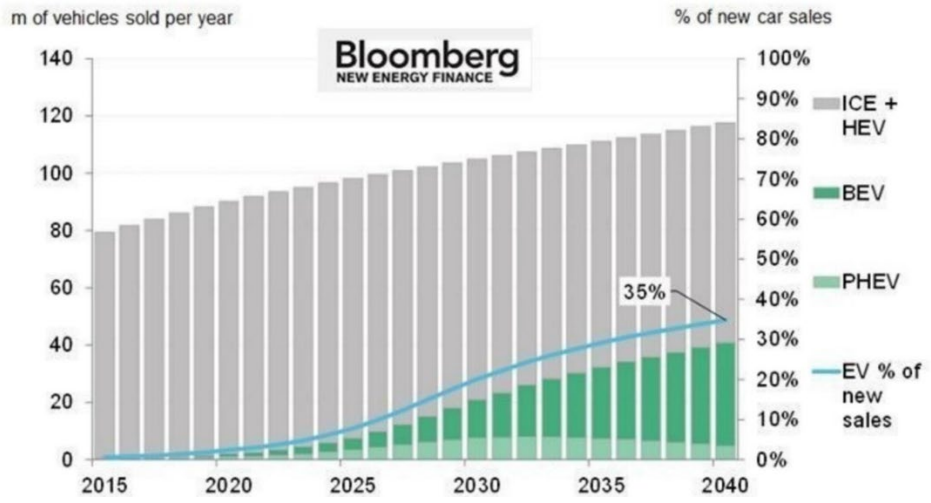

Figure 1.2 Annual global EV sales trends since 2015 and forecast. With increasing number of annual car sales until 2040, the EV sales portion in annual car sales also increases. EV sales will hit 41 million by 2040, representing 35% of new light duty vehicle sales.[4]

As the rapidly increasing global sales of electrical vehicles (EV) predicted by 'Bloomberg' in **Figure 1.2** reflects,[4] the number of people who consider buying EVs due to multiple reasons (such as cost-effectiveness and climate change) is also increasing year by year, and the automotive industry is working hard to develop energy storage systems that perform comparably to ICE vehicles. Furthermore, smart grid technology for effective energy consumption management in a smart city significantly depends on the capacity of stored energy for entire city. Thus, the development of large scale energy storage systems is essential to successfully establish the smart grid network.[5] As can be gleaned from these examples, rechargeable batteries play a key role in reducing fossil fuel use, by storing and providing sufficient energy to the right place at the right time.

Amongst all the rechargeable batteries that have been developed to store the electrochemical energy, lithium-ion batteries (LIBs) and sodium-ion batteries (NIBs) have received the most attention as breakthrough technologies, both to power electrical devices from mobile phones to electrical vehicles, and to provide scalable energy storage systems (ESS) for smart grids. Current Li/Na ion batteries can provide 100 ~ 265 Wh/kg for a specific energy density of 250 ~ 693 Wh/L for volumetric energy density, depending on the materials utilized in the batteries.[6] Such performance levels enable EVs to travel ~ 500 km on a full charge, but there are still many drawbacks to be overcome to compete with ICE. For instance, it takes several hours to charge an EV's batteries once they are fully discharged. In addition, such battery capacity is not enough to travel for long distances, unless there are battery charging stations along the road. Most importantly, while the energy cost of the batteries should be lower than 100 US$/kWh to compete with ICE, as of Dec. 2019 it was ~ 160 US$/kWh.[7] Therefore, developing high energy density electrode materials for Li/Na ion batteries is essential.

1.2 Li-Ion Batteries (LIBs)

Lithium-ion batteries (LIBs) are employed as the primary energy storage system powering commonly-used electric devices such as mobile phones and power tools. Most electrical vehicles currently in production are powered by LIBs. The first rechargeable LIB was reported by Prof. M. S. Wittingham *et al.* in 1976.[8] In that study, the intercalation and deintercalation of Li^+ ions into TiS_2 was demonstrated and the first rechargeable LIB system was established. In 1980, John B. Goodenough reported that lithium cobalt oxide ($LiCoO_2$, LCO)[9] can perform as a positive electrode for LIBs. This invention opened up a new era for LIBs by inspiring other researchers to study transition metal oxide positive electrode materials, such as lithium nickel manganese cobalt oxide ($LiNi_xMn_yCo_zO_2$ ($x + y + z = 1$), NMC), which are currently dominating the positive electrode market. At that time, Li metal or its alloys were employed as a negative electrode for LIBs. However, Li metal electrodes suffer from the intrinsic problem of dendritic growth on the Li metal surface from repetitive charging/discharging. These dendrites continually grow as a result of the electrochemical cell cycling and eventually penetrate the separator, which causes a short circuit of the cell that induces local heat evolution and results in thermal runaway of the LIBs. In addition, most alloy-type negative electrodes experience high volume change during the alloying and dealloying process, which results in a contact loss between the current collector and alloy negative electrode, resulting in capacity fading.

Although graphite displays reversible Li ion intercalation and thus has potential as an alternative negative electrode, the decomposition from commonly used polyethylene (PC) -based organic electrolytes and graphite exfoliation had hindered such LIBs from commercialization. In 1990, however, Jeff Dahn and co-workers reported reversible Li intercalation from a coke (soft carbon) electrode, enabled by the formation of a stable solid electrolyte interphase (SEI) when using an ethylene carbonate (EC) co-solvent.[10] Based on this research, in 1991 Sony successfully commercialized LIBs for the first time by employing an LCO positive electrode with a coke negative electrode, for use in

mobile phones. After D. Guyomard and J. M. Tarascon developed electrolyte mixtures of EC and dimethyl carbonate (DMC) in 1993,[11] LIBs were more actively commercialized, but with a graphite negative electrode.

LIBs consist of four main parts: positive electrode, negative electrode, electrolyte, and separator, as illustrated in **Figure 1.3**. The current collectors on each electrode in the cell are connected to an outer circuit, which is connected to the electric device being operated. Once the cell starts to discharge by operating the electric device, Li ions deintercalate from the negative electrode and migrate to the positive electrode through the electrolyte. At the same time, electrons released from the negative electrode travel to the positive electrode through the outer circuit and power the electric device. The chemical potential difference of electrons and Li ions between the positive and negative electrodes is the origin of the voltage difference in the cell that drives the current flow in the outer circuit and Li ion migration inside the cell. Once the electrons and Li ions reach to the positive electrode, the Li ions intercalate into the positive electrode materials, and the electrons simultaneously reduce the elements in the positive electrode material, such as transition metals or anions, to compensate the charge balance. When charging, the same process occurs, but in the opposite direction between the positive and negative electrodes. However, the charge process is a non-spontaneous reaction that is forced by an applied voltage difference from the outer circuit (or battery charger) that is higher than the electrochemical potential difference between the positive and negative electrodes.

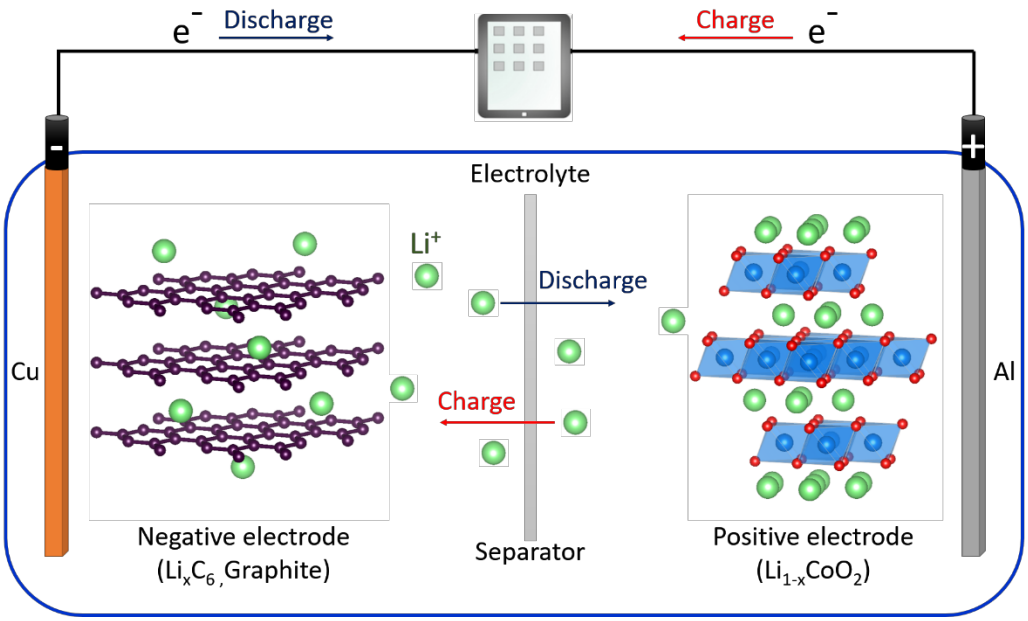

Figure 1.3 Schematic presentation of a Li ion battery employing $LiCoO_2$ and graphite for positive and negative electrode material, respectively.

Each component of the LIB is required to manifest some physical and chemical properties that are suitable for their own purposes. For example, the electrolyte in the cell provides a matrix that the Li ions can migrate or diffuse through in a solvated form. Therefore, the electrolyte should have a good ionic conductivity and it should also be an electronically insulating material to prevent direct current flow between the electrodes; that is, a short circuit of the cell. In order to prevent the short circuit by direct contact between the electrodes or due to possible dendrite growth of Li metal, placing a separator between the electrodes is necessary. Generally, the separators are porous polymer or glass fiber membrane that are permeable to Li ions. Therefore, achieving mechanical and chemical properties that can resist the penetration of Li dendrite growth while providing a good permeability to Li ions and keeping the layer thin are is a key issue for separators. As for current collectors, different types of metals should be employed for the positive and negative electrode sides. For instance, an aluminum

current collector is commonly used for the positive electrode, whereas a copper current collector must be employed for the negative electrode side because aluminum reacts with Li by forming a Li-Al alloy.[12] In addition, the electrode consists of a mixture of the active material, an additive carbon, and a binder. As Li/Na transition metal oxide active materials have low electrical conductivity and experience volume change over the cell cycling, carbon and binder additives are required to enhances the electrical conductivity and maintain contact between the particles in the electrode.

LIBs operate based on the electrochemical redox activities of their electrode materials. For instance, the $LiCoO_2$(LCO)/graphite cell operates by the following electrochemical reactions (1.1 - 1.4):

- Charge:

$$\text{Positive electrode: } LiCoO_2 \rightarrow Li_{1-x}CoO_2 + xLi^+ + xe^- \quad \textbf{(1.1)}$$

$$\text{Negative electrode: } C_6 + xLi^+ + xe^- \rightarrow Li_xC_6 \quad \textbf{(1.2)}$$

- Discharge:

$$\text{Positive electrode: } Li_{1-x}CoO_2 + xLi^+ + xe^- \rightarrow LiCoO_2 \quad \textbf{(1.3)}$$

$$\text{Negative electrode: } Li_xC_6 \rightarrow C_6 + xLi^+ + xe^- \quad \textbf{(1.4)}$$

Starting at the charge process, first, the Li^+ ions deintercalate from the LCO structure while Co^{3+} oxidizes to Co^{4+} to compensate for the positive charge loss by Li^+ extraction. At the same time, electrons released from Co^{3+} oxidation travel to graphite negative electrode side along the outer circuit. The deintercalated Li^+ ions from LCO then migrate to the graphite electrode through the electrolyte and intercalate into the graphite while the electrons reduce Li^+ ions concurrently to form Li_xC_6. From the

consecutive discharge process, the extracted Li ions from the graphite negative electrode migrate to the LCO side and intercalate into the LCO by reducing Co^{4+} to Co^{3+}.

Typically, a LCO/graphite cell using a carbonate based electrolyte (e.g., 1M $LiPF_6$ in EC:PC 1:1 v/v) operates at an average voltage of 3.7 V (V vs. Li/Li^+) within a voltage range of 3.0 - 4.2 V. Although the theoretical capacity of LCO and graphite are 273mAh/$g_{(LCO)}$ and 372 mAh/$g_{(C6)}$, respectively, an irreversible phase transition of LCO occurring at high degree of Li ion extraction (> 0.5 mol of Li) limits the practical capacity of LCO to ~ 140 mAh/g_{LCO} in the LCO/graphite cell. Practically, this unusable portion of LCO means a gravimetric energy density loss in the LCO/graphite cell. The irreversible phase transition of LCO at a high degree of delithiation can be understood by looking at a structural evolution of LCO during charging. First, from the pristine LCO crystal structure, CoO_6 octahedra are 2-dimensionally arranged by sharing their edges to form CoO_2 slabs.

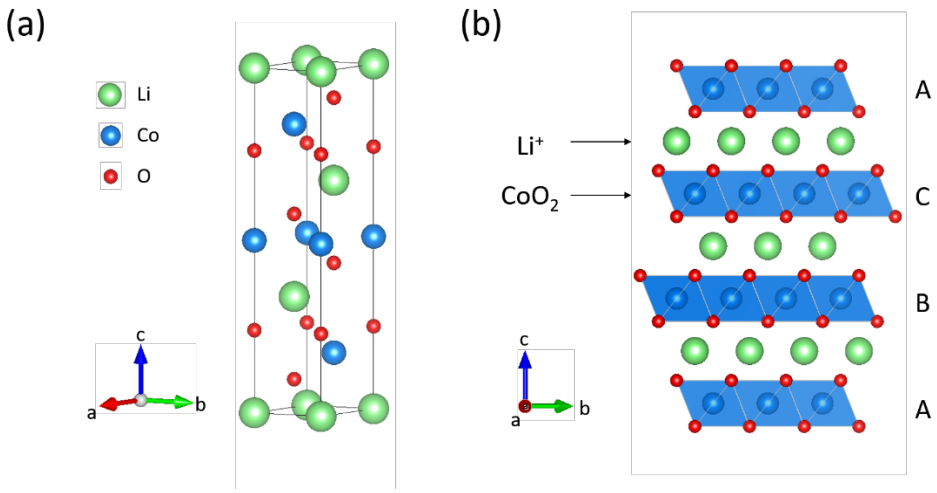

Figure 1.4 (a) crystal structure of $LiCoO_2$ unit cell (space group $\boldsymbol{R\bar{3}m}$) projected along [110] zone axis and (b) schematic presentation of layered structure of $LiCoO_2$.

Three types of the CoO_2 slabs are then separated by interstitial Li layers, resulting in a layered structure of LCO, as shown in **Figure 1.4**. During delithiation, the oxygen layers facing the Li layers space apart from each other due to the repulsive force between the negatively charged lattice oxygens, and rearrange themselves to stabilize the crystal structure. Specifically, the lattice volume expands during the initial charge but shrinks again for further delithiation after ~ 0.5 mol of Li removal. This structural change eventually induces an unstable distorted lattice oxygen arrangement and spreads non-uniform stress within the LCO particle, resulting in a mechanical fractures.[13] More importantly, lattice oxygen escapes from the crystal surface due to the overlapping density of states between 2p (O_2) and "t_{2g}" ($Co^{3+/4+}$) above 4.2 V, and Co^{4+} ions migrate into the Li layer (cation mixing), resulting in a irreversible formation of spinel-like Co_3O_4, which impedes Li^+ de/intercalation.[14-16] Therefore, the practical capacity of LCO is limited by its crystal structural evolution as a function of its Li content.

Considering that a positive electrode material is a main limiting factor hindering improvement in the energy density of LIBs, it is necessary to overcome the drawbacks of LCO and develop a new positive electrode materials. A common strategy to improve the structural stability and the energy density of LCO is substituting Co with other transition metals, such as Mn, Fe, Ni, and Al. Among the many proposed compounds, the $LiNi_xMn_yCo_zO_2$ ($x + y + z = 1$, NMC) families have been spotlighted as the most feasible alternate positive electrode materials, providing higher energy density than LCO, and they have been actively developed to be commercialized.[17] Nowadays, the high nickel containing NMC ($\geq$ 0.8 mol of Ni) are especially called as Ni-rich NMC, and they are replacing LCO in commercialized LIBs. From Ni-rich NMC materials, Mn^{+4} provides superior chemical stability to Co^{3+} and Ni^{2+}, and Ni enables a higher specific capacity of Ni-rich NMC by $Ni^{2+/3+/4+}$ redox, while Ni^{3+} also improves structural stability over Mn^{3+} or Co^{3+} against cation mixing due to its large octahedral site stabilization energy.[18-20] It should be noted that Co^{3+} can improve structural stability by suppressing Ni^{2+} migration into the Li layer that results from the similar sizes of Ni^{2+} and Li^+ ions. The advantages

Parameter	Trend
Chemical stability	Mn > Ni > Co
Structural stability	Co > Ni > Mn
Electrical conductivity	Co > Ni > Mn
Abundance	Mn > Ni > Co
Environmental benignity	Mn > Ni > Co

Table 1.1 Comparison of the characteristics of Mn, Co, Ni in NMC cathodes.[18]

and disadvantages of each transition metal are compared in **Table 1.1**.[18] By utilizing $Ni^{2+/4+}$ and $Co^{3+/4+}$ redox couples, Ni-rich NMC positive electrode material has a typical reversible capacity of ~ 180 mAh $\cdot g^{-1}$ with an average operation voltage of 3.8 V.

In general, including layered-type transition metal oxides (LCO and NMC), there are three transition metal oxide classes of positive electrode materials for LIBs. Their practical specific capacity and average operating voltage are shown below (**Figure 1.5**):

1) Layered oxides: 160 ~ 180 mAh$\cdot g^{-1}$, 3.6 ~ 3.7 V (e.g. $LiNi_{0.6}Mn_{0.2}Co_{0.2}O_2$ and $LiNi_{0.8}Mn_{0.1}Co_{0.1}O_2$)

2) Spinel oxides: ~ 120 mAh$\cdot g^{-1}$, 4.0 ~ 4.7 V (e.g. $LiMn_2O_4$ and $LiNi_{0.5}Mn_{1.5}O_4$)

3) Polyanion oxides: ~ 160 mAh$\cdot g^{-1}$, 3.4 ~ 3.5 V (e.g. $LiFePO_4$ and Li_2FeSiO_4)

Unlike layered structure transition metal oxides, a spinel structure can provide three dimensional lithium ionic path ways and a high operation voltage of ~ 4.7 V, which are beneficial to rate capability and energy density. However, a relatively lower capacity than layered oxides and a Mn^{2+} ion dissolution problem with cell cycling is hindering them from commercialization. Polyanion oxide positive electrode material for Li insertion was introduced by J. B. Goodenough et al. in 1987 by a composition of $Li_2Fe_2(MoO_4)_3$ or $Li_2Fe_2(WO_4)_3$.[21] Later in 1997, one of the most common phosphate-based polyanion materials, olivine $LiFePO_4$, was explored as a cathode material for LIBs by the same group and the material is now powering the electrical vehicles manufactured today.[22] Polyanion oxides mainly

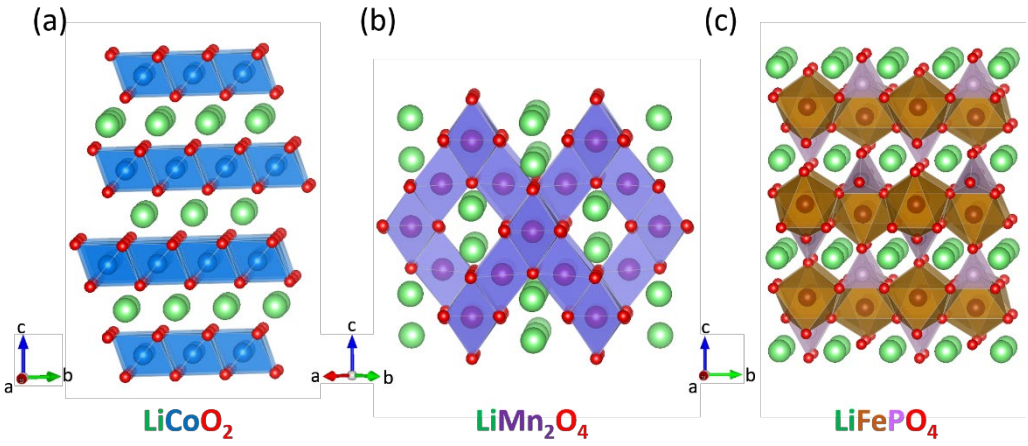

Figure 1.5 Crystal structures of (a) $LiCoO_2$, (b) $LiMn_2O_4$, and (c) $LiFePO_4$. Color of each atom is indicated by the label under the structure.

consist of polyanion groups (XO_4^{n-}, X = Si^{4+}, P^{5+}, S^{6+}, etc.) bonded to transition metals (mainly V, Ti, Fe, Mn) which can provide better structural and thermal stability, and a higher operation voltage with a flatter voltage response upon Li de/lithiation than layered transition metal oxides.[23] These superior chemical and electrochemical properties of polyanion oxides over layered oxides are mainly rooted in their strong covalent bonding between oxygen and the element in the polyanion group that introduces 'inductive effect' in the metal and oxygen (ligand) bond as it is explained below.

The three dimensional link of polyanion moieties to cations provides a structure exhibiting wide lithium ionic pathways and experiencing more reversible volume change with Li (de)intercalation from the LIB cycling compared to layered oxides. In addition, X in polyanion group forming TM-O-X configuration withdraws electrons from the TM-O bond and this inductive effect elevates the redox potential of the cation.[24] Therefore, the redox potential of polyanion materials can be tuned by altering the polyanionic group for cations. For example, a $Fe^{2+/3+}$ redox couple can be utilized from an olivine structure lithium iron phosphate ($LiFePO_4$). Generally, a $Fe^{2+/3+}$ redox couple exhibits too low a redox potential (~ 2.27 V vs. Li/Li^+) to be a positive electrode material for LIBs. By contrast, a $Fe^{3+/4+}$ redox

couple normally can not be utilized for LIBs with carbonate based electrolytes due to its high redox potential, which exceeds the voltage stability window of the organic electrolyte (~ 4.6 V). However, from the $LiFePO_4$ compound, the PO_4^{3-} group weakens the covalency of the Fe-O bond and enables the $Fe^{2+/3+}$ redox at 3.4 V. As a trade-off for the increased redox potential of transition metals, polyanion materials are heavier than layered transition metal oxides in molar mass and have poor electronic ionic conductivity. To overcome these drawbacks, particle size reduction, aliovalent cation doping, and conductive carbon coating have been applied, and all showed enhanced cell cycling performance with increased electronic and ionic conductivity.[25-27]

Among the three classes of lithium transition metal oxides, layered transition metal oxide material is the most actively explored to improve its practical capacity and capacity retention over the Li cell cycling. As is mentioned above, one of the strategies for developing the positive electrode material is increasing the Ni content in the $LiNi_xMn_yCo_zO_2$ ($x + y + z = 1$) compounds, since $Ni^{2+/3+/4+}$ redox mainly contributes capacity performance while the other elements provide structural and thermal stability. However, increasing the Ni content in NMC brings up new issues that hinder the Ni-rich NMC family ($x \geq 0.8$) from commercialization.

The first issue is the formation of surface impurities derived from the material's air sensitivity. When Ni-rich NMC is exposed to the air, it results in a spontaneous reduction of Ni^{3+} to Ni^{2+} concomitant with a lattice oxygen (O^{2-}) oxidation to O^- at the surface of the material (**reaction 1.5 ~ 1.9**).[28] Then, the generated O^- reacts with other O^- forming O and active O^{2-}. Eventually, this active O^{2-} reacts with CO_2 and H_2O from the atmosphere and forms Li_2CO_3 and LiOH impurities on the surface of Ni-rich NMC. The Li_2CO_3 and LiOH impurities on the electrode surface can significantly deteriorate cell performance by generating high surface resistance, evolving CO_2 gas during the initial cell cycling.

$$Ni^{3+} + O^{2-}_{lattice} \rightarrow Ni^{2+} + O^{-} \quad \textbf{(1.5)}$$

$$O^{-} + O^{-} \rightarrow O^{2-}_{active} + O \quad \textbf{(1.6)}$$

$$O^{-} + O \rightarrow O^{-}_{2} \quad or \quad O + O \rightarrow O_2 \uparrow \quad \textbf{(1.7)}$$

$$O^{2-}_{active} + CO_2 / H_2O \rightarrow CO^{2-}_{3} / 2OH^{-} \quad \textbf{(1.8)}$$

$$2Li^{+} + CO^{2-}_{3} / 2OH^{-} \rightarrow Li_2CO_3 / 2LiOH \quad \textbf{(1.9)}$$

Furthermore, the LiOH impurity reacts with CO_2 producing Li_2CO_3 and H_2O which eventually forms HF through a chemical reaction with a lithium salt ($LiPF_6$) in the common electrolyte (**reaction 1.10 - 1.12**).[20, 29] Then, HF attacks the electrode material, causing continuous transition metal dissolution and battery component corrosion, which are critical issues for maintaining capacity over cell cycling.

$$2LiOH + CO_2 \rightarrow Li_2CO_3 + H_2O \quad \textbf{(1.10)}$$

$$LiPF_6 \rightarrow LiF + PF_5 \quad \textbf{(1.11)}$$

$$PF_5 + H_2O \rightarrow POF_3 + 2HF \quad \textbf{(1.12)}$$

Therefore, preventing Ni-rich NMC from air exposure while assembling the cell is extremely important for cell performance.

The second main issue for Ni-rich NMC is the anisotropic volume change during lithiation and delithiation of the material in LIBs. As Ni content in Ni-rich NMC materials increases from x = 0.5, the material experiences a greater *c* lattice parameter change during charge and discharge in the operation voltage range of 3.0 V to 4.3 V.[30] This phenomena pulverizes Ni-rich NMC particles over the cell cycling, creating inactive small particles which have no electrical contact with the electrode. Furthermore, the newly-opened particle surface reacts with the electrolyte, forming a cathode electrolyte interphase (CEI), with additional consumption of electrolyte. Therefore, the increasing Ni

content causes more rapid capacity degradation by losing contact with the active material particles, and increased surface resistance from the Ni-rich NMC electrode over the cell cycling.

1.2.1 Lithium-rich Layered Transition Metal Oxides

In addition to the research that is focused on increasing Ni content in NMC to improve energy density, increasing the Li content in NMC material also has been actively explored and developed. The concept of a Li-rich transition metal oxide was first introduced in 1993 by M. M. Thackeray et al., using a Li_2MnO_3 system (alternatively $Li[Li_{0.33}Mn_{0.67}]O_2$).[31, 32] In their study, they applied Li_2MnO_3 as a positive electrode material for LIBs and showed that Li_2MnO_3 could be overly lithiated to $Li_{1.09}Mn_{0.9}O_2$ by a chemical reaction using LiI in an acetonitrile solution. In 1997, K. Numata et al. successfully synthesized a solid solution of $LiCoO_2$–Li_2MnO_3 and explored its electrochemical performance as a positive electrode material for LIBs.[33] In 2001, J. R. Dahn's group created a $xLiNiO_2$-$(1-x)Li_2MnO_3$ (x = 1/3, 5/12, and 1/2) solid solution, alternatively $Li[Li_{(1/3-2x/3)}Ni_xMn_{(2/3-x/3)}]O_2$, and demonstrated its reversible electrochemical performance for LIBs.[34, 35] In 2004, M. M. Thackeray's group successfully synthesized a $xLi_2(TM)O_3$–$(1-x)LiMn_{0.5}Ni_{0.5}O_2$ (TM (transition metal) = Ti, Mn, Zr; $0 \leq x \leq 0.3$) solid solution and confirmed its electrochemical properties as a positive electrode material for LIBs.[36] Following this pioneering research, in 2007 Thackeray reported a xLi_2MnO_3–$(1-x)Li(TM)O_2$ (TM = Mn, Co, Ni) solid solution compound, current called Li-rich NMC or HE-NMC.[37]

Li-rich NMCs have been highlighted because they can deliver high specific capacity exceeding 270 mAh/g within an operation voltage window of 2.0 V – 4.8 V (V vs. Li/Li^+), which is higher than other layered transition metal oxide materials, such as LCO (~ 150 mAh/g) or NMC811 (200 mAh/g). In order to explain the high capacity performance of Li-rich NMC, a thorough understanding of its structure evolution and redox mechanism during the first cycle is required. First, Li-rich NMC is regarded as a solid solution of $LiMO_2$ (a trigonal $R\bar{3}m$ structure, M = transition metal) and Li_2MnO_3 (a

monoclinic *C*2/*m* structure) (**Figure 1.6**).[38-40] The two structures share a cubic close-packed oxygen array with similar lattice parameters. The alternating layers of octahedral sites in the solid solution structure are filled by Li and transition metals for the $LiMO_2$ phase, and by Li and Li/Mn (1:2 ratio) for

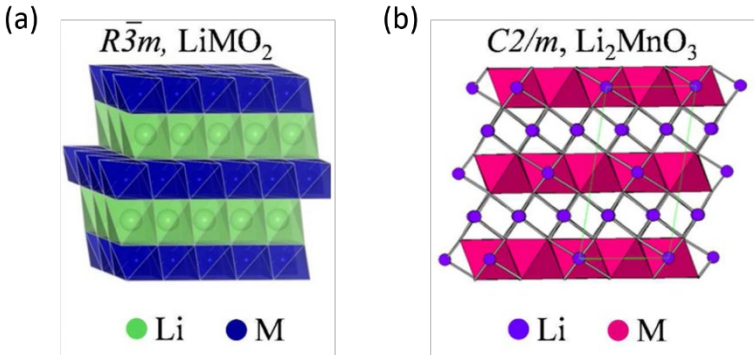

Figure 1.6 Li-rich NMC end-member structures (a) $LiMO_2$ and (b) Li_2MnO_3. The latter contains extra Li^+ within in Mn^{4+} site with 1:2 ratio.[40]

the Li_2MnO_3 (or alternatively $Li[Li_{1/3}Mn_{2/3}]O_2$) phase. The ordered distribution of Li^+ in the Mn^{4+} site with a 1:2 ratio from the $Li[Li_{1/3}Mn_{2/3}]O_2$ phase induces a structural distortion, resulting in different space groups (C2/m), and forms a honeycomb pattern in the $[Li_{1/3}Mn_{2/3}]O_2$ layer, where Li^+ ions are surrounded by six Mn^{4+} (**Figure 1.6**).[40]

This unique structure of Li-rich NMC allows the material to perform at a high specific capacity (~ 270 mAh/g), which is superior to Ni-rich NMC (~ 200 mAh/g). In order to explain the operation mechanism of Li-rich NMC, $0.5Li_2MnO_3$-$0.5LiNi_{0.33}Mn_{0.33}Co_{0.33}O_2$, alternatively $Li_{1.2}Ni_{0.13}Mn_{0.54}Co_{0.13}O_2$, can be taken as an example. Starting from the first charge process in **Figure 1.7**, the Li^+ ions are extracted from the $LiNi_{0.33}Mn_{0.33}Co_{0.33}O_2$ phase by oxidizing Co^{3+} to Co^{4+} and Ni^{2+} to Ni^{4+} until the cell voltage reaches ~ 4.5 V (V vs. Li/Li^+). From the following charge, the Li^+ ions are

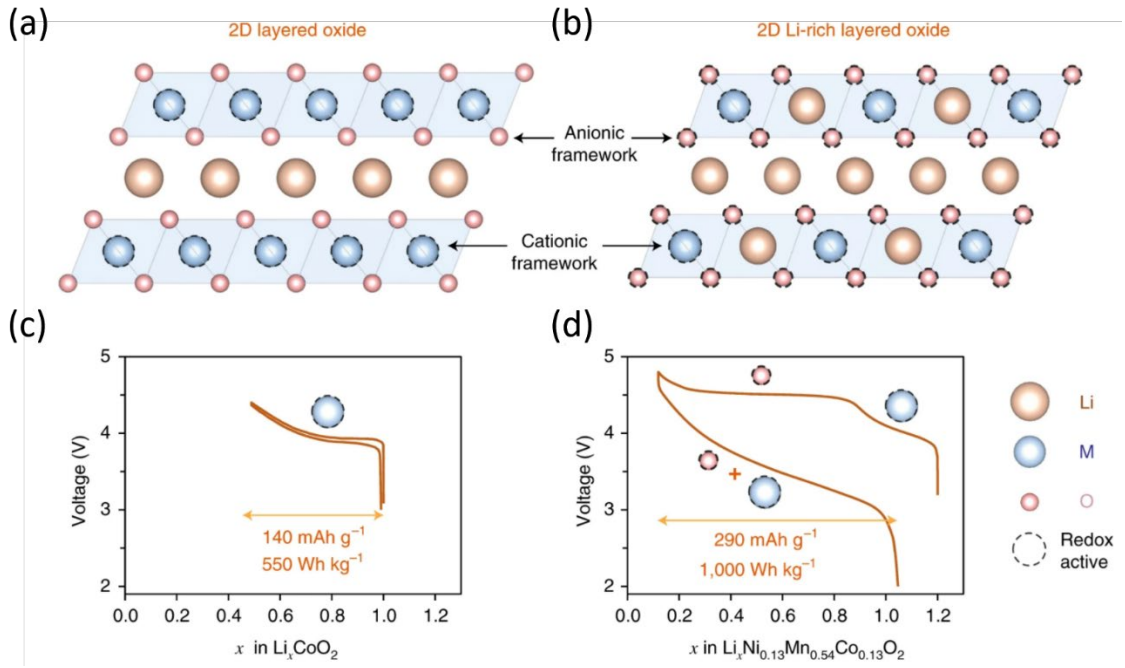

Figure 1.7 The comparison of crystal structures and electrochemical properties between (a) common layered oxides, such as $LiCoO_2$ and (b) Li-rich layered oxides, such as $Li_{1.2}Ni_{0.13}Mn_{0.54}Co_{0.13}O_2$ (Li-rich NMC). From the corresponding voltage profiles in (c) and (d), Li-rich NMC shows higher dis/charge capacity and specific energy compared to $LiCoO_2$ due to the cumulative cation and anion redox. The redox active ions for corresponding voltage range are indicated on the voltage profiles.[41]

further extracted from the Li_2MnO_3 component and this process can be maintained at ~ 4.5 V for an extended potential plateau. It should be noted that Li_2MnO_3 was initially considered to be an inactive material because Mn^{4+} cannot be oxidized further and there is no extra site in the structure for accommodating Li^+ ions. However, M. M. Thackeray et al. discovered that Li_2MnO_3 becomes electrochemically active by leaching out Li_2O from the structure, and tested its feasibility as a positive electrode material for LIBs.[31] As those studies showed, the extra Li^+ ions from Li_2MnO_3 can be extracted with a loss of xLi_2O to form $Li_{2-x}MnO_{3-x/2}$ (MO_2 if x = 2), which is compatible with the delithiated $LiMnO_2$ phase. It should be mentioned that the removal of Li_2O refers to a formation of oxygen species, such as Li_2O, $O^{\bullet-}$, and O_2, from the oxidized lattice oxygen. This process is referred

to as an "electrochemical activation of Li_2MnO_3" in the Li-rich NMC electrode. At that early stage of research, it was believed that the irreversible lattice oxygen loss from the material was mostly compensating the charge capacity during the activation process, resulting in the densification of the electrode surface.[41, 42] However, recent research on Li-rich NMC suggests that the oxygen loss from the electrode surface is quite insufficient to explain the extra charge capacity for the first charge, and that lattice oxygen in the bulk is rather oxidized and participated in the redox process.[41-44] This phenomena is referred to as an "oxygen anion redox" ($O^{-/2-}$) in LIBs and will be further explained in section 1.4.

From previous studies, Li_2MnO_3 domain was considered as a responsible component for the anion redox and high voltage plateau region.[45] Namely, the activation process of Li_2MnO_3 continues until the disappearance of the 4.8 volt plateau while oxidizing lattice oxide ions in LRLO. In contrast, in 2020, Peter Bruce's group revealed that the oxygen redox occurs from the trapped O_2 molecules formed by disproportionation of two oxidized oxide ions ($O^- + O^- \rightarrow O^{2-} + O^0$, $2O^0 \rightarrow O_2$) in TM vacancy clusters during the first charge,[44] rather than oxide ion redox from the delithiated Li_2MnO_3 domain. For consecutive discharge, the process doesn't mirror the charge process. From the high voltage region, the Li^+ ions intercalate into the Li layer in the TMO_2 layer with reducing the oxidized oxygen from O^- to O^{2-}. Then, the reduction of Co^{4+} and Ni^{4+} to Co^{3+} and Ni^{2+} from the $Li_{1-x}Ni_{0.33}Mn_{0.33}Co_{0.33}O_2$ domain compensates the discharge capacity during the Li^+ intercalation upon further discharge to 2.0 V. It should be noted that the oxygen loss from the surface of LRLO induces an irreversible phase transition of the layered $Li(TM)O_2$ to spinel-TM_3O_4 and rocksalt-TMO, due to the cation mixing.[46] This irreversible phase transition continues to evolve from the layered $Li(TM)O_2$ from the first activation cycle and it becomes an origin of capacity fading and operation voltage decay over the cell cycling. In addition, the evolved singlet oxygen ($O^{\bullet-}$) reacts with carbonate based electrolytes at high voltage (> 4.6 V) and decomposes carbonate electrolytes producing side products, such as CO_2,

Li_2CO_3, and alkyl carbonates that can significantly increase the surface resistance of the positive electrode and degrade the cell performance.[47-49]

1.3 Na-Ion Batteries (NIBs)

Na-ion batteries (NIBs) have been spotlighted as an alternative energy storage system to Li-ion batteries due to the abundancy of Na on the earth's crust and the competitive energy density of Na positive electrode materials. Although, Na (22.99 g/mol) is heavier than Li (6.94 g/mol) and its redox potential (-2.73 V vs. standard hydrogen electrode, SHE) is slightly higher than Li (-3.04 V vs. SHE), the energy penalty is small enough to be compensated by the cost-effectiveness and sustainability of Na electrode materials, especially for large scale energy storage system applications. For instance, Na allows use of an aluminum current collector rather than expensive Cu foil on the anode side, as it does not form an alloy with aluminum. Taking into account the portion of total LIB cost represented by Cu foil (~ 12 %, 13 USD/kg) and Al foil (~ 3 %, 6 USD/kg)[50, 51] NIBs are a promising candidate for future large scale energy storage system.

NIBs can adopt most of the electrode materials from LIBs by substituting Li with Na, and the cell also operates in a similar way to LIBs. The first rechargeable NIB was reported in 1980.[52] After the discovery of the electrochemical intercalation of Li ions into TiS_2 by Whittingham in 1976,[8] G. H. Newman et al. demonstrated the Na ion intercalation into TiS_2 from $NaTiS_2$/Na cell. After the introduction of LCO by John B. Goodenough in 1980,[9] P. Hagenmuller et al. demonstrated Na ion intercalation into the layered structure $NaCoO_2$ (NCO) in the sodium cell in 1981.[53] Although NCO has a similar layered structure to LCO, the larger ionic radii of sodium ions (1.02 Å) to Li ions (0.76 Å) induces a different structural evolution compared to LCO, and this results in a different charge/discharge profile compared to LCO. To be specific, as is shown in **Figure 1.8,** the electrochemistry of NCO shows distinct multiple voltage plateaus, indicating multiple phase transition

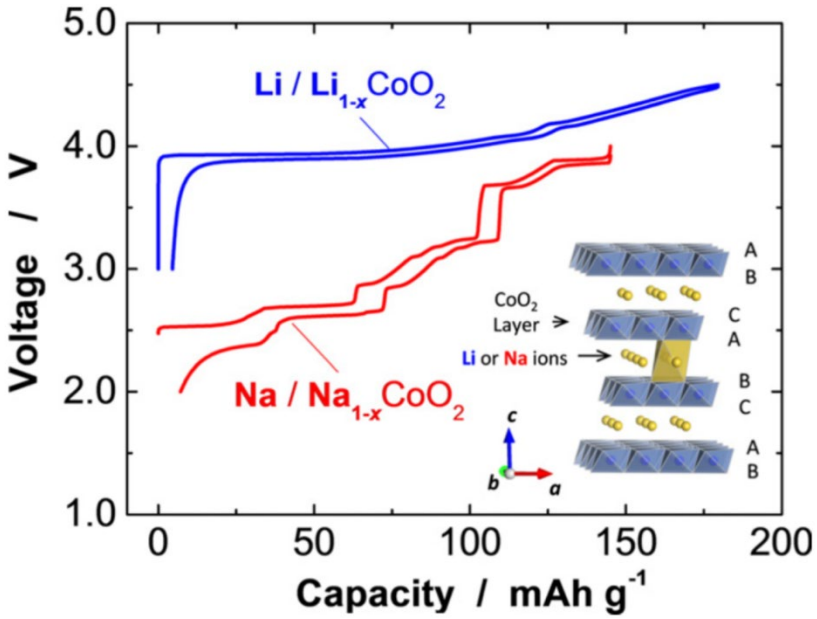

Figure 1.8 Charge/discharge curves of $Li/Li_{1-x}CoO_2$ (blue) and $Na/Na_{1-x}CoO_2$ (red) cells, and a schematic illustration of (Li or Na)CoO_2 crystal structure.[55]

over the cell cycling, unlike LCO.[54, 55] In addition, the lower operation voltage of Na cell results in 30% lower specific energy density of the NCO.

Along with NCO, other Na-layered TM oxide cathode materials employing earth-abundant transition metals, such as $NaMnO_2$,[56] $NaFeO_2$,[57] and $NaCrO_2$,[58] were also explored in their electrochemical performance related to the structural evolution over the Na cell cycling. It should be noted that Na substitution for Li from redox inactive $LiFeO_2$ and $LiCrO_2$ enables the $Fe^{3+/4+}$ and $Cr^{3+/4+}$ redox from $NaFeO_2$ and $NaCrO_2$, because the different stacking schemes in synthesized Na layered oxides with larger Na ions allows reversible Na de/intercalation from those compounds. This unique electrochemical property of the Na layered transition metal oxides indicates that NIBs are a promising candidate for sustainable and low-cost large scale energy storage systems. However, irreversible phase

transition and cation mixing problems, which are triggered by Jahn-Teller active Mn^{4+} and Fe^{4+}, need to be overcome in order to commercialize cost-effective NIBs.

To the best of the author's knowledge, spinel sodium transition metal oxide analogues of $LiMn_2O_4$ have not been reported, due to the unavailability of sodium in tetrahedral sites. On the other hand, sodium polyanionic materials have been actively studied due to their thermal stability by robust covalent frameworks, tunable redox potential by inductive effect, and a flat voltage response by structural energetics.[59-61] In addition, the larger ionic radius of Na enables relatively lower activation energy of Na migration in polyanion oxides compared to that of Li in layered transition metal oxides, and also relatively lower sodium de/solvation energy from polar solvent electrolytes.[62-64]

As for electrolytes, common sodium salt (e.g., $NaClO_4$ and $NaPF_6$) dissolved in a mixture of organic solvents (e.g., ethylene carbonate (EC), propylene carbonate (PC) and diethyl carbonate (DEC)) is used as an electrolyte for NIBs. In order to stabilize the passivation layer on the hard carbon (non-graphitizable, or disordered carbon) or Na metal negative electrodes and enhance capacity retention by suppressing reductive electrolyte decomposition, a fluoroethylene carbonate (FEC) electrolyte additive is usually applied.[65] However, even with an FEC additive, safety concerns like dendrite growth and unstable passivation from organic electrolytes obstruct the use of Na metal as a negative electrode for a NIB full cell.[66] Therefore, hard carbon has been studied the most as a negative electrode for NIBs, because its electrochemical potential of Na de/intercalation is close to that of sodium metal.[67, 68] From the hard carbon negative electrode, Na ions intercalate into turbostratic nano-domains, followed by pore filling in the disordered hard carbon structure, which hardly occurs with graphite.[68, 69]

1.3.1 Classification of Sodium Layered Transition Metal Oxides

The sodium layered transition metal oxides consist of layers of edge-sharing TMO_6 (TM: transition metal) octahedra stacking along [001] axis and sodium ions occupying interstitial layers between the

TMO_6 layers. Various orientation and stacking sequence combination of the TMO_6 layers result in various types of TMO_6 layer packed crystal lattices accommodating sodium ions. According to the notation established by D. Claude et al., synthesized sodium layered transition metal oxides commonly crystalize in two polytypes, P2 and O3, as shown in **Figure 1.9**.[70] From this notation, 'P' and 'O' refer to the trigonal prismatic and octahedral sites, respectively, respectively, at which sodium ions occupy Na layers. The number (2 and 3) following the sodium site (P and O) indicates the number of sodium layers in each unit cell. For instance, a P2-type sodium layered transition metal oxide contains two types of prismatic Na ion layers in between octahedral TM oxide layers in the crystal lattice (**Figure 1.9**).

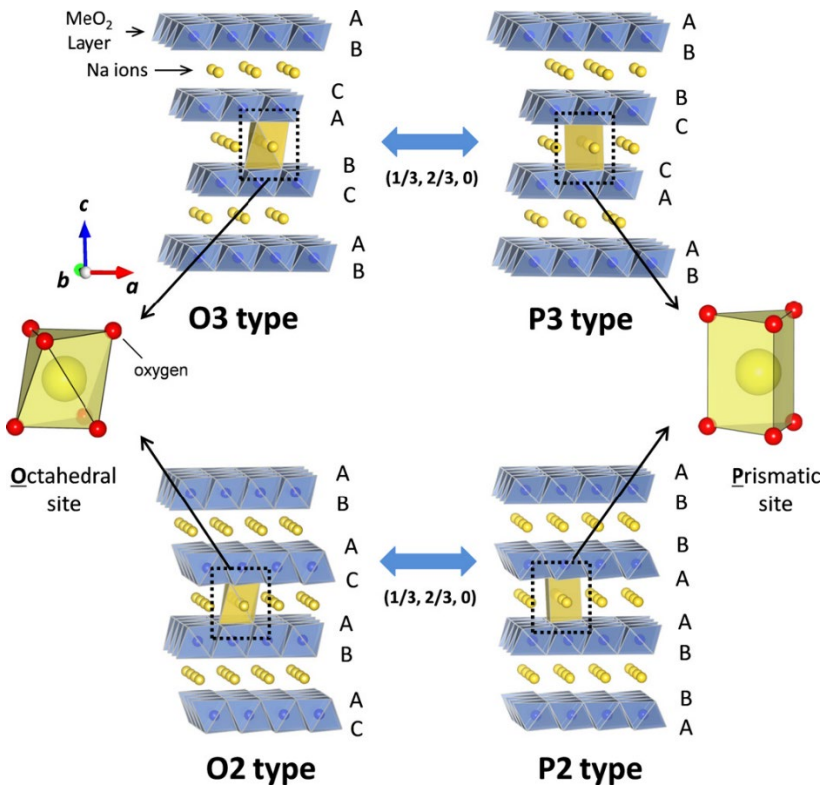

Figure 1.9 The classification of layered sodium transition metal oxides.[55]

Therefore, P2-type sodium layered transition metal oxides exhibit ABBA oxygen stacking along the *c*-axis. In this structure, one half of the trigonal prismatic sites for sodium shares edges with the TMO_6 octahedra and the other half shares faces. Typically, the P2-type sodium layered compound can be obtained when the off-stoichiometry condition of sodium (Na_xMO_2, $0.6 < x < 0.7$) is applied to synthesis process (e.g. $Na_{0.67}MnO_2$, $Na_{0.67}Mn_{0.5}Fe_{0.5}O_2$, and etc.). Normally, adding a prime symbol (') indicates an in-plane distortion from the crystal lattice, such as from hexagonal P2-Na_xMnO_2 ($P6_3/mmc$, $\sim 0.4 < x < \sim 0.8$) to orthorhombic distortion in P'2-Na_xMnO_2 ($Cmcm$, $\sim 0.8 < x \leq 1$).[71, 72]

O3-type sodium layered transition metal oxides consist of a cubic close packed (ccp) oxygen array exhibiting an ABCABC stacking order of oxygen along the c-axis (**Figure 1.9**). Na and transition metal ions are accommodated in distinct octahedral sites due to the larger Na ion size, compared to trivalent transition metal ions.[73] Similar to P2-type compounds, the O3-type sodium layered oxides can be commonly obtained by controlling the stoichiometric ratio of sodium to transition metal close to 1:1 in a sodium compound (e.g. $NaCrO_2$, $NaMnO_2$, $NaFeO_2$, and etc.). In short, the phases of sodium layered transition metal oxides can be controlled by multiple synthesis conditions, such as the stoichiometry of precursors, synthesis atmosphere, sample preparation (grinding and pelletizing), heat treatment temperature, and cooling rate.[74, 75]

Electrochemical extraction or insertion of sodium ions from sodium layered oxides induces a reversible phase transition by the gliding of TMO_2 slabs owing to the charge interaction between oxygen layers facing each other across the sodium layer. In detail, if sodium ions are partially extracted from an O3 phase $Na_{1-x}TMO_2$, the removal of the sodium ions increases the repulsive charge interaction between oxygen layers facing across the sodium layer resulting in the gliding of TMO_2 slabs. The changed TMO_2 slab orientation transforms the octahedral sites in the sodium layer to trigonal prismatic sites and results in the transformation of O3 phase to P3 phase without breaking the metal-oxygen bonds (**Figure 1.9**).[55, 76, 77] On the other hand, P2 phase (e.g. $Na_{0.67}Mn_{0.5}Fe_{0.5}O_2$) reversibly transforms to the

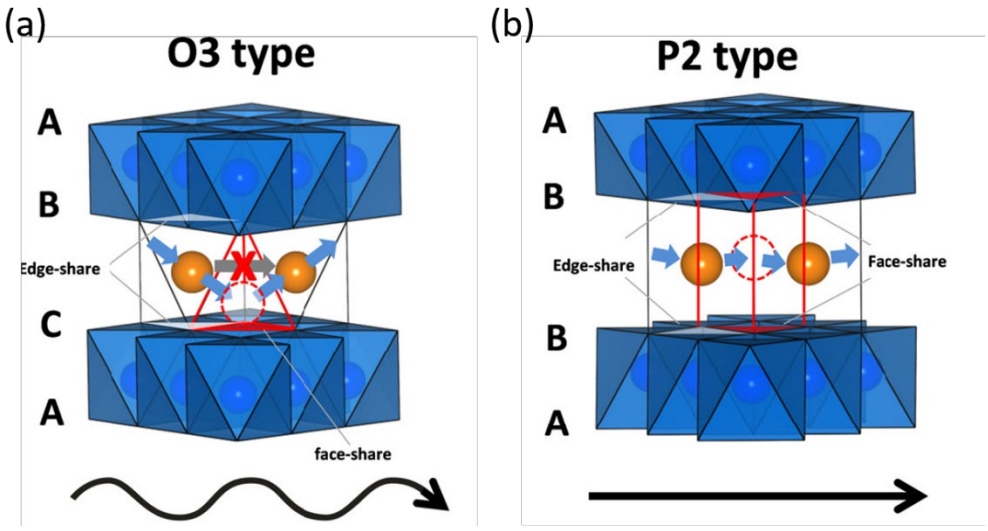

Figure 1.10 Schematic illustration of sodium ion migration paths in (a) O2 and (b) P2 type structures.[55]

O2-type phase ($Na_{0.14}Mn_{0.5}Fe_{0.5}O_2$) by electrochemical sodium extraction as it is energetically more favorable.[78, 79] The sodium ion coordination environment in the sodium layered oxides significantly affects the sodium ion migration energy. For instance, in an O3-type structure, sodium ions migrate between octahedral sites through the face sharing interstitial tetrahedral sites (**Figure 1.10**). However, in a P2-type structure, sodium ions migrate from one prismatic site to an adjacent one by hopping to adjacent prismatic vacancy site which shares wide rectangle windows. The larger size of the prismatic site compared to the octahedral site containing sodium ion also leads to smaller repulsive interactions between the sodium ion and the cations in the adjacent TMO_2 layers. Therefore, the sodium ion migration from the P2-type structure requires relatively smaller activation energy than the O3-type structure; therefore, P2-type materials generally exhibit a higher ionic conductivity compared to that of O3-type materials at the same sodium/vacancy concentrations.[80] It is noteworthy that the phase transitions over the de/intercalation of sodium ions from the sodium layered structure materials (e.g., O3-P3 or P2-O2) changes the site coordination for sodium ion migration, and affects ion migration

activation energy. According to research conducted by D. H. Lee et al., P2-O2 phase transition in $Na_x[Ni_{1/3}Mn_{2/3}]O_2$ ($x < 1$) increases activation energy for sodium ion migration by more than 100 meV.[81]

1.3.2 Developing P2-type sodium Layered Transition-Metal Oxide Positive Electrodes

The structural evolution of sodium layered transition metal oxides depending on synthesis conditions was investigated by J. R. Dahn et al. in 1999 and 2000.[82, 83] P2-$Na_{2/3}[Mn_{1-x}M_x]O_2$ (M = Co, Ni, and Li) and $Na_{2/3}[M^{2+}{}''_{1/3}M^{4+}{}''_{2/3}]O_2$ ($M^{2+}{}''$ = Ni, Mg, $M^{4+}{}''$ = Mn, Ti) compounds were synthesized and their structure dependency on synthesizing temperature was studied. In 2012, S. Komaba et al. developed two types (O3 and P2) of layered $Na_x[Fe_{1/2}Mn_{1/2}]O_2$ ($x \leq 1$) compounds and confirmed their promising electrochemical properties as positive electrode materials for NIBs.[78] They found that the P2-$Na_x[Fe_{1/2}Mn_{1/2}]O_2$ compound delivers a high specific capacity of ~ 190 mAh·g-1 by utilizing $Mn^{3+/4+}$ and $Fe^{3+/4+}$ redox couple, with an average operation voltage of ~ 2.75 V (V vs. Na/Na^+). Interestingly, while charging the cell up to 4.2 V, XRD study indicated that the initial P2 phase transformed into an OP4-like structure (consisting of a mixture of two O and two P-type stacking) exhibiting TMO_2 layers with stacking faults, and that this phase reversibly transformed back into a crystalline P2 phase upon discharge to 3.0 V. However, the poor crystallinity of the OP4-like structure limited identifying the exact structure that evolved from the charged $Na_x[Fe_{1/2}Mn_{1/2}]O_2$ electrode. In 2015, L. F. Nazar's group suggested an O2-type layered structure for the charged $Na_x[Fe_{1/2}Mn_{1/2}]O_2$ rather than OP4-type, based on a comparison study between the high voltage phase (denoted as "Z-phase") of P2-$Na_x[Mn_{0.5}Fe_{0.5}]O_2$ and P2-$Na_x[Mn_{0.65}Fe_{0.2}Ni_{0.15}]O_2$.[79] From the combined analyses of synchrotron X-ray diffraction, neutron diffraction, pair distribution function (PDF), and ^{57}Fe Mossbauer spectroscopy at Z-phase, a

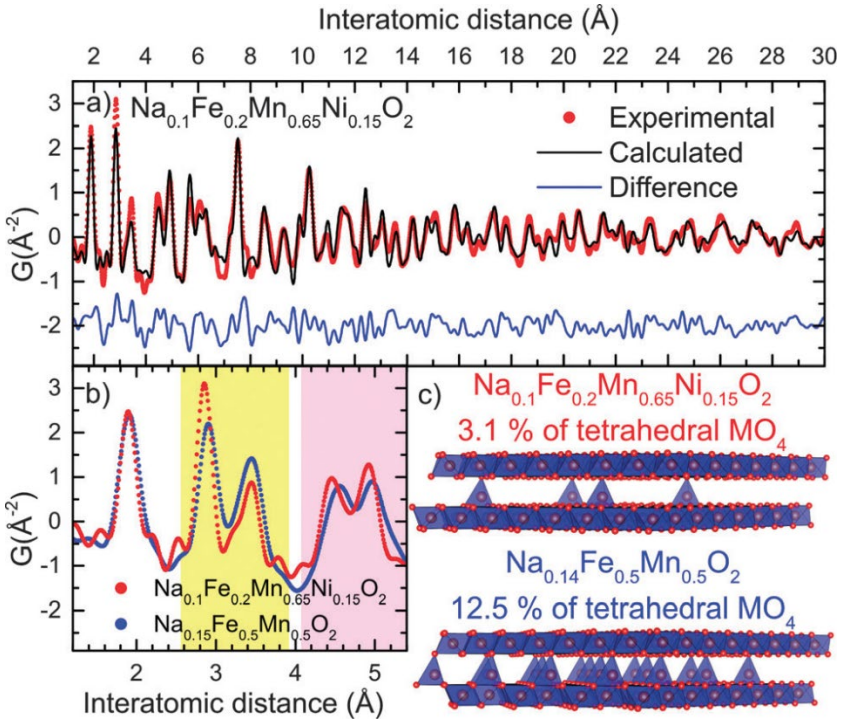

Figure 1.11 (a) Fit of the PDF curves of chemically oxidized Z-$Na_{0.1}Fe_{0.2}Mn_{0.65}Ni_{0.15}O_2$ (b) comparison of the short range experimental PDF of Z-$Na_{0.14}Fe_{0.5}Mn_{0.5}O_2$ and Z-$Na_{0.1}Fe_{0.2}Mn_{0.65}Ni_{0.15}O_2$ showing the evolution in the MO_6/MO_4 ratio (yellow shading) and the contraction of the bilayer thickness (lavender shading); (c) schematic representation of the two structures.[79]

significant transition metal (especially Fe^{3+}) migration to the Na layer at Z-phase of $Na_x[Mn_{0.5}Fe_{0.5}]O_2$ was demonstrated while it is suppressed from $Na_x[Mn_{0.65}Fe_{0.2}Ni_{0.15}]O_2$ (**Figure 1.11**). Significantly, the Mossbauer spectroscopy result from electrochemically desodiated electrodes demonstrated that most of the migrated transition metal ions from the TMO_2 layer to the tetrahedral site in the Na layer were Fe^{3+} rather than Fe^{4+}, due to ligand metal charge transfer in the Fe-O bond, which is also known as oxygen redox. Although oxygen redox in the P2-type layered oxides is proposed in this report, the link between the local structural evolution and oxygen redox needs to be investigated. Some reports suggest the local structure environment enables the oxygen anion redox from the Li-rich transition metal oxide materials.[41, 84, 85] Those studies suggest that a Li-O-Li_{TM} or Li-O-□$_{TM}$ (Li_{TM} = Li in the TM site of the

TMO_2 layer, $\square_{TM}$ = cation antisite vacancy defect in the TMO_2 layer formed by cation migration) local atomic configuration in the layered transition metal oxides is required to oxidize the oxide ion at high voltage (4.6 V vs Li/Li^+). However, some questions still remain: Are there other possible structural environments that enable oxygen redox? And is oxygen redox concomitant with or triggered by transition metal migration? What transition metals can cause oxygen redox? In chapter 3 and 4 of this thesis, the link between oxygen redox and local structural evolution in P2-type $Na_{0.67-x}[Mn_{0.5}Fe_{0.5}]O_2$ and its Cu and Ni substituted compounds is explored to seek answers for those questions..

Generally, the phase transition in sodium layered oxide materials brings structural instability over the cell cycling, owing to strain in the crystal structure and transition metal migration to the Na layer that are mainly induced by TMO_2 layer gliding and a local structural distortion at high desodiated states, respectively. Therefore, transition metal (e.g., Ti, Ni, and Cu) substitution for Jahn-Teller active Fe^{3+} ion in P2-type $Na_{0.67-x}[Mn_{0.5}Fe_{0.5}]O_2$ was suggested as one of the solutions to improve the structural stability and capacity retention of the electrode materials.[86-89] Along with this approach, redox inactive alkali metal substitution is also suggested as one of the strategies to improve the structural stability of P2-type layered oxide materials over the cell cycling. In 2014, Y. S. Meng et al. reported the Li substitution effect on the structural and electrochemical properties of a P2-$Na_x[Li_yNi_zMn_{1-y-z}]O_2$ ($0 < x, y, z < 1$).[88] From their report, a P2-$Na_{0.8}[Li_{0.12}Ni_{0.22}Mn_{0.66}]O_2$ compound (**Figure 1.12**) showed a sloping voltage profiles for charge/ discharge, which indicates a solid solution process for sodium de/intercalation without Z-phase transition. The material exhibits a discharge capacity of ~ 115 mAh/g within a voltage range of 2.0 ~ 4.4 V and 91% capacity retention after 50 cycles. An in-situ synchrotron x-ray diffraction study on P2-$Na_{0.8}[Li_{0.12}Ni_{0.22}Mn_{0.66}]O_2$ proved that there is no phase transition in the structure upon charge, and implied the emergence of local TMO_2 layer stacking faults at high voltage region by showing the broadening of the initial XRD peaks. This result contrasts with the other P2-type sodium electrodes (e.g., P2- $Na_{0.67-x}[Mn_{0.5}Fe_{0.5}]O_2$, $Na_{0.67-x}[Mn_{0.65}Fe_{0.2}Ni_{0.15}]O2$, and

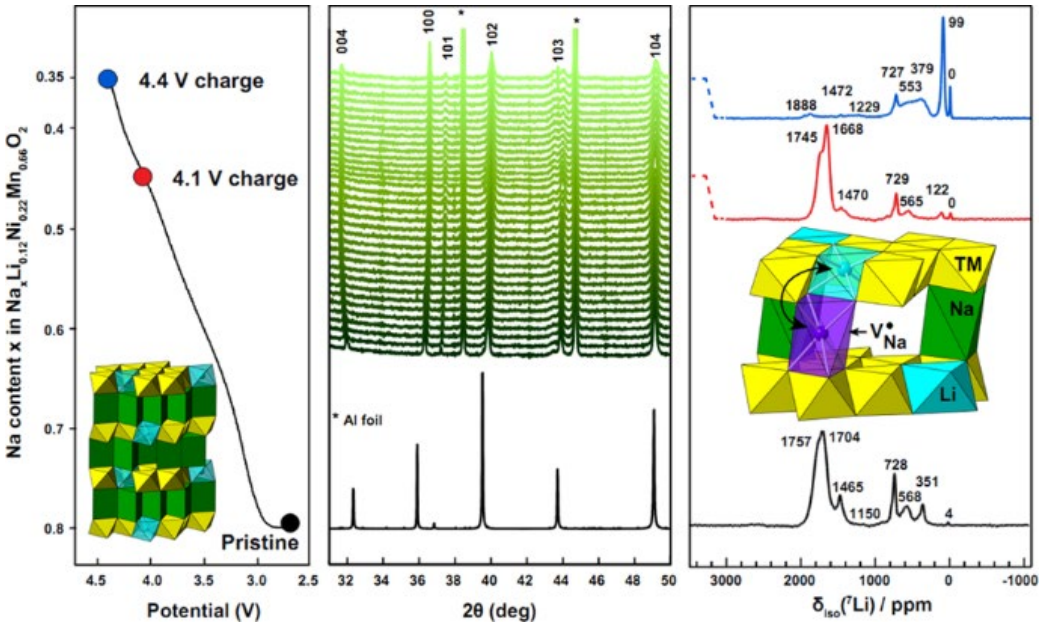

Figure 1.12 (Left) Charge profile of $Na_{0.8-x}[Li_{0.12}Ni_{0.22}Mn_{0.66}]O_2$. (Middle) In situ XRD of $Na_{0.8-x}[Li_{0.12}Ni_{0.22}Mn_{0.66}]O_2$ indicates the preserved initial-P2 type structure upon charge to 4.4 V with increasing O2-like staking faults. (Right) Ex-situ solid state NMR reveals the reversible migration of Li^+ ions from the transition metal layer to the Na^+ layer upon charge.[88]

$Na_{2/3-x}[Ni_{1/3}Mn_{2/3}]O_2$),[77, 79] which experience a P2 to O2-type phase transition while charged to 4.4 V in an Na cell. In addition, Li substitution for transition metal also enabled higher Na^+ contents in P2-$Na_{0.8}[Li_{0.12}Ni_{0.22}Mn_{0.66}]O_2$ compared to non-substituted P2-$Na_{0.67}TMO_2$, due to the lower valence of Li^+ ions than TM ions in the electrode material. Further, ex-situ solid state nuclear magnetic resonance (NMR) spectroscopy demonstrated reversible Li migration from the octahedral site in the TMO_2 layer to a tetrahedral site in the Na layer upon charging, with an evolution of stacking faults. Consequently, Li substitution for transition metal inhibited the P2 to O2-like phase transition in the $Na_{0.8-x}[Li_{0.12}Ni_{0.22}Mn_{0.66}]O_2$ upon charging to 4.4 V, and demonstrated a stable discharge capacity of ~ 110 $mAh{\cdot}g^{-1}$ from $Ni^{2+/4+}$ redox over 50 cycles.

In 2014, S. Komaba's group reported a P2-$Na_{5/6}[Li_{1/4}Mn_{3/4}]O_2$ compound performing a high capacity of ~ 180 mAh/g which is close to its theoretical capacity based on $Mn^{3+/4+}$ redox.[90] In this report, an ex-situ synchrotron X-ray diffraction (SXRD) study conducted on charged $Na_x[Li_{1/4}Mn_{3/4}]O_2$ electrode showed that there is no phase transition from P2 to O2 nor OP4 phases similar to the P2-$Na_{0.8}[Li_{0.12}Ni_{0.22}Mn_{0.66}]O_2$ phase discussed above. Interestingly, the first charge profile of the material showed a long voltage plateau at 4.0 V which is also observed with the Li-rich NMC as it is presented in section 1.2.1.[91, 92] The SXRD study further indicated that the material has a superlattice structure associated with Li/Mn ordering in the TMO_2 layer, similar to Li_2MnO_3 in Li-rich NMC, and the superlattice XRD peak disappears when the cell is charged to 4.5 V. Based on the SXRD and electrochemistry results, the authors claimed that the long voltage plateau from the first charge is an indication of in-plane cation rearrangement and partial removal of lattice oxygen from the structure to compensate the charge in the material. The high reversible discharge capacity (~180 mAh/g) and capacity retention of ~ 97 % up to 20 cycle showed that $Na_{5/6}[Li_{1/4}Mn_{3/4}]O_2$ is a promising candidate for high energy density NIBs.

On the other hand, in 2014 P. G. Bruce et al. approached with Mg^{2+} ion to substitute transition metal in P2-$Na_{0.67}MnO_2$ and reported P2-$Na_{0.67}[Mn_{1-x}Mg_x]O_2$ ($0 \leq x \leq 0.2$) compound.[93] Compared to P2-$Na_{0.67}MnO_2$, the P2-$Na_{0.67}[Mn_{0.8}Mg_{0.2}]O_2$ electrode had an enhanced discharge capacity of ~ 150 mAh/g within a 1.5 - 4.0 V range, with capacity retention of 96 % over 25 cycles, decreased voltage hysteresis, and suppressed phase transitions from P2 to OP4-like. It should be noted that archiving structural stability by Mg substitution results in a loss of capacity, as it removes redox active Mn from the electrode. From a further study of the quenching effect on the crystal structure evolution and electrochemical performance of P2-$Na_{0.67}[Mn_{1-x}Mg_x]O_2$ ($0 \leq x \leq 0.2$), it was demonstrated that quenching can suppress orthorhombic distortion in the compounds by decreasing the amount of Jahn-Teller active Mn^{3+} ions.

In the same year (2014), S. Komaba et al. also reported Mg substituted P2 sodium layered transition metal oxide electrodes, P2-$Na_{0.67}[Mg_{0.28}Mn_{0.72}]O_2$,[94] which is similar to P2-$Na_{0.67}[Mg_{0.2}Mn_{0.8}]O_2$ presented by P. G. Bruce.[93] P2-$Na_{0.67}[Mg_{0.28}Mn_{0.72}]O_2$ has a reversible discharge capacity of ~ 220 mAh/g when charged to 4.5 V, which is higher than less Mg substituted electrode ($Na_{0.67}[Mn_{0.8}Mg_{0.2}]O_2$) when charged to 4.0 V. Indeed, the high reversible discharge capacity value of $Na_{0.67}[Mg_{0.28}Mn_{0.72}]O_2$ exceeds its theoretical capacity calculated based on the $Mn^{3+/4+}$ redox from the compound. According to the report, $Na_{0.67}[Mg_{0.28}Mn_{0.72}]O_2$ electrodes show a long voltage plateau at 4.2 V during the first charge, which is similar to the $Na_{5/6}[Li_{1/4}Mn_{3/4}]O_2$ compound described above.[90] S. Komaba et al. attributed this electrochemical property of the material to the oxide ion redox enabled by Mg ion substitution. To the best of the author's knowledge, this is the first report of an oxide ions redox induced by Mg ions in TMO_2 layer that is similar to the effect of Li in the transition metal site from Li-rich NMC and P2-$Na_{5/6}[Li_{1/4}Mn_{3/4}]O_2$.

Following this report, P. G. Bruce's group further explored the Mg substitution effect on the electrochemical properties of $Na_{0.67}[Mg_{0.28}Mn_{0.72}]O_2$.[94] From their experiments, they observed no O_2 gas evolution upon charging up to 4.5 V, but did notice changes in the electron structure of the lattice oxygen by monitoring the O K-edge peak over the voltage plateau evolution at 4.2 V. Based on the experimental data and density functional theory (DFT) calculation result, they suggested that the relatively high energy of Mg^{2+} 3s state compared to O 2p in Mg-O interactions results in weak ionic Mg-O bonds and places the O 2p states in a relatively high energy position, at which oxygen redox is accessible within the voltage stability window for organic electrolytes. This is in contrast to the strong covalent TM–O interactions, which push the O 2p states down in energy and let the electrolyte decompose before oxidizing the oxide ion.(**Figure 1.13)** Although the Bruce group's proposed mechanism of oxygen redox in $Na_{0.67}[Mg_{0.28}Mn_{0.72}]O_2$ is similar to the study on oxygen redox involving a Li^+- O 2p - Li^+ interaction in $Li[Li_{0.2}Ni_{0.13}Co_{0.13}Mn_{0.54}]O_2$ that was reported by G. Ceder et al. in

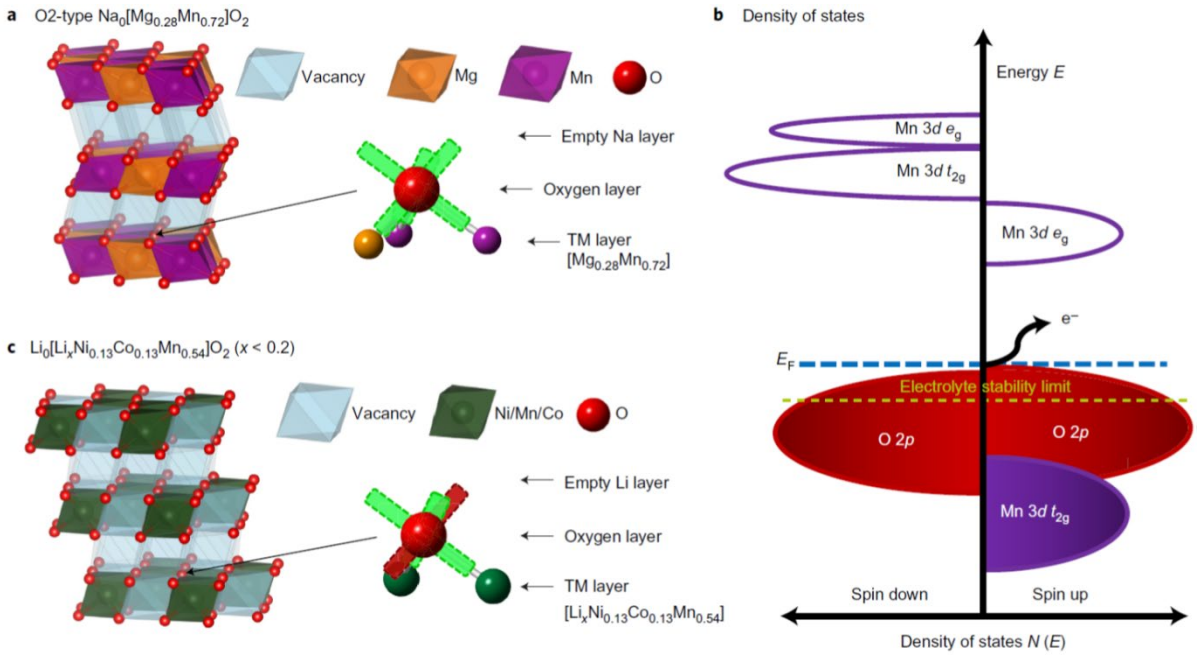

Figure 1.13 (a) Left: O2 structure of the sodium-deficient phase $Na_0[Mg_{0.28}Mn_{0.72}]O_2$. The layers of translucent octahedra represent the vacant Na sites. Right: coordination around oxygen in the O2 structure of $Na_0[Mg_{0.28}Mn_{0.72}]O_2$, in which oxygen is coordinated octahedrally by two Mn and one Mg from the TM layer and three vacancies from the AM-ion layer. (b) Schematic that illustrates the energy versus density of states in the sodium-deficient phase of $Na_0[Mg_{0.28}Mn_{0.72}]O_2$. (c) Left: O3 structure of the lithium-deficient phase $Li_0[Li_xNi_{0.13}Co_{0.13}Mn_{0.54}]O_2$, x < 0.2. Li and $(Ni_{0.13}Co_{0.13}Mn_{0.54})$ in the octahedral sites in the TM layers are shown by blue and green octahedra, respectively. The layers of translucent octahedra represent the vacant Na sites. Right: coordination around oxygen in an alkali-rich compound in which all the AM ions have been removed (x = 0) to leave an oxygen with only two coordinating cations and a completely non-bonded O 2p orbital (red). Other O 2p orbitals are shown in green. Adopted with permission from ref. 85. Copyright 2016 Nature Publishing Group.

2016,[84] this work further suggests that oxygen redox is indeed possible without excess alkali metal ion in the sodium layered TM oxides. The details of the suggested oxygen redox mechanisms in Li/Na layered TM oxide materials are described in section 1.4.

As has been presented so far, the redox inactive metal substitution for transition metals for P2 layered Na_xTMO_2 can improve the structural stability and capacity performance by suppressing cation mixing and enabling oxygen redox activation. Along with this approach, utilizing the biphasic stricture from

Na layered transition metal oxides has been proposed as a promising strategy to achieve high energy density positive electrodes for Na-ion batteries. In 2015, H. Zhou et al. reported on P2 + O3 composite type $Na_{0.66}Li_{0.18}Mn_{0.71}Ni_{0.21}Co_{0.08}O_{2+\delta}$ synthesized by a co-precipitation reaction. Their Rietveld refinement result indicated a P2:O3 ratio of 94:6 (wt%) in the material and the TEM result showed that the O3 type phase was integrated in the P2 type structure. The positive electrode material performed at a specific capacity of about 200 mAh g-1, cycled between 1.5 - 4.5V.[95] Stefano Passerini's group also reported $Na_{0.76}Mn_{0.5}Ni_{0.3}Fe_{0.1}Mg_{0.1}O_2$, consisting of 41 wt% of P2 + P3 phase, 49 wt% of O3, and 10 wt% of cubic phases. The electrochemistry of the material showed a specific capacity of 155 $mAh{\cdot}g^{-1}$ at 15$mA{\cdot}g^{-1}$ cycling within a potential range of 2.0 - 4.3V.[96] Early in 2018, Teofilo Rojo's group published a paper on P2 + O3 composite $Na_{2/3}Li_{0.18}Fe_{0.2}Mn_{0.8}O_2$ by solid-state synthesis, which utilizes only the earth abundant elements, Mn and Fe. The electrode material had a discharge capacity of ~ 125 $mAh{\cdot}g^{-1}$ for the first cycle (1.5 - 4.2 V) and poor structural stability resulting in a low capacity retention of 69 % at 0.1 C after 100 cycles.[97] Recently, G. K. Veerasubraman et al. reported on P2 + O3 biphasic $Na_{0.5}Li_{0.1}[Fe_{0.5}Mn_{0.5}]_{0.9}O_2$ performing ~ 120 mAh g-1 at 20 $mA{\cdot}g^{-1}$ (1.5 - 4.0 V) with a capacity retention of 92.5 % over 30 cycles,[98] and Teofilo Rojo's group also reported a Co- and Ni- free P2 + O3 biphasic lithium stabilized $Na_{0.8}Li_{0.2}Fe_{0.2}Mn_{0.6}O_2$ (P2 : O3 = 34 : 60), synthesizing the material by sol-gel method and shifting the voltage window to higher values (2.0 - 4.6 V) (**Figure 1.14**).[99] The galvanostatic cycling test of the material showed that the electrode delivered an initial capacity of 174 $mAh{\cdot}g^{-1}$ with a capacity retention of 82% over 100 cycles. However, the charging voltage profile exhibited a huge voltage polarization during the first 20 cycles, which is indicative for some restructuring/ordering, as well as Fe migration from the octahedral site to the sodium site. On the other hand, R. R. Li et al. reported Li free P2 + O3 biphasic $Na_{0.67}Ni_{0.33}Mn_{0.67-x}Sn_xO_2$ (x = 0, 0.05, 0.1, 0.2) compounds, which can achieve a P2:O3 ratio of 1:1 (wt%) for an x = 0.1 compound, which can perform ~ 150 mAh g-1 at 30 mA g-1 (2.0 - 4.3 V) with a capacity retention of ~ 61.5 % over 30 cycles.[100] Although these biphasic structure

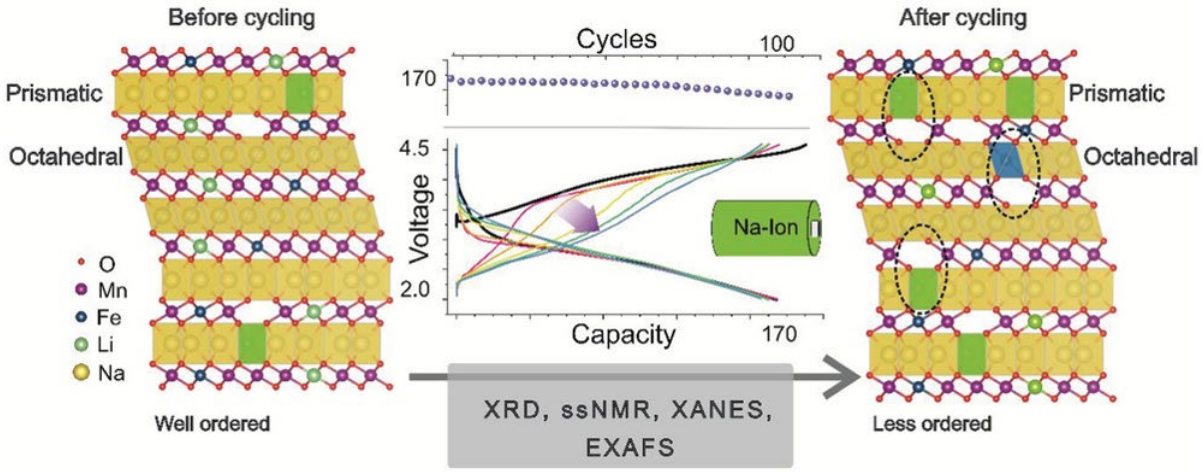

Figure 1.14 Schematic presentation of $Na_{0.8}Li_{0.2}Fe_{0.2}Mn_{0.6}O_2$ (P2 : O3 = 34 : 60) crystal structure before and after cycling, capacity retention, voltage profiles, and used analytical tools. The crystal structure changes along with ions migrations over cell cycling influenced over all electrochemical performance.[99]

materials show promising electrochemistry as a positive electrode for high energy density Na-ion batteries, their cycle life, voltage, and capacity need further improvement.

As is presented here, P2-type sodium layered transition metal oxide materials have been actively developed to overcome the drawbacks of prior materials, such as structural instability by phase transition, capacity degradation and voltage fading by cation mixing. However, the question still remains how to design the structural features of the sodium layered transition metal oxides with respect to high voltage redox for high energy density Na-ion batteries. To answer this question, a deep understanding of local structure evolution in various layered oxide materials enabling cation and anion redox and their mechanism is required to develop high energy density positive electrode materials for Na-ion batteries. In the next section, the concepts of an anion redox mechanism, and of structural environment enabling the oxygen redox in sodium layered transition metal oxides, are further described.

1.4 Anion Redox in Li/Na Layered Transition Metal Oxide Electrode Materials

1.4.1 Evidence of anion redox from Li/Na transition metal oxide positive electrodes

The concept of anion redox in Li-ion batteries evolves from Li-ion batteries employing $LiTiS_2$ positive electrodes, as proposed by Whittingham.[8] In a theoretical study conducted by P. Moreau et al. in 1996, a charge transfer shared between the Ti and the S ions in $LiTiS_2$ positive electrodes upon charging the Li cell was first suggested.[101] In the same year, Z. Y. Wu et al. measured S K-edge XAS and also demonstrated that the charge transfer is shared by the Ti and S ions upon charging the $LiTiS_2$ electrode.[102] For transition-metal dichalcogenides and trichalcogenides, such as FeS_2 and TiS_3, J. Rouxel et al. used ligand-hole chemistry and demonstrated the possibility for sulfur ligands to exist in a higher oxidization state of S than 2- due to the transition metal 3d band penetrating the ligand 2sp bands at charged states (**Figure 1.15**).[103, 104] Later in 1999, the oxygen redox activity was observed from the $LiNi_{1-x}Co_xO_2$ (x = 0, 0.3, and 1) positive electrode charged to high voltage (~ 4.6 V vs. Li/Li^+), based on slightly shortened O–O distances in CoO_6 octahedra measured by synchrotron X-ray diffraction.[105] A further interesting study conducted by M. H. Lindic in 2005 on mixed anions in the oxygen and sulfur compound TiO_ySz, indicated that S ions actually contribute more than Ti ions to the redox process, without the O ion redox.[106] This is due to a higher energy band of S 3p than the O 2p that largely overlaps with the M d bands over O 2p. This would explain the absent of oxygen redox when sulfur redox is activated.(**Figure 1.16**)

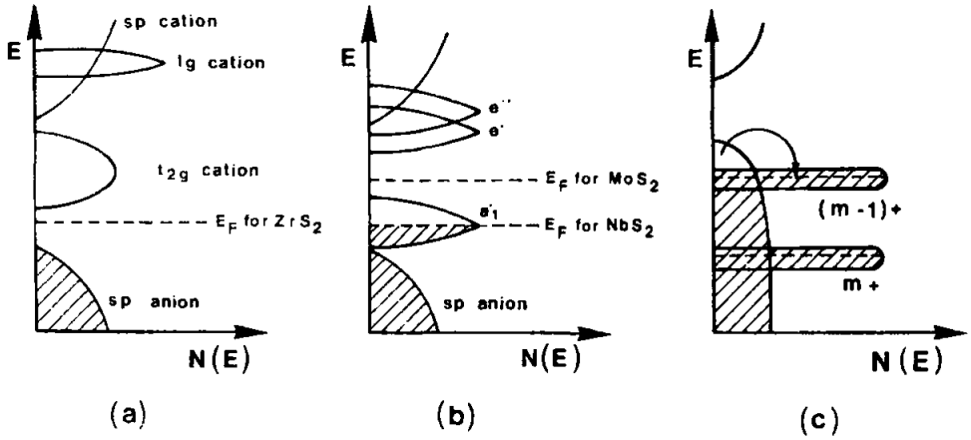

Figure 1.15 Band structure models for layered dichalcogenides of (a) ZrS_2 and TiS_2 in octahedral coordination and (b) NbS_2 and MoS_2 in trigonal prismatic coordination. (c) Lowering of d levels and sp to d electron transfer on moving to the right-hand side of the periodic table. Adopted with permission from ref. 103.

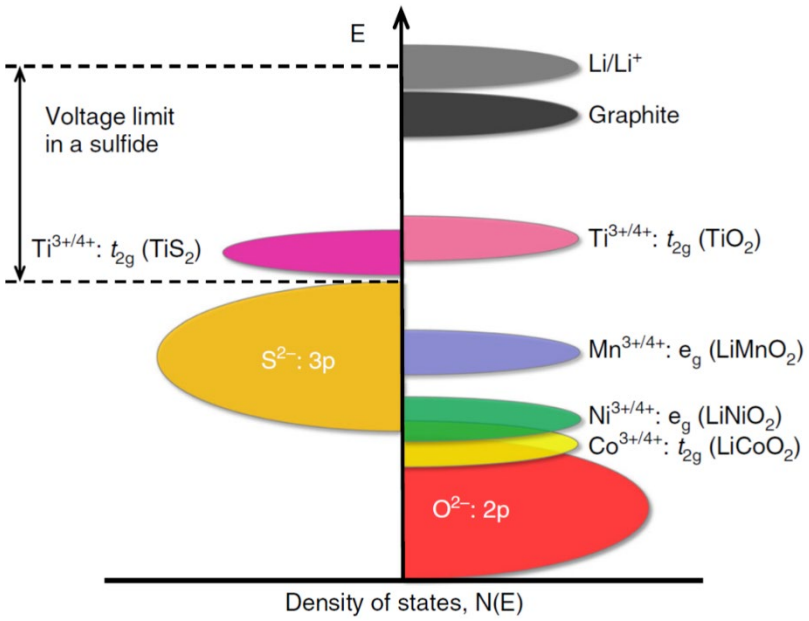

Figure 1.16 Positions of the redox energies relative to the top of the anion: p bands. The S^{2-} 3p band energy is lying at a higher than the O^{2-} 2p band energy.[18]

Meanwhile, after the development of Li-rich NMC (LRLO) in 2004,[36] H. Koga et al. proposed reversible oxygen redox from the lattice oxygen in LRLO, by combining multiple characterization techniques,[107, 108] such as operando X-ray absorption spectroscopy for transition metal K-edges, which indirectly indicated the oxygen redox by showing the insufficient overall charge compensation from cationic redox upon Li cell charge. In addition to this proposal, the oxygen redox was further explored by J. M. Tarascon's group in 2015, who employed other Li-rich transition metal oxides (Li_2TMO_3, TM = Ru, Ir), which are isostructural with Li_2MnO_3 in LRLO.[109, 110] From those reports, the oxidation state change of lattice oxygen from O^{2-} to $(O_2)^{n-}$ species were indicated by x-ray photoelectron (XPS) and electron paramagnetic resonance (EPR) spectroscopy. In addition, the O-O dimer ($(O_2)^{n-}$) formation that is visualized through transmission electron microscopy (TEM) images and neutron diffraction was suggested as evidence of oxygen redox. A year later, K. Luo et al. experimentally proved the reversible oxygen redox activity in LRLO by employing ^{18}O substituted LRLO with operando mass spectroscopy to quantify the amount of O_2 and CO_2 that evolved from the first activation cycle.[85] From this experiment, a lower amount of evolved O_2 and CO_2 from the LRLO particle was observed than was expected from the charge capacity estimated as oxygen redox. In addition, O K-edge soft x-ray absorption spectroscopy (SXAS) further demonstrated the reversible electron structure change from the lattice oxygen upon the charge/discharge of the Li cell. In 2017, W. E. Gent et al. utilized resonant inelastic x-ray scattering (RIXS) to observe the electron structure change in O 2p state from Li-rich NMC positive electrodes, and demonstrated reversible oxygen redox from the electrode by showing the preserved RIXS feature of oxygen redox after 500 galvanostatic cycles (**Figure 1.17**).[43]

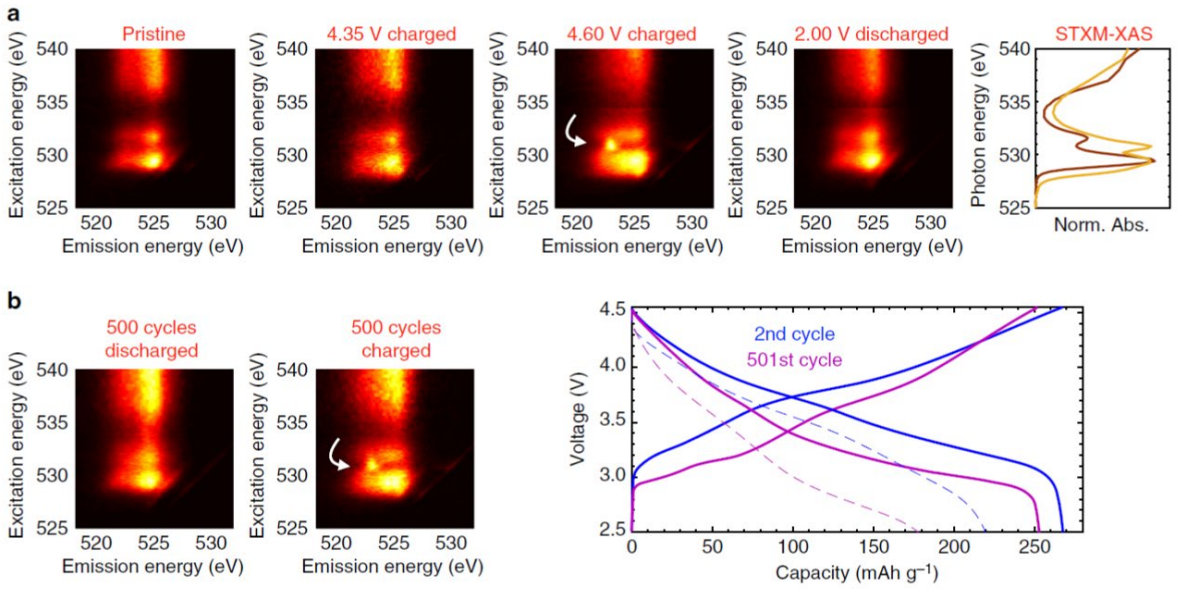

Figure 1.17 Probing the nature and stability of oxygen redox. (a) The unique emission signature at 4.60 V indicated by the white arrow supports an electronic restructuring associated with O redox. Right: XAS obtained in the pristine (brown) and fully charged (tan) state during the first cycle for comparison. (b) RIXS maps acquired before and after the 501st charge on an electrode cycled 500 times at 1C/2C charge/discharge rate, showing that the reversible oxygen redox feature persists for hundreds of cycles. The voltage curves for the second and 501st cycles at C/68 (solid) and 2C (dashed) show that most of the capacity fade over 500 cycles is from increased impedance and overpotential, and that the intrinsic capacity is largely retained.[43]

Importantly, this study demonstrated a correlation between the transition metal migration and lattice oxygen redox upon the delithiation of LRLO.

Recently, R. A. House et al. reported different anion redox features between honeycomb-ordered $Na_{0.75}(Li_{0.25}Mn_{0.75})O_2$ and ribbon-ordered $Na_{0.6}(Li_{0.2}Mn_{0.8})O_2$ by combining experimental (high resolution resonant inelastic X-ray scattering (HR-RIXS), X-ray diffraction, neutron diffraction, and ^{6}Li magic angle-spinning NMR) and theoretical studies (DFT calculation).[111] Especially, the HR-RIXS confirmed the low energy loss feature (near to elastic X-ray scattering line) in charged $Na_{0.75-x}[Li_{0.25}Mn_{0.75}]O_2$ electrode which is indicative of the formation of O_2 molecule in the structure. The combined study revealed that the O_2 molecule actually responsible for the oxygen redox for $Na_{0.75-}$

$_x[Li_{0.25}Mn_{0.75}]O_2$ electrode rather than oxide ion redox which is conventionally accepted idea for oxygen redox in the layered TM oxide materials. In 2020, the same group employed HR-RIXS together with ^{17}O magic angle spinning NMR, and further revealed that the reversible oxygen redox in Li-rich NMC is also due to the O_2 molecule trapped in TM vacancy cluster rather than oxide ion.[45] These findings are contrast to the widely accepted idea about oxygen redox mechanism in Li-rich NMC, and highly impact the future research direction for utilizing oxygen redox in Li-rich NMC materials.

1.4.2 Understanding anion redox mechanism in Li/Na transition metal oxide positive electrodes

In order to understand the oxygen redox mechanism in Li/Na layered transition metal oxide positive electrodes, various hypotheses were proposed for the local structural environment satisfying oxygen redox. The conventional understanding of oxygen redox in lithium layered transition metal oxides can be explained by $LiCoO_2$ (LCO). The lattice oxygen contribution to the redox behavior of LCO was normally explored by measuring the electronic structure change of oxygen by X-ray absorption spectroscopy (XAS), which is indicative of electron excitation from O 1s to oxygen hole state in Co 3d-O 2p hybridized orbital.[112] The creation of oxygen hole state in Co 3d-O 2p bond can be described as follows. From the energy band diagram in **Figure 1.18**, Co^{3+} (d^6) is generally in a low spin state in CoO_6 octahedra, and the remaining six 3d electrons are present in nonbonding "t_{2g}" (d_{xy}, d_{yz}, and d_{xz}, quotation mark indicate t_{2g}-like band in distorted octahedra) bands while Co 3d bands overlap with O 2p bands due to the high covalence of the Co-O bond. Upon charging the LCO positive electrode, the electrons in the Co 3d states ("t_{2g}" band) will be removed first, and the Fermi level will move towards a lower energy level near the top of the O 2p states and trigger oxygen redox as soon as the electrons in O 2p states exceed the Fermi level (**Figure 1.18**).[16] The most important concept here is a ligand to metal charge transfer (LMCT) process resulting from the removal of electrons in O 2p bands. Namely, the LMCT occurs in Co-O bond at the deep charged state of LCO, such that the Co remains

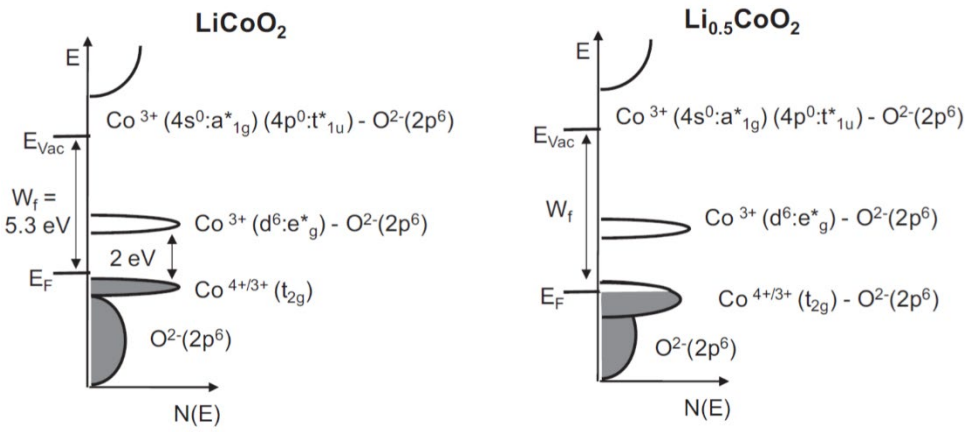

Figure 1.18 Electronic band structure of $LiCoO_2$ (left) and $Li_{0.5}CoO_2$ (right) as deduced from DFT calculations and XAS measurements.[16]

less oxidized by receiving electrons from oxygen and holes are generated on the oxygen. As is mentioned above, in 1999, J. M. Tarascon et al. had suggested the formation of electron holes in anions of $LiNi_{1-x}Co_xO_2$ (x = 0, 0.3, and 1) upon delithiation, due to electron transfer from O 2p to transition metal 3d bands. In addition, they demonstrated the shortening of the interplanar O-O bond in delithiated CoO_2 and NiO_2 end members by utilizing in-situ synchrotron x-ray diffraction.[105]

Since the development of LRLO, studies regarding a local structural environment for enabling the reversible oxygen redox from the Li-rich transition metal oxides have been undertaken by many battery scientists. In 2016, D. H. Seo et al. suggested that the non-bonded (or unhybridized) O 2p orbital from the Li-O-Li configuration existing in Li-rich transition metal oxides (especially Li_2TMO_3 compounds) or cation-disordered compounds enables the oxygen redox rather than introduced holes in O 2p-TM 3d hybridized orbitals.[84] Based on DOS calculation results from the various possible local atomic environments in cation-disordered layered TM oxides, they demonstrated that the non-bonded O 2p orbital energy in the Li-O-Li configuration is higher than hybridized O 2p orbitals ("$t_{1u}^b, a_{1g}^b, e_g^b$"), and it locates slightly higher than the "t_{2g}" band of d orbital of TMs (**Figure 1.19**). Therefore, the oxygen

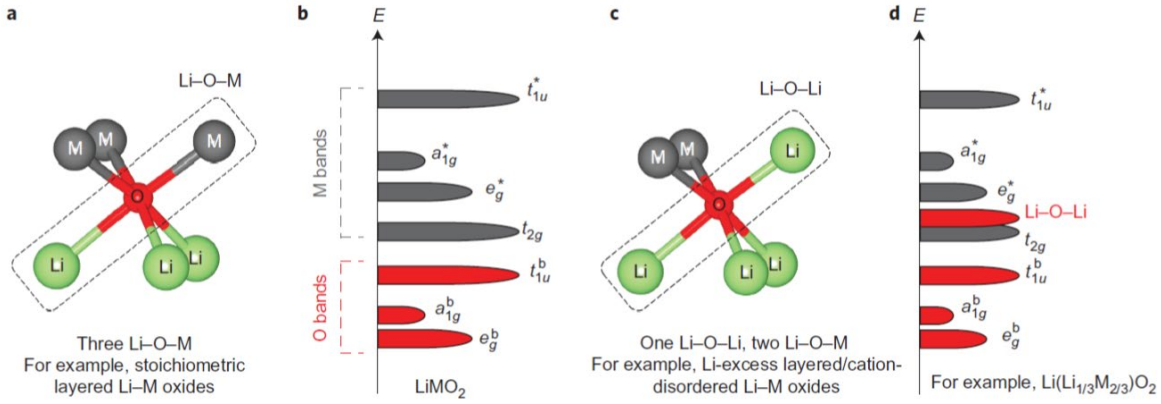

Figure 1.19 Schematic presentation of origin of the oxygen redox from the Li-O-Li configuration. (a) Local atomic coordination around oxygen consisting of three Li-O-M configurations in stoichiometric layered Li metal oxides (Li-M oxides). (b) Schematic of the band structure for stoichiometric layered Li-M oxides such as $LiCoO_2$. (c) Local atomic coordination around oxygen with one Li-O-Li and two Li-O-M configurations in Li-excess layered or cation-disordered Li-M oxides. (d) Schematic of the band structure for Li-excess layered Li-M oxides such as Li_2MnO_3. Adopted with permission from ref. 84. Copyright © 2016, Nature Publishing Group.

in the Li-O-Li local structure can be more easily oxidized than TM, as the non-bonded O 2p orbital provides electrons before the oxidation of TM upon the delithiation of the positive electrode materials in Li-ion batteries. This theory also brought up the important point that oxygen redox doesn't change the number of electrons from the hybridized TM d states, as implied by the observed negligible change in TM K-edge energy shift upon charging the LRLO positive electrode. In addition to the energy states of non-bonding O 2p orbitals, 3d orbital energy states of TMs in a positive electrode material are also necessary to better understand the oxygen redox. From the report by G. Assat et al., the importance of understanding Mott-Hubbard splitting in O 2p - TM 3d hybridized orbitals that enables anion redox in Li-rich NMC electrodes is well emphasized by showing three different scenarios where Mott-Hubbard splitting determines the charge compensation upon the delithiation of Li-rich NMC electrode.[41] The energy band structure from common TM layered oxide ($LiTMO_2$) and honeycomb type TM layered oxide (Li_2TMO_3) in LRLO are compared by band energy diagrams, as shown in **Figure 1.20a and b**.

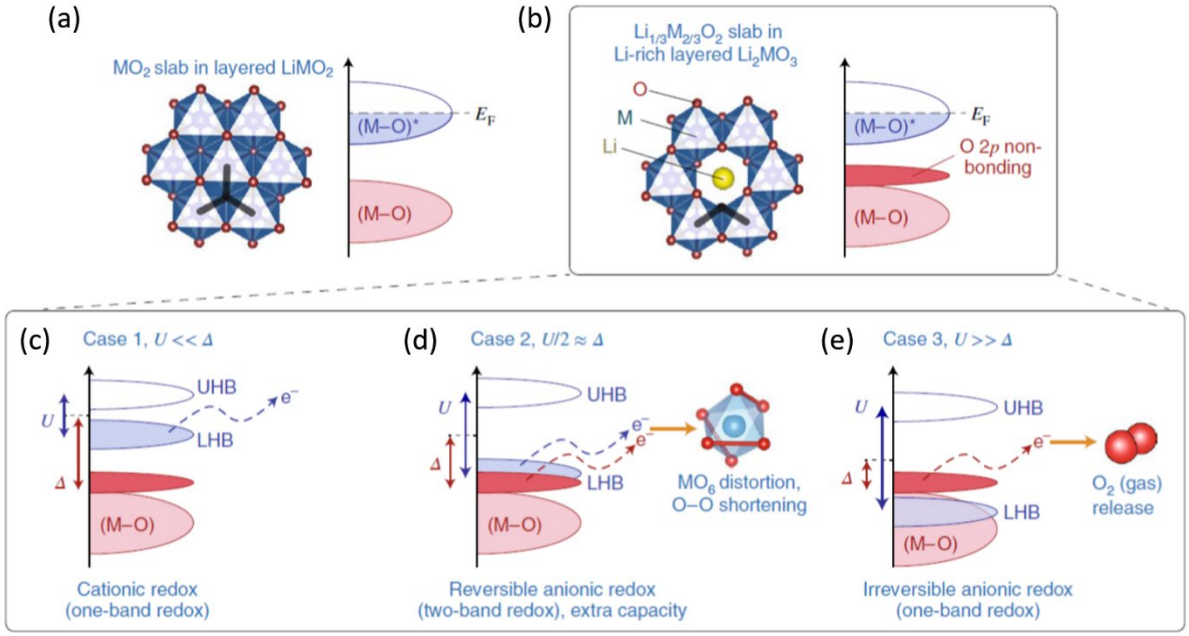

Figure 1.20 Band structure of oxides and the anion redox mechanism. A crystal structure comparison of (a) $LiTMO_2$ and (b) Li-rich Li_2TMO_3 and their band structures. The Li_2MO_3 band structure is further classified under three cases (c-e) depending on the relative positions between the d–d Coulomb repulsion (U) and the charge transfer (Δ). Note that these are schematic band structures without taking into account electron–electron correlations. UHB and LHB denote the upper and lower Hubbard bands respectively. Reproduced with permission from ref. 41. Copyright © 2018, The Springer Nature.

In both band structures, overlapping orbitals between the TM 3d orbital and the O 2p orbital degenerates into bonding (M–O) and antibonding (M–O)* bands, which show ligand and metal characters, respectively. The energy difference between bonding (M–O) and antibonding (M–O)* bands is represented by the charge transfer term "Δ," which reflects the electronegativity difference "Δχ" between TM and O (**Figure 1.20c-e**). From the honeycomb type TM layered oxides (Li_2TMO_3), the non-hybridized O 2p orbital in the Li site of the TMO_2 layer is positioned slightly over the hybridized O 2p - TM 3d (M-O) orbital. At this point, Mott-Hubbard splitting of antibonding (M–O)* bands determines the accessibility to oxygen redox from the TM oxide electrode materials upon charge process. In **Figure 1.20c-e**, the d–d Coulomb interaction (U) splits the partially filled (M–O)* band

(Mott–Hubbard splitting), resulting in empty upper-Hubbard bands (UHB) and filled lower-Hubbard bands (LHB). As U is inversely proportional to the d orbital volume, the type of TM in the lithium TM oxide systems strongly affects the extent of Mott–Hubbard splitting. From the honeycomb type layered TM oxide in Li-rich NMC, the relative position of LHB to the non-bonded O 2p orbital depends on the values of U to Δ that result in three different cases for electron extraction from the orbitals upon charging lithium layered TM oxide electrodes, as shown in **Figure 1.20c-e.** The first case is U << Δ (**Figure 1.20c** represents the highly ionic TM-O bond performing a classic one-band cationic redox. In this case, electrons are extracted from the filled LHB upon charging the lithium layered TM oxide electrode. For the opposite case of U >> Δ (**Figure 1.20e**), one-band redox also occurs upon the charge process but the electron is directly removed from the non-bonded O 2p orbital owing to its higher energy state than LHB. In this case, oxidized lattice oxygen forms reactive oxygen species (e.g., $O^{\bullet-}$, O_2^{-}), which react with the electrolyte. This side reaction eventually results in irreversible loss of the lattice oxygen from TM oxides and deteriorates the electrode performance over the cell cycling. If U and Δ values are U/2 ≈ Δ (**Figure 1.20d**), the LHB and non-bonded O 2p orbitals overlap and this enables the cation and anion redox to occur simultaneously upon delithiation of the electrode material. The electron extraction from the overlapped LHB and non-bonded O 2p band leads to a Fermi level degeneracy upon delithiation, and destabilizes the structure of the TMO_6 octahedra in the honeycomb type electrode materials. In order to stabilize the degenerated Fermi level, that is, to re-stabilize the overall energy of TMO_6 octahedra, the TMO_6 octahedra symmetry must be lowered by Jahn-Teller distortion or Peierls distortion, which are accompanied by peroxo (O-O) dimer formation through the shortening O-O distance (in **Figure 1.20d**).[113] Consequently, TM-$(O_2)^{n-}$ interactions can be stabilized in distorted TMO_6 and this reversible process allows the honeycomb type layered TM oxide to perform at a higher charge/discharge capacity than their theoretical capacity, which only takes cation redox into account.

In contrast to the oxygen redox theories above, Bruce's group recently reported the new anion redox mechanism through a systematic comparison study of the link between voltage hysteresis and anion redox feature from honeycomb-ordered $Na_{0.75}(Li_{0.25}Mn_{0.75})O_2$ and ribbon-ordered $Na_{0.6}(Li_{0.2}Mn_{0.8})O_2$.[111] By combining experimental studies (high resolution resonant inelastic X-ray scattering (HR-RIXS), X-ray diffraction, neutron diffraction, and ^{6}Li magic angle-spinning NMR) and theoretical studies (DFT calculation), the O_2 molecule formed in TM vacancy cluster (which is formed by in-plane TM migration) in charged $Na_{0.22}(Li_{0.25}Mn_{0.75})O_2$ was suggested as an oxygen redox center, while e^- hole formation in oxide ion in charged $Na_{0.21}(Li_{0.2}Mn_{0.8})O_2$ is responsible for the oxygen redox rather than O_2 molecule due to the restricted O_2 formation by absence of TM vacancy cluster. Based on these observation, the higher voltage hysteresis evolution from honeycomb-ordered $Na_{0.75-x}(Li_{0.25}Mn_{0.75})O_2$ electrode compared to ribbon-ordered $Na_{0.6}(Li_{0.2}Mn_{0.8})O_2$ is attributed to the reversible formation and cleavage of O_2 molecule. In 2020, the same group further revealed that the reversible oxygen redox in LRLO is also due to the trapped O_2 molecule in TM vacancy cluster as shown in **Figure 1.21**.[45] As it was demonstrated from honeycomb-ordered $Na_{0.75}(Li_{0.25}Mn_{0.75})O_2$, the energetically favorable O_2 molecule is formed by disproportionation of oxidized oxygen ions ($O^- + O^- \rightarrow O^{2-} + O^0$, $2O^0 \rightarrow O_2$) in the TM vacancy cluster during the first charge, and the O_2 molecule reversibly reduces to O^{2-} (O_2 cleavage) during the subsequent discharge forming a very weak ionic bond with Li ion that induces voltage hysteresis. For subsequent charge, the O_2 molecule forms again in the TM vacancy cluster, but at lower voltage (~ 3.6 V) than the first charge (~ 4.6 V), and the O_2 molecule oxidize again due to its higher band energy than the oxide ion that enables the reversible oxygen redox over the subsequent cycling. Therefore, the formation of O_2 molecule can stabilizes oxygen redox in the honeycomb-ordered layered TM oxide materials, while restricted formation of TM vacancy cluster in ribbon-ordered layered TM oxides stabilizes oxygen redox by forming oxygen electron hole state without oxygen dimerization.

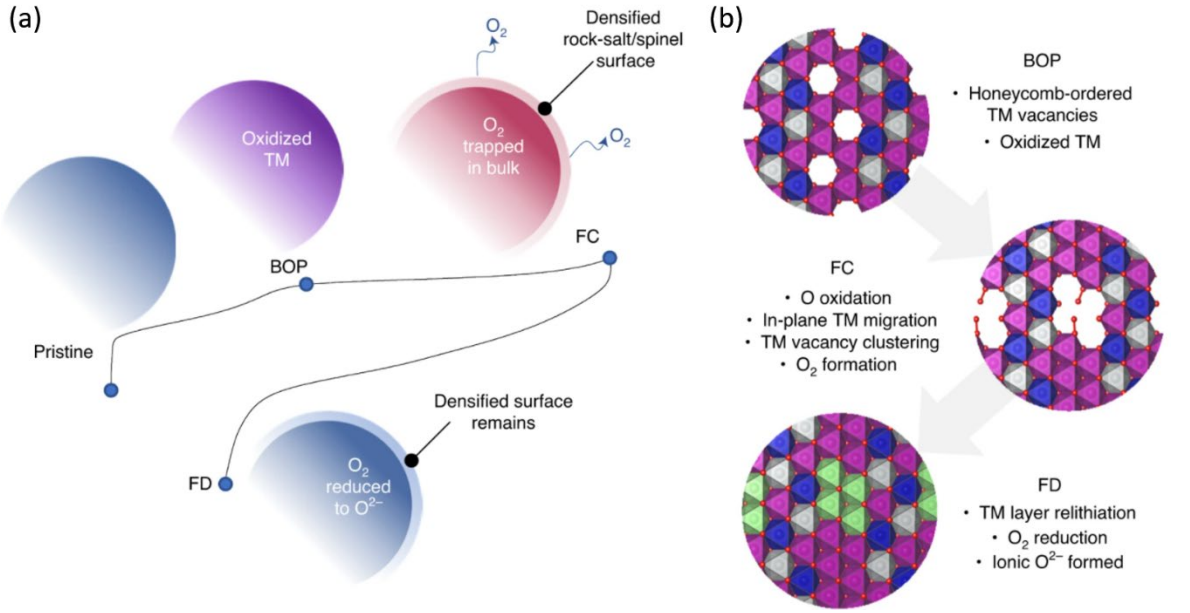

Figure 1.21 Mechanism of first-cycle voltage hysteresis. (a) Macroscale changes to the cathode particles: pristine to BOP, predominantly TM redox and some overlap with O-redox. BOP to FC, O^{2-} is oxidized to form O_2 gas, which is lost at the surface of the particles and leads to surface densification (rock salt/spinel). Trapped O_2 molecules in the bulk can be reduced on discharge to reform O^{2-}. (b) Atomic-scale changes to ordering within the TM layer: BOP to FC - as O^{2-} is oxidized in the honeycomb-ordered TM layer, in-plane TM migration into the sites vacated by Li^+ is triggered. The most energetically favoured motif is the vacancy cluster, which allows for the formation of molecular O_2 (FC). On subsequent discharge Li^+ returns to the TM layers, but now in different sites (occupied previously by TM ions).[45]

As the suggested anion redox mechanism explained so far is based on the Li_2TMO_3 systems,[41, 114] such a theory is facing some challenges with the discovery of new materials and studies of different alkali or alkaline-earth metal ion containing systems. For instance, Li or Mg containing P2-type sodium layered transition metal oxides, such as $Na_{0.66}Li_{0.18}Fe_{0.12}Mn_{0.7}O_2$,[115] $Na_{2/3}[Mg_{0.28}Mn_{0.72}]O_2$,[94] and $Na_{2/3}Mn_{0.72}Cu_{0.22}Mg_{0.06}O_2$,[116] and $NaLi_{1/3}Mn_{2/3}O_2$ [117] exhibit Na-O-Li or Na-O-Mg configurations, which provide the high energy state of the non-bonded O 2p band for oxygen redox, as is discussed above with Li-O-Li. However, recent studies on other P2-type sodium positive electrode materials, such as $Na_{0.67}Mn_{0.5}Fe_{0.5}O_2$,[79] P2-$Na_{0.78}Co_{1/2}Mn_{1/3}Ni_{1/6}O_2$,[118] and $Na_{2/3}Ni_{1/3}Mn_{2/3}O_2$,[119] suggest that those

materials also perform the reversible oxygen redox over the Na cell cycling even though they have Na-O-(Li or Mg) configurations in the crystal structure. Therefore, further research is needed to fully understand the environment that enables oxygen redox in Li/Na layered transition metal oxides and apply them to developing high energy density positive electrode materials for Li/Na ion batteries.

1.5 All solid state batteries

In addition to the development of electrode materials with high energy density for LIBs, the safety concerns of high voltage (> 4.0 V vs Li/Li^+) LIBs have emerged and remained as one of the most challenging issues associated with their commercialization. The existing LIBs adopt organic electrolytes that enable TM oxide positive electrodes to work at a high voltage by forming a cathode electrolyte interphase (CEI) layer. While the CEI layer prevents continuous electrolyte decomposition for the subsequent cycling, it also increases the overall resistance of the electrodes. As the organic electrolytes are intrinsically flammable and volatile, it acts as a fuel when the LIB catches fire due to thermal runaway caused by high internal cell resistance and/or short circuit due to Li dendrite penetration from the anode to the cathode. To eliminate the risk factor of battery explosion, research on non-flammable solid electrolyte (SE), which has been spotlighted as a breakthrough technology, is crucial.

All-solid-state batteries (ASSBs) consist of SE/active material mixture electrodes and an SE separator layer as shown in **Figure 1.22**.[120] The composite structured electrodes can be fabricated by grinding active materials with SE or through heat treatment with SE precursors, depending on the types of SEs. Once all the materials are prepared, they should be pelletized under a certain pressure to ensure good contact between each component. Therefore, the performance of ASSBs highly depends on the physical and electrochemical properties of SEs. To compete with conventional LIBs, SEs need to overcome multiple challenges, such as high ionic conductivity, a wide electrochemical stability window,

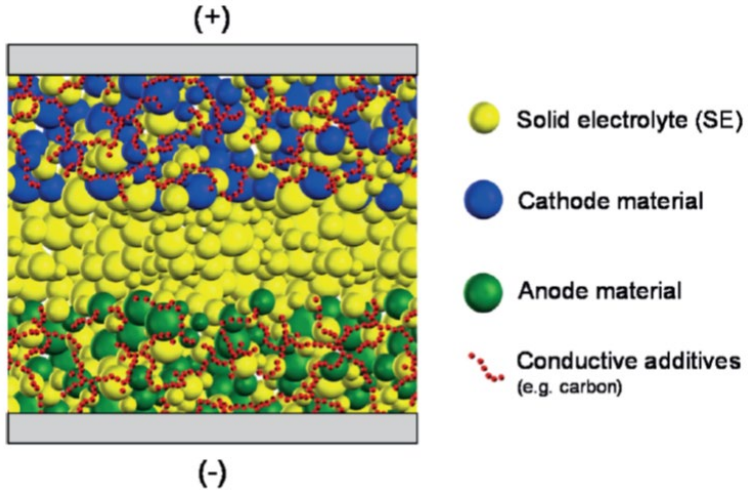

Figure 1.22 Schematic diagram of all-solid-state lithium batteries (ASSBs) using sulfide solid electrolyte (SE).[120]

and chemical stability with active materials. First, archiving the high Li ionic conductivity ($\geq 10^{-3}$ S·cm^{-1}) of SE at room temperature is one of the most important issues. **Figure 1.23** shows the Li-ion conductivities of some representative SEs from oxide, sulfide, chloride, and solid polymer materials together with conventional liquid electrolytes.[121–123] As shown in the plot, sulfide solid electrolytes exhibit ionic conductivity that is comparable to the liquid electrolytes at room temperature. However, sulfide solid electrolytes have poor electrochemical oxidation stability due to the oxidation of S^{2-} anions occurring at ~ 2.5 V,[124, 125] which hinders their direct use with high voltage cathode materials for high energy density ASSBs. Although the oxide SEs can provide better electrochemical stability when compared to sulfide SEs, their ionic conductivities are generally lower than sulfide SEs.[126] In addition,

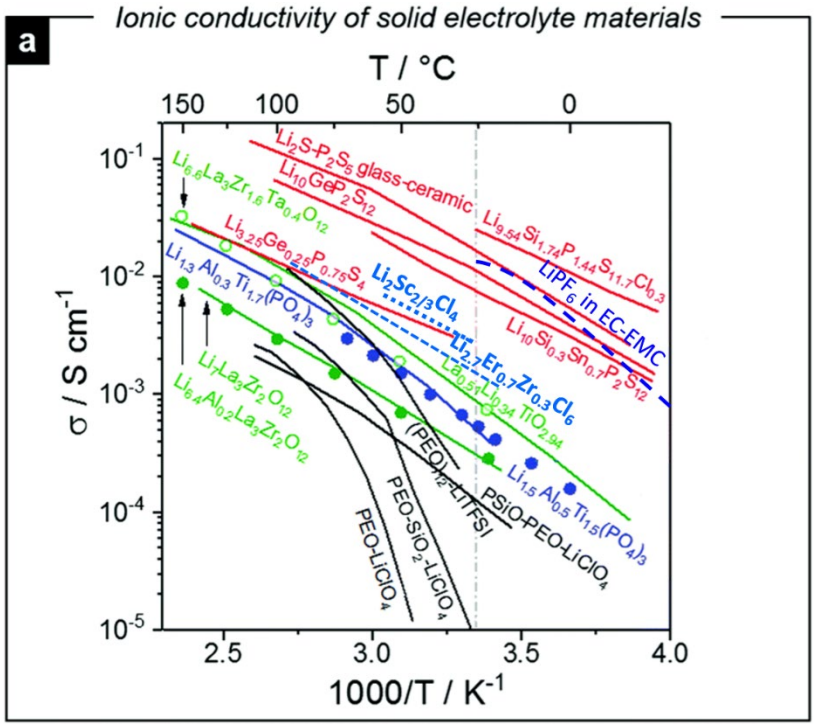

Figure 1.23 Comparison of the ionic conductivity of various SSEs.[121-123]

they require a high-temperature sintering process to ensure adequate contact with active materials, which accompanies side reaction with TM oxide electrode materials and results in a significant increase in resistance at the surface of the active materials.[127, 128] Although solid polymer electrolytes (SPE) can provide better contact with active materials, flexibility, and chemical stability, which enable the direct use of Li metal as an anode, their low ionic conductivities ($10^{-4} \sim 10^{-5}$ S·cm^{-1}) at room temperature, low electrochemical oxidation stability limit (< 4.0 V), and vulnerability to dendrite growth have restricted them from commercialization.[129, 130] Lithium phosphorus oxynitride (LiPON)-type solid electrolytes generally exhibit Li-ion conductivity (~ 10^{-6} S·cm^{-1}) that is too low to compete with liquid electrolytes, so they are ruled out for practical ASSB application. Along with these types of solid electrolytes, lithium metal halide solid electrolytes have also been reported to apply to ASSBs. Conventionally,

lithium metal halide solid electrolyte was known to exhibit low ionic conductivity ($\leq 10^{-5}$ S·cm^{-1}) and low oxidation voltage.[131] However, recent theoretical and experimental studies demonstrated that lithium metal halide solid electrolytes exhibit high ionic conductivities ($\geq 10^{-3}$ S·cm^{-1}), high oxidative stability (~ 4.3 V), and good chemical stability to oxide cathode materials, which enable them to apply to ASSEs, whereas they are chemically unstable to lithium metal anode.[132] These findings urged researchers in the ASSB field to revisit metal halide solid electrolytes and explore the physical and chemical properties of halide solid electrolytes. In this thesis, among many lithium superionic conductors, the author focuses on the lithium chloride solid electrolyte, especially lithium lanthanide chlorides.

1.5.1 Lithium Chloride Solid Electrolyte

Recently, lithium metal chlorides have been spotlighted as a promising solid electrolyte due to their high ionic conductivities and wide electrochemical stability window.[133, 134] Among the various halide solid electrolytes, lithium metal chloride/bromide solid electrolytes were extensively explored and their high ionic conductivities were theoretically and experimentally demonstrated.[123, 133–138] In 1992, H. D. Lutz et al. first reported the ternary chloride Li compounds $M'_3M''Cl_6$ (M' = Li, Na, Ag; M'' = In, Y) and their ionic conductivities at various temperature (e.g., Li_3YCl_6 = ~ 10^{-5} S·cm^{-1}, Li_3InCl_6 = ~ 10^{-3} S·cm^{-1} at 200 °C).[139] Later, in 1997, G. Meyer et al. reported the crystal structures of the ternary chloride of rare-earth elements (Li_3MCl_6, M = Tb-Lu, Y, Sc) and analyzed the ionic motion from their structures through ^{7}Li-NMR spectroscopy. This study showed ternary lithium metal chlorides crystalize into three types of crystal phases likely due to the ionic radius ratio between chloride and the metal ions: trigonal (Li_3ErCl_6), orthorhombic (Li_3YbCl_6), and monoclinic (Li_3ScCl_6). Along with lithium lanthanide (Er, Yb) chlorides, Li_3YCl_6 has also been extensively explored due to higher earth abundancy and much lighter atomic mass of Y when compared to lanthanides,[140] while Li_3YCl_6 and

Table 1.2 Chloride SEs with group 3 elements (Sc, Y, Ho, Er, and Yb)

Material	Conductivity (S·cm^{-1}) - measured	Structure	Ref.
Li_3YCl_6	0.51 x 10^{-3} (at 25 °C)	Trigonal ($P\bar{3}m1$)	135
$Li_{2.5}Y_{0.5}Zr_{0.5}Cl_6$	1.4 x 10^{-3} (at 25 °C)	Orthorhombic ($Pnma$)	123
Li_3ErCl_6	3.3 x 10^{-4} (at 25 °C)	Trigonal ($P\bar{3}m1$)	137
$Li_{2.633}Er_{0.633}Zr_{0.367}Cl_6$	1.1 x 10^{-3} (at 25 °C)	Orthorhombic ($Pnma$)	123
Li_3YbCl_6	~ 10^{-4} (at 300 °C)	Orthorhombic ($Pnma$)	138
	Conductivity (S·cm^{-1}) - calculated		
Li_3ScCl_6	29 x 10^{-3} (at 25 °C)	Trigonal ($P\bar{3}m1$)	134
Li_3YCl_6	14 x 10^{-3} (at 25 °C)	Trigonal ($P\bar{3}m1$)	134
Li_3HoCl_6	21 x 10^{-3} (at 25 °C)	Trigonal ($P\bar{3}m1$)	134
Li_3ErCl_6	3 x 10^{-3} (at 25 °C)	Trigonal ($P\bar{3}m1$)	136

Li_3ErCl_6 were reported to show the same trigonal (space group of *P*-3m*1*) crystal structure and similar ionic conductivities (**Table 1.2**). The recent investigation of Li_3YCl_6 (LYC) and Li_3YBr_6 (LYB) by T. Asano et al. in 2018 significantly boosted research on lithium metal chloride solid electrolytes that prove the possibility of using them for practical ASSBs.[135] According to their report, Li_3YCl_3 (trigonal) and Li_3YBr_3 (monoclinic) synthesized by a ball-milling method exhibited high ionic conductivities of 0.51 × 10^{-3} S·cm^{-1} and 0.72 × 10^{-3} S·cm^{-1} at room temperature, respectively. The bond valence site energy (BVSE) study showed the ionic pathways for both materials in accord with an *ab initio* molecular dynamics study performed by Y. Mo et al. in 2019.[134] Importantly, this study demonstrated that Li_3YCl_6 solid electrolyte is compatible with uncoated LCO showing the ASSB cycling up to 100 cycles (see **Figure 1.24**). This finding inspired other researchers working in the solid electrolyte field to revisit and explore the various lithium chloride solid electrolytes. Another type of lithium chloride solid electrolyte, Li_3ErCl_6 with trigonal structure, was predicted by A. D. Sendek et al.to be a promising solid electrolyte based on its calculated high ionic conductivity (3 × 10^{-3} S·cm^{-1}, RT) through DFT molecular dynamics simulations.[136] S. Muy et al. also predicted the high ionic conductivity and wide electrochemical stability window (~ 3.6 V) of Li_3ErCl_6 via high-throughput screening from the Materials Project database using a lattice dynamic descriptor (lithium-phonon band center).[137]

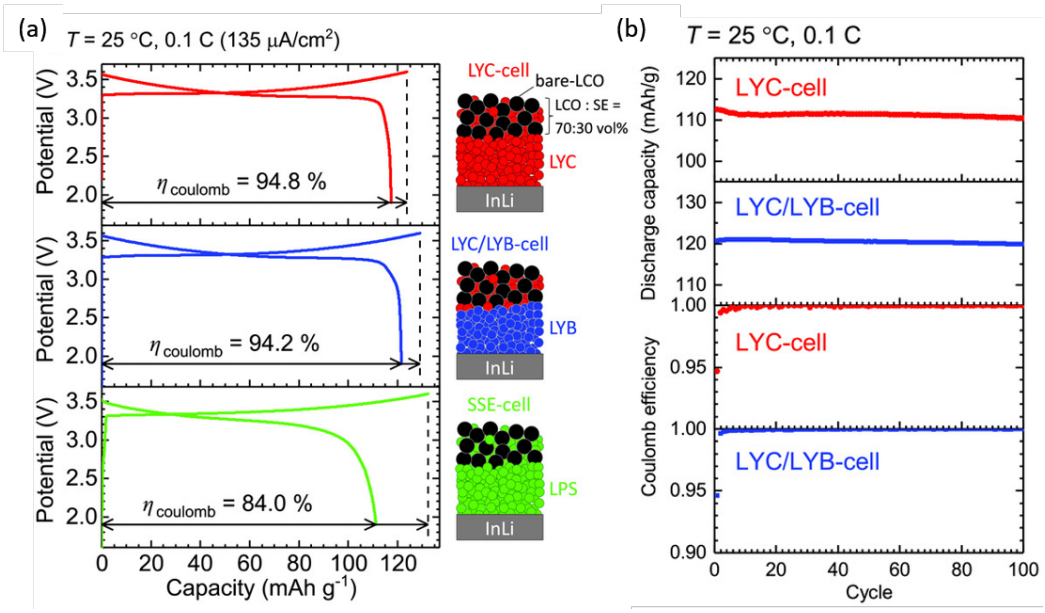

Figure 1.24 (a) Initial charge/discharge curves of bulk-type ASSB cells. The schematic cell structures are shown on the right side of each plot. (b) The discharge capacity retention and coulombic efficiency of the LCO/LYC (Li_3YCl_6)/Li-In cell and the LCO/LYC+LYB (Li_3YBr_6)/Li-In cell for 100 cycles. Reproduced with permission from ref. 135. Copyright © 2018 WILEY-VCH Verlag GmbH & Co. KGaA, Weinheim

In addition, they further synthesized Li_3ErCl_6 through ball-milling and measured ionic conductivity of 3.3×10^{-4} S·cm^{-1} at room temperature. As the previous studies showed that Li_3ErCl_6 and Li_3YCl_6 crystalize into the same trigonal phase (space group of *P*-3*m*1) due to the similar ionic radii of Er (89 pm) and Y (90 pm), similar ionic transport properties were also demonstrated.[141] In 2020, K. H. Park et al. further showed that the aliovalent metal substitution for Er^{3+} and Y^{3+} with Zr^{4+} in both materials ($Li_{3-x}(Y/Er)_{1-x}Zr_xCl_6$, $0.1 \leq x \leq 0.8$) also results in the same trigonal (*P*-3*m*1) to orthorhombic (*Pnma*) phase transition and the similar ionic conductivity improvement from ~ 10^{-5} S·cm^{-1} to ~ 10^{-3} S·cm^{-1}.[123] The combined single-crystal x-ray diffraction, neutron diffraction, and BVSE studies demonstrated that the improved ionic conductivity of Zr-substituted materials is due to the newly introduced lithium sites and vacancies in the structure that play key roles in changing the energy landscape for Li-ion migration.

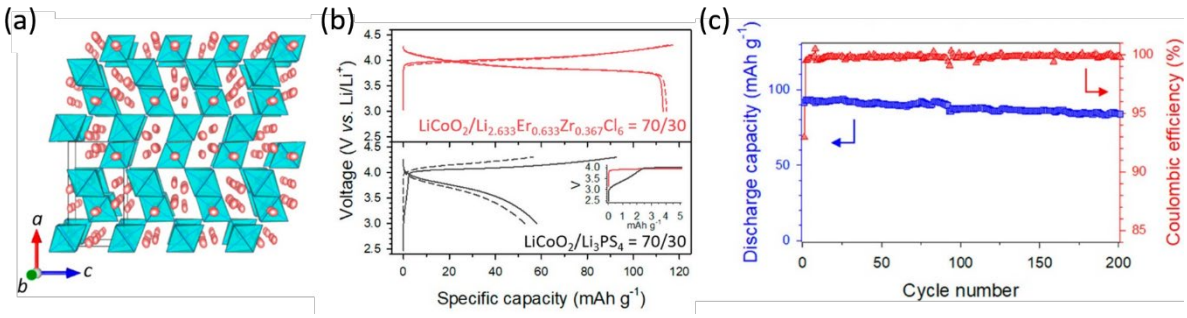

Figure 1.25 (a) View along the [010] direction in $Li_{2.5}Er_{0.5}Zr_{0.5}Cl_6$. The $(Er/Zr)Cl_6$ octahedra are shown in blue, and Li ions are shown as red spheres. (b) The first (solid line) and second (dotted line) cycles of LCO + SE cathode composite using $Li_{2.633}Er_{0.633}Zr_{0.367}Cl_6$ (red) and Li_3PS_4 (black) as the SE (0.11 $mA{\cdot}cm^{-2}$, ~ 0.1 C). Inset shows the voltage plateau at ~ 3.1 V from Li_3PS_4 SE cell that is indicative of sulfur oxidation. (c) Room-temperature cycling performance of the $LiCoO_2$/chloride-SE|Li_3PS_4|$Li_{11}Sn_6$ cell employing $Li_{2.633}Er_{0.633}Zr_{0.367}Cl_6$ as the chloride SE in the cathode composite. The cycling test was conducted at a current density of 0.55 $mA{\cdot}cm^{-2}$ (3.0 - 4.3 V vs. Li/Li^+). Reproduced with permission from ref. 123. Copyright © 2020 American Chemical Society.

The high electrochemical stability window (~ 4.3 V) and chemical stability of $Li_{2.633}Er_{0.633}Zr_{0.367}Cl_6$ solid electrolyte to uncoated LCO was also demonstrated by showing the stable LCO ASSB cell cycling up to 200 cycles at room temperature as shown in **Figure 1.25**. This year (2021), Y. S. Jung et al. investigated Fe substituted Li_2ZrCl_6 as a solid electrolyte and reported the ionic conductivity of 0.5 mS/cm (30 ℃) for $Li_{2.25}Zr_{0.75}Fe_{0.25}Cl_6$ synthesized by ball-milling.[142] Although Fe substitution for Zr increases ionic conductivity, Fe^{3+} oxidation to Fe^{4+} is observed upon a cycling of LCO adopted ASSB within the voltage window of 3 ~ 4.3 V (Li/Li^+). On the other hand, no oxidation state change of Zr^{4+} is confirmed by XPS after 100 cycles.

In conclusion, Li_2ZrCl_6 and $Li_{2.1}Zr_{0.9}Fe_{0.1}Cl_6$ (low Fe content) solid electrolytes showed good electrochemical stability enabling the use of uncoated LCO cathode in ASSBs for 100 cycles (at 0.5 C) with discharge capacity retention of ~ 92 % (~ 152 $mAh{\cdot}g^{-1}$ → ~ 140 $mAh{\cdot}g^{-1}$). Since the feasibility of the lithium chloride solid electrolytes that enable the use of 4V-class TM oxide cathode materials

without any coating was confirmed by the aforementioned reports, further development in processing lithium chlorides as a coating material layer for high voltage cathode materials is required to propel the commercialization of high voltage ASSBs.

1.6 Scope of Thesis

This thesis presents our study for developing high energy density positive electrode materials for Li and Na ion batteries and developing a new chloride solid electrolyte enabling to use 4 V-class positive electrode materials without coating. To be specific, Li-rich NMC positive electrode is explored to for LIBs, while layered and polyanion type sodium transition metal oxides positive electrodes are explored for NIBs. In addition, a lithium chloride solid electrolyte is synthesized and its structure and electrochemical properties are explored in ASSBs.

Chapter 1 presents a brief introduction to the Li-ion and Na-ion batteries with a focus on the essential achievements and findings to date on Li and Na transition metal oxide positive electrodes, including the concept of anion redox. Chapter 2 is an overview of the synthesis and characterization techniques that were used in this thesis.

Chapter 3 presents our study of polydopamine (PDA) coating effect on Li-rich NMC positive electrode material with respect to chemical property of PDA that scavenges reactive oxygen species (ROS, e.g. $O_2^{\bullet-}$, $^1O_2$). A solution based PDA coating method that enables the conformal coating for porous Li-rich NMC without altering the crystal structure is demonstrated. The ROS scavenging PDA coating effect is demonstrated by comparing the bare and coated electrodes in terms of accumulation of undesirable cathode electrolyte interphase layer on the electrode surface and CO_2 and O_2 gas evolution during the first activation cycle. Importantly, these results indicate less oxidized oxygen from the PDA coated electrode surface demonstrating the suppressed oxygen loss and the suppressed undesirable layered-to-rocksalt phase transition. These PDA coating effects are reflected in the

enhanced rate capability (lower cell impedance) and discharge capacity retention compared to bare electrode.

Chapter 4 investigates high-valent oxygen redox in the P2-$Na_{0.67-x}[Fe_{0.5}Mn_{0.5}]O_2$ positive electrode where Fe is partially substituted with Cu (P2-$Na_{0.67-x}[Mn_{0.66}Fe_{0.20}Cu_{0.14}]O_2$) or Ni (P2-$Na_{0.67-x}[Mn_{0.65}Fe_{0.20}Ni_{0.15}]O_2$). From a combined analysis of X-ray pair distribution function (PDF) profiles and electrochemical voltage hysteresis with resonant inelastic X-ray scattering (RIXS) and X-ray absorption near-edge structure (XANES), the link between antisite-vacancy defect formed by transition metal migration and high-valent oxygen redox is demonstrated. In addition, density of states calculation elaborates considerable anion redox in NMF and NMFC without the widely accepted requirement of an A-O-A' local configuration in the pristine materials (where A= Na and A'= Li, Mg, vacancy, etc.).

Chapter 5 presents our study on new findings of particular local structures which stabilize reversible anion redox from layered $Na_{2-x}Mn_3O_7$. By combining experimental and theoretical studies, we show that coulombic interactions between oxidized oxide-anions and the negatively charged Na vacancies can stabilize hole polarons on oxygen at 4.2 V vs. Na/Na^+. This result highlights the role of coulombic interactions for stabilizing anion redox and suggests a new design rule to stabilize high-valent oxygen for application to high energy density positive electrode materials for NIBs.

Aiming at developing a high energy density positive electrode for SIBs, a new 4V class Na^+ intercalaion polyanion material is studied in addition to sodium layered transition metal oxides. In Chapter 6, a microwave assisted hydrothermal synthesis route is presented as a rapid synthesis method for nanostructured $Na_2Co_2(SeO_3)_3$/graphene oxide composite. By virtue of its moderately inductive polyanionic framework, the air and moisture stable selenite $Na_2Co_2(SeO_3)_3$ electrode displays a highly suitable redox potential of ≈ 4 V versus Na/Na^+ based on the Co^{2+}/Co^{3+} couple. This study suggests a

selenite polyanion positive electrode for the first time in the battery field by proving that $Na_2Co_2(SeO_3)_3$/graphene oxide composite is compatible with conventional liquid organic electrolytes.

Chapter 7 reports a discovery of metastable Li_3YbCl_6 and its mixed-metal halide solid electrolytes, $Li_{3-x}Yb_{1-x}Zr_xCl_6$, synthesized at 350 °C. The trigonal structure of metastable Li_3YbCl_6 phase is solved by multiple diffraction methods (neutron, single-crystal, and powder X-ray). An aliovalent substitution of Yb by Zr is presented as a strategy to improve ionic conductivity of Li_3YbCl_6. The phase transition from trigonal to orthorhombic is observed while the ionic conductivity of $Li_{3-x}Yb_{1-x}Zr_xCl_6$ ($0.1 \leq x \leq 0.5$) solid electrolytes increases. Bond valence site energy of materials are compared to study the effect of Zr substitution on the improved ionic conductivity with respect to Li-ion migration energy barrier in the Zr substituted material. The high electrochemical oxidation stability of mixed-metal halide solid electrolyte is demonstrated by the stable all-solid-state cell cycling with uncoated > 4 V-class cathodes.

Chapter 8 summarizes the work of the entire thesis and challenges to address for future work.

Chapter 2

Characterization Methods and Techniques

2.1 Overview

Designing and developing high energy density electrode materials for Li or Na ion batteries require profound understanding of the science upholding each process of battery manufacturing from the material synthesis to electrochemistry measurement. In this thesis, the electrode materials were synthesized by either conventional or by testing out new methods, including solid-state synthesis, wet synthesis, microwave assisted hydrothermal synthesis, which lead to the crystallization of desired materials for insertion and extraction of Li or Na ions over discharge/charge of battery system. The studies were mainly focused on a link between the local structural evolution and redox properties of cations and anions consisting of Li or Na layered transition metal oxides. Several techniques to characterize the crystal structure and electron structure of materials were employed for this purpose.

Powder X-ray diffraction (PXRD) was carried out and combined with Rietveld refinement to determine the crystal structures of the electrode materials and pair distribution function (PDF) analysis was employed to characterize the low-crystalline phase evolved over the charge of positive electrodes. The phase transitions while charge and discharge the electrodes were monitored by operando XRD analysis. The local structure evolution and oxidation state of each transition metal near the surface or in the bulk of electrode upon charge and discharge were probed by X-ray photoelectron spectroscopy (XPS) and X-ray absorption spectroscopy (XAS), respectively. The oxidation state of lattice oxygen ion in the electrode material was confirmed by resonant inelastic X-ray scattering (RIXS). Scanning electron microscopy (SEM) and transmission electron microscopy (TEM) were conducted to observe the morphology of the particles and energy dispersive X-ray spectroscopy (EDX) was coupled with an

SEM or TEM to analyze the chemical composition for the particles. Raman spectroscopy was conducted to observe the chemical structure of organic materials on the surface of electrode after charge and discharge. The magnetic susceptibility of the electrode materials was measured by a Superconducting Quantum Interference Device (SQUID). Thermogravimetric analysis (TGA) was employed to confirm the thermal stability of the materials.

The electrochemical properties of the synthesized electrode materials was examined by cyclic voltammetry (CV) or gavanostatic charge and discharge cycling at various C-rates. The electrochemical Impedance Spectroscopy (EIS) was employed to measure the surface film resistance and charge transfer resistance of the positive electrodes. Ionic conductivity and activation energy of synthesized positive electrode materials were measure by EIS and Arrhenius plot from measured ionic conductivity at various temperature. In order to monitor the gas (O_2 and CO_2) evolution upon charging the Li-rich NMC electrode, online electrochemical mass spectroscopy (OEMS) method is employed. In this chapter, a brief basic introduction for each experimental method and characterization technique employed in this research are presented.

2.2 Synthesis Techniques

2.2.1 Solid State Synthesis

Solid state reaction is one of the most widely utilized method for synthesizing Li or Na containing transition metal oxide materials. In order to induce solid state reaction between precursors and recrystallization into desired materials, first, a stoichiometric ratio of powder precursors need to be evenly mixed by hand grinding or ball-milling followed by heat treatment. Especially, the ball milling can optimize the particle sized of grinded powder by controlling the milling time and speed. In addition, choosing the size, type and number of grinding balls significantly affects to the particle size of milled powder. For instance, either increasing the number of grinding balls or decreasing the size of grinding

balls result in decreasing the particle size of mixture powder, but selecting optimal number and size of grinding balls is required depending on the precursor powder mixture as grinding balls generate heat while colliding in the ball-mill jar that possibly changes the oxidation state of precursors. Adding nonreactive solvent to the powder mixture for the ball-milling is sometimes helpful to keep the temperature and improve the mixing level of precursor powder. Besides, a minimum amount of powder also has to be considered to prevent the ball-mill jars and balls are grinding each other. For the solid state synthesis, an effective reaction area, where the precursor particles contact each other, highly affects to the solid state reaction in terms of the number of nucleation sites and reaction kinetics determining the purity of final crystal and the total synthesis time. Pelletization of the mixture powder can provide one of the solutions for ensuring the contact among the precursor particles and facilitating the solid state reaction. The other approach to enhance the mixing level and increase the reaction sites of precursors is decreasing the particle size by sol-gel method. The sol-gel method introduces dissolution of precursors in a solvent and dry the solution to precipitate precursors mixed in a molecular level. It should be noted that the reactivity and solubility of precursors to the solvent have to be considered to obtain the precursors mixture maintaining targeted stoichiometric ratio after drying. Depending on the chemical stability of precursor or synthesized materials to the air or moisture, each synthesis process should be performed under either air or inert gas atmosphere, such as argon or nitrogen. Once the powder mixture of precursor is prepared, the powder is contained in alumina or platinum crucible and transferred to a furnace to carry out heat treatment under air, oxygen, or inert gas atmosphere. As the solid state reaction requires energy to destabilize atoms in reactants and form thermodynamically stable compound through the rearrangement (or diffusion) of the atoms, a temperature that is higher than two-third of the melting point (K) of the lower melting reactant is required to induce the solid state reaction (Tamman's rule). After heating the precursor powder for desirable reaction times, the crystalized powder is then cooled and collected from the furnace.

2.2.2 Wet Synthesis: Microwave Assisted Hydrothermal Synthesis

Along with solid state synthesis, wet synthesis method involves solvent playing a key role as chemical reaction mediator for dissolved precursor ions or molecules. Based on the type of mediator between aqueous and non-aqueous solvent, the wet synthesis methods can be classified as hydrothermal or solvothermal reaction synthesis, respectively. Wet synthesis method utilizes an autoclave (which can seal the solution in an airtight container) to reach to a temperature that is higher than liquid sample's boiling point under the high-pressure and induce the reaction for material synthesis. Generally, as the transfer of ions or molecules in liquid are much facile compared to the solid, synthesizing materials at much lower temperature with shorter reaction time can be done by wet synthesis. Furthermore, the kinetic reaction control in the wet synthesis can provide meta-stable phase of materials, which are hard to obtain by solid state synthesis as its reaction is under thermodynamic control. The synthesized particle size, morphology, crystallinity can be modified by selecting the type of solvent, temperature, salt concentration, and heat treatment time.

In addition to the conventional wet synthesis heating the sealed metal autoclave from an oven, microwave assisted wet synthesis method is developed that can directly heat the solution inside of autoclave by an alternating electric field of the radiation. If solvent molecules has dipole momentum, the electromagnetic field from microwave acts to align the dipole moments of molecules. While the oscillating electromagnetic field changes its direction rapidly, the solvent molecules rotate following the electromagnetic field and generate heat from the friction between moving molecules. The ions in the solvent also response to the oscillating electromagnetic field and generate the heat from the friction of rapidly moving ions. Therefore, to use microwave heating, at least one of the precursor components in the reaction container must absorb microwave and the container should be transparent to the microwave. The synthesized powder material after the microwave irradiation is then collected by filtration and washing to remove the solvent and any remained precursors.

2.2.3 Chemical Oxidation

Most of lithium/sodium transition metal oxide electrode materials in batteries experience the phase transition while electrochemical extraction of alkali metal ions from the crystal structure. This charge process accompanies with the transition metal oxidation to balance out the total charge in the charged electrode. The similar process can be done by chemical oxidation of the electrode material using an oxidizing agent as an electron acceptor that the counter electrode plays the role in the battery system. This chemical oxidation method enables synthesizing and analyzing the poor crystalline phase of electrode material formed after extracting alkali metal ions, especially without intervention of other amorphous materials consisting electrode such as conducting carbon or binder.

The chemical oxidation of electrode material is performed by reacting electrode material with oxidizing agent dissolved in solution, such as NO_2BF_4, Br_2 or I_2 dissolved acetonitrile solution. Based on the targeted composite, the solvent and oxidation agent should be chosen not to decompose the solvent or over-oxidize the electrode material.

2.3 Diffraction Techniques

2.3.1 Powder X-Ray Diffraction (XRD)

X-ray diffraction (XRD) is one of the most powerful non-destructive techniques for analyzing the crystal structure of materials. X-ray is an electromagnetic radiation having the wavelength ranging from ~ 0.01 Å to ~ 100 Å which are corresponding to energies in the range from ~ 100 eV to 200 keV. Generally, the wavelengths in the range of 0.5 Å ~ 2.5 Å has been the most commonly used for analysing the crystal structure as they are on the similar length scale as interatomic distance in a crystal. When electrons in the atom is irradiated by X-ray beam, each electron becomes a secondary point source of X-ray scattering and diffracts X-ray beam waves. The diffracted waves then overlap each other resulting in constructive or partial destructive interference and form an X-ray diffraction pattern.

Bragg's law explains the appearance of X-ray diffraction pattern by adopting a crystalline solid as a stacked parallel lattice planes with the interplanar distance d (**Figure 2.1)**. In this model, when two parallel monochromatic X-ray beams are irradiated to the crystal, the two neighboring parallel lattice plane reflect the each X-ray beam with the same angle (θ) to the incident beam. After the reflection, if

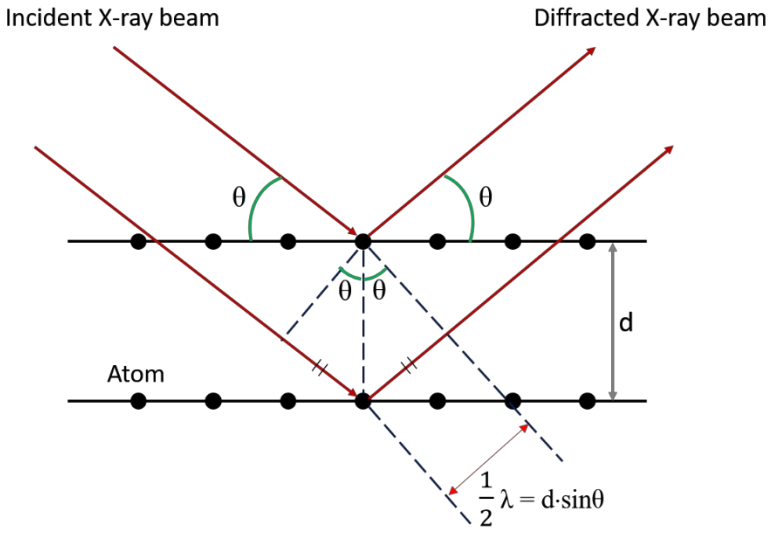

Figure 2.1 Schematic representation of Bragg's law where the black dots represents the atoms and the red solid line describes the X-ray beam with wave length of λ.

the travel distance difference of X-ray beams (2d sinθ) is equal to an integer multiple (n) of the wavelength of X-ray (λ), the reflected X-ray beams interfere constructively and remain in phase. This relationship is known as Bragg's law and can be expressed by **equation 2.1**.

$$n\cdot\lambda = 2d\cdot\sin\theta \qquad \textbf{Equation 2.1}$$

Especially, when the incident X-ray angle θ is satisfying the Bragg's law for a certain value of λ and d, the angel is called as Bragg angle θ_B where the X-ray diffraction occurs. If the incident X-ray beam

angle does not satisfy the Bragg's law, the X-rays interfere destructively showing no distinct X-ray diffraction peak from the diffraction pattern.

From a crystal, X-ray is scattered by the electrons of atoms and the diffracted beam intensity (I) is determined by the number and position of the electrons. The correlation between these factors and X-ray reflection can be expressed by structure factor (F) as shown in **equation 2.2 and 2.3**.

$$F_{hkl} = \Sigma f_j \exp[2\pi i(hx_j + ky_j + lz_j)] \qquad \textbf{Equation 2.2}$$

$$I = A \cdot F^2 \qquad \textbf{Equation 2.3}$$

Here, (hkl) is the Miller index of the planes, (x,y,z) is the coordinates of the atom and f is the atomic scattering factor (form factor) that is related to the number of electrons in the atom as well as X-ray beam scattering angle. Based on structure factor (F), the intensity of the X-ray diffraction peak (I) is proportional to A and F squared, where A includes other factors such as polarization, absorption and temperature for X-ray diffraction measurement. Therefore, the XRD pattern provides important information to analyze the crystal structure of materials.

In order to obtain reliable X-ray diffraction data from materials, choosing a proper diffractometer setup depending on samples is required. Generally, for single crystal, the mounted crystal on sample holder has to be rotated along the various axis to collect the diffraction pattern of spots corresponding to a family of crystal planes h k l. However, for polycrystalline powder materials, crystallites are already randomly oriented in every possible directions that can be regarded as rotated single crystals. Therefore, either the sample or incident beam need to be rotated only one direction with respect to the other one for a certain range of angles while moving detector is collecting diffracted beam pattern from various reflection angles.

The Bragg-Brentano geometry in **Figure 2.2a** is the most common diffractometer setup for powder X-ray diffraction (PXRD) measurement. The powder sample is located on a flat sample holder

and X-ray beam and detector is moving along the semi-circle above the sample for 2θ degrees towards each other. The collected PXRD pattern contains the crystal structure information of measured sample and they are presented by diffracted peak positions, peak intensities, and peak broadness for each Bragg angle. Specifically, the Bragg peak position depends on the X-ray wavelength and spacing between the crystallographic planes in unit cell. Besides, the Bragg peak intensities are determined by atomic parameters, such as atoms type, position of atoms, symmetry of atomic position, site occupancy of atoms in crystal structure, atomic displacement factor. In addition, the broadness of the peaks depends mainly on instrumental parameters together with the particle size of sample powder. If the crystals have a preferred orientation, this could result in aligning the crystals in one particular direction while the sample preparation and diffracted beam from the sample could show more intensive peak for a certain plane. To avoid this issue, Debye-Scherrer geometry for diffractometer can be employed with preparing powder sample by filling a glass capillary. As it is shown in **Figure 2.2b,** the powder sample filled glass capillary is then mounted on sample stage perpendicular to the incident X-ray beam for rotation

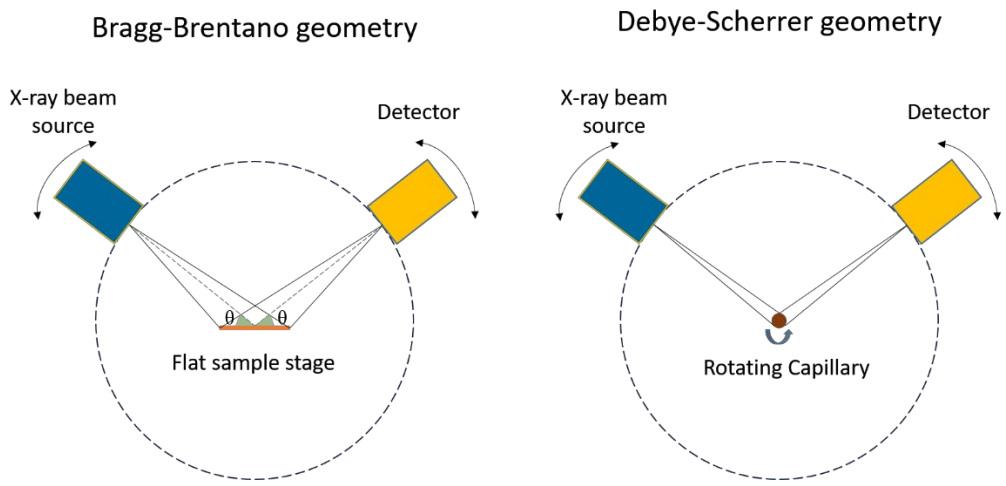

Figure 2.2 Schematic presentation of (a) Bragg-Brentano and (b) Debye-Scherrer geometries.

during the diffraction pattern measurement. The Debye-Scherrer setup is collecting diffraction data by X-ray transmission through sample containing capillary and this results in overall lower diffraction signal intensity compared to Bragg-Brentano geometry setup.

In this thesis, PXRD patterns were collected on a PANalytical Empyrean instrument using Cu Kα radiation (λ = 1.5405 Å). To refine the crystal structure, powder samples were loaded in 0.3 mm or 0.5 mm diameter capillary and the XRD patterns were recorded with a PIXcel bi-dimensional detector with Debye-Scherrer geometry using a parabolic X-ray mirror for the incident beam optics. The lattice parameters were determined using the Le Bail method within the FullProf software suite. The steady state powder samples on a flat sample stage were measured in the range from 10° to 70° (2θ) at a step size of 0.025° with Bragg–Brentano geometry equipped with a PIXcel bidimensional detector with a Ni Kβ filter. For air-sensitive samples, the capillary preparation process was done from argon gas filled glove box and the capillary was sealed to avoid the air exposure. Air stable samples were mounted on the powder sample holder and diffraction patterns were collected by Bragg-Brentano geometry setup from the same diffractometer. In addition to XRD measurement on steady-state samples, in-situ XRD measurement on materials during the electrochemical reaction also carried out by PANalytical Empyrean diffractometer and home made in-situ XRD cell to show the real-time crystal structural evolution of the electrode materials during the battery cycling. The lattice parameters evolution during the in-situ XRD experiments was confirmed by the Le Bail fitting method using the FullProf software suite.

2.3.2 Rietveld Refinement

Rietveld refinement is a technique for characterizing the crystal structure of materials by employing the least squares fitting method to minimize the profile difference between observed XRD pattern and calculated XRD pattern. To utilize this method, a starting model which is sufficiently close

to the target crystal structure should be given and the PXRD data also should contain enough information of the measured crystal allowing us to distinguish the reflections from different family of hkl planes but showing similar d spacing.

To start Rietveld refinement, applying Le Bail fit on the measured XRD pattern first is convenient to determine the background, profile shape, sample displacement, lattice parameters and space group of the crystal. This method takes into account all diffraction peaks by assigning intensities and archive the best fit through least squares method. Based on the fixed parameters obtained from Le Bail fitting, scale factors, atom positions, atomic displacement factor, occupancies, other structural parameters can be refined in Rietveld mode. The result of the Rietveld refinement can be evaluated by the degree of profile agreement between an observed XRD and a simulated XRD profiles for the refined crystal model. There are a few agreement factors that we can employ to determine how the crystal model matches well with practical crystal stricture based on figures of merits from the agreement factor equation including weighted profile factor R-factor (R_{wp}), expected R-factor (R_{exp}), Bragg residual (R_{Bragg}) and goodness of fit (χ^2) as shown from **equation 2.4 ~ 2.7**.

$$R_{wp} = \{\Sigma w_i[y_i(obs) - y_i(cal)]^2 / \Sigma w_i y_i(obs)^2\}^{1/2} \qquad \textbf{Equation 2.4}$$

$$R_{exp} = \{(N\text{-}P+C) / \Sigma w_i y_i(obs)^2\}^{1/2} \qquad \textbf{Equation 2.5}$$

$$R_{Bragg} = \Sigma \left| I_{obs} - I_{cal} \right| / \Sigma \left| I_{obs} \right| \qquad \textbf{Equation 2.6}$$

$$\chi^2 = (R_{wp}/R_{exp})^2 \qquad \textbf{Equation 2.7}$$

where w_i is the weight of the i th data point ($=1/Y_i(obs)$) , $Y_i(obs)$ is the observed intensity of the i th Bragg peak, $Y_i(cal)$ is the calculated intensity of the i th Bragg peak, N is the total number of data

points used in the refinement, P is the number of refined parameters, C is the number of constraints. By achieving minimum figures of merits from those factors through Rietveld refinement, the refined crystal structure model is considered as the most similar crystal to the measured crystal sample as long as the refined crystal structure model makes sense physically and chemically.

Rietveld refinement presented in this thesis were performed by using FullProf suite software.

2.3.3 Pair Distribution Function (PDF)

From the conventional X-ray diffraction and neutron diffraction analysis, the averaged crystal structure information is mainly obtained from the position and intensity of the Bragg peaks. However, additional structural information, such as deviations from the perfect crystal in diffuse scattering, is discarded in the form of background. Therefore, the conventional XRD analysis is not desirable for analyzing materials with extensively disordered structure. In order to analyze the disordered or low crystalline structure, both the Bragg peaks and diffuse scattering can be treated on equal basis through total scattering techniques. Fourier analysis of the total scattering data is known as atomic pair distribution function (PDF) analysis.

First, the relative inter atomic distance in a crystal can be described as $\{r_{\nu\mu}\}$ where ν and μ refer to the individual atoms. Assuming the system is macroscopically isotropic, the interatomic distance can be given by

$$\rho(r) = \rho_0 g(r) = \frac{1}{4\pi N r^2} \sum_{\nu} \sum_{u} \delta(r - r_{\nu u}) \qquad \textbf{Equation 2.8}$$

where ρ_0 is the number density of atoms in the system of N atoms and δ is a Dirac-delta function. The function $\rho(r)$ is the 'atomic pair density function' and $g(r)$ is the 'atomic pair distribution function' (PDF). PDF is a one-dimensional function which depicts the inter atomic distance between ν th and μ

th atoms, $r_{v\mu} = |r_v - r_\mu|$, as a peak from the graph. As $\rho(r)$ and $g(r)$ give information about deviations from average behavior of atoms, they are called 'pair correlation functions'.

The total scattering method is based on the normalized scattering intensity directly measured from a sample, known as the total scattering structure function S(Q). Q is the magnitude of momemtum transfer vector of the scattering particle ($Q = 4\pi \sin(\theta)/\lambda$) which is defined as $Q = k_{ini} - k_{final}$, where k_{ini} and k_{final} are the incident and scattered wavevectors, respectively. The Fourier transform of the scattered intensity, in the form of S(Q), results in PDF, $g(r)$, which indicates the probability of finding two atoms separated by a distance r. As atomic pair density function, $\rho_0 g(r)$, represent the microscopic atomic pair density and Fourier transformed structure function, S(Q), represents atomic pair distribution, their correlation allows us to directly measure the relative position of atoms in crystal. Through utilizing the reduced structure function, F(Q) = Q[S(Q) – 1], a numerical Fourier transformation of measured S(Q) can be obtained as a form of reduced paid distribution function, $G(r)$, by calculating the following equation

$$G(r) = 4\pi r \rho_0 (g(r) - 1) = \frac{2}{\pi} \int_0^\infty Q[S(Q) - 1] \sin(Qr)\, dQ \qquad \textbf{Equation 2.9}$$

where ρ_0 is the number density of atoms, Q is the magnitude of momentum transfer vector, S(Q) is total scattering structure function. In the Fourier transform, as a step to get from S(Q) to the corresponding PDF, $G(r)$, the data are truncated at a finite maximum value of the momentum transfer (Q) rather than infinite (∞), called Q_{max}. Based on the λ of X-ray from the instrument, Qmax value can be varies. For example, silver tubes give Q_{max} of around 22 $Å^{-1}$ with Q step-size of 21.6 $Å^{-1}$ (0.29 Å) which can be satisfactory (though not optimal) for PDF measurements even in crystalline materials at room temperature. Q_{min} is the lower boundary of the Fourier transform and it is affected by the particle size and shape of measured sample. For instance, the smaller particle size (such as a few nanometer in diameter), the higher Q_{min} value is required for more reliable PDF result. The reduced pair

distribution function, $G(r)$, provides two important advantages over $g(r)$ even it is less physically intuitive function. First, it is directly related to the obtained data as this function is directly calculated from the Fourier transform of S(Q). In contrast, assuming the number density of atoms, ρ_0, is required to obtain $\rho(r)$ or $g(r)$. Second, the direct Fourier transform of the intensity data provides the constant random uncertainties along r for $G(r)$, whereas $\rho(r)$ and $g(r)$ shows the uncertainty falling off as 1/r due to the statistical fluctuations. As $g(r)$ is normalized, as $r \rightarrow \infty$, $g(r) \rightarrow 1$ and as $r \rightarrow 0$, $g(r) \rightarrow 0$. Therefore, from equation 2.9, as $r \rightarrow \infty$, $G(r)$ oscillations near at zero and as $r \rightarrow 0$, $G(r)$ plot shows a slope of $-4\pi r\rho_0$.

A further advantage of the $G(r)$ is that the amplitude of the oscillations is directly related to the structural coherence of the measured sample. For instance, from a perfect crystal, oscillation in $G(r)$ shows a constant peak-peak amplitude over the infinite Q-resolution. However, from a real crystal which has the limitation on the spatial coherence, the finite Q-resolution results in the gradual peak-peak amplitude signal decrease over the increasing r. If a sample has disordered structure, the signal amplitude decrease faster due to the low structural coherence. The final example is the appearance of termination ripples (false oscillation) with a wavelength of $\sim 2\pi/Q_{max}$ that is because S(Q) is collected over a finite range of Q in a real experiment.

Contrary to $G(r)$, the radial distribution function, $R\,(r)$, is the most physically intuitive function which is correlated with $g(r)$ by

$$R\,(r) = 4\pi r^2\rho_0 g(r) = \sum_\nu \sum_\mu \frac{b_\nu b_\mu}{\langle b \rangle^2}\,\delta\big(\mathrm{r} - r_{\nu\mu}\big) \qquad \textbf{Equation 2.10}$$

where b values are the atomic scattering length of the ν and μ ions at position r_ν and r_μ with respect to some origin. ⟨b⟩ is the average scattering amplitude of the sample. From a crystal, the coordination number of atoms for a specific coordination shell, N_C, is given by

$$N_C = \int_{r1}^{r2} R(r)\, dr \qquad \textbf{Equation 2.11}$$

as R(r)dr gives the number of atoms in an annulus of thickness dr between the atoms spacing from r_1 to r_2. Here, r_1 and r_2 define the RDF peak which is corresponding to the coordination shell in our question. The reduced pair distribution function, $\mathrm{G(r)}$, can be obtained by combination of **equations 2.10 and 2.11**.

$$\mathrm{G(r)} = \frac{1}{r}\sum_i \sum_j \left[\frac{b_i b_j}{\langle b \rangle^2}\delta(r - r_{ij})\right] - 4\pi r \rho_0 \qquad \textbf{Equation 2.12}$$

In conclusion, PDF function gives information about the average interatomic distances by the peak positions and the coordination number of the corresponding pair of atoms by the integrated intensity of the peaks. In addition, the probability distribution of the atomic pairs is related to the shape of the peaks from PDF function.

In this thesis, PDF data was collected by a PANalytical Empyrean diffractometer equipped with Ag tube (Q_{max} = 22 $Å^{-1}$), a Rh Kβ filter, and a NaI scintillation point detector as shown in **Figure 2.3**. Samples were loaded in a 0.5 mm glass capillary from an argon gas filled glovebox and air-tight sealed. The data collection time was increased for high Q region resulting in total data collection time of 48 h. The scattering intensity contribution from the capillary and the diffractometer were taken into account by performing the same measurement with an empty capillary and subtracting it from the sample data. The collected XRD data was processed by PDFGetX3 software and the obtained real space data was fitted by PDFgui software (Q_{max} to 20 $Å^{-1}$ used for PDF fitting). A standard silicon sample was measured to determine the instrument dependent Q damping factor for the PDF data fitting.

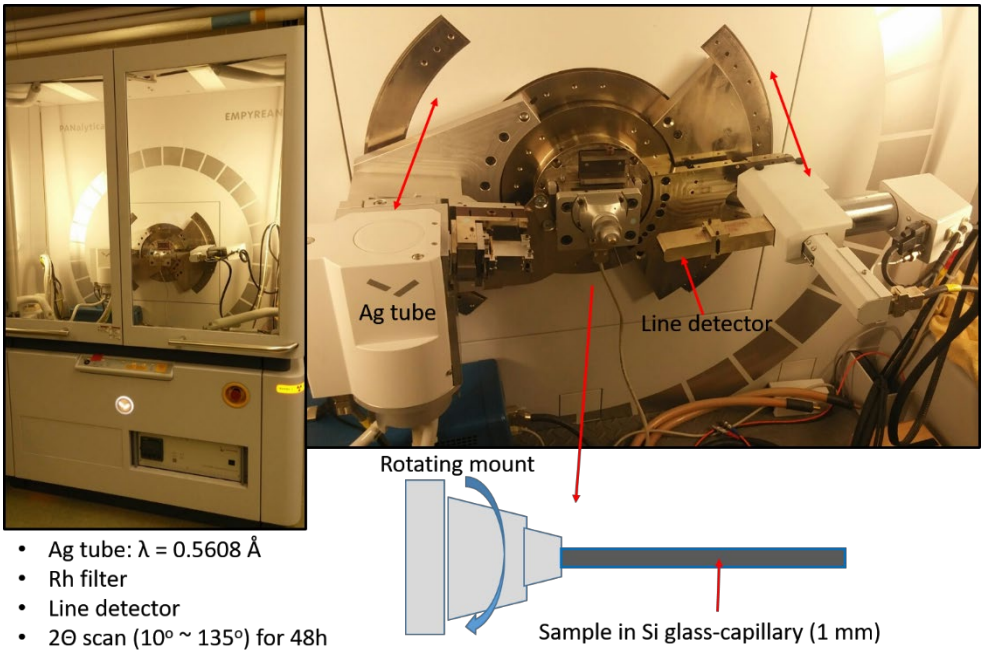

Figure 2.3 XRD machine (Empyrean, PANalytical) setting up for PDF measurement with Debye-Sherrer geometry.

2.4 Online Electrochemical Mass Spectroscopy (OEMS)

Generally, mass spectroscopy (MS) is an analytical technique for measuring the mass to charge ratio (m/z) of ions. For the various gases, the MS system separates, identifies and analyzes the gas species through a detector based on their m/z ratio after ionization. The MS system used in this thesis is a Stanford Research System RGA 200 quadrupole mass spectrometer. For the first step of the MS, the sample gases go through ionization region. Specifically, the gas molecules enter into the vacuum chamber through a fused silica capillary (50 um ID) and bombarded by a high energy beam of electrons emitted from a tungsten filament. The gas molecules then collide with high energy electrons resulting in an ionization by removing an electron from the gas molecule. The ionized molecules could be separated into several ion fragments or neutral species. In the next stage, the generated ions pass through the four rod-type quadrupole ion filter region and the trajectory of each positive ion is separated by

electric and magnetic fields based on their m/z ratio. By tuning the DC and AC voltages of quadrupole mass analyzer, the mass sensitivity or the mass resolution of MS can be improved. Once the positive ion filtered through the quadrupoles, the ions collide with a continuous dynode electron multiplier (CDEM) detector. As the detector has a negative voltage biased cone at the front end, positive ions accelerated upon entrance and collide with the electron multiplier generating the secondary electrons which are then detected by a negative electrode at the end of the detector. Finally, the electrical signal from the electrode is conversed to ion current and we can observe or analyze the types and amount of gases evolved from sample.

In this research, the gas evolution from a positive electrode of Li-ion battery was analyzed with an online electrochemical mass spectrometer (OEMS) by utilizing a modified setup based on a previous report by N. Tsiouvaras *et al*.[1] A commercial electrochemical flow cell (EL-Cell, ECC-DEMS) was connected in-line to a gas flow controller (Bronkhurst, F-200CV) and a quadrupole mass spectrometer (Standford Research Systems, RGA 200). The cell was leak tested under O_2 pressure using a high accuracy pressure transducer to measure any pressure drop (Omega PX409-USBH), and was found to be hermetically sealed. The evolved gases from the positive electrode of the operating cell were transferred to the entrance of quadrupole mass spectrometer through a fused silica capillary (50 μm ID) by argon gas (Praxair, 5.0 grade) sweeping with a controlled flow rate (0.5 ml/min). The pressure inside the MS chamber was 3×10^{-6} Torr during operation. Prior to measurement, the mass spectrometer was calibrated to establish a relationship between the measured ion current (A) and target gas concentration (ppm). With the use of known gas concentrations (from 2000 ppm of O_2/Ar balance and 2000 ppm of CO_2/Ar balance mixtures) mixed with different amounts of Ar, a linear relationship between the gas concentration and ion current was established.

2.5 Time of Flight Secondary Ion Mass Spectroscopy (TOF-SIMS)

Time of flight secondary ion mass spectroscopy (TOF-SIMS) is a surface sensitive analytic technique using ion (O_2^+, O^-, Ar^+, Ga^+, Cs^+ or neutrals) beam bombardment to eject secondary ion particles from the sample of interest and analyze them. The generated secondary ion particles from the sample are then determined by time of flight mass spectroscopy. Generally, a pulsed primary ion beam bombards the solid sample and transfer the energy to the atoms in the target via atomic collision, thereby starts a "collision cascade".[2] The excess energy transferred from ion beam allows the atoms and molecular fragments to escape from the target surface as positive or negative secondary particles by overcoming the binding energy. Once the secondary ions freed from the target surface, a high voltage potential extract the ions and transfer them to a mass analyzer to determine their mass based on time of flight difference from the sample to the detector. The mass of secondary particle and its charge ratio (m/z) determines the time required for the particle travels from the sample surface to the detector. Finally, the mass spectrum and secondary ion images can be utilized to obtain the information about the composition, distribution and molecular components of the sample surface.

TOF-SIMS is a highly surface sensitive technique which is capable to resolve the secondary particles from m/z = 1 to m/z = 10000 (positive or negative). However, as it is a primarily qualitative analysis system, a proper and accurate standard sample is required for a quantitative analysis. In addition, the sample surface is required or preferred to be free from contaminants and atomically flat with a stability at ultra high vacuum ($\leq 10^{-9}$ Torr) to avoid erroneous results.

In this study, TOF-SIMS is employed to confirm the conformal polydopamine coating layer on the surface of lithium-rich transition metal oxide primary particles by sputtering a spherical shape single secondary particle which is formed by an agglomeration of the nano-size primary particles. TOF-SIMS measurement was carried out in an ION-TOF 5 system (IONTOF GmbH), equipped with a 2 m long

reflectron TOF analyzer operated in the negative polarity mode, and a Bi^{1+} ion analysis beam source and an Cs^{+} ion sputtering beam source (1 keV) over an area of 200 × 200 μm^2. Depth profiling was carried out in the spectrometry mode (non-interlaced) with an analysis ion beam current of 1.4 pA, a cycle time of 150 μs, and a sampling area of 50 × 50 μm^2 (256 × 256 pixels). A single spherical particle of each sample was located on the Si wafer substrate and the ion fragment signal was collected while sputtering the particle.

2.6 X-Ray Photoelectron Spectroscopy (XPS)

X-ray photoelectron spectroscopy (XPS) is surface sensitive analytical technique utilizing photoelectric effect to characterize the oxidation states of elements in the target material. When an atom of the sample absorb an X-ray photon with known photon energy (hν), the photoelectron is emitted with kinetic energy (E_K). The binding energy of ejected electron from the atom then can be determined by the Einstein equation

$$E_B = h\nu - E_K - \varphi \qquad \textbf{Equation 2.13}$$

where E_B is the binding energy of the electron in the sample and φ is the spectrometer work function. As the X-ray source of spectrometer determine the hν and detector probes the kinetic energy and the number of photoelectrons, the binding energy of the electron can be estimated. The binding energy shift from the core level is highly correlated with the chemical environment of the atom in the material and it can provide information about an oxidation state and local bonding characters of the elements. In order to escape from the surface of materials and generate the characteristic photoelectric peak signal, the photoelectrons have to be ejected without further collision while traveling from the subsurface layer to vacuum. Therefore, XPS is extremely surface sensitive. The known inelastic mean free path of an electron is 0.5 nm to 10 nm, depending on the kinetic energy of X-ray (2 ~ 2000 eV).

In the present work, the XPS data was collected by employing a multi-technique ultra-high vacuum Imaging XPS Microprobe system (Thermo VG Scientific ESCALab 250) equipped with a hemispherical analyser (of 150 mm mean radius). A monochromatic Al Kα and non-monochromatic Al Kα source from twin anode were used for non-conductive and conductive materials, respectively. All samples were prepared from argon gas filled glove box and transported to the XPS chamber through an argon filled glove bag, and then transferred into chamber quickly without air exposure. The obtained XPS spectra were process with CasaXPS software using Gaussian-Lorentzian functions for fitting and Shirley-type background. The binding energy of all elements were calibrated by the C 1s peak at 284.8 eV.

2.7 X-ray Absorption Spectroscopy (XAS)

X-ray absorption spectroscopy (XAS) is a broadly used method that uses synchrotron radiation to investigate atomic local structure as well as electronic states of certain elements in a material. When X-ray is irradiated to a sample with intensity of I_0, the transmitted beam intensity I_t follows Beer's law (**equation 2.14 and 2.15**).

$$I_t = I_0 e^{-u(E)t} \qquad \textbf{Equation 2.14}$$

$$u(E) \approx \frac{\rho Z^4}{AE^3} \qquad \textbf{Equation 2.15}$$

where E is the photon energy, A is atomic mass, ρ is sample density, Z is atomic number, t is the thickness, and u(E) is the energy dependent X-ray absorption coefficient of the corresponding sample. When the irradiated photon energy (eV) exceeds the binding energy of a core-electron, such as 1s or 2p level, a sharp increase in the absorption coefficient appears with excitation of core-electron into an empty valence level or to the vacuum level. The element specific spectrum is obtained by plotting the absorption coefficient as a function of photon energy. The plot can be separated into three energy regions showing the pre-edge, X-ray absorption near-edge structure (XANES), and extended X-ray

absorption fine structure (EXAFS) as shown **in Figure 2.4**.[3] The first two energy regions showing pre-edge and XANES peaks in the plot correspond to the excitation of core-electrons to empty valence band, thus deliver information of the corresponding element's electronic structure. The last EXAFS region is typically starting ~ 50 eV above the absorption edge. It evolves due to the scattering of the ejected photoelectrons from the absorbing atom with the neighboring atoms. Therefore, EXAFS is sensitive to the atomic arrangement around the absorber atom and provides quantitative information about the bond length and the coordination number.

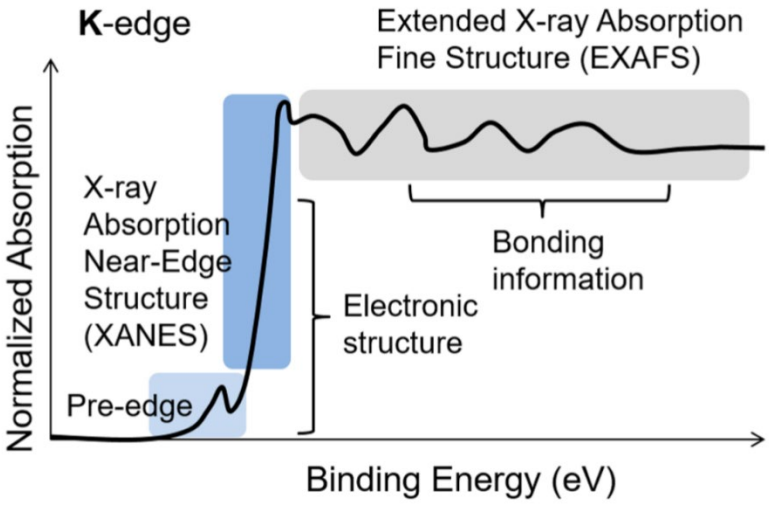

Figure 2.4 Scheme showing an example XAS spectrum that consists of three regions.[3]

2.8 Resonant Inelastic X-ray Scattering (RIXS)

Resonant Inelastic X-ray Scattering (RIXS) is a technic that measures both X-ray Absorption Spectroscopy (XAS) and X-ray Emission Spectroscopy (XES) features of an element by scanning the incident and emitted energies of a photon. The RIXS event can be described as a two-step process as depicted in **Figure 2.5**. From the initial state, incident photon transfers its energy and momentum to excite the core electron to the valence band, leading to the creation of a core hole in an excited intermediate state. After the excitation of the core electron, the core hole is refilled by a decay of valence

electron emitting a photon that leads to the final state. Therefore, the photon absorption process provides information on the empty electronic states, while the photon emission process provides information about the occupied states of the corresponding element. From the RIXS experiment, we can obtain a scanning map of convoluted XAS and XES spectrum as a function of excitation energy and emission energy, respectively. Therefore, the RIXS spectrum is often plotted to show the difference between the photon's incident energy and the emitted energy. It should be noted that RIXS is an element

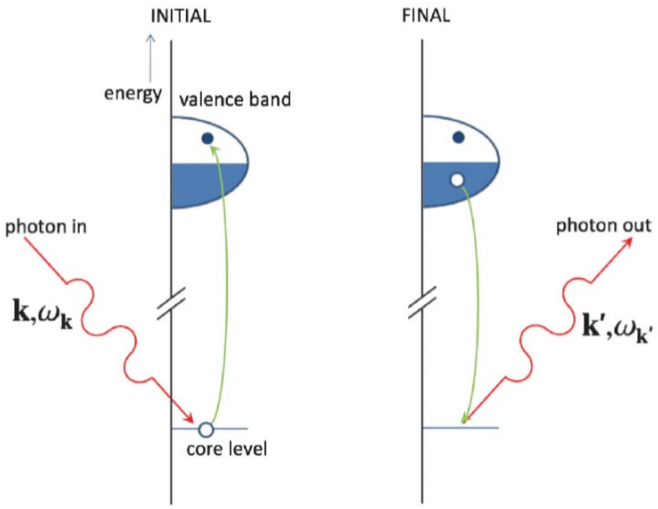

Figure 2.5 In a direct RIXS process the incoming X-rays excite an electron from a deep-lying core level into the empty valence band. The empty core state is then filled by an electron from the occupied states under the emission of an X-ray.[4]

and orbital specific technic. In addition, RIXS can differentiate between the same chemical element at sites with inequivalent chemical bondings, with different valencies or at inequivalent crystallographic positions as long as the X-ray absorption edges in these cases are distinguishable.[4]

2.9 Superconducting QUantum Interference Device (SQUID)

Almost all atoms have multiple electrons which are paired up in orbitals with another electron of the opposite spin. This electron pairing up states in an atom response to an external magnetic field (H) and the magnetization (M) of material is proportional to H by

$$M = \chi H \qquad \textbf{Equation 2.16}$$

where χ is the magnetic susceptibility of the material. When all of the electrons on an atom are paired, the atom is said to be diamagnetic. For diamagnetism, there is a very small magnetic moment associated with an electron traveling in closed shells around the nucleus which causes a material to be repelled by H ($\chi < 0$). On the other hand, other types of magnetism, such as paramagnetism, ferromagnetism, anti-feromagnetism, ferrimanetism, and etc., require unpaired electron spins in an atom and the interactions among electron spins determine the type of magnetism. Especially, the unpaired electrons and paramagnetism are associated with the presence of either transition metal or lanthanide (actinide) ions. In many transition metal compounds, only the spin moment is needed to be taken into account as the surrounding anions or ligands quench the orbital angular momentum in an atom. Given that, this thesis focuses on the paramagnetism as it can be applied to transition metal oxide electrode materials. In Paramagnetic materials, the magnetic moments are randomly oriented and rapidly reorienting without interaction, so there is no permanent and spontaneous magnetic moment. All forms of magnetism have a critical temperature (T_C, Curie temperature) and there is some interaction of moments below this point, whereas paramagnetic property evolves above T_C. The magnetic susceptibility of paramagnetic material (χ_p) can be expressed as a function of T following the Curie Law or Curie-Weiss Law in **equation 2.15 or 2.16**, respectively.

$$\chi_p = \frac{C}{T} \quad \textbf{Equation 2.17} \qquad \text{or} \qquad \chi_p = \frac{C}{T-\theta} \quad \textbf{Equation 2.18}$$

where C is Curie constant and θ is Weiss constant (the temperature at which the dielectric constant is a maximum) indicative of intermolecular interactions among the moments. The Weiss constant is somewhat higher than the actual Curie temperature, and Weiss constant (θ) can be replaced by Curie temperature (T_C) if $T >> T_C$. Therefore, some scientists call θ the Weiss constant to distinguish it from the temperature of the actual Curie point. If $\theta > 0$, the moments have ferromagnetic interactions (not ferromagnetism) and if $\theta < 0$, the moments have anti-ferromagnetic interactions (not anriferromagnetism). Ideally, it should give a straight line if the Curie-Weiss Law is obeyed. Therefore, we can extract the Curie constant from the inverse of the slope and Weiss constant from the x-intercept.

$$\frac{1}{\chi_p} = \frac{(T+\theta)}{C} = \frac{T}{C} + \frac{\theta}{C} \qquad \textbf{Equation 2.19}$$

The Curie constant gives us the size of the moment per unit.

$$C = \left(\frac{N_A}{3k}\right)\mu^2 \rightarrow \mu = \left(\frac{3kC}{N_A}\right)^{\frac{1}{2}} = 2.84\, C^{\frac{1}{2}} \qquad \textbf{Equation 2.20}$$

where N_A is Avogadro's number, k is Boltzman's constant and μ is the magnetic momentum. Therefore, by measuring magnetization of sample (M) under the known external magnetic field (H) as a function of temperature, we can calculate the magnetic susceptibility, thereby obtain the magnetic momentum of sample.

In Chapter 6, magnetic susceptibility measurements on the pristine and charged/discharged samples were performed as a function of temperature using a MPMS SQUID VSM magnetometer (Quantum Design Inc.) in a magnetic field of 1000 Oe upon cooling the samples from 350 to 2 K.

2.10 Raman Spectroscopy

When light illuminate molecules, the predominant mode of scattering is elastic scattering (Rayleigh scattering). This scattering is more effective as the wavelengths is getting shorter and it is

proportional to the fourth power of the frequency.[5] On the other hand, it is also possible that the photons gains or loses its energy after interacting with molecules and the frequency of scattered photons are shifted. This phenomena is called inelastic scattering (Raman scattering). Raman spectroscopy is a technique based on Raman scattering of photons from the vibrational, rotational, and other low-frequency modes of a molecules.[6] When monochromatic light (laser) is irradiated to the molecules, the electromagnetic radiation is generated and collected by a detector through a lens and monochromator collecting the signal. Rayleigh scattering radiation corresponding to the laser wavelength from the interaction is filtered out by multiple filters (e.g. notch filter and band pass filter) while Raman scattering radiation is reaching to the detector.

The Raman effect is correlated with polarizability of electrons in a molecule as they exhibit a change in their electric dipole-electric dipole polarizability from the vibrational coordinate when exposed to the monochromatic light. When laser hits the molecules, the Raman scattering excites the molecules and put it to a virtual energy state. While further Raman scattering, the total energy of molecule remains constant by moving the energy state of molecule to a new rotational, vibrational electronic state. As a result, the scattered photon is shifted in their energy to higher or lower energy state so that the total remains the same. If the scattered photon energy shifts to lower than irradiated light, it is called a Stokes shift, and if the energy shifts to higher, it is called an anti-Stokes shift. Based on the energy shift by Raman scattering, the structural fingerprint of molecules can be identified that allows us to analyze the molecular structure of the sample.

In chapter 3, Raman spectroscopy was performed on a LabRam HR system (HORIBA Jobin Yvon) using a 532 nm laser in the range of 700 to 2000 cm^{-1}. The Raman spectrum of all samples, including those described below, were recorded ex-situ by placing them on a glass slide and sealed by epoxy resin with a cover glass. Samples were prepared inside an Ar filled glove box.

2.11 Scanning Electron Microscopy (SEM)

A scanning electron microscopy provides a high-resolution image of a sample surface using a focused electron beam and delivers information about the morphology together with chemical composition of the specimen. In an SEM instrument, an electron gun produces electrons and the potential drop accelerates the generated electrons to an energy level of 5 - 30 keV for a typical use. When the energetic electron beam is focused on the specimen through lenses and apertures under vacuum (~ 10^{-6} Torr), the interaction between beam and specimen generates several signals such as secondary electrons, backscattered electrons, and characteristic X-rays as it is shown in **Figure 2.6**. To be specific, if the incident electrons elastically scattered and deflected back of the specimen, they are called backscattered electrons (BSE).

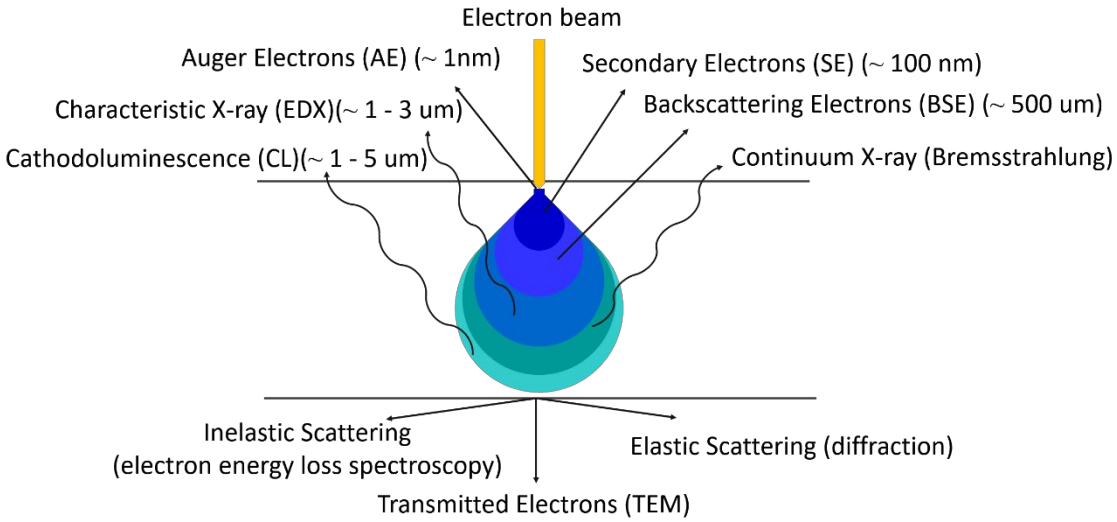

Figure 2.6 Scheme diagram of types of signals (electrons and photons) emitted from different interaction volume in sample for SEM.

As the extent of scattering of BSE is proportional to the atomic number of the scattering element, BSE can provide information about chemical contrast from the specimen with the depth resolution of 1 ~ 3 um.

On the other hand, if the incident electrons interact inelastically with the electrons in the specimen, the loosely bonded electrons are ejected emitting the low energy (< 50 eV) which are called secondary electrons (**Figure 2.6**). The low kinetic energy of secondary electron allows only those under ~ 100 nm from the surface to escape and reach the detector. However, its spatial resolution close to the spot size of the beam lets us use secondary electrons to image the surface of the specimen. In addition to the BSE and secondary electrons for imaging the morphology of specimen, other kinds of emissions may occur by the interaction of the electron beam and the material, such as photons for cathodoluminescence and Auger electron. If the secondary electron leaves a electron hole in the core level of electron orbital in the atom, an electron from an outer shell drops to the lower energy level orbital to fill the electron hole with emitting energy as X-ray. As each element exhibits their characteristic X-ray emissions depending on orbital energies, identification and quantification of the elements consisting of the specimen is possible by analyzing the X-ray signal except for light elements, such as helium and lithium. This technique is called energy dispersive X-ray spectroscopy (EDS).

In this thesis, the SEM images were recorded utilizing a Zeiss Ultra or LEO 1530 field emission SEM equipped with an EDX at 15 kV in the secondary electron mode. The molar ratios of transition metal ions of the samples were verified by energy dispersive X-ray spectroscopy (EDX). Before transfer the specimens into SEM chamber, they were coated by gold puttering to increase the electron conduction.

2.12 Transmission Electron Microscopy (TEM)

Transmission electron microscopy (TEM) is a microscopic technique which can provide a high resolution images of specimen, especially in an atomic scale. Similar to SEM, TEM utilizes a electron beam, but with much higher energy (100 ~ 400 keV) and shorter wavelength ($\lambda = 0.025$Å). Therefore, TEM images can provides the atomic structure of the specimen. As TEM generates an image by electrons which interact and transmit through a specimen, an ultra-thin (< 100 nm) specimen is required to observe the atomic structure from the specimen.

The electron beam source or cathode can be a tungsten filament or a lanthanum hexaboride (LaB_6) single crystal. For emitting electrons, high voltage source is coupled with electron guns and sufficient current is applied to the gun to emit electrons by thermionic or field electron emission. A thermionic type source utilize the Wehnelt cylinder to focus and stabilize the current. On the other hand, a field emission type source uses electrostatic electrodes to control the shape and intensity of electric field.

The electron beam can be manipulated by coupling two physical effects; magnetic fields and electrostatic fields. The magnetic fields allows for the formation of a magnetic lens of variable focusing power and shape and the electrostatic fields control the emitted electrons to be deflected with a constant angle. Utilizing these two deflections in opposing directions can control the electron beam path, which is important for scanning TEM (STEM).

After the electron beam is adjusted the focus and intensity by passing through electron lenses and apertures in a vacuum column, an imaging system process the electron waves and generates the TEM images. The scattering of the electron beam by sample induces the amplitude and phase change in electron wave resulting in the contrast in TEM image. Specifically, amplitude contrast is due to the removal of electrons by absorption from the sample or high scattering angels which is going out of detection limit. On the other hand, phase contrast occurs when electron beam is interact with specimen with uniform thickness. In this case, the electron waves change its phase while interacting with the

specimen and form the images displaying the contrast difference in the detected area based on the number of electrons detected after hitting the sample. Through the processing the signal from the phase contrast, High Resolution TEM (HR-TEM) images can be obtained which also provides the information of atom stacking sequence in the corresponding crystal. The most common TEM mode is the bright field (BF) imaging mode which is employing amplitude contrast. In this mode, an objective aperture only permits the non-diffracted beam though the back focal plane and creates the Bright-Field (BF) image. For the specimen which is thicker and heavier by elements in the detected area, the contrast image will become darker, while the vacuum space will show bright background. Contrary to BF image, if the aperture is moved to receive the signal from the diffracted electron beam satisfying Bragg condition beyond back focal plane, we can obtain Dark-Field (DF) images providing information on the orientation of the crystals in a polycrystalline material. For instance, crystalline parts from the specimen will show bright image while low crystalline or amorphous parts shows dark image together with vacuum space. In addition, by adjusting the back focal plane on the imaging apparatus, a diffraction pattern can also be obtained that allows us to investigate the space group of the crystal.

As it is mentioned from SEM part, the incident electrons interact with an atoms and lose characteristic energy depending on the types of element by colliding and ejecting the electrons bonded to atom. Electron Energy Loss Spectroscopy (EELS) is a technique that analyzing this energy loss from the indent beam and allow us to investigate the elemental composition, oxidation state and bonding state of the elements in the specimen.

For chapter 3 and 6 in this thesis, HR-TEM studies were carried out on a FEI Titan 80-300 STEM equipped with a high-brightness field-emission gun (X-FEG), aberration corrector on image-forming lens system, a monochromator and a Gatan image filter Tridiem spectrometer, operated at 200 kV.

Especially for chapter 3, the pristine bare and coated Li-rich NCM particles with varying weight percent of PDA were dispersed in ethanol and a drop was casted on lacy carbon TEM grids for HRTEM analysis. To further study the structural changes after long-term cycling, coated and bare Li-rich NCM electrodes after 100 cycles were disassembled in an argon-filled glove box and TEM specimens were prepared using Zeiss NVision 40 dual beam, focused ion beam/scanning electron microscope (FIB/SEM). Atomic-number sensitive (Z-contrast) high-angle annular dark-field (HAADF) images were obtained and annular bright-field (ABF) images were obtained at the beam convergence semi-angle of 19.1 mrad using a detector angular range of 79.5-200 mrad and 10-20 mrad, respectively.

2.13 Thermal Gravimetric Analysis (TGA)

Thermal gravimetric analysis (TGA) is carried out combined with differential scanning calorimetry (DSC) to observe the physical and chemical property changes of material, such as phase transformation or the thermal decomposition, as a function of temperature. While heating up the sample under air or argon gas flow, the balance and DSC sensor detect and record the weight change and heat flow from the system by comparison with the reference. By analyzing the TGA and DSC data, the thermal stability, phase transformation temperature, and oxidation/reduction temperature of the materials can be obtained. In this thesis, the TGA and DSC was employed to determine the thermal stability of synthesized sodium transition metal selenite and reduced graphene oxide composites. TGA analysis was conducted at a heating rate of 5 °C/min under dry air using a TA Instruments SDT Q600.

2.14 Electrochemical Measurement

The electrochemical properties of the electrode materials are tested by galvanostatic charge/discharge, Cyclic Votammetry (CV), and impedance spectroscopy.

2.14.1 Gavanostatic charge/discharge test

The galvanostatic charge/discharge cycling test is one of the most common procedures for evaluating the electrochemical performance of the electrode material from battery. For the test, the constant current is applied to the battery cell until the cell voltage reaches to a cut off voltage, and the cell voltage is measured as a function of time. Once the cell voltage reaches the cut off voltage, then the reverse current is applied to the cell until the cell voltage reaches to another cut off voltage. While the constant current is flowing through the outer circuit of battery tester, the electrode material is oxidized or reduced with the deintercalation or intercalation of mobile cations (Li^+, Na^+, Ca^{2+}, Mg^{2+} and etc.), respectively. Through this technique, the specific charge/discharge capacity and rate capability can be evaluated.

To determine the current density for the battery cycling, theoretical capacity of the electrode material needs to be calculated based on the molar mass of the active material and the number of electrons which is involving electrochemical reaction. The theoretical capacity (C) can be estimated by the **equation 2.21**.

$$C = \frac{n \cdot F}{M} \qquad \textbf{Equation 2.21}.$$

where n is the mole of electrons involved in electrochemical reaction, F = 96800 mA·h/mole is the Faraday constant for the charge from one mole of electrons, and M is the molar mass of active material. Based on this equation, the specific capacity of active material can be expressed by a unit of mAh/g. The specific energy (Wh/g) can also be calculated by multiplying the cell operation voltage and specific capacity. Based on the calculated theoretical capacity from the electrode material, the current applied to the cell can be expressed by using the term "C-rate". Here, the 'C' represent the theoretical specific capacity assumed by the full de/intercalation of mobile cations from the electrode material, and C/x value represents the current density required to reach the theoretical capacity within x hours. Therefore,

the actual current that should be applied to the cell can be calculated by multiplying the theoretical specific current density by the actual mass of active material, and this current value can be converted into C-rate term. It should be noted that the theoretical capacity can hardly be achieved from the most of cathode materials due to the limited electrolyte stability window and the internal resistance rooted from the mass transfer and electronic currents in the practical cell. In addition, the current density affect significantly to the operation voltage and specific capacity of the cell. In this regard, the rate capability test on electrode materials shows the ability of retaining the charge/discharge capacity at various current density over the cell cycling. Together with rate capability test, the capacity retention rate and Couloumbic efficiency (the ratio of the charge capacity to the subsequent discharge capacity) are crucial criteria to evaluate the electrochemical performance of the electrode material over the galvanostatic charge/discharge cycling. The operation voltage fade over the cell cycling is also needed to be investigated over the cell cycling as it directly affects the specific energy and cycling stability of the electrode material.

2.14.2 Cyclic voltammetry (CV)

Cyclic voltammetry (CV) is a potentiodynamic electrochemical technique which measures the current response from the working electrode while potential sweeping of the cell. By setting the potential range to measure and repeating the sweeping process, CV test provides some information about electrochemical properties of electrode material through the Randel-Sevcik **equation 2.22.**

$$i_p = 0.4463\, nFAC\left(\frac{nFvD}{RT}\right)^{\frac{1}{2}} \qquad \textbf{Equation 2.22}.$$

where, i_p is maximum current (Amps), n is number of electrons involved in the electrochemical reaction, A is electrode area (cm^2), F is Faraday constant ($C \cdot mol^{-1}$), D is diffusion coefficient ($cm^2 \cdot s^{-1}$),

C is molar concentration of reactant ($mol \cdot cm^{-3}$), ν is potential sweeping rate ($V \cdot s^{-1}$), R is ideal gas constant ($J \cdot K^{-1} \cdot mol^{-1}$), and T is temperature (K). Through this equation, CV can be further utilized to observe the rate capability of the electrode material, in addition to the stability window of testing electrolytes. It should be noted that the A and C values should be carefully measured when applying this principle as those values might be able to keep changing over the cell cycling. In addition, CV could force the electrochemical reaction beyond its kinetic limit and this makes hard to evaluate the capacity of the cell through this technique. I also note that the Randel-Sevcik equation is valid only for linear diffusion. On the other hand, the capacity derivative plot against voltage (dQ/dV plot), which can be obtained from gavanostatic cell cycling data, provides the similar information to CV and the capacity also contains the cell capacity information.

2.14.3 Electrochemical Impedance Spectroscopy (EIS)

An impedance in an electrochemistry cell is a crucial factor which is affecting the energy efficiency of the cell and it also significantly affects to the thermal runaway of the cell. Therefore, it is not too much say that investigating the impedance evolution from the cell is inevitable to evaluate the accurate the electrode performance and deal with the overheating issue from the cell.

Electrochemical impedance spectroscopy is a non-destructive technique which allows to estimate the resistance of the electrode by measuring the current response to the sinusoidal potential at various frequencies from the cell. As the EIS enables us to distinguish the dielectric and electric properties of individual contributions of cell components, a value of resistance and capacitance from the electrode surface can be determined by modeling of the electrochemical data. Therefore, EIS is frequently employed to investigate the behavior of a solid electrolyte interphase (SEI) layer or coating layer on electrode for battery system. In order to investigate the complex non-linear behavior of the electrochemical dynamics at the electrode interphase, EIS is performed with a perturbation potential

with small AC voltage (1 ~ 10 mV) at various frequencies (1 mHz ~ 1 MHz) to achieve the pseudo-linear response from the electrode under an equilibrium state (or open circuit voltage).

The measured EIS data can be displayed as Nyquist plot or Bode plot, which shows the impedance evolved at various frequencies from the each component of an electrochemical cell. From Nyquist plot, y-axis represents imaginary impedance in negative value and x-axis represents the real impedance. On the Nyquist plot, the impedance can be represented as a vector of length |Z| and the shift in phase ϕ is the angle between this vector and the x-axis as they are shown in **Figure 2.7**. Therefore, when ϕ is zero, the plot only exhibits the real impedance part. If ϕ is not zero, the value of the y-axis can be shown if there is capacitance value. It should be noted that the Nyquist plot doesn't show the frequency where the impedance is recorded. From the Nyquist plot, the impedance at high frequencies are recorded on the left side of the x-axis and lower frequency impedance data are recorded on the right side of the plot. On the other hand, Bode plot shows the log frequency on the x-axis and both the absolute value of the impedance ($|Z| = Z_0$) and phase-shift on the y-axis.

As it is shown in **Figure 2.7**, the Nyquist plot from the cell usually displays semicircles at high frequency region followed by straight line at low frequency region. Before the first semicircle in high frequency region, the x intercept point R_S indicates the ohmic resistance cause by the multiple factors,

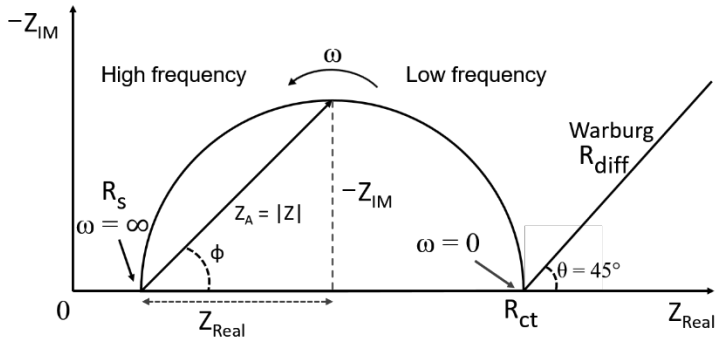

Figure 2.7 Schematic illustration of Nyquist plot (semicircle) and Warburg plot (linear line)

such as the mass transfer in the electrolyte, contact resistance from the cell, and etc. The next high frequency region (e.g. 500 kHz ~ 100 Hz) where the semicircle start to evolved contains information about the surface resistance (or film resistance), R_S, of the electrode. Once the voltage perturbation enters into middle frequency region (e.g. 100 Hz ~ 100 mHz), the diameter of the semicircle indicates the charge transfer resistance, R_{ct}, of the electrode. For the last, the straight line at low frequency region (e.g. < 100 mHz) indicates the ion diffusion from the surface toward the bulk of finite space in electrode. Especially, this line is called Warburg impedance, R_{diff}.

The data in a Nyquist plot can be fitted by simulating an equivalent electrical circuit model with the impedance components, such as resistors, capacitors, and inductors. For modeling the equivalent circuit, it should be noted that each element in the circuit model should response to the electrochemistry of the system and the minimum number of elements should be used. For EIS measurement, a three-electrode cell deign is preferred to avoid an intervention of unwanted impedance rooted from the counter electrode. The details about three electrode cell is described in the next section.

EIS results represented in chapter 3 were performed by three-electrode cell design using a VMP3 potentiostat/galvanostat with EIS/Z capabilities and EC-Lab software. For EIS measurements, the DC voltage was maintained at open-circuit voltage and an AC voltage of 10 mV in amplitude was applied with a frequency of 200 kHz ~ 3 Hz.

2.14.4 Electrochemical Cell Configurations

The electrochemical performance of the cathode materials presented in this thesis were tested by two electrode 2325 coin cell system. **Figure 2.8** shows a schematic description of the coin cell parts and their assembly order from the bottom part. Once the positive electrode is prepared by following the instructions in each later chapters of this thesis, all other coin cell assembly procedures were conducted from the argon gas filled glove box. After placing the positive electrode on the bottom current collector, the positive and the negative electrodes were separated by a layer of glass fiber separators (Merck

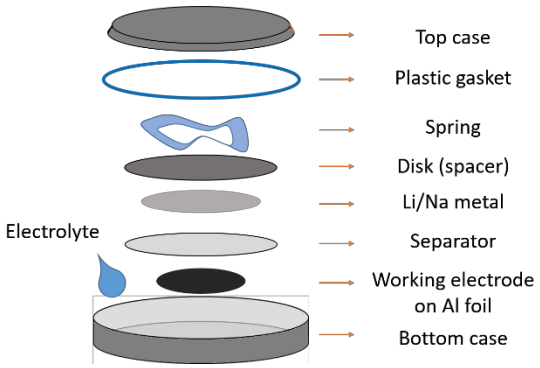

Figure 2.8 Schematic presentation of coin cell components

Millipore or VWR international). The negative electrode is chosen between lithium and sodium metal placed on a stainless steel disk depending on the purpose of the electrochemical cell test. A stainless spring is placed on the negative electrode disk to ensure good contact between the components of the cell after crimping the cell. Before the cell crimping, the plastic gasket and current collect cap is placed on the other cell components and crimped by coin cell crimper.

Even the two electrode system provides sufficient information about electrochemical properties of the electrode materials in the cell, it is not possible separating the electrochemical response signal only from the one side of electrodes. For instance, the side reactions occurring while the cell cycling, such as electrolyte decomposition, cracking the cathode particles by volume change, irreversible phase transition of electrode materials, and etc., affect the chemical potential of the positive and negative electrodes every cycle, and make it hard to investigate the absolute potential change of one side of electrodes solely at equilibrium status of the cell. Therefore, setting a reference electrode within a system which is stable in chemical potential over the cell cycling is helpful to investigating the electrode. As the reference electrode do not participate in the electrochemical reaction and maintain its initial chemical potential over the cell cycling, it can provide the accurate potential change from the positive

or negative electrode. Therefore, it enables the in depth study of redox properties and phase transition of the electrode materials over the cell cycling.

Among multiple cell designs establishing the three electrode system, three electrode electrochemical cell (Conflat cell)[7] in **Figure 2.9** is employed for EIS study in this thesis. In the conflate cell, Li metal was employed as counter electrode and reference electrode. For the reference electrode, Li metal was punched into a ring shape and placed on a stainless steel (SS) ring that contacts the middle can part of conflate cell.

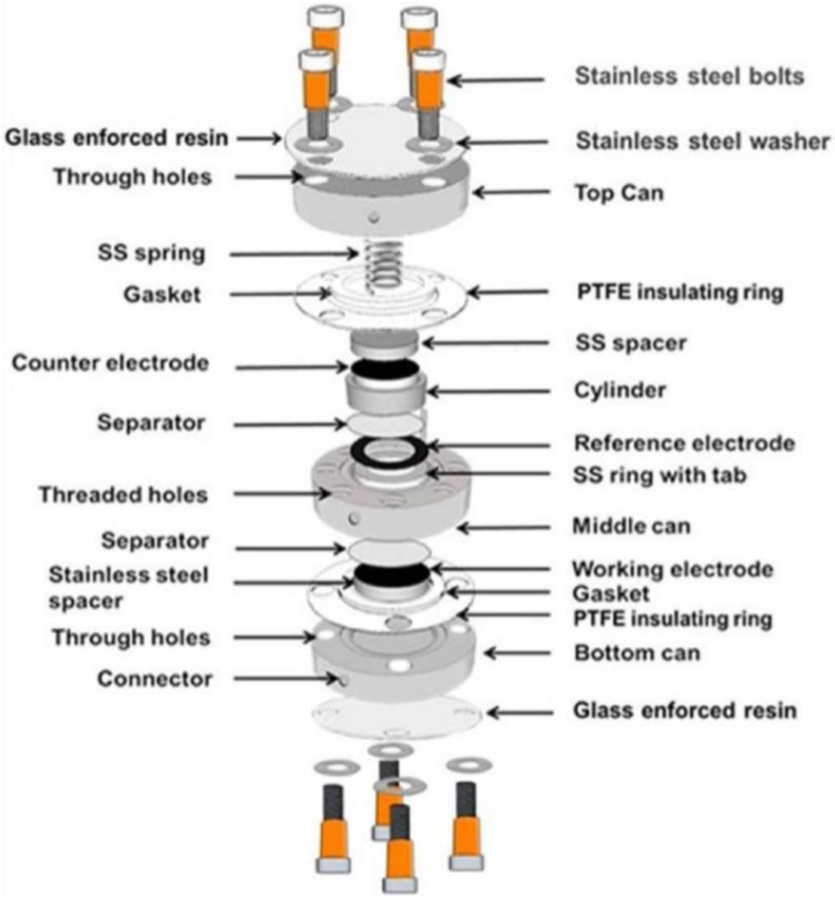

Figure 2.9 Exploded view of a 3-electrode Conflat cell. Adopted from ref 7 with permission. Copyright © 2014 IOP Publishing, Ltd.

Chapter 3

Inhibiting Oxygen Release from Li-rich, Mn-rich Layered Oxides at the Surface with a Solution Processable Oxygen Scavenger Polymer

3.1 Introduction

Increasing demand for energy storage systems to power a variety of devices ranging from robots to electric vehicles (EVs) has led to a rush to develop high energy density lithium ion batteries (LIBs) that are necessary to fulfill their requirements.[1] However, although LIBs have been intensively developed and commercialized for various applications in industry, their energy density still needs to be improved to achieve goals in cost and energy efficiency.

In this context, Li-rich Mn-rich layered oxides (xLi_2MnO_3 - $(1-x)LiMO_2$, M=Ni, Mn, Co) or "LRLOs" have attracted significant attention because their reversible capacities usually exceed 250 $mAh{\cdot}g^{-1}$, well above that of conventional lithium transition metal (TM) layered oxides ($LiTMO_2$, TM=Ni, Mn, Co). Early on, several studies determined that the origin of such high capacity lies not only in transition metal redox but also in anion redox processes ($O^{2-\delta}/O^{2-}$ or $2O^{2-}/O_2^{n-}$) which contribute to the reversible capacity.[2] This was suggested to occur mainly in the bulk, with irreversible oxygen loss occurring at the surface.[3] Previous reports also showed that a substantial amount of Li removal - together with oxygen loss from the lattice - facilitates cation migration and structural rearrangement which triggers conversion to a disordered-spinel (TM_3O_4) and rock-salt structure (TMO-type) at the surface.[4] Recently, using a combination of high-resolution resonant inelastic X-ray scattering (HR-RIXS) and solid-state ^{17}O NMR spectroscopies, Bruce's group showed that the reversible oxygen redox

in LRLO is attributed to molecular oxygen formed in the bulk lattice during the first charge.[5] The O_2 (trapped in the bulk within TM vacancy cluster defects generated by TM migration) is reversibly reduced back to oxide ions on discharge, while the O_2 at the surface is lost, incurring the densification of the surface to spinel/rock-salt and a ~ 25 % loss of the O-redox capacity (i.e., 13% redox active lattice oxygen). DFT studies suggested the drop in charging voltage from the first to second cycle is because the oxide ions within the TM cluster undergo O^{2-}/O_2 redox at a lower potential than in the pristine material. This voltage drop (which continues on cycling albeit to a much lesser degree) lowers the energy density and in combination with the other factors, hinders the practical use of these materials.[6] In addition to the structural degradation of LRLO, the released oxygen at the surface causes capacity fading becuase of its side reactions with the organic electrolyte. Previous investigations identified that the O_2 is released as oxygen radicals and singlet O_2.[3g, 4b, 7] These highly reactive oxygen species (ROS) attack carbonate-based electrolytes such as dimethyl carbonate (DMC) and ethylene carbonate (EC), and cause their decomposition.[3g, 4b, 8] The resulting gradual accumulation of a thick solid cathode-electrolyte interphase (CEI) layer on the electrode surface, and leads to inferior rate capability and poor cyclability because of impedance build-up.[4b, 9] Suppressing the oxygen release to inhibit phase transitions and parasitic reactions at the surface is thus crucial to the employment of oxygen redox in LRLO as a high energy density cathode material for LIBs.

Previous researchers have suggested surface modification may be a solution to this problem. Much research has been devoted to coating LRLOs to prevent undesired reactivity between the electrolyte species and electrode.[10] Both inorganic [11] and organic coatings [12] have been shown to be helpful in enhancing the electrochemical performance by reducing side reactions at the cathode-electrolyte interface. These coatings represent simple physical barriers.[13] A different approach that has not been explored to date is the use of a chemical approach to mitigate oxygen release. Such a coating

would limit the ROS evolution from the oxide surface that gives rise to electrolyte decomposition by acting both as a chemical and physical protection layer.

Human eyes also suffer from ROS caused by sunlight exposure (i.e., by UV irradiation). To protect them from detrimental attack, the iris in the eye contains the pigment melanin (which is responsible for eye color) that scavenges ROS[14] such as singlet oxygen ($^1O_2$), and oxygen radicals ($O_2^{\bullet -}$). [14a, 15] Taking a cue from this approach, researchers developed a synthetic melanin called polydopamine (PDA), composed of 3,4-dihydroxy-L-phenylalanine (L-DOPA) and lysine-containing catechol and amine functional groups, respectively.[16] The catechol structure in dopamine is widely known as the key which enables PDA to act as an antioxidant and free radical scavenger. [17] The use of PDA in ROS-related fields such as biology,[18] biomedicine,[19] and energy storage systems,[20] inspired us to explore it as an oxygen capture agent for LRLO materials. The free radical/singlet oxygen scavenging nature of PDA suppresses reactivity of the cathode surface (generated by oxygen loss on the activation (and subsequent) cycles) with the electrolyte, thereby altering the interphase formed at the cathode-electrolyte interface while providing an amorphous polymer layer that is permeable to Li-ions. Herein, we demonstrate that PDA provides a chemically protective, conformal layer that leads to diminished CO_2 and O_2 gas evolution, significantly suppressed structural transformation which enhances cyclability, and reduced CEI formation and hence improved rate capability. Our findings suggest an important influence of this polymer to mitigate surface oxygen evolution in Li-rich Mn-rich layered oxides.

3.2 Experimental Details

All synthesis and characterization studies were carried out at the University of Waterloo, with the exception of the high-resolution TEM studies that were performed by Dr. Shahrzad Hosseini at the Canadian Centre for Electron Microscopy at McMaster University.

3.2.1 Polydopamine coating on LRLO

To prepare the PDA coated lithium-rich, manganese-rich transition metal oxide (LRLO), the LRLO crystalline powder (BASF SE) was immersed into a Trizma buffer solution (10 mM, pH 8.5) in distilled (DI) water in a volume ratio of 8:2. Dopamine hydrochloride powder (Sigma-Aldrich) was then added to the mixture in the targeted stoichiometric ratio, where it undergoes self-polymerization. The thickness of the coating layer was controlled with the amount of dopamine hydrochloride that was added (0.3, 0.5, and 2 wt% of active material). The mixture was stirred at room temperature for 30 min, and the filtered powder was washed with ethanol and DI water several times to remove any residual unpolymerized dopamine hydrochloride. The powder was then dried at 100°C in a vacuum oven overnight. Based on the amount of dopamine precursor, the PDA coated Li-rich layered powder samples are denoted as bare (0 wt%), PD3 (0.3 wt%), PD5 (0.5 wt%) and PD20 (2.0 wt%).

3.2.2 Oxygen radial ($O_2^{\bullet -}$) reacted polydopamine powder

First, PDA powder is collected by oxidizing dopamine hydrochloride powder (Sigma-Aldrich) in Trizma buffer solution as described above except for adding LRLO powder. Oxygen radial ($O_2^{\bullet -}$) reacted PDA powder is prepared by exposing PDA to $O_2^{\bullet -}$ in acetonitrile (ACN) solvent. To generate $O_2^{\bullet -}$ radical, 21.3 mg of potassium dioxide (Sigma-Aldrich) and 79.35 mg of 18-crown-6 ($\geq$ 99.0 %, Sigma-Aldrich) were added to 5 ml of ACN solvent containing 15 mg of PDA powder. The prepared solution was then stirred for 6 h in the amber glass vial without exposing to the light and centrifuged several times to remove the unreacted chemicals. The collected PDA powder after centrifuging is transferred for dynamic vacuum drying at room temperature.

3.2.3 Preparation of Electrodes for On-Line Electrochemical Mass Spectroscopy (OEMS)

The working electrodes were prepared by drop-casting mixtures of 92.5 wt % LRLO active material (BASF SE), 4 wt % Super P carbon black (TIMCAL), and 3.5 wt % polyvinylidene-fluoride binder (PVDF, Solef 5130, Solvay, Belgium) suspended in an N-methylpyrrolidone solvent (99.5%, Sigma-Aldrich) directly on titanium mesh current collectors. The prepared electrodes were then dried at 120 ℃ for 12 h under vacuum and transferred into an argon-filled glovebox (O_2 and H_2O < 0.1 ppm) before being assembled into the electrochemical OEMS cells with lithium metal foil as a counter electrode. The average electrode loading with respect to the active material was ~ 10 ± 0.5 mg·cm^{-2} and 1 M lithium hexafluorophosphate ($LiPF_6$) in ethylene carbonate (EC) and propylene carbonate (PC) (1:1 v/v) solution (Gotion inc.) was used as the electrolyte. The electrochemical data was collected using an Arbin battery cycler.

3.2.4 Electrochemistry

For electrode fabrication, the LRLO powder (BASF SE) was mixed with 4 wt % Super P carbon black (TIMCAL), and 3.5 wt % polyvinylidene-fluoride binder (PVDF, Solef 5130, Solvay, Belgium) suspended in an N-methylpyrrolidone solvent (99.5%, Sigma-Aldrich) to achieve a final weight ratio of active material: carbon: binder in the cathode of 92:4:4. This mixture was cast on aluminum foil with a typical loading of 6 ~ 7 mg·cm^{-2}. Roll pressed electrodes of 1 cm^2 geometric area were punched and dried at 120 °C in a vacuum oven. The electrochemical properties of the materials were evaluated in 2325 coin cells using 1 M lithium hexafluorophosphate ($LiPF_6$) in a Diethyl carbonate (DEC) and highly fluorinated ether (K2) solution (BASF SE) containing fluoroethylene carbonate (FEC) as the electrolyte, glass fiber (Merck Millipore) as separators, and Li metal (99.9%, Sigma Aldrich) as the counter electrode, respectively. Coin cell assembly was performed inside a glove box under argon (O_2

and H_2O < 0.1 ppm). Galvanostatic cycling tests were conducted at 23 °C within a potential window of 2.0–4.7 V (vs Li/Li^+) using a multichannel battery tester (Model 4000, Maccor Inc.).

3.2.5 Electrochemical Impedance Spectroscopy (EIS)

Three electrode cells were prepared with Li metal foil as the counter electrode and as the reference electrode which was placed within the electrode-sandwich formed by the cathode and anode. AC impedance measurements were performed using a signal with amplitude 10mV over a frequency range from 200 kHz to 3Hz using an (VMP3, Bio-Logic). After the first activation cycle at 0.05C (15 mA/g), the cell is cycled at various C rates as it is described in **Figure 3.13a**. EIS data is collected at 4.0 V during discharge of the cell from the first, 7th, 46th, and 85th cycles. After the cell reached to 4.0 V during discharge, the cell was held at the voltage for 2 h followed by 10 h of resting and AC impedance spectra were recorded at the open circuit voltage.

3.3 Results and Discussion

3.3.1 Polydopamine (PDA) coating methodology and characterization

The SEM image of pristine LRLO is shown in **Figure 3.1**. The spherical secondary particles are comprised of an aggregation of nano-sized primary crystallites. To verify the formation of the self-polymerized PDA layer on the surface of LRLO, XPS analyses were conducted on a bare oxide surface, and an oxide coated with 5 wt% PDA ("PD5") as an example. The XPS spectrum of PD5 (inset, **Figure 3.1a**) shows a peak in the N 1s region (~ 400 eV) which was deconvoluted into two components. The two main peaks centered at 398 eV and 401 eV are definitively assigned to C-N=C and -NH- functional groups of the PDA, respectively.[21]

The success in uniformly, conformally and controllably coating the LRLO with PDA was demonstrated using high resolution TEM (HRTEM). In **Figure 3.1b**, the lattice-resolved representative

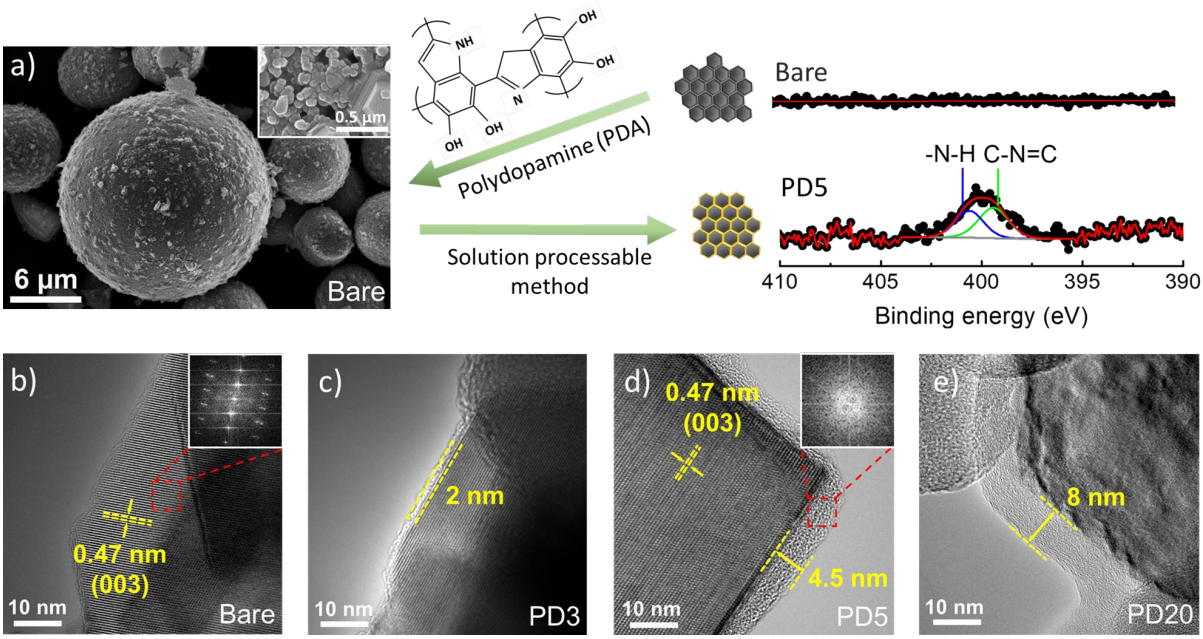

Figure 3.1 Characterization of PDA coating on the surface of Li-rich layered oxide. (a) A schematic diagram of the solution processable method with SEM image of bare and XPS spectra of bare and PD5. (b) - (d) HRTEM image of bare and PDA coated samples (0.3, 0.5, and 2 wt% of PDA, respectively, deemed PD3, PD5, and PD20).

HRTEM image of uncoated LRLO and the corresponding fast Fourier transform (FFT) of the image (inset) shows the single-crystalline nature of the particles. The resolved lattice planes show a spacing of 0.47 nm, corresponding to the (003) plane. The HRTEM images of PDA-coated LRLO with variable PDA content are shown in **Figure 3.1c-e** for materials with 0.3, 0.5, and 2 wt% of PDA, deemed PD3, PD5, and PD20, respectively. The HRTEM images show that the thickness of the PDA coating layer is readily controllable with our simple solution-based approach. They reveal the formation of a uniform layer of PDA on the surface in all cases, with a thickness ranging from about 2 nm to 13 nm. In the case of PD5, the PDA coated layer is about 4 ~ 5 nm thick. The corresponding FFT from the coating layer (inset of **Figure 3.1d**) shows its amorphous nature. While all three coated materials were subjected to rigorous analysis and probes of their electrochemistry, since the properties of the 0.3% and 0.5 wt% PDA materials were found to be optimum -

presenting a coating neither too thick nor too thin – PD5 and PD3 are the focus of the studies reported here. The X-ray diffraction (XRD) patterns of the coated materials are the same as that of bare LRLO, as expected, as confirmed by Le-Bail fitting of the XRD patterns (**Figure 3.2**). The difference in the lattice parameters in the *R-3m* space group between the bare material and PD5, for example, is less than 0.1 % and no impurity phases were detected: this indicates that the PDA coating process does not alter the bulk structural properties (see **Figure 3.2** for details).

As shown in the inset of **Figure 3.1a**, the presence of macro-sized pores in the secondary particles of LRLO could hinder the uniform surface coating of primary crystallites in the interior. To investigate whether this indeed is a factor, we carried out ToF-SIMS measurements on secondary particle agglomerates modified with PDA. PD5-LRLO was used for these studies owing to its higher PDA content, and hence easier detection. Since the amine group in PDA yields a CNO^- fragment as a secondary negative ion, monitoring that fragment signal during ToF-SIMS provides vital spatial information about the coating of the particles that reside in the interior of the agglomerate. **Figure 3.3a** shows the negative ion ToF-SIMS chemical mapping of CNO^- and MnO^- ion fragments obtained during sputtering of the bare and PD5 particles. The negative ion images demonstrate the absence of CNO^- ion fragments from bare LRLO but show that the CNO^- ion is evolved from within the entire PD5 particle, where CNO^- is found to be highly concentrated in the centre of the secondary particle agglomerate. Meanwhile, chemical mapping of the MnO^- ion and the depth profiling results in **Figure 3.4** show that the manganese fraction in the secondary particle agglomerate is very similar in the bare and coated materials. This serves as an internal reference. The 3D contrast image in **Figure 3.3b** shows the measured spots (~ 95 nm in spatial resolution) representing the change in intensity of the CNO^- fragment evolved during sputtering of the PD5 particle, viewed along the (111) axis of virtual cubic space and from the cross section of the particle along the (00-1) axis while sputtering, respectively.

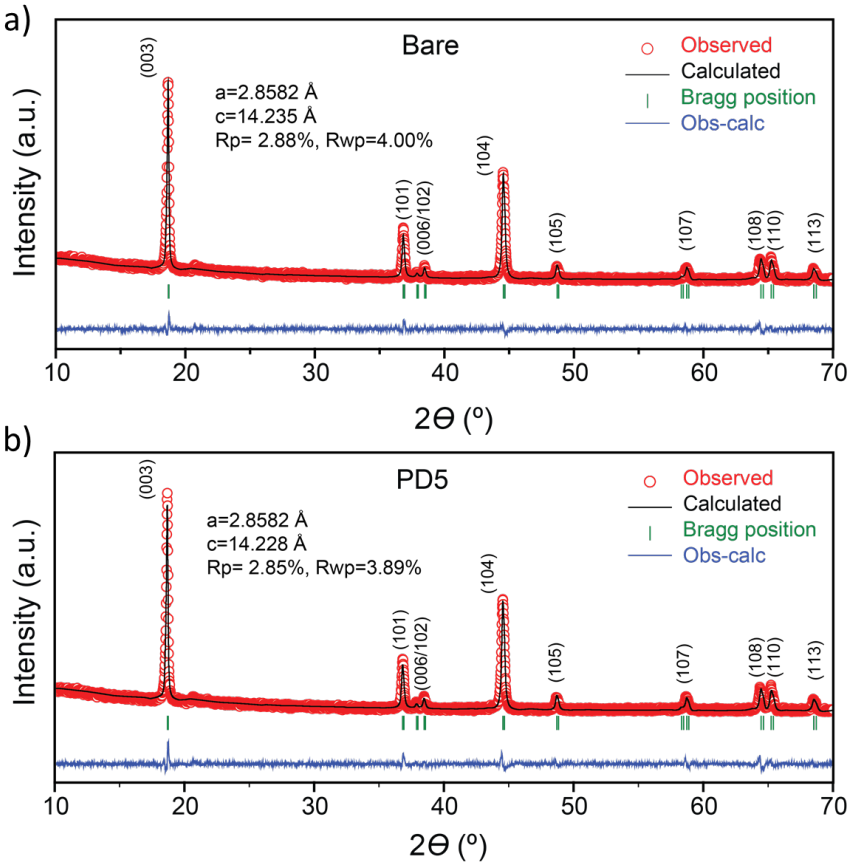

Figure 3.2 Powder XRD pattern and Le Bail fitting of the (a) Bare and (b) PD5. The diffraction patterns of bare-LRLO and PD5-LRLO show that both patterns are refined by a full-pattern fit in the trigonal space group $\boldsymbol{R\bar{3}m}$ with superstructure peaks at 20-23°. The lattice parameters show no significant difference, and the bulk properties are not altered by the coating process.

As an ion fragment is evolved from the top surface of the spherical shape sample and projected to the detector, the collected signal from the sample gives a conical shape contrast image during sputtering. The CHO^- ion fragment detected from the entire and the cross-sectional contrast image of PD5 indicates that PDA completely infiltrates the pores of the secondary particle, thus coating the entire material.

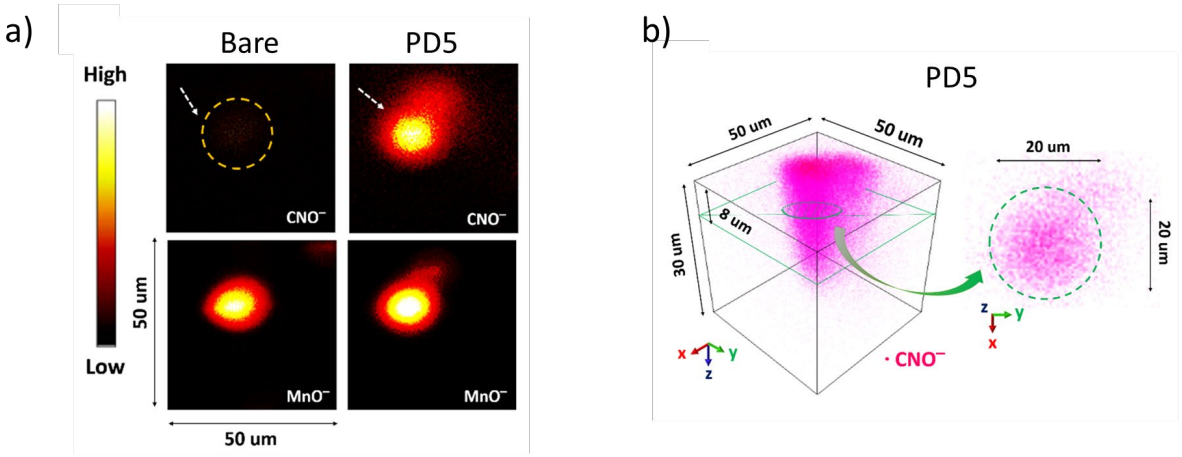

Figure 3.3 Investigation of impregnated PDA coating on LRLO. (a) TOF-SIMS chemical maps of two secondary ion fragments, CNO^- (upper) and MnO- (lower), on bare-LLRO (left column) and PD5-LRLO (right column) particle. (b) The 3D contrast image of the measured CNO^- fragments from PD5 during particle sputtering viewed along (111) axis of the virtual cubic space (left) and from the cross section of the particle along (00-1) axis (right).

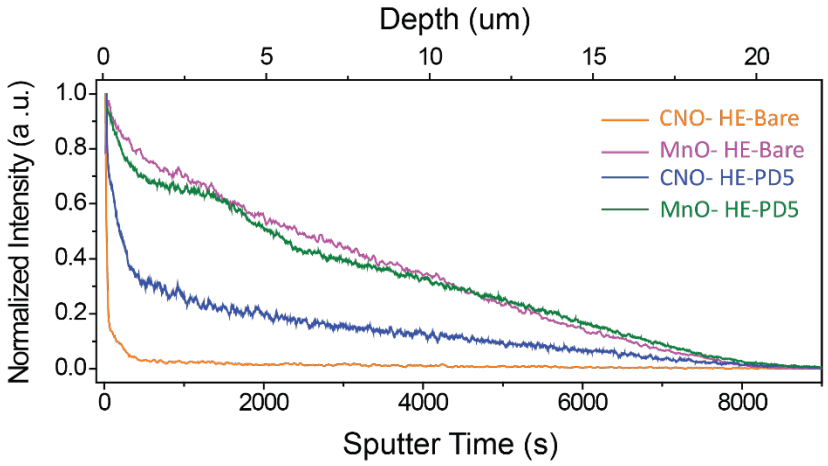

Figure 3.4 Normalized (to maximum) depth profiling of CNO^- and MnO^- secondary ion fragments in the ToF-SIMS spectra from the bare-LRLO and PD5-LRLO particles. The depth is calculated based on the calibrated Cs ion sputtering rate of ~ 2.0 nm/s for the active material.

3.3.2 PDA coating on LRLO: initial activation step and OEMS studies

The first oxidation cycle of LRLO triggers the well-known electrochemical activation of Li_2MnO_3 domains in the lattice above 4.4 V, incurring electrolyte decomposition alongside irreversible loss of lattice oxygen.[4b, 8] This reaction leads to both gas emission and metal cation migration which causes voltage fade, capacity fade, and poor kinetics.[3g, 7, 22] The activation process within the Li_2MnO_3 domains of LRLO is accompanied by oxygen radical[4b, 8] and/or O_2 gas evolution.[23] The latter has been recently identified as $^1O_2$ [3h, 24], and the O_2 is proposed to result from the combination of two O^0 radicals generated by disproportionation of unstable O^- formed on initial oxidation of O^{2-} ions. At the surface, these reactive oxygen species (ROS) react with the carbonate electrolyte, forming a CEI impedance layer in parallel with some irreversible loss of oxygen.[4b, 25] Therefore, LRLO needs a design strategy such as a ROS scavenger (i.e., PDA) to mitigate this loss. We first established the electrochemical stability of PDA by cyclic voltammogram (CV) measurements between 2.0 - 4.8V (**Figure 3.5**). PDA shows no significant oxidation peaks in the CV profile while the response stabilized upon cycling.

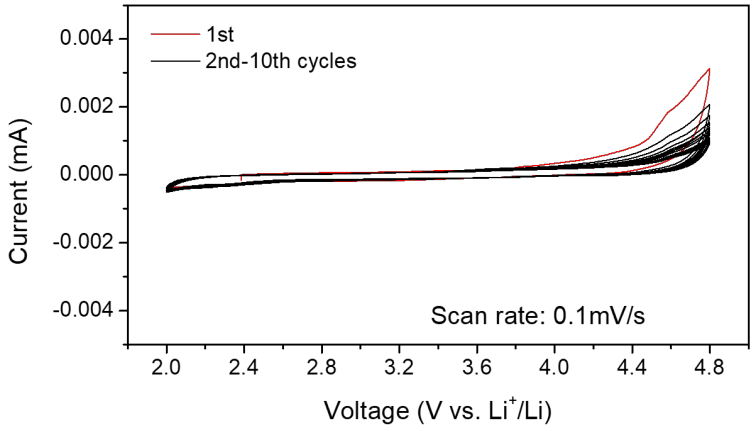

Figure 3.5 Cyclic voltammetry (CV) scan of the PDA electrode at a scan rate of 0.1 mV/s in the voltage window between 2.0 V and 4.8 V (V vs. Li^+/Li) (composition of electrode: PDA : Carbon : PVDF = 90 : 5 : 5 wt%).

To monitor the PDA scavenging effect, LRLO materials were first activated in the voltage window 2.0 - 4.8V at a current rate of C/20 (12.5 mA/g) in a half-cell. **Figure 3.6a** depicts the charge-discharge profile of bare-LRLO and PD5-LRLO. In the charging process below 4.4 V (Region I), the capacity of both bare and PD5 reaches the same value of 142 $mAh \cdot g^{-1}$, indicating the oxidation of transition metals (Co^{3+}/Co^{4+} and Ni^{2+}/Ni^{4+}) in layered $LiTMO_2$ (TM = transition metal) in LRLO.[26] The plateau above 4.4 V (Region II) - corresponding to O oxidation[5] - exhibits a capacity of 169 $mAh \cdot g^{-1}$ and 155 $mAh \cdot g^{-1}$ for bare-LRLO and PD5-LRLO, respectively. Accordingly, the derivative (dQ/dV) plot of PD5-LRLO shows decreased peak intensity in this region (**Figure 3.6b**) indicating a little less charge compensation from generation of localized holes on the oxygens coordinated by Mn^{4+} and Li^{+} ions (possibly on the surface).[3b] The discharge curve of the dQ/dV plot reveals a feature near 3.3 V that correlates to the reduction of transition metals and oxidized oxygen in bare LRLO accompanied by a possible structural change from a layered structure to a spinel-like structure that is further related to the anion redox activity.[5, 27] By comparison, this feature is slightly diminished in PD5-LRLO.

While we propose that the reaction of evolved ROS from the oxide surface with PDA would result in an oxygenated and/or cross linked polymer, the PDA layer was unfortunately too thin to reliably analyse. Therefore, we fabricated an LRLO electrode coated with 20 wt% PDA (PD20-LRLO) without adding active carbon or binder, and cycled it at a slow C-rate (1/50 C) to minimize the voltage polarization from the low electrical conductivity due to lack of carbon additive. For comparison, pure PDA powder was treated with $O_2^{\bullet -}$ generated by a reaction between KO_2 and 18-crown-6 in acetonitrile (see experimental section for details).

Raman spectroscopy in **Figure 3.7a** shows the pure PDA exhibits two bands in the region between 800 and 2000 cm^{-1}: the 1350 cm^{-1} peak (A) corresponds to the stretching vibration of the aromatic C-N bond, and the 1570 cm^{-1} peak (B) is the stretching vibration of the aromatic C=C bond.

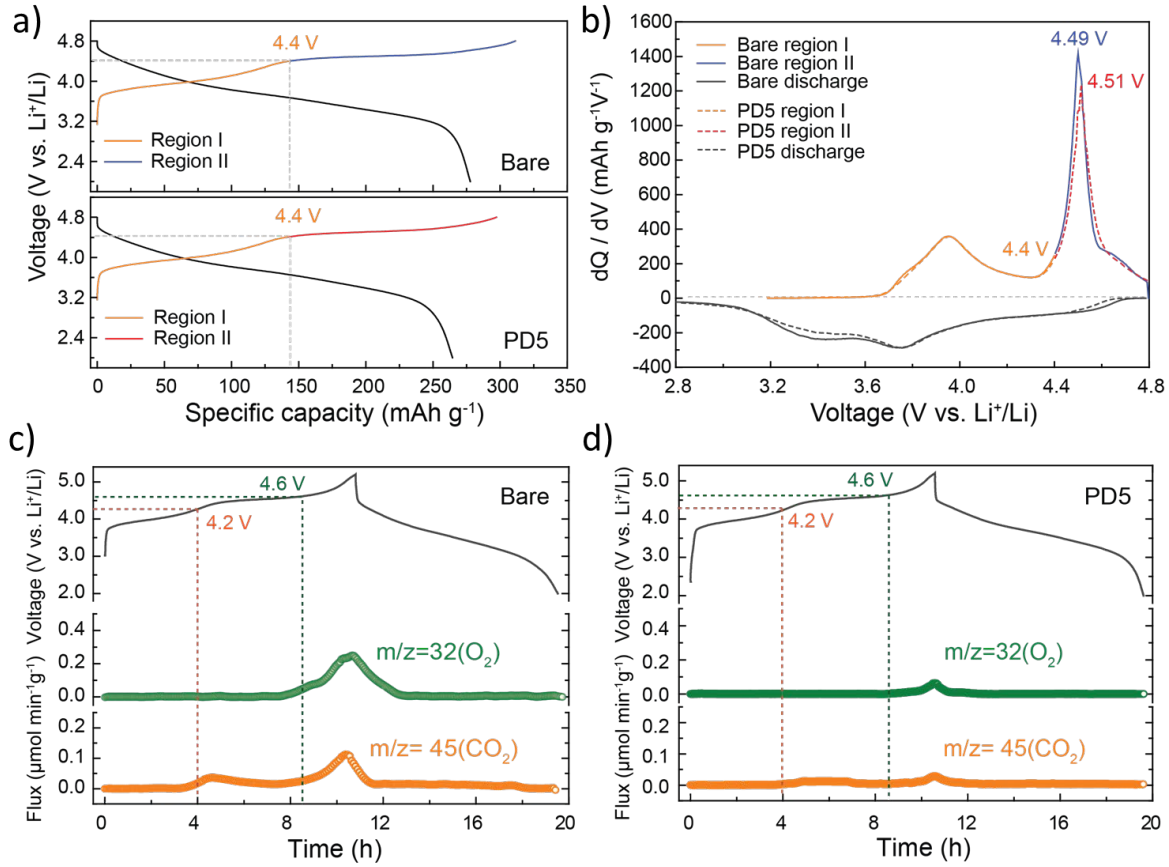

Figure 3.6 The oxygen radical scavenging effect by PDA. (a) Comparison of first charge/discharge profiles and (b) derivative plots of bare and PD5 electrodes. The voltage window of both electrodes was 2.0 - 4.8 V vs. Li^+/Li at a rate of C/15. (1C = 250 mAh·g^{-1}) (c) Potential and gas evolution profiles of CO_2 and O_2 measured during galvanostatic cycling of bare-LRLO and (d) PD5-LRLO electrodes cycled in the 2.0 - 5.2V window at C/10.

Upon reaction with superoxide, oxidation of the dopamine group is signalled by the sharp 33% increase in the A/B peak intensity ratio owing to cyclization of the dopamine group to 5,6-dihydroxyindole.[28] There is no change in the ratio upon subjecting pure PDA to a 4.8V "charge" in the absence of LRLO, since no ROS species are generated (**Figure S3a**). However, the spectrum of the charged PD20-LRLO electrode in **Figure 3.7b**, shows a distinct increase in the A/B ratio compared to that of the as-prepared electrode (**Table 3.1**). The increase (12%) is consistent with a lower degree of reaction (*vs* the treatment

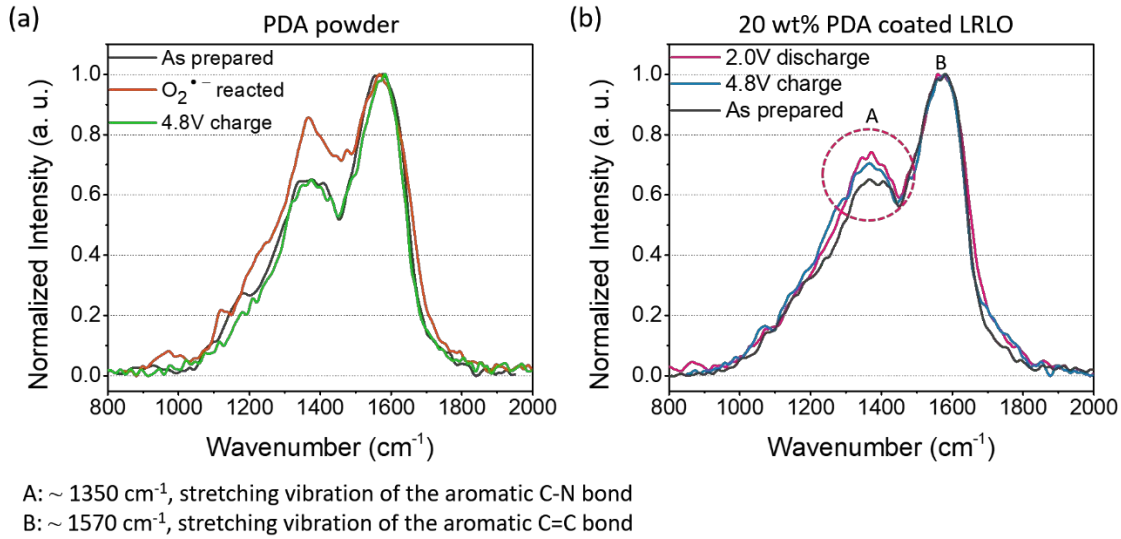

Figure 3.7 Normalized ex-situ Raman spectra of (a) PDA powder as-prepared; after reaction with superoxide; and PDA powder electrode held at 4.8 V for 2 hrs after applying a constant current (1 mA/g) up to 4.8 V (charge); (b) 20 wt% PDA coated LRLO electrode (PD20-LRLO) as-prepared; after 4.8 V charge; and after 2.0 V discharge. In the case of PDA powder held at 4.8 V (green curve) in (a), the electrode was fabricated by pressing PDA powder on Al foil without LRLO, active carbon, or binder (see experimental section). The Raman spectra in **Figure 3.7a** demonstrate that PDA could not be electrochemically oxidized but could be chemically oxidized by reacting it with the superoxide radical. In the Raman spectra collected on 20 wt% PDA coated-LRLO electrodes in **Figure 3.7b**, the slightly higher 'A' peak intensity of the discharged electrode (pink curve) compared to the charged electrode (blue curve) may be due to the overall longer exposure time of PDA to ROS in the electrochemical experiment. The residual 'A' peak intensity from the discharged electrode indicates the irreverible ROS scavenging reaction of PDA.

Table 3.1 A and B peak intensity ratio of the Raman spectrum from **Figure 3.7**.

Sample	Peak ratio (A/B)
PDA powder	
As prepared	0.64
$O_2^{\bullet -}$ radical reacted	0.85
4.8 V charged	0.64
20 wt% PDA coated LRLO	
As prepared	0.65
4.8V charged	0.71
2.0V discharged	0.74

with pure superoxide in solution, as expected) and clearly indicates that PDA scavenges the evolved ROS from LRLO. The same is anticipated in charged PD5-LRLO.

On-line mass spectrometry (OEMS) studies were performed to quantify the role of PDA coating on gas evolution during the first cycle. **Figures 3.6c and d** show the O_2 and CO_2 gas evolution detected in the OEMS measurement during the 1st activation cycle of the bare-LRLO and PD5-LRLO electrodes, respectively, in a potential window from 2.0 to 5.2 V at a current rate of 0.1 C (25 mA g^{-1}). The galvanostatic charge/discharge profile of both electrodes from the OEMS cell shows a similar potential plateau and capacity region as addressed above. In **Figure 3.6c**, the CO_2 evolution spans two regions. The first CO_2 peak at an initial voltage at 4.2 V is attributed to the oxidation of carbonate impurities such as Li_2CO_3 on the surface of LRLO.[3g, 23] On charge above 4.6 - 5.0 V, the formation of highly reactive $^1O_2$ (that presumably immediately decays to its stable triplet form) [3h] and $O_2^{\bullet -}$ radicals [8, 29] at the surface of LRLO has been established. Others have further suggested that the unstable oxygen hole-state initially formed on oxidation disproportionates ($2O^- \rightarrow O^{2-} + O^0$), and the latter dimerizes to O_2, [5] while slightly earlier studies identified the initially oxidized species simply as "O^{n-} ($n < 2$)". The second CO_2 evolution that commences above 4.6 V and peaks at 5.2 V originates from the chemical reaction of these evolved ROS with carbonate electrolyte to give rise to decomposed species that produce CO_2 [3g, 23]. Hence CO_2 evolution is accompanied by O_2 gas release, whose evolution rate decreases after reaching a maximum at 5.2 V. Most importantly, the PDA coating significantly affects this production. While the CO_2 and O_2 evolution in bare-LRLO is 0.11 $\mu mol \cdot min^{-1} \cdot g^{-1}$ and 0.24 $\mu mol \cdot min^{-1} \cdot g^{-1}$, respectively, in PD5-LRLO, the gas evolution is four-fold lower: 0.028 $\mu mol \cdot min^{-1} \cdot g^{-1}$ (CO_2) and 0.06 $\mu mol \cdot min^{-1} \cdot g^{-1}$ (O_2) were detected on the first cycle. The diminished CO_2 release of PD5-LRLO at 4.2 V is likely affected by the nature of the solution-based coating process, which removes some of the surface carbonate impurities. The reduction of CO_2 evolution between 4.6 -5.2 V that we see, however,

is clearly due to lowered reactivity of evolved ROS with the carbonate electrolyte, owing to the $O_2^{\bullet -}$ and/or $^1O_2$ being scavenged by the PDA. In parallel, this leads to reduced O_2 evolution above 4.6 V and suggests that the PDA coating inhibits the accompanying side reactions. This is further demonstrated by surface studies described below.

3.3.3 PDA coating effect on LRLO: XPS studies

Along with OEMS, ex-situ XPS measurements (**Figure 3.8**) were conducted to determine if gas evolution was correlated with the formation of organic oxygenated species on the surface of the electrode materials that resulted from reaction of the ROS with the carbonate electrolyte. XPS spectra from the O 1s core level indicate the change in binding energy between O^{2-} and O^{n-} ($n < 2$), and thus provide insights into ROS evolution.[26, 30] The spectra of bare-LRLO and PD5-LRLO for the Li 1s, O 1s, and F 1s core levels were recorded on pristine materials; those charged at 4.8 V; and then discharged at 2.0 V. For brevity, only XPS spectra obtained for the O 1s core are presented in **Figure 3.8** (see **Figure 3.9** for Li 1s and F 1s spectra). In **Figure 3.8a**, the O 1s region of pristine bare-LRLO is characterized by one distinct component at 529.5 eV ascribed to lattice oxygen (O^{2-}) in the bulk. Other components at 531.9 eV and 533.7 eV are attributed to surface species on LRLO such as carbonate, alkyl carbonate, alkoxide and hydroxide groups.[4b, 26] In the charged state at 4.8 V, the intensity of the features with binding energies at 531.9 eV and 533.7 eV significantly increase. New peaks at 530.5 eV and 535.8 eV are observed (note that additional components were introduced only if spectral fitting was not possible in their absence). These new components signify the formation of alkyl carbonate, alkoxide and hydroxide groups indicating parasitic reactions between the cathode and electrolyte. The small peak centered at 535.8 eV is indicative of the deposition of inorganic oxygen species on the electrode surface including phosphates, and fluorophosphates ($Li_xPO_yF_z$) which result from degradation of the $LiPF_6$ electrolyte salt during initial charge.[31]

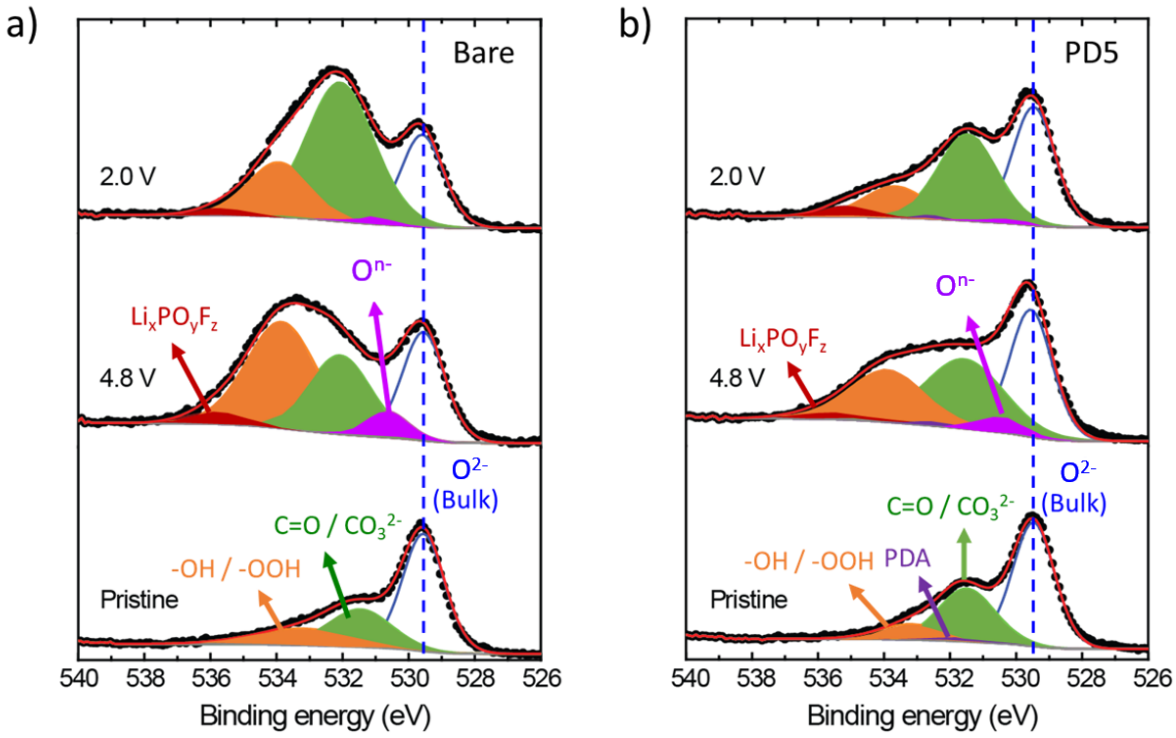

Figure 3.8 O 1s XPS surface component analysis of bare and PDA coated LRLO on the first cycle. O 1s XPS spectra acquired on (a) bare and (b) PD5 electrodes from pristine (bottom), after 1st charge (middle) and 1st discharge (top) samples. Blue dashed lines point to the components originating from lattice oxygen (O^{2-}) as a reference. Green, orange, and red arrows point to the components originating from the surface species formed during galvanostatic cycling or reaction with air in the case of the pristine sample.

The increased peak intensity of the surface species confirms that the carbonate electrolyte is decomposed by reaction with evolved ROS during the initial charge,[4b, 8] resulting in accumulation of oxygenated products on the electrode surface which form the cathode-electrolyte interphase, or CEI. The new component at 530.5 eV on charge to 4.8 V is assigned to the oxidation of surface oxide ions O^{2-} to O^{n-} ($n < 2$),[32] and/or localized oxygen hole states, based on previous studies.[5] On discharge, this feature essentially disappears as expected, whereas the oxy-organic species continue to grow.

The O 1s core spectra of PD5-LRLO are displayed in **Figure 3.8b**. The spectra of pristine PD5 and bare electrodes are very similar, except for one additional peak at 532.5 eV which can be attributed

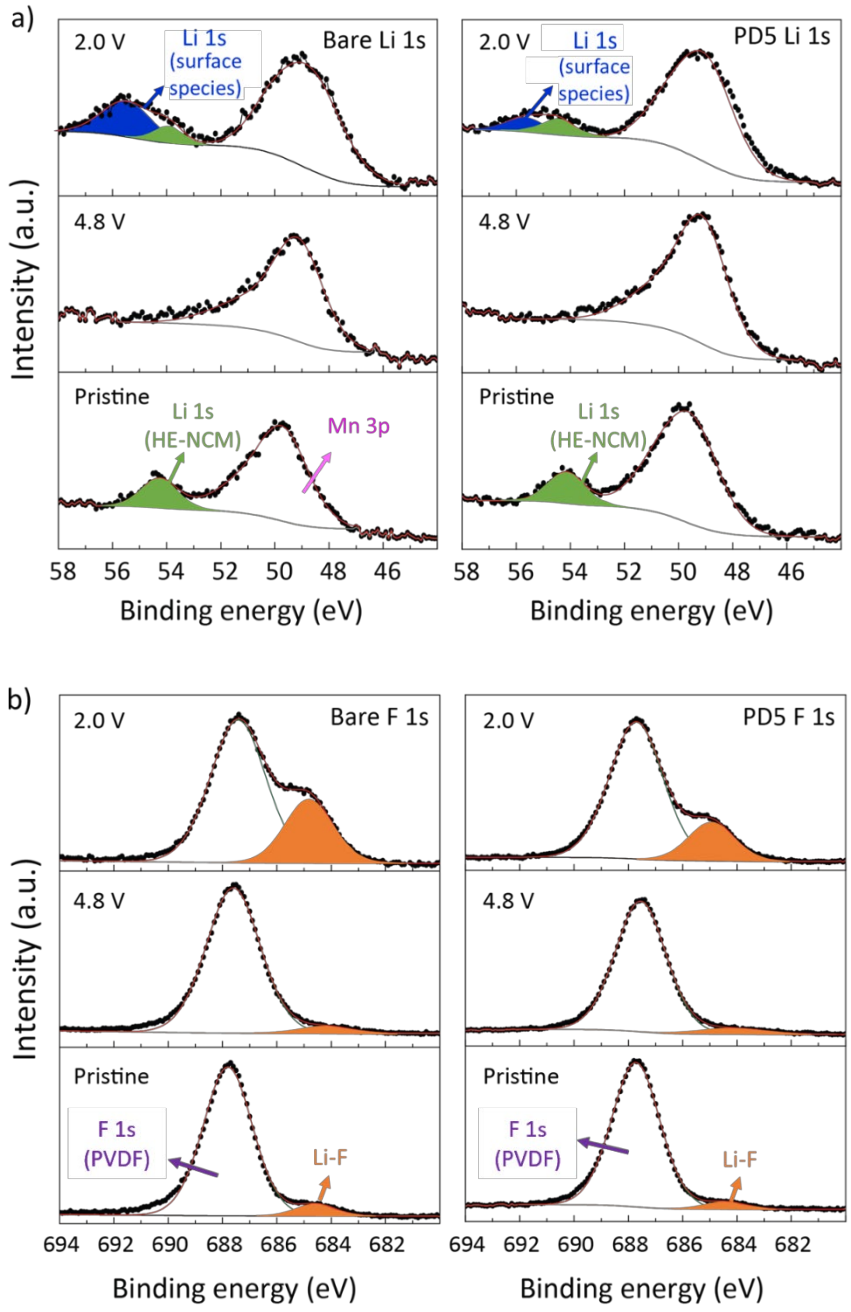

Figure 3.9 XPS spectra before acquired on bare and PD5 electrodes from the pristine material, and after 1st charge to 4.8 V and 1st discharge to 2.0 V; (a) Li 1s spectra; (b) F 1s core level spectra. Blue, green and orange arrows point to the Li 1s and F 1s photoelectron peaks of spectra from LRLO and the surface species formed during galvanostatic cycling. Magenta and purple arrows indicate the Mn 3p and F 1s core level peaks that originate from LRLO and the binder (PVDF), respectively.

to the O-C and O=C bonds in PDA (**Figure 3.1a**).[20b, 33] However, the O 1s spectra from the charged and discharged electrodes of PD5-LRLO show distinctive features compared to bare-LRLO. The intensity of the peaks evolved from surface species above 531 eV on the first charge to 4.8 V for PD5-LRLO is considerably lower than bare-LRLO. Furthermore, the intensity of the peak attributed to O^{n-} (relative to lattice O^{2-} as a reference) is significantly lower in PD5-LRLO, indicating that the O^{n-} has been consumed by reaction with the PDA. Unfortunately, the O 1s signature of oxidized PDA cannot be resolved from the oxygen in PDA itself.[20b, 34] After discharge, the O 1s core spectrum for PD5-LRLO also exhibits a much lower fraction of surface species than bare-LRLO. The lower contribution of surface decomposition species in PD5 is also confirmed by the Li 1s and F 1s core spectra displayed in **Figure 3.9**. The diminished fraction of surface species strongly supports the process of PDA scavenging the oxygen radicals on charge, to form a barrier that results in reduced surface reactivity.

3.3.4 Structural analysis of cycled Li-rich electrodes by STEM

Scanning transmission electron microscopy (STEM) studies of pristine LRLO along the [100] zone axis show that it displays a layered structure except in the first few unit cells at the surface (mainly on (100) facets) indicative of a characteristic $Fd\bar{3}m$ spinel phase (**Figure 3.10**). To investigate the effect of PDA coating on the surface structure of LRLO after cycling, electrodes prepared from bare and PDA-coated LRLO were analyzed by STEM after 100 cycles. The electrode material was extracted at discharge and subjected to analysis. While we acknowledge that STEM only samples a miniscule fraction of the electrode material, the results presented are representative of many replicate studies of materials sampled at random from the electrodes. Most importantly, they echo the findings in the electrochemical studies described below. Bare-LRLO (**Figure 3.10a-d**) and coated (**Figure 3.11a-d**) LRLO-PD3 electrode materials were analyzed by HAADF-STEM, and a series of images were acquired from various regions of particles.

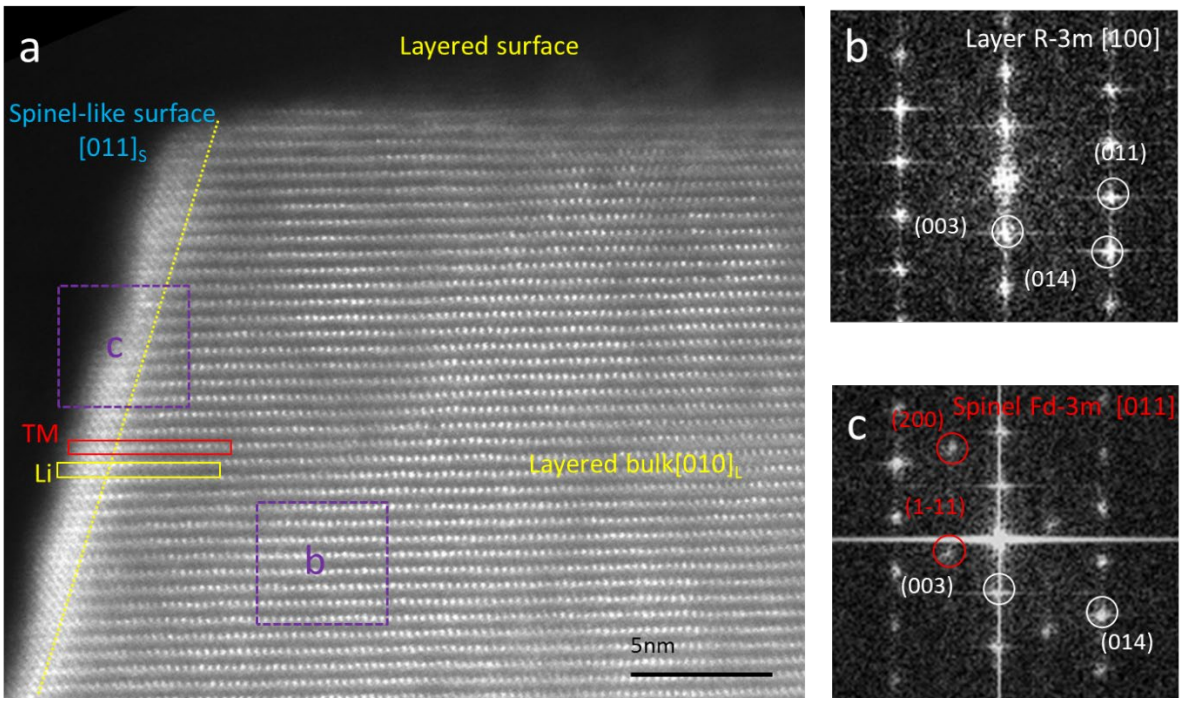

Figure 3.10 (a) HAADF-STEM image of pristine bare LRLO with the dotted yellow line delineating the surface spinel from the bulk layered region of the particle; the purple boxed region on the figure highlights the area that FFT was performed on shown in b and c. (b) FFT of the bulk region showing the reflections of the layered $\boldsymbol{R\bar{3}m}$ crystal structure, and (c) FFT of the surface region with extra reflections highlighted by the red circle from the spinel $\boldsymbol{Fd\bar{3}m}$ structure**.**

After 100 cycles, bare-LRLO shows very jagged edges on the primary particles, likely due to reaction with the electrolyte (**Figure 3.11a, b**). The thickness of the surface spinel layer significantly increases (5-7 nm) in bare-LRLO after cycling, accompanied by formation of a rock-salt-like (TMO type) structure in many regions (**Figure 3.11b**). Additionally, as **Figure 3.11c** shows, the surface spinel layer is no longer limited to the (100) facets of the LRLO particles. Transformation to a rock-salt-like structure also extends from the surface into the bulk of the bare-LRLO particles. The atomic resolution HAADF-STEM image (**Figure 3.11d**) clearly delineates layered, spinel and disordered rock salt regions, where the electron scattering intensity increases gradually from the inner part of the particle to

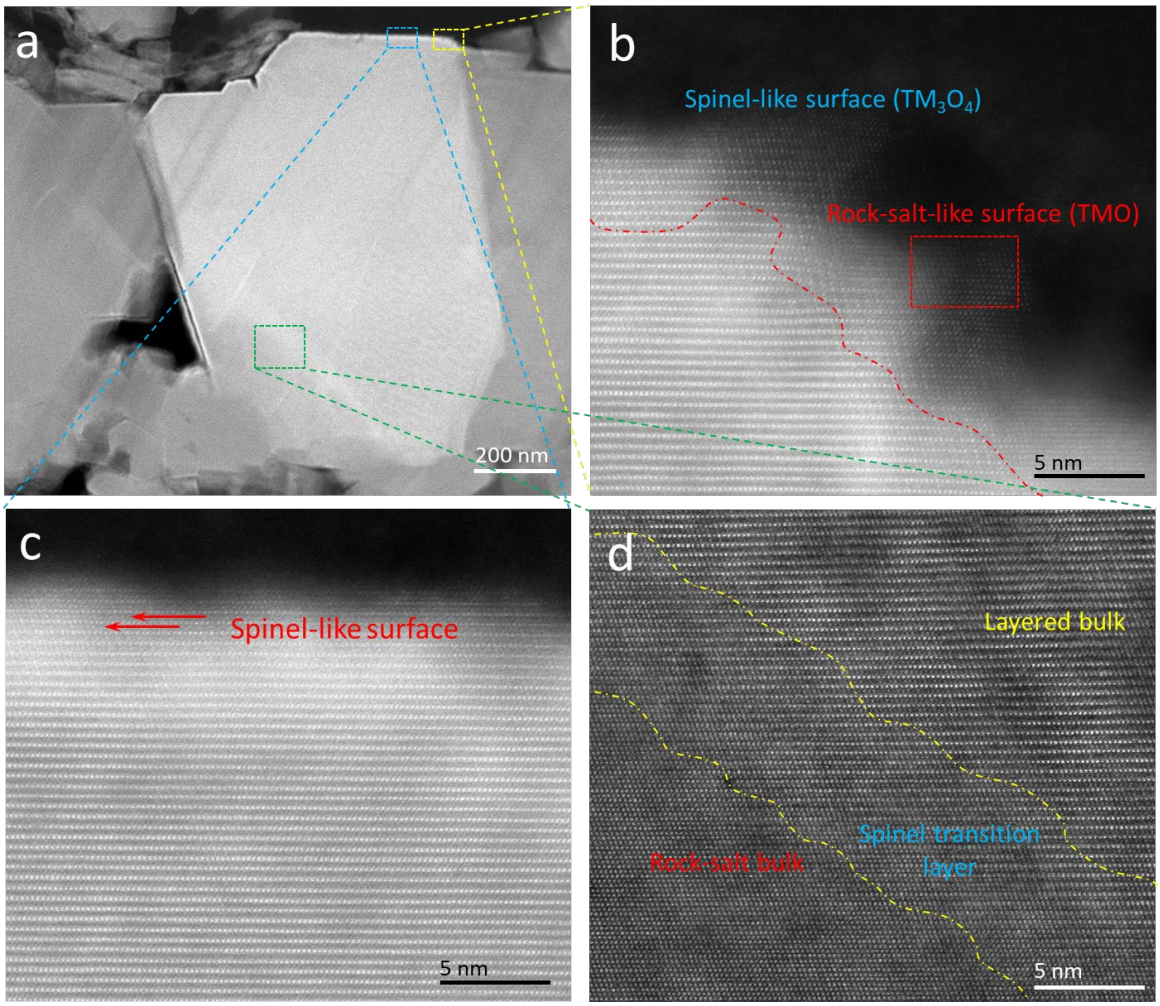

Figure 3.11 HAADF-STEM images of bare-LLRO after 100 cycles. (a) Low-magnification image of multiple LRLO primary particles with a jagged surface. (b) Atomic-resolution image of the region highlighted in yellow dashed box in (a), the red dashed line indicating surface spinel and rock-salt structures. (c) Atomic-resolution image of the region highlighted in the blue dashed box in (a), showing the TM atoms in Li layers, and (d) atomic-resolution image of the region highlighted in the green dashed box in (a) revealing the extension of the rock salt structure into the surface region of the particle (rock-salt surface, in red).

the outer disordered rock-salt region, indicating that the Li sites are partially occupied by transition metal ions in the latter case.

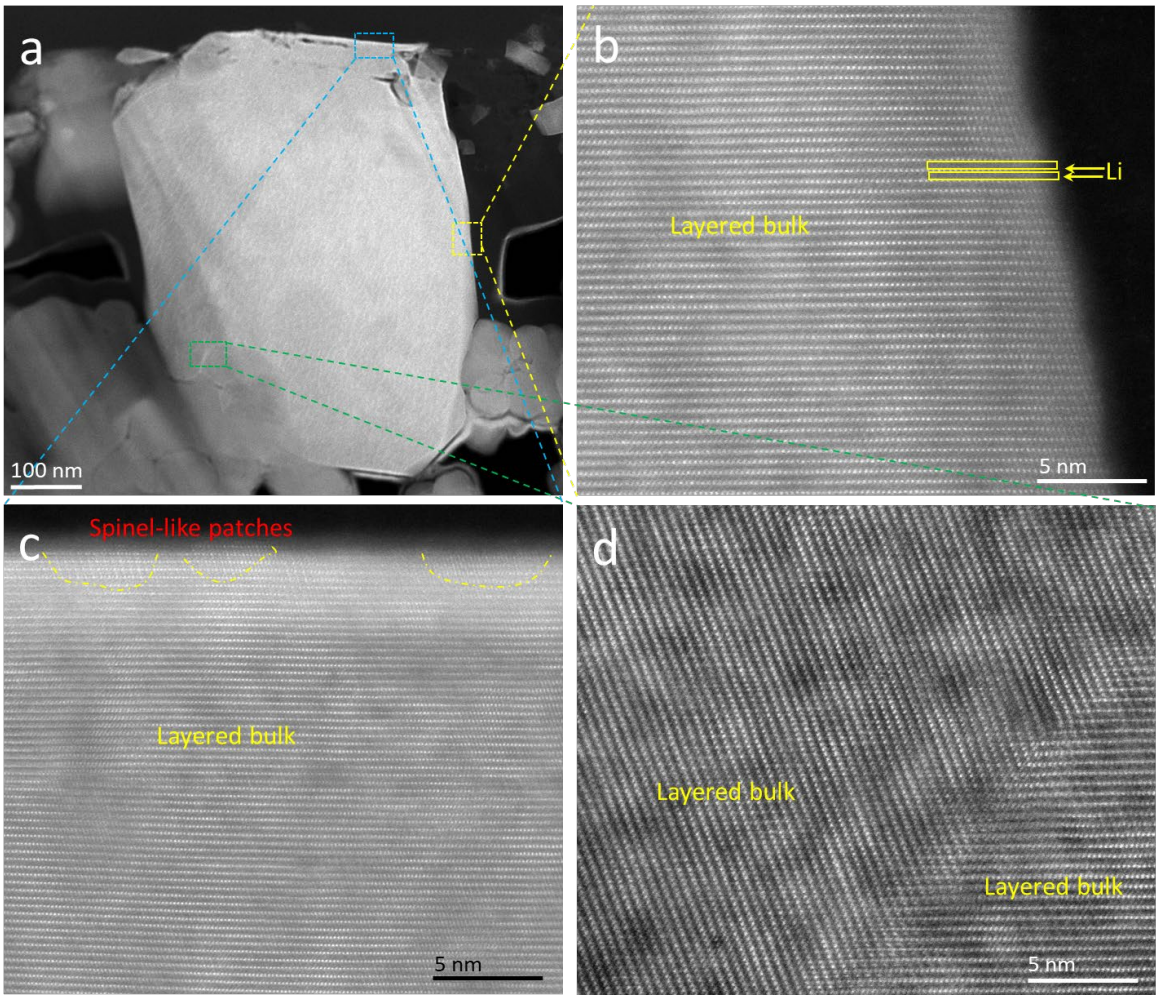

Figure 3.12 HAADF-STEM images of PDA-coated LRLO after 100 cycles. (a) Low-magnification image of multiple LRLO primary particles with no significant surface damage as the bare particles. (b) Atomic-resolution image of the region highlighted in the yellow dashed box in (a). (c) Atomic-resolution image of the region highlighted in the blue dashed box in (a), showing the pockets of spinel like structure at the surface, and (d) atomic-resolution image of the region highlighted in green dashed box in (a) revealing the region just below the particle surface with no indication of rock-salt domains.

In contrast, the PDA coated LRLO particles show substantially altered (and improved) surface chemistry after 100 cycles (**Figure 3.12a-d**). Unlike bare-LRLO (**Figure 3.11b**), the surface of the particles (**Figure 3.12a, b**) is much more even. Surface spinel is no longer observed as a uniform layer in the PDA-coated LLRO after cycling (**Figure 3.12b**) and is contained in very small patches along the

surface; some facets are even terminated with no spinel at the surface (**Figure 3.12c**). Although the contrast in the low magnification image (**Figure 3.12a**) highlighted in the green dashed box suggests that there might be some rock-salt like transformation, atomic resolution HAADF-STEM image in **Figure 3.12d** does not reveal any obvious rock-salt domains; shown, for example, is a twin boundary formed by two grains of LRLO with a layered structure.

These studies imply that suppressing ROS evolution from the surface by the PDA coating enhances the stability by mitigating the cation migration from the TMO_6 layer into the Li layer in LRLO at the surface, thus inhibiting spinel and irreversible rock-salt phase evolution. While the latter may help to trap redox-active molecular oxygen in the bulk by forming a surface densified layer, they also greatly increase impedance. The effect on capacity retention on long term cycling is discussed next.

3.3.5 Electrochemical performance of PDA coated Li-rich NCM

For long-term cycling performance, electrodes comprised of bare and PDA coated LRLO materials were examined in the voltage window between 2.0 to 4.7 V over 200 cycles, after the initial activation step up to 4.8 V (as described in the above section). Half-cells were initially run at a rate of C/10 (25 $mAh \cdot g^{-1}$) for a few cycles, with an excursion to a 3C rate on discharge (and C/2 on charge with a constant potential hold for 12 min) for a few cycles. The cells were then discharged at a C rate for 33 cycles (and charged at C/2 with a constant potential hold for 12 min) before the entire loop protocol was repeated. While we examined materials with various thicknesses of the PDA coating layer, PD3 (0.3 wt% PDA) was chosen as the exemplar owing to its slightly lower surface resistance compared to PD5 (**Figure 3.1b-e**).

Figure 3.13a shows the cycling performance at different current rates from C/10 to 3C for bare-LRLO and PD3-LRLO electrodes including the first activation cycle at C/15. Overall, the PDA coated LRLO materials showed much better behavior than bare LRLO over long term cycling. At a rate

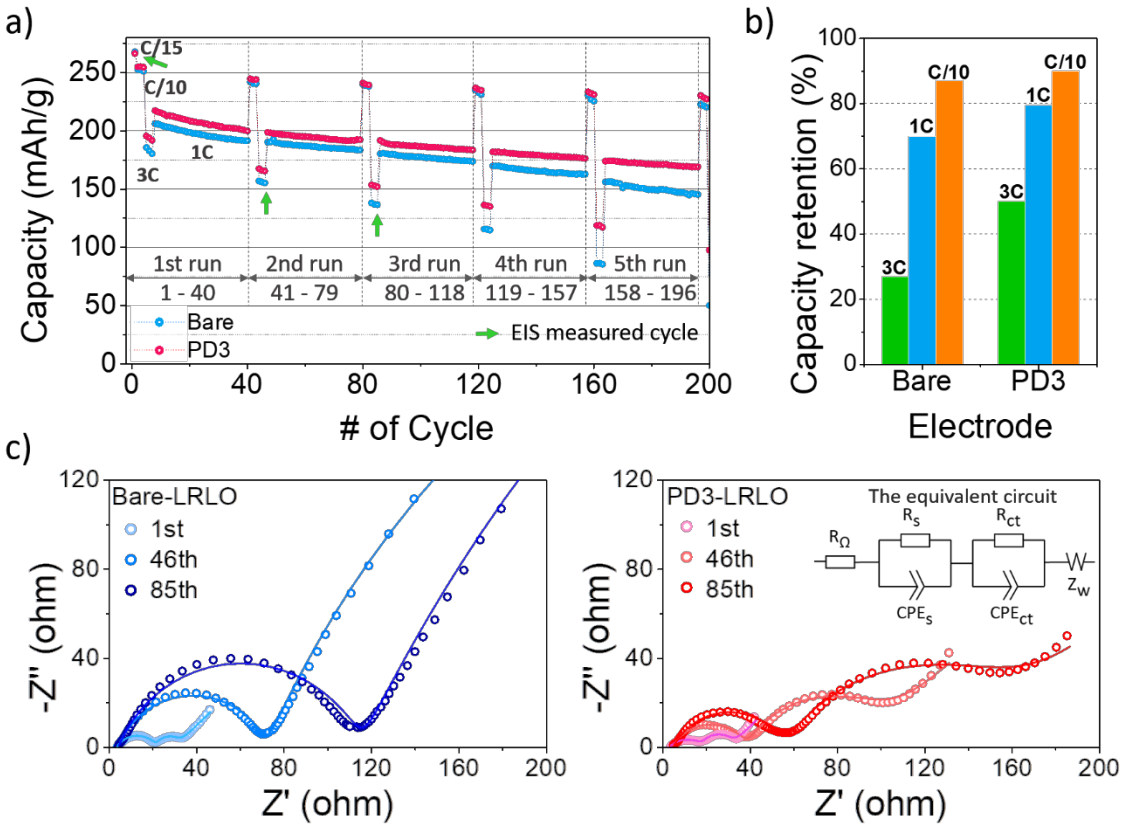

Figure 3.13 Electrochemical performance of bare and PDA coated LRLO. (a) Cycling performance of bare-LRLO and PD3-LRLO in the voltage range from 2.0 to 4.7 V vs. Li^+/Li (1C = 250 mAh·g^{-1}) at different rates from C/10, 1C and 3C (constant charge rate of C/2 for 1C and 3C) after the first activation step (C/15, 2.0 to 4.8 V). Green arrows indicate the cycles where EIS was measured. (b) Capacity retention of bare-LROLO and PD3-LRLO at different current rates (from C/10 to 3C) over 200 cycles. (c) EIS results of bare-LRLO and PD3-LRLO measured at 4.0 V during discharge from the first activation cycle and following 46th and 85th 3C cycles. The cells were held at 4.0 V for 2 h followed by 10 h of rest and AC impedance spectra were recorded at the open circuit voltage. The solid lines represent the fits using an equivalent circuit shown in the EIS plot on the right (inset); the data is summarized in **Table 3.2**.

of 1C, the discharge capacity of PD3-LRLO (initially 211 mAh·g^{-1}) drops to 173 mAh·g^{-1} after 200 cycles, corresponding to a capacity retention of ~ 82%. By contrast, the capacity of bare-LRLO dropped from 206 mAh·g^{-1} to 145 mAh·g^{-1} over the same period, corresponding to only ~ 70% capacity retention. Capacity retention of the bare and PDA-coated materials are summarized in **Figure 3.13b**

Table 3.2 Surface resistance (R_s, Ω), charge transfer resistance (R_{ct}, Ω) and Warburg impedance (Z_w) of bare-LRLO and PD3-LRLO cathodes corresponding to the EIS result in **Figure 3.13c**. Data were collected in three electrode cells to differentiate cathode from anode impedance.

Electrode	Cycle	1st	46th	85th
Bare-LRLO	R_s	8.7	68.1	111.1
	R_{ct}	18.3	825.7	1263
	Z_w	3	15	21
PD3-LRLO	R_s	12.0	34.16	50.8
	R_{ct}	15.9	58.76	100
	Z_w	2	4	4

that illustrates the positive effect of the coating, especially at a fast rate of 3C. This effect is partly rooted in kinetics owing to the surface impedance build-up which is much more significant for the bare *vs* the PDA-coated material as shown by electrochemical impedance spectroscopy (EIS). The EIS data in **Figure 3.13c** measured at 4.0V during the discharge of the first and every third 3C cycle from the second and third running set in three electrode cells. EIS measurements conducted on the cathode over the cell cycling show the PD3-LRLO electrode exhibits greatly suppressed growth of surface resistance (R_s) and charge transfer resistance (R_{ct}) compared to bare-LRLO (**Table 3.2**). This drop in resistance explains the higher discharge capacity performance of PDA-LRLO, especially at fast rates (3C). It reflects the lack of the layer to rock-salt type phase transformation in PD3-LRLO at the surface (as suggested by the STEM studies), and/or the lesser build-up of a CEI impedance layer which correlates with the XPS study (**Figure 3.8** and **3.9**). Both factors are known to cause inferior electrochemical performance.[7, 22] Another factor may relate to stabilization of loss of oxygen from the bulk due to the PDA coating. While P. G. Bruce et al. reported that molecular O_2 trapped within small TM vacancy clusters in the bulk LRLO lattice is responsible for a significant portion of the reversible redox ($O_2 \leftrightarrows O^{2-}$) on the first cycles,[5] it is unlikely that such entrapment would be stable over many tens of cycles. Rather, some fraction of the molecular O_2 would be expected to ultimately diffuse to the surface, triggered by reconstruction of the TM vacancy clusters on continuous redox. Microcracking of the bare

LRLO surface - which is is well established to occur upon cycling[35] - would allow its escape that would be suppressed by a conformal and flexible PDA polymer layer. Thus, not only would reversible oxygen capacity be better preserved, but reaction of the O_2 with the electrolyte at high potential would be mitigated, thus decreasing the accumulation of surface impedance as observed.

3.4 Conclusions

We have demonstrated the stabilising effect of a polydopamine (PDA) coating on a Li-rich Mn-rich NCM (LRLO) cathode material during lithium cell cycling, which we ascribe to its ability to scavenge reactive oxygen species (ROS). To the best of our knowledge, gas phase atomic layer deposition coating techniques can often be limited in their ability to coat internal primary particles within secondary agglomerates because of the difficulty in delivering the coating precursors deep within the agglomerate. The impregnation technique of self-polymerizing PDA easily enables coverage. Characterization using XPS, HRTEM, and ToF-SIMS analysis confirmed that the thickness of the PDA coating layer can be well controlled, and furthermore that the PDA infiltrates into the interior of the porous LRLO particle to cover the entire surface area of the primary particles. The role of ROS scavenging by PDA was determined by a combination of surface science and electrochemical studies. XPS measurements conducted during the first cycle confirmed there is significantly less CEI formation in PDA-coated LRLO compared to the bare LRLO material. OEMS study also shows greatly reduced O_2 and CO_2 gas evolution for the PDA coated LRLO, demonstrating the suppression of lattice oxygen release. Comparing the cycling performance and the impedance evolution of bare and PDA coated LRLO, we demonstrated the improved capacity retention and rate capability of PDA coated LRLO are attributed to the suppressed rock-salt type phase transformation in the layered structure and reversible oxygen redox activity with decreased irreversible oxygen loss. These findings are supported by HRTEM study which reveals less evolution of spinel and rock-salt type phases at the surface. Therefore,

the structural stability of LRLO is improved via conformal PDA coating by the ability of this polymer to mostly retain surface oxygen from reactive oxygen release in the layered structure, leading to enhanced capacity retention and rate capability.

References

[1] a) M. Li, J. Lu, Z. W. Chen, K. Amine, *Adv Mater*. **2018**, *30*, 1800561; b) M. S. Whittingham, *Chem Rev*. **2004**, *104*, 4271-4301.

[2] a) M. M. Thackeray, C. S. Johnson, J. T. Vaughey, N. Li, S. A. Hackney, *J Mater Chem*. **2005**, *15*, 2257-2267; b) Y. K. Sun, D. H. Kim, H. G. Jung, S. T. Myung, K. Amine, *Electrochim Acta*. **2010**, *55*, 8621-8627; c) H. J. Noh, S. Youn, C. S. Yoon, Y. K. Sun, *J Power Sources*. **2013**, *233*, 121-130.

[3] a) H. Koga, L. Croguennec, M. Menetrier, P. Mannessiez, F. Weill, C. Delmas, *J Power Sources*. **2013**, *236*, 250-258; b) K. Luo, M. R. Roberts, R. Hao, N. Guerrini, D. M. Pickup, Y. S. Liu, K. Edstrom, J. H. Guo, A. V. Chadwick, L. C. Duda, P. G. Bruce, *Nat Chem*. **2016**, *8*, 684-691; c) M. Saubanere, E. McCalla, J. M. Tarascon, M. L. Doublet, *Energ Environ Sci*. **2016**, *9*, 984-991; d) M. Sathiya, G. Rousse, K. Ramesha, C. P. Laisa, H. Vezin, M. T. Sougrati, M. L. Doublet, D. Foix, D. Gonbeau, W. Walker, A. S. Prakash, M. Ben Hassine, L. Dupont, J. M. Tarascon, *Nat Mater*. **2013**, *12*, 827-835; e) R. A. House, U. Maitra, M. A. Perez-Osorio, J. G. Lozano, L. Jin, J. W. Somerville, L. C. Duda, A. Nag, A. Walters, K. J. Zhou, M. R. Roberts, P. G. Bruce, *Nature*. **2020**, *577*, 502-508; f) R. A. House, U. Maitra, L. Y. Jin, J. G. Lozano, J. W. Somerville, N. H. Rees, A. J. Naylor, L. C. Duda, F. Massel, A. V. Chadwick, S. Ramos, D. M. Pickup, D. E. McNally, X. Y. Lu, T. Schmitt, M. R. Roberts, P. G. Bruce, *Chem Mater*. **2019**, *31*, 3293-3300; g) B. Strehle, K. Kleiner, R. Jung, F. Chesneau, M. Mendez, H. A. Gasteiger, M. Piana, *J Electrochem Soc*. **2017**, *164*, A400-A406; h) J. Wandt, A. T. S. Freiberg, A. Ogrodnik, H. A. Gasteiger, *Mater Today*. **2018**, *21*, 825-833.

[4] a) H. J. Yu, Y. G. So, Y. Ren, T. H. Wu, G. C. Guo, R. J. Xiao, J. Lu, H. Li, Y. B. Yang, H. S. Zhou, R. Z. Wang, K. Amine, Y. Ikuhara, *J Am Chem Soc*. **2018**, *140*, 15279-15289; b) E. Castel, E. J. Berg, M. El Kazzi, P. Novak, C. Villevieille, *Chem Mater*. **2014**, *26*, 5051-5057.

[5] R. A. House, G. J. Rees, M. A. Perez-Osorio, J. J. Marie, E. Boivin, A. W. Robertson, A. Nag, M. Garcia-Fernandez, K. J. Zhou, P. G. Bruce, *Nat Energy*. **2020**, *5*, 777-785.

[6] a) D. Mohanty, J. L. Li, D. P. Abraham, A. Huq, E. A. Payzant, D. L. Wood, C. Daniel, *Chem Mater*. **2014**, *26*, 6272-6280; b) H. J. Yu, H. S. Zhou, *J Phys Chem Lett*. **2013**, *4*, 1268-1280; c) P. Rozier, J. M. Tarascon, *J Electrochem Soc*. **2015**, *162*, A2490-A2499.

[7] S. Hy, F. Felix, J. Rick, W. N. Su, B. J. Hwang, *J Am Chem Soc*. **2014**, *136*, 999-1007.

[8] J. Hong, H. D. Lim, M. Lee, S. W. Kim, H. Kim, S. T. Oh, G. C. Chung, K. Kang, *Chem Mater*. **2012**, *24*, 2692-2697.

[9] a) S. H. Guo, H. J. Yu, P. Liu, X. Z. Liu, D. Li, M. W. Chen, M. Ishida, H. S. Zhou, *J Mater Chem A*. **2014**, *2*, 4422-4428; b) A. Manthiram, J. C. Knight, S. T. Myung, S. M. Oh, Y. K. Sun, *Adv Energy Mater*. **2016**, *6*, 1501010.

[10] a) E. Y. Zhao, X. F. Liu, H. Zhao, X. L. Xiao, Z. B. Hu, *Chem Commun*. **2015**, *51*, 9093-9096; b) B. Qiu, J. Wang, Y. G. Xia, Z. Wei, S. J. Han, Z. P. Liu, *Acs Appl Mater Inter*. **2014**, *6*, 9185-9193; c) B. Qiu, M. H. Zhang, L. J. Wu, J. Wang, Y. G. Xia, D. N. Qian, H. D. Liu, S. Hy, Y. Chen, K. An, Y. M. Zhu, Z. P. Liu, Y. S. Meng, *Nat Commun*. **2016**, *7*, 12108; d) Z. Zhu, D. W. Yu, Y. Yang, C. Su, Y. M. Huang, Y. H. Dong, I. Waluyo, B. M. Wang, A. Hunt, X. H. Yao, J. Lee, W. J. Xue, J. Li, *Nat Energy*. **2019**, *4*, 1049-1058.

[11] a) F. Wu, N. Li, Y. F. Su, L. J. Zhan, L. Y. Bao, J. Wang, L. Chen, Y. Zheng, L. Q. Dai, J. Y. Peng, S. Chen, *Nano Lett*. **2014**, *14*, 3550-3555; b) J. M. Zheng, M. Gu, J. Xiao, B. J. Polzin, P. Yan, X. L. Chen, C. M. Wang, J. G. Zhang, *Chem Mater*. **2014**, *26*, 6320-6327; c) Q. Y. Wang, J. Liu, A. V. Murugan, A. Manthiram, *J Mater Chem*. **2009**, *19*, 4965-4972.

[12] a) J. Zhang, Q. W. Lu, J. H. Fang, J. L. Wang, J. Yang, Y. N. NuLi, *Acs Appl Mater Inter*. **2014**, *6*, 17965-17973; b) F. Wu, J. R. Liu, L. Li, X. X. Zhang, R. Luo, Y. S. Ye, R. J. Chen, *Acs Appl Mater Inter*. **2016**, *8*, 23095-23104; c) G. L. Xu, Q. Liu, K. K. S. Lau, Y. Liu, X. Liu, H. Gao, X. W. Zhou, M. H. Zhuang, Y. Ren, J. D. Li, M. H. Shao, M. G. Ouyang, F. Pan, Z. H. Chen, K. Amine, G. H. Chen, *Nat Energy*. **2019**, *4*, 484-494.

[13] Z. H. Chen, Y. Qin, K. Amine, Y. K. Sun, *J Mater Chem*. **2010**, *20*, 7606-7612.

[14] a) M. Rozanowska, T. Sarna, E. J. Land, T. G. Truscott, *Free Radical Bio Med*. **1999**, *26*, 518-525; b) P. A. Riley, *Int J Biochem Cell B*. **1997**, *29*, 1235-1239; c) T. Sarna, B. Pilas, E. J. Land, T. G. Truscott, *Biochim Biophys Acta*. **1986**, *883*, 162-167.

[15] a) M. Tada, M. Kohno, Y. Niwano, *J Clin Biochem Nutr*. **2010**, *46*, 224-228; b) P. Meredith, T. Sarna, *Pigm Cell Res*. **2006**, *19*, 572-594; c) B. L. L. Seagle, K. A. Rezai, E. M. Gasyna, Y. Kobori, K. A. Rezaei, J. R. Norris, *J Am Chem Soc*. **2005**, *127*, 11220-11221; d) L. Panzella, G. Gentile, G. D'Errico, N. F. Della Vecchia, M. E. Errico, A. Napolitano, C. Carfagna, M. d'Ischia, *Angew Chem Int Edit*. **2013**, *52*, 12684-12687; e) A. Kladna, P. Berczynski, I. Kruk, T. Michalska, H. Y. Aboul-Enein, *Luminescence*. **2013**, *28*, 450-455.

[16] a) H. Lee, S. M. Dellatore, W. M. Miller, P. B. Messersmith, *Science*. **2007**, *318*, 426-430; b) M. Jaber, J. F. Lambert, *J Phys Chem Lett*. **2010**, *1*, 85-88.

[17] a) G. C. Yen, C. L. Hsieh, *Biosci Biotech Bioch*. **1997**, *61*, 1646-1649; b) B. Newland, P. Wolff, D. Z. Zhou, W. Wang, H. Zhang, A. Rosser, W. X. Wang, C. Werner, *Biomater Sci-Uk*. **2016**, *4*, 400-404.

[18] M. Boulton, M. Rozanowska, B. Rozanowski, *J Photoch Photobio B*. **2001**, *64*, 144-161.

[19] E. E. Sam, N. Verbeke, *J Neural Transm-Park*. **1995**, *10*, 115-127.

[20] a) B. G. Kim, S. Kim, H. Lee, J. W. Choi, *Chem Mater*. **2014**, *26*, 4757-4764; b) T. Sun, Z. J. Li, H. G. Wang, D. Bao, F. L. Meng, X. B. Zhang, *Angew Chem Int Edit*. **2016**, *55*, 10662-10666.

[21] a) Y. F. Deng, H. Xu, Z. W. Bai, B. L. Huang, J. Y. Su, G. H. Chen, *J Power Sources*. **2015**, *300*, 386-394; b) J. R. Feng, H. L. Fan, D. A. Zha, L. Wang, Z. X. Jin, *Langmuir*. **2016**, *32*, 10377-10386.

[22] M. Gu, I. Belharouak, J. M. Zheng, H. M. Wu, J. Xiao, A. Genc, K. Amine, S. Thevuthasan, D. R. Baer, J. G. Zhang, N. D. Browning, J. Liu, C. M. Wang, *Acs Nano*. **2013**, *7*, 760-767.

[23] S. E. Renfrew, B. D. McCloskey, *J Am Chem Soc*. **2017**, *139*, 17853-17860.

[24] a) N. Mahne, B. Schafzahl, C. Leypold, M. Leypold, S. Grumm, A. Leitgeb, G. A. Strohmeier, M. Wilkening, O. Fontaine, D. Kramer, C. Slugovc, S. M. Borisov, S. A. Freunberger, *Nat Energy*. **2017**, *2*, 17036; b) N. Mahne, S. E. Renfrew, B. D. McCloskey, S. A. Freunberger, *Angew Chem Int Edit*. **2018**, *57*, 5529-5533.

[25] M. N. Ates, Q. Y. Jia, A. Shah, A. Busnaina, S. Mukerjee, K. M. Abraham, *J Electrochem Soc*. **2014**, *161*, A290-A301.

[26] G. Assat, D. Foix, C. Delacourt, A. Iadecola, R. Dedryvere, J. M. Tarascon, *Nat Commun*. **2017**, *8*, 2219.

[27] a) W. E. Gent, K. Lim, Y. F. Liang, Q. H. Li, T. Barnes, S. J. Ahn, K. H. Stone, M. McIntire, J. Y. Hong, J. H. Song, Y. Y. Li, A. Mehta, S. Ermon, T. Tyliszczak, D. Kilcoyne, D. Vine, J. H. Park, S. K. Doo, M. F. Toney, W. L. Yang, D. Prendergast, W. C. Chueh, *Nat Commun*. **2017**, *8*, 2091; b) J. M. Zheng, P. H. Xu, M. Gu, J. Xiao, N. D. Browning, P. F. Yan, C. M. Wang, J. G. Zhang, *Chem Mater*. **2015**, *27*, 1381-1390.

[28] a) S. Hong, Y. S. Na, S. Choi, I. T. Song, W. Y. Kim, H. Lee, *Adv Funct Mater*. **2012**, *22*, 4711-4717; b) M. d'Ischia, A. Napolitano, V. Ball, C. T. Chen, M. J. Buehler, *Accounts Chem Res*. **2014**, *47*, 3541-3550; c) V. Capozzi, G. Perna, A. Gallone, P. F. Biagi, P. Carmone, A. Fratello, G. Guida, P. Zanna, R. Cicero, *J Mol Struct*. **2005**, *744*, 717-721; d) G. Perna, M. Lasalvia, V. Capozzi, *Polym Int*. **2016**, *65*, 1323-1330; e) J. Liebscher, R. Mrowczynski, H. A. Scheidt, C. Filip, N. D. Hadade, R. Turcu, A. Bende, S. Beck, *Langmuir*. **2013**, *29*, 10539-10548; f) S. H. Ku, J. S. Lee, C. B. Park, *Langmuir*. **2010**, *26*, 15104-15108.

[29] J. Hong, H.-D. Lim, M. Lee, S.-W. Kim, H. Kim, S.-T. Oh, G.-C. Chung, K. Kang, *Chem Mater*. **2012**, *24*, 2692-2697.

[30] G. Assat, A. Iadecola, C. Delacourt, R. Dedryvere, J. M. Tarascon, *Chem Mater*. **2017**, *29*, 9714-9724.

[31] a) Q. Li, G. S. Li, C. C. Fu, D. Luo, J. M. Fan, J. Zheng, D. J. Xie, L. P. Li, *Electrochim Acta*. **2015**, *154*, 249-258; b) X. B. Li, M. Q. Xu, Y. J. Chen, B. L. Lucht, *J Power Sources*. **2014**, *248*, 1077-1084.

[32] A. J. Naylor, E. Makkos, J. Maibach, N. Guerrini, A. Sobkowiak, E. Bjorklund, J. G. Lozano, A. S. Menon, R. Younesi, M. R. Roberts, K. Edstrom, M. S. Islam, P. G. Bruce, *J Mater Chem A*. **2019**, *7*, 25355-25368.

[33] Y. Zou, X. F. Chen, P. Yang, G. J. Liang, Y. Yang, Z. P. Gu, Y. W. Li, *Sci Adv*. **2020**, *6,* eabb469.

[34] L. X. Qin, X. Q. Li, S. Z. Kang, J. Mu, *Colloid Surface B*. **2015**, *126*, 210-216.

[35] E. H. R. Tsai, J. Billaud, D. F. Sanchez, J. Ihli, M. Odstrcil, M. Holler, D. Grolimund, C. Villevieille, M. Guizar-Sicairos, *Iscience*. **2019**, *11*, 356-365.

[36] A. Le Bail, *Powder Diffr*. **2005**, *20*, 316-326.

[37] D. Kundu, R. Black, B. Adams, K. Harrison, K. Zavadil, L. F. Nazar, *J Phys Chem Lett*. **2015**, *6*, 2252-2258.

[38] Y. C. Lu, A. N. Mansour, N. Yabuuchi, Y. Shao-Horn, *Chem Mater*. **2009**, *21*, 4408-4424.

Chapter 4

The role of metal substitution in tuning anion redox in P2-type sodium metal layered oxides

4.1 Introduction

Li-ion batteries (LIBs) are promising devices for both the transportation and utility sectors as they provide high energy density capability to store intermittent renewable sources of energy. However, the high abundance of sodium (100 times that of Li)[1] and compatibility of a sodium anode with an aluminum current collector - which is lower cost than copper collectors used in LIBs - makes Na ion batteries (NIBs) viable options for large-scale applications.

Recently, low-cost and non-toxic NIBs made from Mn and Fe have drawn considerable attention in the battery community.[2] N. Yabuuchi et al. demonstrated the effectiveness of layered oxide P2-$Na_{2/3}[Fe_{0.5}Mn_{0.5}]O_2$ as a positive electrode material. It delivered a reversible capacity of 190 mAh/g at room temperature with charge compensation that was presumed to be through $Fe^{3+/4+}$ redox.[2a] The considerably improved electrochemical reversibility compared with that in Li-ion positive electrodes such as $LiFeO_2$ demonstrated the potential of sodium-based electrodes to deliver high capacity using earth-abundant materials such as Fe and Mn. However, the practical use of these materials is inhibited by their reactivity with moisture and CO_2 in air[2e] as well as their structural instability[2b, 3] upon deep desodiation. In the pristine materials, the transition metals (TMs), Fe and Mn, reside in octahedral sites in the TMO_2 layer. However, X-ray and neutron diffraction studies have shown that the TMs shuffle into tetrahedral sites in the Na layers upon desodiation, leading to structural degradation, capacity fade, and decreased rate capability.[2b, 2c] Although partial substitution of Fe with

Mn, Ni, Co, Cu, or Ti has been shown to mitigate these issues,[2b, 2c, 4] a full understanding of the effect of TM substitution on structural stability-redox coupling has remained elusive.

Similar to Li layered TM oxides, improving capacity by accessing both cation and anion redox has been demonstrated in several Na-ion layered TM oxides. The often-discussed requirement for anion redox is the presence of A-O-A' (where A stands for an alkali metal and A' stands for species with no covalent bonding interaction with the oxygen; for example, Li-O-Li, Na-O-Mg/Zn or Na-O-Vacancy) local configurations in positive electrode materials.[4e, 8c, 8e, 8g, 9] The configuration has been linked to the formation of nonbonding oxygen 2p states below the Fermi-level which will participate in charge compensation upon charging. This proposal has been adopted to explain the anion redox activity in sodium electrode materials such as $Na_{0.6}Li_{0.2}Mn_{0.8}O_2$, Na_2RuO_3, $Na_2Mn_3O_7$, $Na_{0.67}Mg_{0.28}Mn_{0.72}O_2$, $Na_{0.67}Zn_{0.28}Mn_{0.72}O_2$ and $Na_{0.78}Ni_{0.23}Mn_{0.69}O_2$.[5] However, anion redox has also been linked with structural disorder[6] that results in voltage hysteresis and fade of both voltage and capacity, impeding its practicality in devices.[6-7] Recently, R. A. House et al. showed that superstructure control in sodium positive electrodes could mitigate the structural disorder linked with anion redox.[8] Another report by J. H. Song et al. examined the oxygen density of states (DOS) of ordered Li_2TMO_3 (TM = 3d TMs) compounds and proposed that TMs surrounding a Li-O-Li local configuration have a nontrivial π-type interaction with oxygen which modulates the energy level of O 2p and TM "t_{2g}" states. Based on the DOS results, they further demonstrated that the oxygen redox activity could be estimated by the types and numbers of TMs surrounding Li-O-Li in Li_2TMO_3 systems.[9] Although partial metal substitution has been generally used to diminish structural disorder on cycling,[2b, 2c, 4] a design rule that involves a specific metal or synthesis method is further needed to be developed to disrupt the link of structure-redox coupling in anion redox of positive electrode materials.

Previously, our group examined the effect of substituting Fe by Cu and Ni in P2-$Na_{0.67-x}[Mn_{0.5}Fe_{0.5}]O_2$ (NMF) on electrochemical performance,[2b, 2c] showing that Ni was particularly effective

in controlling capacity fade. In P2-$Na_{0.67-x}[Mn_{0.66}Fe_{0.20}Cu_{0.14}]O_2$ (NMFC) and P2-$Na_{0.67-x}[Mn_{0.65}Fe_{0.20}Ni_{0.15}]O_2$ (NMFN), charge compensation on charge would be typically achieved by transition metal redox. However, those studies hinted that oxygen redox also occurs in NMF and NMFC, accompanied by the TMs migrating from octahedral sites (pristine state) to tetrahedral sites (desodiated state).[2b, 2c] Such "site swapping" (i.e., TM migration) is only partly reversible.

As part of a "deep dive" into understanding redox mechanisms in positive electrodes on electrochemical cycling, this chapter proves the existence of anion-redox activity in NMF, and its modification by Cu/Ni substitution. By combining analysis of local structure with spectroscopic probes - specifically, resonant inelastic X-ray scattering (RIXS) and X-ray near edge structure (XANES) – I demonstrate how TM substitution tunes the structure-redox relationship. This chapter unveil the structure–redox link in NIBs, further corroborating this relationship that has been previously observed in LIBs in electrode materials such as $Li_{1.17-x}Ni_{0.21}Co_{0.08}Mn_{0.54}O_2$[6] and $Li_xIr_ySn_{1-y}O_2$.[10] It is found that substitution is a vital strategy to lower structural disorder in the presence of anion redox, by reducing Jahn-Teller distortion due to Fe^{4+} and modulating the TM-O covalency. In addition, by performing density-functional theory (DFT) calculations, this chapter further explore why NMF and NMFC exhibit considerable anion redox even though they do not satisfy the widely accepted requirement local configuration of A-O-A' (Li-O-Li, Na-O-Mg/Zn or Na-O-Vacancy) in the pristine materials.[5e, 11]

4.2 Experimental Details

4.2.1 Materials Synthesis

NMF, NMFC, and NMFN powders were synthesized using solid-state methods, as described in our previous publications on these materials.[2b, 2c] A mixture of stoichiometric amounts of Na_2CO_3 (EMD Millipore, ≥ 99.5%), Mn_2O_3 (Sigma- Aldrich, 99%), Fe_2O_3 (Sigma-Aldrich, ≥ 99%), and CuO (J. T. Baker, 99.5%) or NiO (Sigma-Aldrich, 99.8%) precursors were ball-milled at 250 rpm for 1 h.

The collected powder was pelletized and heated at 700 °C for 4 h, followed by heating at 900 °C for 6 h in air. Because the pellets are sensitive under ambient atmosphere, they were transferred to an Ar-filled glovebox in a sealed tube. Before being transferred, they were first cooled to 600 °C under Ar flow for 4 h and finally cooled to room temperature. To chemically oxidize NMF, NMFC, or NMFN, the powder was mixed with an over-stoichiometric amount of NO_2BF_4 (98%, Sigma-Aldrich) in acetonitrile (HPLC grade, Sigma Aldrich) and stirred for two days in an Ar-filled glovebox. The chemically oxidized powder was then washed with excess acetonitrile and dried at room temperature under vacuum.

4.2.2 Electrochemistry

The electrochemistry of the positive electrode materials was measured in 2325 coin cells against a Na metal counter electrode. Electrode fabrication was performed inside an Ar-filled glovebox (O_2 and H_2O < 1 ppm) to avoid air contamination. Each active material was mixed with 10 wt% carbon black and 10 wt% polyvinylidene fluoride (PVDF) (Sigma-Aldrich, average Mw: ~ 534 000) suspended in N-methyl-2-pyrrolidinone, NMP) (Sigma-Aldrich, 99.5%) and cast on aluminum foil with a typical loading of 7-9 $mg \cdot cm^{-2}$. The electrodes were dried in a vacuum oven at 90 °C overnight. The electrolyte was $NaClO_4$ (Alfa Aesar, ~98%) in propylene carbonate (BASF, 99.98%) with 2 vol% of 4-fluoro-1,3-dioxolan-2-one (FEC) (Sigma-Aldrich, 99%). The electrodes were separated by glass fiber separators (Merck Millipore), which were dried at 200 °C for 12 h under a dynamic vacuum before use. Galvanostatic cycling was performed using a MPG-2 (Bio-Logic) cycler at room temperature with a current density of C/20.

4.2.3 Structural Characterization

Reciprocal space data for PDF analysis were obtained using a PANalytical Empyrean equipped with Ag-K_α radiation, a Rh K_β filter, and a NaI scintillation point detector. The powder sample was loaded in a 1-mm glass capillary in an Ar-filled glovebox, and each PDF data set was collected for 48 h. The data reduction was performed using PDFGetX3 software, and real space data were fitted using PDFgui.[12] The damping factor associated with this instrumental configuration was calibrated by refining the structure of a silicon sample as a reference.

4.3 Result and Discussion

4.3.1 Link between voltage hysteresis and antisite–vacancy defect (AVDF) formation

To provide background, the electrochemical properties and X-ray pair distribution function (PDF) analysis of the NMF, NMFC and NMFN electrodes are compared in **Figure 4.1**. P2-type layered $Na_{0.67}TMO_2$ encounters a change in stacking order during desodiation. A phase transition from the P2 to a very poorly crystalline O2-like phase (hereafter, called the Z-phase) occurs on deep charge as it is shown in **Figure 4.2**.[2b, 2c] The changes in the first cycle are summarized and depicted by different colors in **Figure 4.1(a)**. Here, to rigorously assess voltage hysteresis between sodiation and desodiation, we performed cycling at different rates (1C, 0.5C, 0.1C and 0.05C; **Figure 4.3**). While hysteresis is more dominant at the faster C-rates as expected, it is still quite significant for NMF at and below 0.1 C (i.e. 0.05 C). This indicates a kinetic limitation due to TM shuffling into the tetrahedral sites (as previously described for lithium metal oxides)[12] and formation of so-called antisite-vacancy defects (AVDF)[6] discussed below. Above 3.1 V, the hysteresis gap amongst the three electrodes diverge, as shown in **Figure 4.1(b)**. To directly compare the voltage hysteresis, the voltage difference at a given state-of-charge was quantified (**Figure 4.1(c)**). The largest hysteresis occurs during the P2 to Z phase

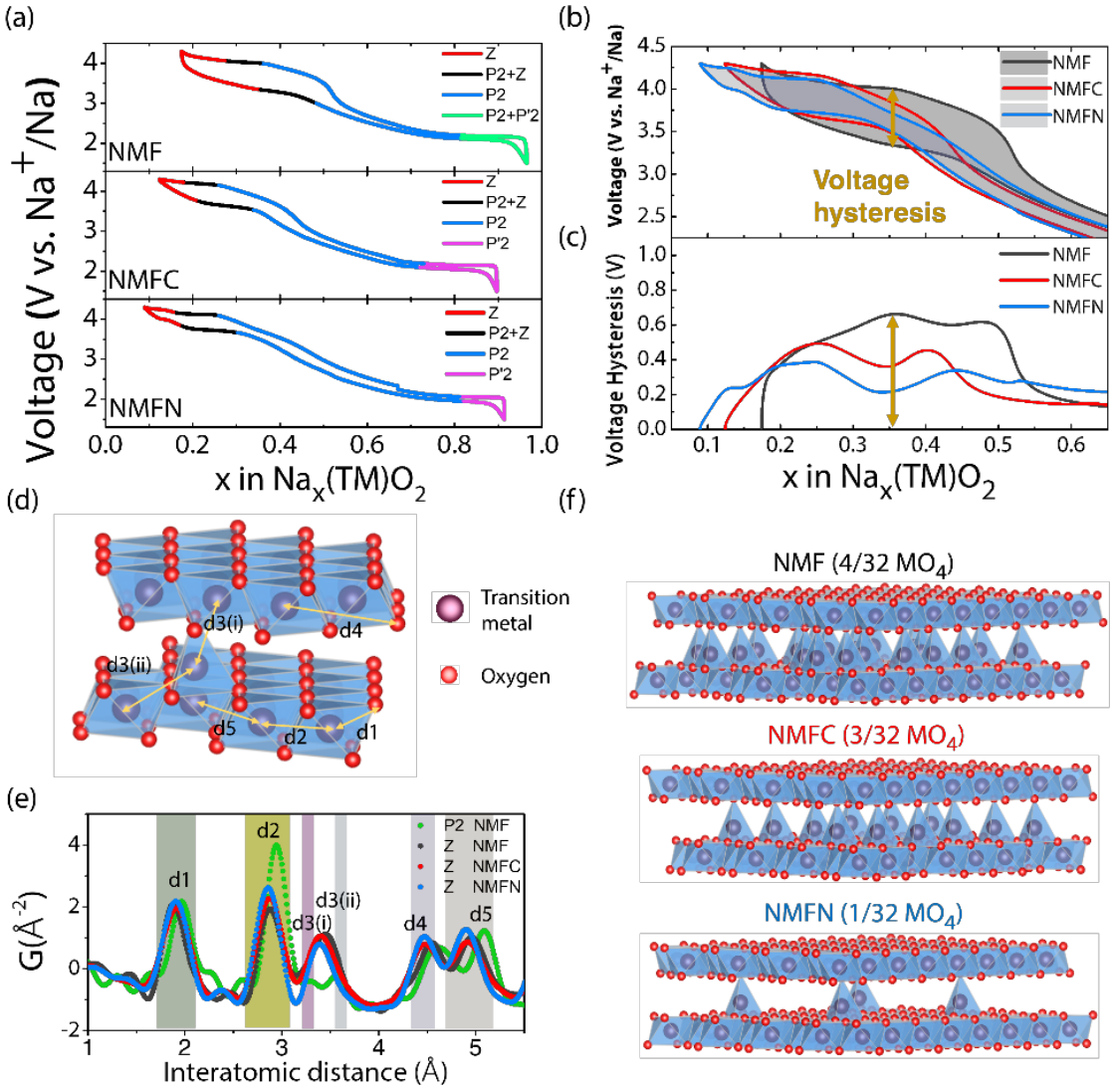

Figure 4.1 Effect of TM substitution on electrochemistry. (a) First cycle electrochemistry for NMF, NMFC, and NMFN cycled at 0.1 C. (b) and (c) Comparison of the first cycle and voltage hysteresis upon desodiation, respectively, of the three electrodes cycled at 0.1 C. The substitution of Fe with Cu or Ni in $Na_{0.67}Mn_{0.5}Fe_{0.5}O_2$ reduces the hysteresis gap and pushes the start of the plateau at high voltage to higher voltage. (d) Scheme of the bilayer model used to fit the pair distribution function (PDF) curve of NMF, NMFC, and NMFN. The purple and red spheres represent the transition metals and oxygen atoms, respectively. The yellow arrows indicate the atomic distance, as labeled. (e) Comparison of the experimental X-ray PDF data of pristine P2-NMF with Z-phase NMF, NMFC, and NMFN. (f) Schematic models of Z-phase NMF, NMFC, and NMFN. The antisite-vacancy defect (AVDF) formation in NMF is mitigated by substituting Fe with Cu or Ni.

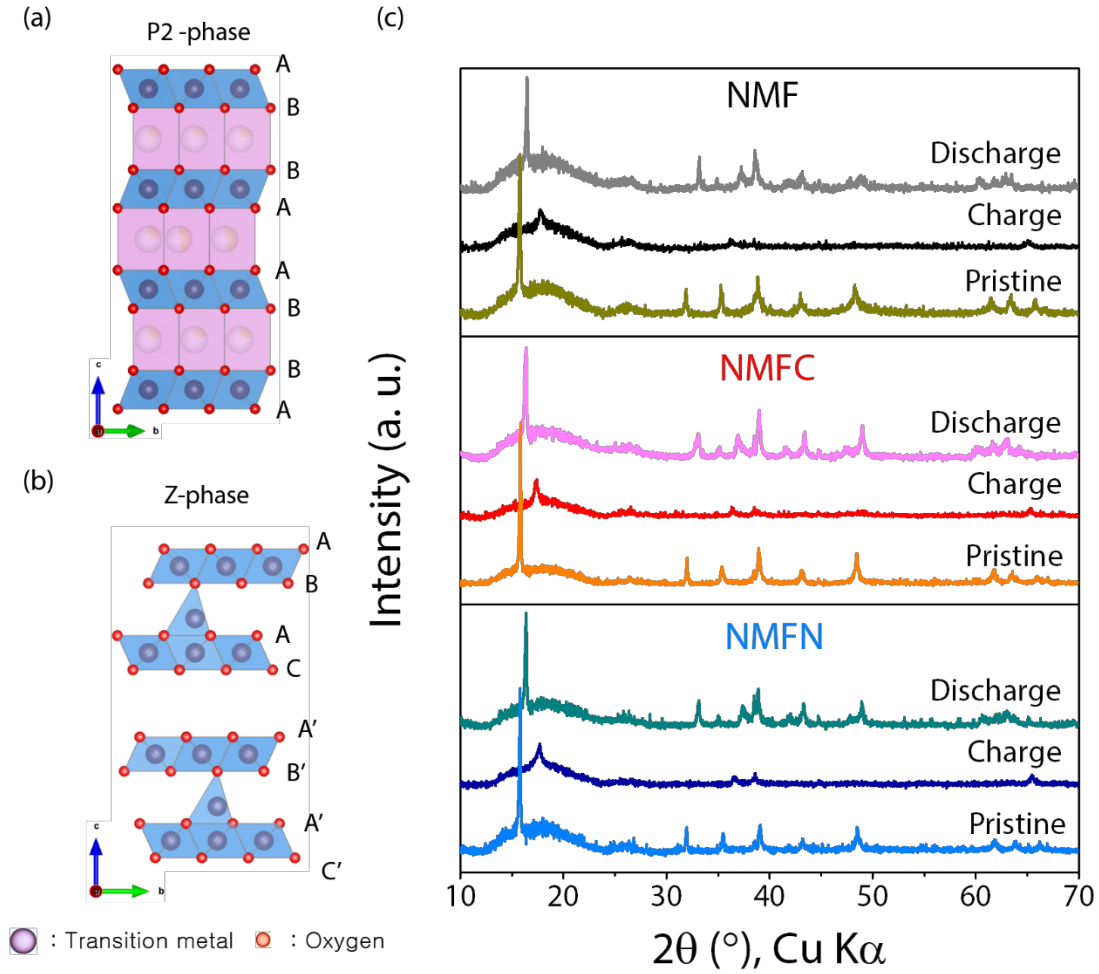

Figure 4.2 The schematic presentation of (a) P2 and (b) Z-phase structures showing the stacking sequence. (c) Powder X-ray patterns of pristine, 4.3V charged and discharged from NMF, NMFC and NMFN electrodes. The broad peak at 30° (2θ) is from the Kapton film X-ray window.

transformation at a Na composition of ~ 0.35, ~ 0.25 and ~ 0.25 mol for NMF, NMFC and NMFN, respectively. Substitution of Ni decreases the maximum hysteresis from 0.66 V to 0.38 V. Thus the hysteresis is the greatest in NMF, followed by NMFC and then NMFN.

To elucidate the underlying factors governing the difference in voltage hysteresis, first, we re-visited the local structure of the Z-phase in the three P2-oxides. X-ray PDF analysis quantifies the

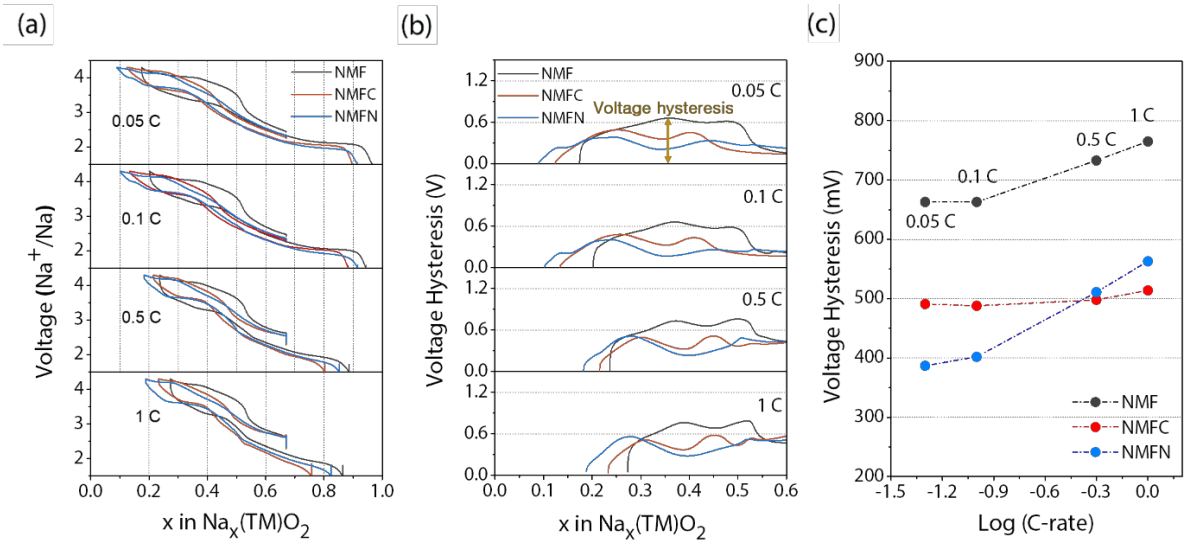

Figure 4.3 Voltage hysteresis evolution from NMF, NMFC and NMFN electrodes with various C-rates for the first cycle. (a) Charge/discharge profiles of NMF, NMFC and NMFN electrodes cycled at 0.05 C, 0.1 C, 0.5 C, and 1 C (from top to bottom). (b) Voltage hysteresis evolution plots from the corresponding charge/discharge profiles in (a). (c) Quantified voltage hysteresis at various C-rates (on a log scale) from NMF, NMFC, and NMFN. Voltage hysteresis exhibits negligible dependence on the C-rate when the C-rate is less than 0.1 C. Therefore, voltage hysteresis at 0.05 C is presumed to be due to AVDF.

amount of AVDF in chemically de-sodiated samples, i.e., the degree of TM migration.[2c] For simplicity, we assumed the total mass of the AVDF pair is preserved in the structure during the Z-phase evolution. The PDF curve fitting (**Figure 4.4**) was conducted by adopting a 4 × 4 × 10 supercell extended from an O2-type bilayer model in **Figure 4.1(d)**, whose origin was described previously.[2b, 2c] The decreased intensity of the d3(i) and d3(ii) PDF peaks in **Figure 4.1(e)** in NMFC and NMFN compared with that of NMF confirms that the AVDF concentration in the Z-phase decreases upon Cu or Ni substitution.[2c] The corresponding bilayer models of the Z-phases from each material are displayed in **Figure 4.1(f)**. The effect of Cu or Ni substitution - namely to reduce AVDF formation in the NMFC and NMFN electrodes - is reflected in a lower voltage hysteresis evolution upon forming the Z-phase. This suggests that the two factors are linked.

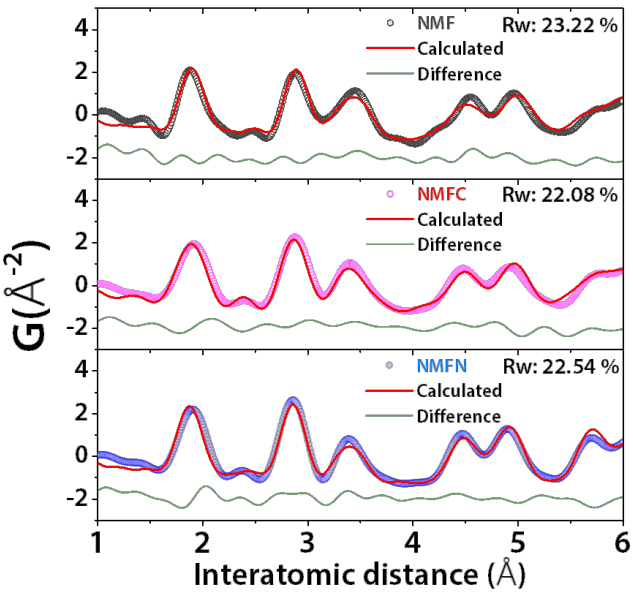

Figure 4.4 (a) Least-squared fits of the PDF curves of NMF, NMFC, and NMFN for the Z-phase in the interatomic distance range of 1.5 - 6 Å.

4.3.2 Redox mechanism: Role of anion redox in charge compensation

To understand why Cu and Ni substitution affect the voltage hysteresis and the concentration of the AVDFs, insight into the redox behavior of each element is needed. XANES and RIXS have been widely used to investigate element-specific redox behavior and to correlate structural evolution and oxidation state change in TM oxide materials. In our previous reports[2b, 2c], the possible involvement of lattice oxygen in the redox behavior of NMF and NMFC was inferred from in-situ XANES measurements at the Mn, Fe and Cu K-edges along with ^{57}Fe Mössbauer spectroscopy analysis. In these studies, the XANES spectra of each cation showed a shift to higher energy upon charge to 4.1 V, but further desodiation to 4.3 V did not result in any discernible energy shift in the spectra.[2a, 2c] Here, TM XANES studies are employed to probe the behavior of the Ni-analogue, NMFN (**Figure 4.5**). The Ni K-edge XANES spectra in **Figure 4.5(a)** demonstrate that Ni is oxidized, compensating for charge at

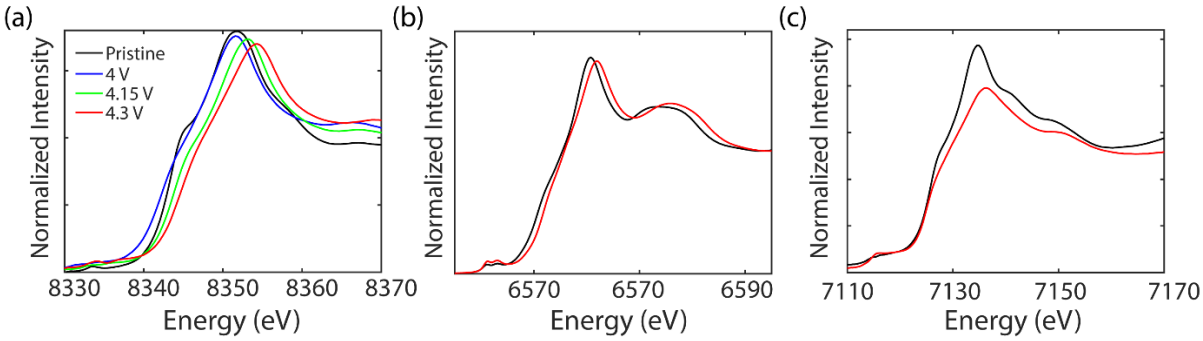

Figure 4.5 Normalized XANES spectra of NMFN at the Ni-K (a), Mn-K (b) and Fe-K edge (c).

potentials above 4.1 V. This is evidenced by a white line shift from 8352 eV to 8355 eV ($Ni^{2+/4+}$) and decreasing peak maxima which are typical redox features of Ni, in agreement with previous observations of P2- $Na_{2/3}[Ni_{1/3-y/2}Mn_{2/3-y/2}Fe_y]O_2$ and O3-$NaFe_{0.3}Ni_{0.7}O_2$.[13] These results confirm that the high-voltage, Z-phase capacity in NMFN involves significant TM (specifically Ni) redox, whereas this is not the case for NMF and NMFC.[2b, 2c] It suggests that the NMFN Z-phase is inactive for anion redox, while NMF and NMFC are active.

To directly quantify the extent of oxygen redox, RIXS at the O K edge was conducted on each electrode at different states during the first oxidation cycle. Points were chosen between 3.9 and 4.3 V (**Figure 4.1(a)**) to sample the uppermost state of charge. RIXS has been used extensively to determine the presence of depopulated O 2p states in Li and Na oxides.[6, 10, 11e, 14] By combining XANES and RIXS analyses on the TMs and oxygen, respectively, we can explore the correlation between cation disorder and cation/anion redox.

RIXS maps for NMF charged to between 3.9 and 4.3 V are shown in **Figure 4.6**. In pristine NMF, we observed two excitations involving intermediate state transitions into the unoccupied hybridized TM 3d-O 2p* and TM 4sp-O 2p* states appearing at approximately 528-533 eV and > 535 eV in excitation energy, respectively. Accompanying emission occurs at approximately 522-527 eV

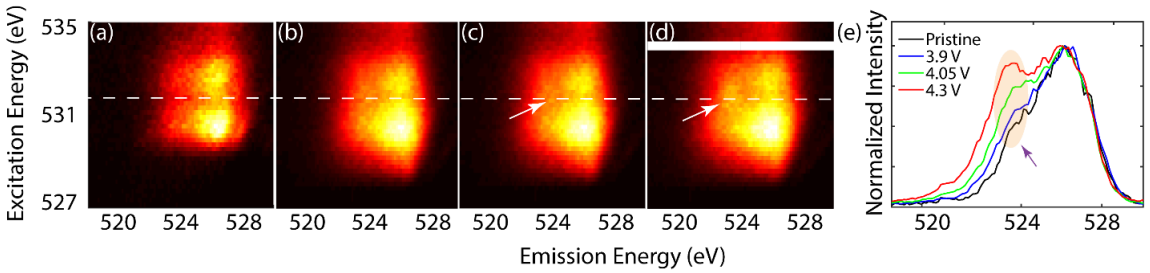

Figure 4.6 O K-edge RIXS measurement of NMF. (a) - (d) RIXS maps of the pristine electrode and of electrodes at 3.9, 4.05, and 4.3 V, respectively. A white dotted line is drawn across the maps to indicate the region of the map (~531.5 eV in excitation energy) where the anion redox feature should be located. (e) Integration of the map at ~531.5 eV excitation. The integration reveals a localized shoulder at approximately 523 eV in emission energy. Therefore, oxygen is involved in compensation of charge during desodiation above 3.9 V.

due to decay from the relatively broad (delocalized) oxygen valence band states to fill the excited O 1s core hole.[14] The TM 3d-O 2p* feature corresponds to the pre-edge of O K-edge spectroscopy and is dominated by TM 3d character through a strong TM-O hybridization effect which evolves during cationic redox (**Figure 4.7**).[14-15]

The O K-edge RIXS map of NMF at 4 V (**Figure 4.6c**) reveals similar excitation and emission states to the pristine electrode. In contrast, for electrodes desodiated to 4.15 and 4.3 V, a sharp feature appears at 531.5 eV in excitation and at 523.3 eV in emission, which differs from the broad 522-527 eV emission features. This localized feature has been linked to anion redox.[2a, 2h, 6, 10, 11e, 16] To further examine this feature, single-energy RIXS spectra at an excitation energy of 531.5 eV were obtained (**Figure 4.6(e)**). A peak emerges at an emission energy of ~ 523 eV and grows with voltage, indicating anion oxidation above 3.9 V. The oxygen redox suggested here is consistent with the absence of Mn and Fe redox activity in XANES in the same voltage range.[2a, 2c]

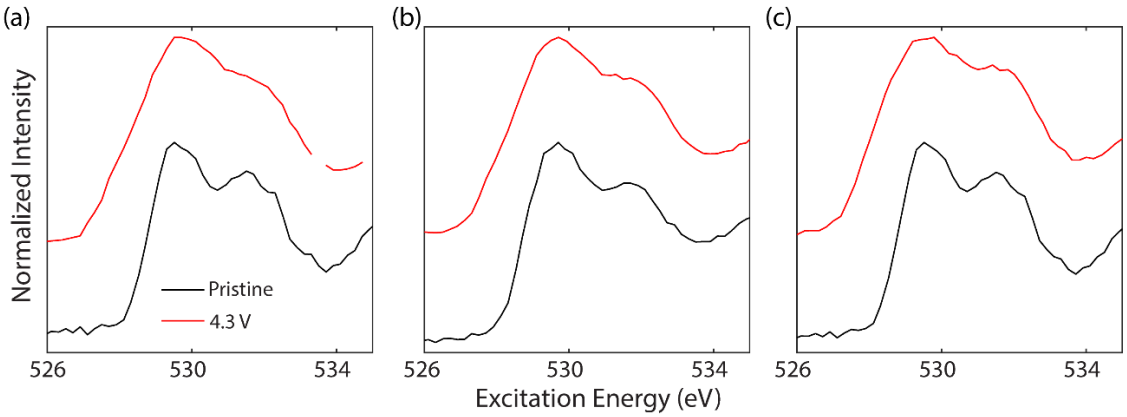

Figure 4.7 O-K edge XAS of (a) NMF, (b) NMFC and (c) NMFN. The "pre-edge" of O-K spectroscopy (~529.5 eV) are dominated by TM 3d character through a strong TM-O hybridization effect. The pre-edge evolves with electrochemical states and its broadening in (a)-(c) is thus due to changes in the valence state of TMs upon charge.[16]

Similar to NMF, the RIXS evolution in NMFC confirms the existence of an oxygen redox feature in the 4.3 V-charged electrode (**Figure 4.8(d)**). However, the oxygen redox feature from the single-energy RIXS spectra at 531.5 eV excitation energy in **Figure 4.8(e)** indicates that the onset of oxygen oxidation occurs at a higher voltage than in NMF, specifically, above ~ 4.15 V.

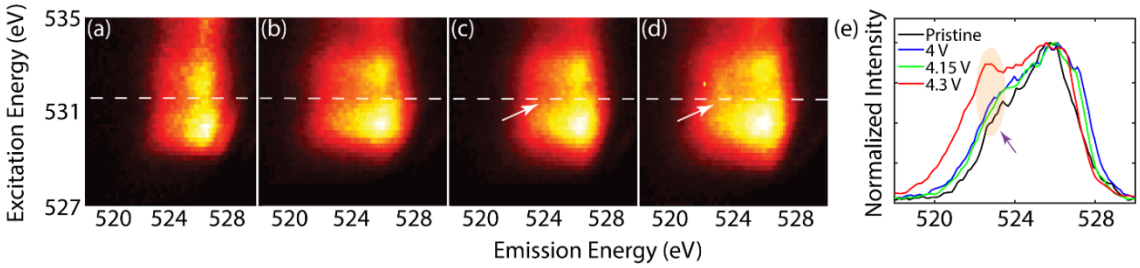

Figure 4.8 O K-edge RIXS measurement of NMFC. (a) - (d) RIXS maps of the pristine electrode and of electrodes at 4, 4.15, and 4.3 V, respectively. (e) Integration of the map at 531.5 eV (white line in b-e). The integration reveals a localized shoulder appearing at approximately 523 eV in emission energy, indicating that oxygen is involved in charge compensation during desodiation above 4.15 V.

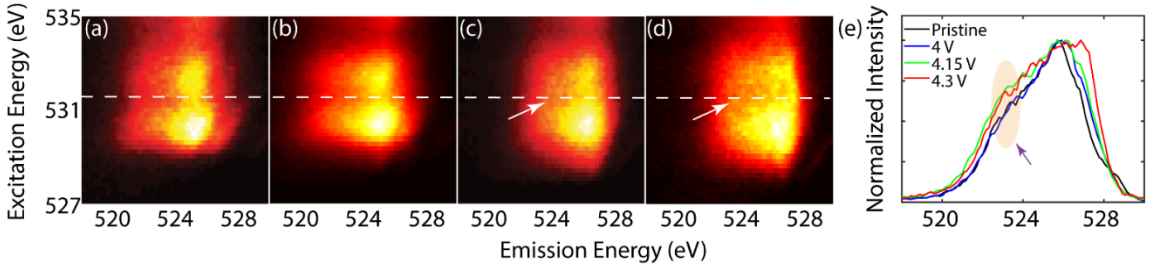

Figure 4.9 O K-edge RIXS measurement of NMFN. (a) - (d) RIXS maps of the pristine electrode and of electrodes at 4, 4.15, and 4.3 V, respectively. (e) Integration of the map at 531.5 eV (white line in a-d). The integration reveals no localized shoulder appears at approximately 523 eV in emission energy. Therefore, oxygen involvement in charge compensation during desodiation at higher voltage is negligible.

In contrast to NMF and NMFC, the O-K edge RIXS maps of NMFN exhibit no discernible oxygen redox feature upon desodiation to 4.3 V, which is also confirmed by the single-energy RIXS spectra (**Figure 4.9**). Consistent with this finding, the Ni K-edge XANES white line shifts by 3 eV between 4 and 4.3 V (**Figure 4.5(a)**). This confirms that Ni, rather than oxygen, oxidation occurs upon desodiation of NMFN at high voltage (> 4.1 V).

Here, the redox mechanism in the three electrodes is summarized by combining the XANES, RIXS and Mössbauer spectroscopy (Fe) results from this and previous studies in **Figure 4.10**.[2a-c] We followed two methods to quantify oxygen's involvement in redox.

- Method 1.

  First, we calculated how much capacity is unaccounted for by the TM redox from XANES and Mössbauer spectroscopy as described below.

A. Oxidation state determination for pristine positive electrode materials

1. In-situ XANES study[1b] confirmed:

- $Na_{0.67}Mn^{3+}_{0.17}Mn^{4+}_{0.33}Fe^{3+}_{0.5}O^{2-}_{2}$ for NMF

- $Na_{0.67}Mn^{3+}_{0.19}Mn^{4+}_{0.47}Fe^{3+}_{0.5}Cu^{2+}_{0.14}O^{2-}_{2}$ for NMFC

2. Mössbauer study showed only Fe^{3+} is present in pristine NMF and NMFN[1a]

3. For NMFN, 0.15 mol of Ni^{2+} and 0.15 mol of Mn^{4+} are substituted for 0.3 mol of Fe^{3+} from NFM[1a].

Therefore, the oxidation state of Mn and Ni can be determined as:

- $Na_{0.67}Mn^{3+}_{0.17}Mn^{4+}_{0.48}Fe^{3+}_{0.2}Ni^{2+}_{0.15}O^{2-}_{2}$ for NMFN

This result is in accordance with reference compounds.[14a]

4. Composition of oxygen is assumed to be stoichiometric.

Therefore, the oxidation states of elements in the pristine electrodes are

NMF - $Na_{0.67}Mn^{3+}_{0.17}Mn^{4+}_{0.33}Fe^{3+}_{0.5}O^{2-}_{2}$

NMFC - $Na_{0.67}Mn^{3+}_{0.19}Mn^{4+}_{0.47}Fe^{3+}_{0.2}Cu^{2+}_{0.14}O^{2-}_{2}$

NMFN - $Na_{0.67}Mn^{3+}_{0.17}Mn^{4+}_{0.48}Fe^{3+}_{0.2}Ni^{2+}_{0.15}O^{2-}_{2}$

B. Oxidation state determination for 4.3 V-charged positive electrode materials:

To calculate the oxidation state change of TMs and oxygen in the electrodes, the total Na extracted from each electrode in **Figure 4.1(a)** was used for the calculation. The Na composition is assumed to be stoichiometric although the coulombic efficiency varies slightly from cell to cell.

Considering the oxidation of Fe^{3+} to Fe^{4+} based on the Mössbauer data[1a] along with the confirmed oxidation of Mn^{3+}, Cu^{2+}, and Ni^{2+} to Mn^{4+}, Cu^{3+}, and Ni^{4+} based on XANES [1b], the oxidation states of elements in the compounds at 4.3V are:

NMF - $Na_{0.175}Mn^{4+}_{0.5}(Fe^{3+}_{0.3375}Fe^{4+}_{0.1625})\ (O^{-}_{0.1625}O^{2-}_{1.8375})$

NMFC - $Na_{0.125}Mn^{4+}_{0.66}(Fe^{3+}_{0.17}Fe^{4+}_{0.03})(Cu^{2+}_{0.02}Cu^{3+}_{0.12})\ (O^{-}_{0.195}O^{2-}_{1.805})$

NMFN - $Na_{0.09}Mn^{4+}_{0.65}(Fe^{3+}_{0.1684}Fe^{4+}_{0.0316})Ni^{4+}_{0.15}(O^{-}_{0.105}O^{2-}_{0.095})$

*O^{-} : oxidized oxygen anion

Based on this calculation, the moles of extracted Na by element-specific redox from NMF, NMFC and NMFN upon charge to 4.3 V is summarized in **Table 4.1**. To obtain the extent of anion redox (e^{-}/O), we divided the value for $O^{-/2-}$ in the table by 2. The extent of oxygen redox is here defined as the number of electrons per oxygen that contribute to charge compensation during desodiation (**Figure 4.10(b)**). It should be noted that variations of capacity from cell to cell and limits of instrument resolution were used to estimate error bars.

Table 4.1 Moles of extracted Na by element-specific redox from NMF, NMFC and NMFN upon charge to 4.3 V. The oxidation state of transition metals is determined by experiment whereas the oxygen's oxidation state is obtained by charge balance.

	$Mn^{3+/4+}$	$Cu^{2+/3+}$	$Fe^{3+/4+}$	$Ni^{2+/4+}$	$O^{-/2-}$	total
NMF	0.17	0	0.1625	0	0.1625	0.495
NMFC	0.19	0.12	0.03	0	0.195	0.545
NMFN	0.17	0	0.0316	0.3	0.105	0.58

- Method 2.

The intensity of the anion redox feature in the single energy RIXS spectra in **Figure 4.11** is analyzed and quantified the anion redox for each electrode as it is described below.

- First, the integrated RIXS spectra at ~ 531.5 eV excitation energy was scaled (normalized) to the peak at ~525 eV emission energy (the TM-O hybridization peak). Since the TM-O configuration is different for different compounds, the intensity and the background of this peak would depend on the material

under study. However, scaling to this peak will allow us to easily notice changes in anion redox peak. Second, the region for the anion redox peak in the integrated RIXS spectra is identified. Since the localization of the redox feature differed in NMF and NMFC (the feature is more localized in NMFC than in NMF), the region (width of the peak) is different for different materials. Third, the area under the anion redox peak shown in red (A2) at 4.3 V (**Figure 4.11**) is calculated. A similar approach to calculate the area the under curve was established in our previous work.[11e]

- To quantify the extent of anion redox, the area of this peak then compare with the area under the curve of the pristine sample as (A1) having the same width as (A2), region shaded in black. Finally, (A2-A1)/A1 is used as a descriptor for evaluating how much oxygen is involved when charging up to 4.3 V. From this analysis, it is observed that NMFC has more anion redox than NMF, whereas NMFN has the minimal participation of oxygen in the redox process. Since the quantified values of reversibility and cyclability only depend on the intensity contrast (changes) of the characteristic O-redox features, no other spectral normalization method is expected to change the conclusions of this work. Such a comparative intensity change could be seen directly with the raw data plots of the single-energy RIXS spectra. Based on the approach presented here, this study shows the general trend for the extent of anion redox to be NMFC ≥ NMF > NMFN. The trend is the same as what it is found in the above method which involved XANES and Mössbauer Spectroscopy.

Therefore, both method 1 and 2 resulted in the same trend for the extent of anion redox: NMFC ≥ NMF >> NMFN.

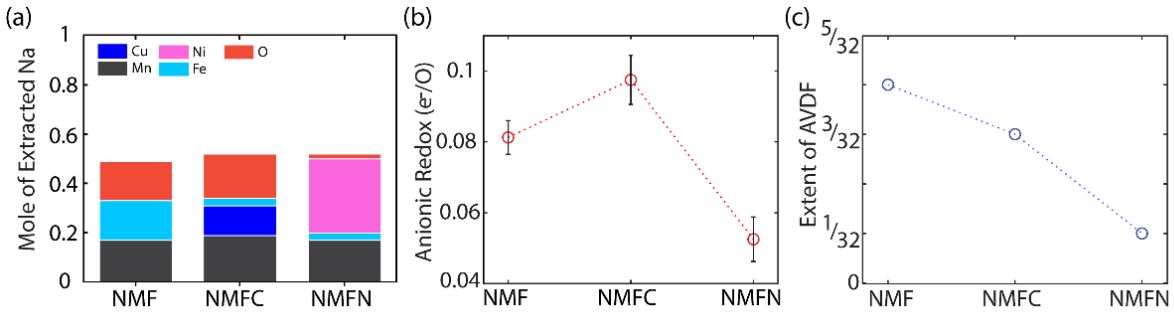

Figure 4.10 (a) Summary of charge compensation in the three electrodes. (b) The extent of anion redox (e^-/O). (c) The extent of AVDF formation (fraction of TMs that swap their position from the octahedral sites in the TM layer to tetrahedral sites in the Na layer.).

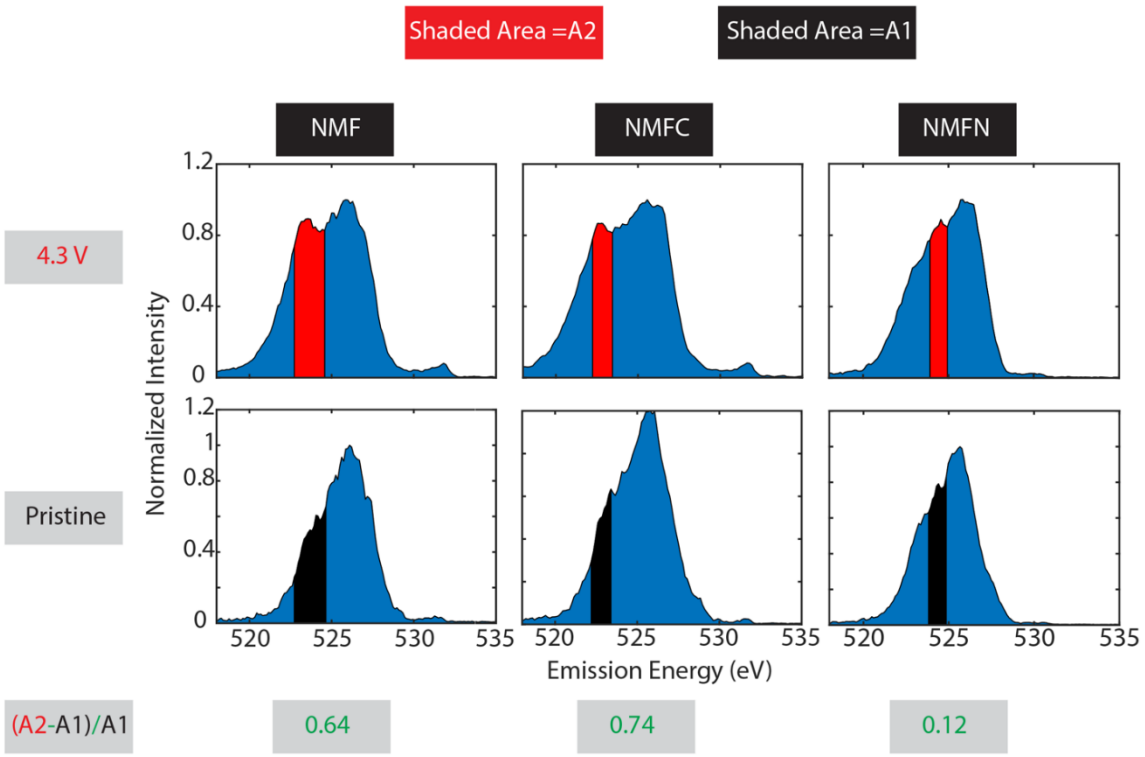

Figure 4.11 Area-under-curve calculation for single-energy RIXS spectra. We selected different areas because each transition metal oxide peak exhibits different broadening owing to variable degrees of transition metal-oxygen hybridization. We chose the region that best represents the peak for a given material.

4.3.3 Structure-anion redox link

The combined structural and spectroscopic characterizations suggest a significant fraction of antisite–vacancy defects form on initial desodiation in NMF and NMFC, and are accompanied by anion oxidation. On the other hand, NMFN exhibits Ni oxidation and does not form such discernible defects. This observation from the sodium layered oxide positive electrodes mirrors the structure–anion redox link reported for Li layered oxide positive electrodes.[6, 10-11, 11e, 14a, 17] The correlation suggests that AVDF formation could be one form of local structure stabilization during oxygen activity.[10, 18] Before discussing what determines the extent of defect formation in these materials, the causation of the anion redox in NMF/C should be addressed first as they are contrary to a prediction from the previous models discussed next.

A local configuration of A-O-A' (Li-O-Li, Na-O-Mg/Zn or Na-O-Vacancy) in the reduced materials has been proposed as a requirement for anion redox. This configuration can form a narrow non-bonding O 2p state that can participate in anion redox[5e, 11]. In this requirement, A and A' have to be redox inactive metals and the A-O bond has to be relatively ionic, so that electrons that form the bond are highly polarized (and more localized on the oxygen anions). Based on this supposition, NMF, NMFC and NMFN are not expected to exhibit anion redox due to the absence of this specific configuration. However, experimental results in this study suggest otherwise. Thus, density of states (DOS) calculations is employed to shed light on the factors that control the fraction of oxygen activity during charging. In order to simplify the calculation and explore the role of a given metal, the number of transition metals in each composition is reduced. Specifically, model compounds kept the Mn content to be ½ of the transition metal sites and filled the other ½ with Fe, Ni, or Cu. This systematic exploration allows us to clearly correlate the changes in the DOS with the type of transition metal. Using three metals per material would make it harder to isolate the role of each. **Figure 4.12** shows the DOS of $Na_{2/3}Mn_{1/2}Fe_{1/2}O_2$ (NMF), $Na_{2/3}Mn_{1/2}Cu_{1/2}O_2$ (NMC), and $Na_{2/3}Mn_{1/2}Ni_{1/2}O_2$ (NMN). The integrated

partial DOS between -1.5 eV and 0 eV was analyzed to estimate how much a given band dominates near the Fermi level (giving an estimate of the fraction of electrons available for redox) (**Figure 6(d)**). The extent to which the oxygen band dominates the band near the Fermi level is in the following order: NMC > NMF > NMN. It should be noted that these calculations are for the pristine materials prior to desodiation. As the charged state is highly disordered and not structurally resolvable, we could not perform DFT. Nonetheless, based on the DOS, Cu and Fe containing materials are expected to have more oxygen-electron availability for redox than Ni during desodiation of the corresponding positive electrode. This is consistent with the experimental observation where the extent of anion redox follows the order NMFC ≥ NMF >> NMFN. This finding corroborates the reliability of the theoretical analysis to predict the redox behavior upon cycling based on the structure of the pristine material.

The relative contribution of a given band near a Fermi level can also be understood as the relative location of the band's centroid (**Figure 4.12(e)**). The more the band dominates, the closer is its centroid to the Fermi level. The effect of the location of the centroid of the band with respect to the Fermi level on the surface exchange kinetics in fuel cells, electrolysis cells[19] and on catalysis activity for the oxygen evolution reaction[20] has also been previously reported. While the A-O-A' configuration forms a nonbonding oxygen 2p state close to the Fermi level and thereby increases the extent of oxygen participation in redox, this work shows that chemical substitution is an effective knob to tune oxygen participation. The type of transition metal, the strength of covalency and local symmetry (among other factors) can play a role in enhancing the presence of O 2p states near the Fermi level. For example, NMF, NMFC and NMFN - despite similar local structure and stoichiometry - have different oxygen band dominance near the Fermi level due to the difference in the transition metal. This introduces oxygen dominance near the Fermi level as a more general descriptor to determine the extent of anion redox.

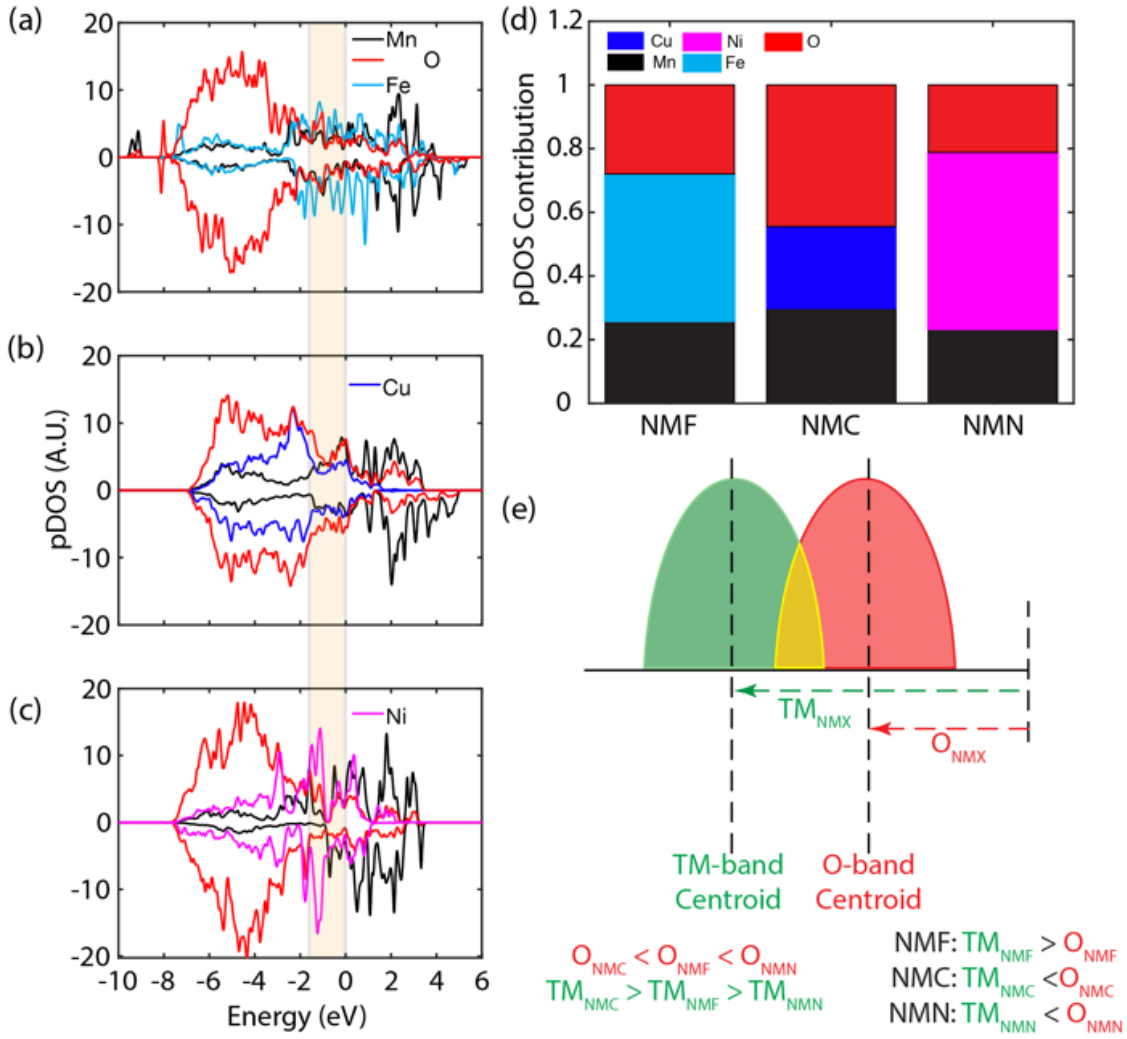

Figure 4.12 DOS calculation for NMF, NMC, and NMN (a), (b) and (c). The area under a given band was calculated between -1.5 eV and 0 eV (highlighted region) to estimate the DOS contribution of each elements (d). From the electrochemistry, we expect to extract ~ 0.5 electrons during this voltage window, and we estimated the -1.5 eV to 0 eV range in the pDOS will contribute to this number of electrons. The DOS contribution of both TM and O is consistent with the respective charge compensation obtained from experiment (Figure 5 (a)). (e) Schematic summarizing the O-band dependence of the extent of anion redox. The more oxygen 2p states near the Fermi level, the more their relative contribution to charge compensation (extent of anion redox). The respective O 2p and TM 3d state contribution compared in the schematic diagram is based on the integrated values from the pDOS between -1.5 to 0 eV.

Note that structural changes upon desodiation may affect the electronic structure and thereby slightly alter the relative cationic and anionic charge compensation mechanism in the resulting oxidized species.[21] However, while the calculations are conducted on the pristine materials here, the relative partial DOS contribution near the Fermi level (**Figure 4.12(d)**) and the charge compensation by the respective ions determined from experiment (**Figure 4.10(a)**) are strikingly similar, confirming the robustness of this method.

The degree of AVDF and the extent of anion redox are not correlated in a 1:1 manner. The trend in the degree of AVDF is NMF > NMFC > NMFN, whereas the trend in the extent of anion redox is NMFC ≥ NMF >> NMFN. This suggests that there is an additional factor that plays a role in determining the extent of AVDF.

Despite its lower anion activity, the extent of AVDF in NMF is higher than NMFC. We propose the higher concentration of Jahn-Teller active Fe^{4+} ions per formula unit in NMF than NMFC can explain this for two main reasons:

1. More Jahn-Teller active Fe^{4+} facilitates the AVDF formation by lowering the energy barrier for TMs to migrate from the octahedral sites in the TMO_2 layer to tetrahedral sites in the Na layer as illustrated in **Figure 4.13(a)**.[22] Poor cycling of O3-$NaFeO_2$ has also been ascribed to Jahn-Teller induced AVDF.[23] The presence of a non-cooperative Jahn-Teller effect of high-spin Fe^{4+} in NMF was previously reported[2a] based on the Debye-Waller factor extracted from EXAFS. We have also confirmed local structural changes in NMFC/N using EXAFS (**Figure 4.14**).

2. Stabilizing the Fe^{4+} ion by ligand metal charge transfer promotes weakening of the TM-O bonding to neighboring TM atoms.[24] Thus, it increases susceptibility to AVDF formation by TM migration in NMF as shown in **Figure 4.13(b)**.

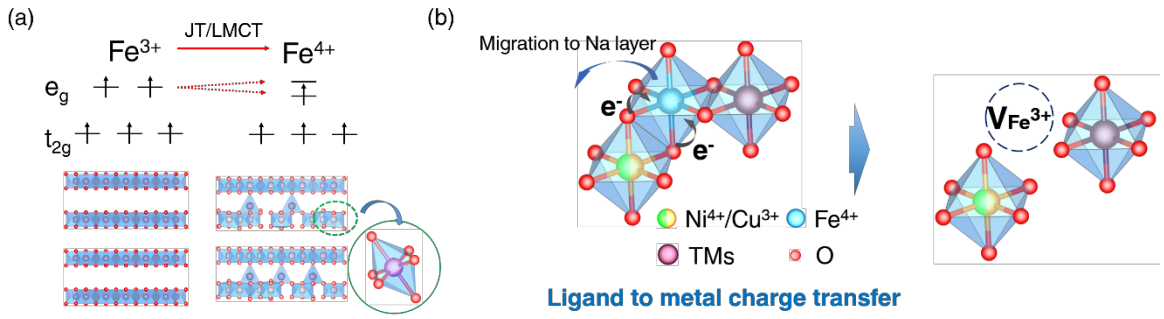

Figure 4.13 Schematic showing the correlation between out-of-plane disorder and concentration of Fe^{4+} ions. (a) JT-assisted distortion could reduce the energy barrier for disorder by reducing the energy difference between the octahedral sites in the TM layer and prismatic sites in the sodium layer.[18] (b) Schematic of the Fe^{3+} migration process by ligand metal charge transfer (LMCT) of Cu/Ni in NMFC or NMFN. LMCT weakens the metal-oxygen bond, which enables the disordering of TMs out of the TMO_2 layers.

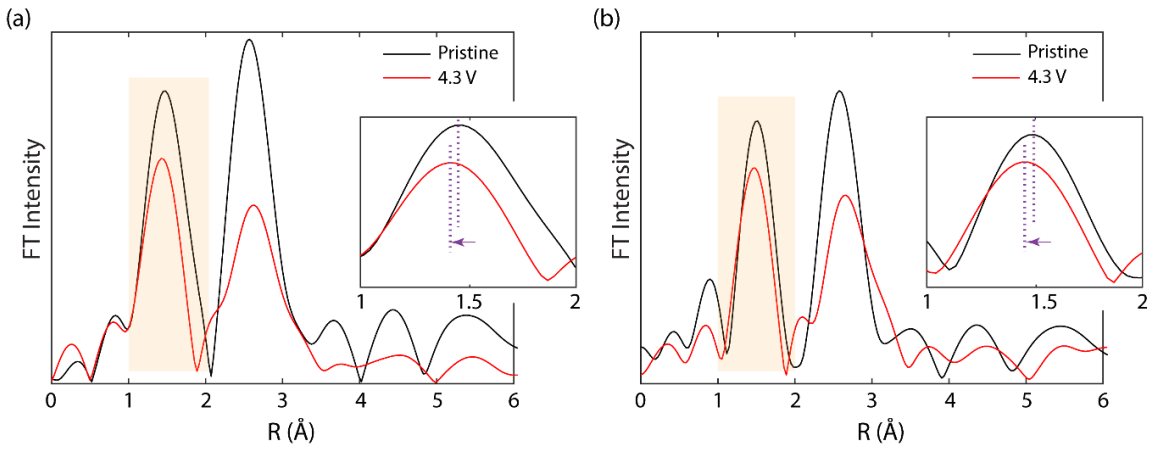

Figure 4.14 Radial distribution around Fe in NMFC (left) and NMFN (right) at the Fe K-edge. From the radial distribution plots of both compounds, Fe-O bond has contracted while the Fe-TM bond length has elongated. The decrease in intensity of Fe-O and Fe-TM bond after charge is an indication of local disorder which is caused by the Jahn-Teller nature of Fe^{4+}, similar to what was observed in NMF.[2a] The presence of a non-cooperative Jahn-Teller effect of Fe^{4+} ion in high-valent state of NMFC and NMFN electrode facilitates AVDF formation.

Comparing NMFC and NMFN, anion redox is more significant in the former than the latter which means the structural changes that could take place to stabilize the oxidized species (such as oxygen dimer or TM=O formation[10, 17a, 18]) are more significant in NMFC. The combination of these two phenomena describes the AVDF trend observed, NMF > NMFC > NMFN (**Figure 4.10(c)**), although the trend for the extent of anion redox is NMFC ≥ NMF >> NMFN (**Figure 4.10(b)**).

4.3.4 Conclusions

Our investigation of the effect of transition metal substitution in sodium layered metal oxides based on P2-$Na_{0.67-x}[Mn_{0.5}Fe_{0.5}]O_2$ (NMF) reveals the complex interplay of the factors that control electrochemical behavior in this material. The study disentangles the complex contributions of anion redox and TM migration to establish a relationship between structural disorder and oxygen redox, demonstrating why partial substitution is a viable method to design Fe based compounds with optimal composition and good properties - a design that takes into account the role of anion redox.

First, the combination of experiment (RIXS, XANES, electrochemistry and PDF analysis) together with theory (density-of-state calculations) indisputably prove the contribution of anion redox and evaluate its effect. While iron-rich sodium metal oxides are a cost-effective, environmentally beneficial choice as Na-battery cathodes, they suffer structural hysteresis on deep charge. This owes to formation of significant antisite-vacancy defects (AVDF) and oxygen anion redox activity in the high-valent state, which results in structural disorder that is further triggered by the Jahn-Teller nature of Fe^{4+}.

While an A-O-A' local structure can increase the amount of O 2p states near the Fermi level, it is not a necessary condition for oxygen redox in the P2 sodium layered TM oxides as previously thought. NMF and its Cu-substituted analogue lack this configuration yet have significant anion redox. DOS calculations show that anion redox is more favored if the oxygen 2p band dominates the band

near the Fermi level in the TM-O bond. The more oxygen 2p states near the Fermi level, the more their relative contribution to charge compensation. Consequently, the covalency of the TM, among other factors, can increase the oxygen density near the Fermi level and thereby the propensity for anion redox.

Reducing the concentration of Fe^{4+} ions in the charged state via their partial substitution is necessary to alter composition, and hence tune anion redox and affect structural stability-redox coupling. We outlined two approaches here: 1) choosing a TM substituent which minimizes AVDF but optimizes anion redox (e.g. Cu); 2) choosing a TM substituent whose band is closer to the Fermi level than the oxygen band in order to suppress anion redox and AVDF formation (e.g. Ni). While it isn't yet clear which strategy is best, we believe our understanding of the mechanisms at play sheds light on design principles and can guide future directions to improve the performance of sodium-ion battery positive electrodes.

References

[1] C. Vaalma, D. Buchholz, M. Weil, S. Passerini, *Nat Rev Mater* **2018**, *3*, 18013.

[2] a) N. Yabuuchi, M. Kajiyama, J. Iwatate, H. Nishikawa, S. Hitomi, R. Okuyama, R. Usui, Y. Yamada, S. Komaba, *Nat Mater* **2012**, *11*, 512-517; b) E. Talaie, V. Duffort, H. L. Smith, B. Fultz, L. F. Nazar, *Energ Environ Sci* **2015**, *8*, 2512-2523; c) E. Talaie, S. Y. Kim, N. Chen, L. F. Nazar, *Chem Mater* **2017**, *29*, 6684-6697; d) D. D. Yuan, X. H. Hu, J. F. Qian, F. Pei, F. Y. Wu, R. J. Mao, X. P. Ai, H. X. Yang, Y. L. Cao, *Electrochim Acta* **2014**, *116*, 300-305; e) V. Duffort, E. Talaie, R. Black, L. F. Nazar, *Chem Mater* **2015**, *27*, 2515-2524; f) S. Kalluri, K. H. Seng, W. K. Pang, Z. P. Guo, Z. X. Chen, H. K. Liu, S. X. Dou, *Acs Appl Mater Inter* **2014**, *6*, 8953-8958; g) E. Gonzalo, M. H. Han, J. M. L. del Amo, B. Acebedo, M. Casas-Cabanas, T. Rojo, *J Mater Chem A* **2014**, *2*, 18523-18530; h) B. M. de Boisse, D. Carlier, M. Guignard, L. Bourgeois, C. Delmas, *Inorg Chem* **2014**, *53*, 11197-11205; i) B. M. de Boisse, D. Carlier, M. Guignard, C. Delmas, *J Electrochem Soc* **2013**, *160*, A569-A574; j) J. T. Xu, S. L. Chou, J. L. Wang, H. K. Liu, S. X. Dou, *Chemelectrochem* **2014**, *1*, 371-374.

[3] D. Susanto, M. K. Cho, G. Ali, J. Y. Kim, H. J. Chang, H. S. Kim, K. W. Nam, K. Y. Chung, *Chem Mater* **2019**, *31*, 3644-3651.

[4] a) D. Kim, E. Lee, M. Slater, W. Q. Lu, S. Rood, C. S. Johnson, *Electrochem Commun* **2012**, *18*, 66-69; b) H. Yoshida, N. Yabuuchi, S. Komaba, *Electrochem Commun* **2013**, *34*, 60-63; c) S. Y. Xu, X. Y. Wu, Y. M. Li, Y. S. Hu, L. Q. Chen, *Chinese Phys B* **2014**, *23*; d) M. H. Han, E. Gonzalo, N. Sharma, J. M. L. del Amo, M. Armand, M. Avdeev, J. J. S. Garitaonandia, T. Rojo, *Chem Mater* **2016**, *28*, 106-116; e) Y. Ono, Y. Yui, M. Hayashi, K. Asakura, H. Kitabayashi, K. I. Takahashi, *Ecs Transactions* **2014**, *58*, 33-39; f) D. Kundu, E. Talaie, V. Duffort, L. F. Nazar, *Angew Chem Int Edit* **2015**, *54*, 3431-3448; g) L. Liu, X. Li, S. H. Bo, Y. Wang, H. L. Chen, N. Twu, D. Wu, G. Ceder, *Adv Energy Mater* **2015**, *5*, 1500944.

[5] a) K. Du, J. Y. Zhu, G. R. Hu, H. C. Gao, Y. T. Li, J. B. Goodenough, *Energ Environ Sci* **2016**, *9*, 2575-2577; b) X. H. Rong, J. Liu, E. Y. Hu, Y. J. Liu, Y. Wang, J. P. Wu, X. Q. Yu, K. Page, Y. S. Hu, W. L. Yang, H. Li, X. Q. Yang, L. Q. Chen, X. J. Huang, *Joule* **2018**, *2*, 125-140; c) B. M. de Boisse, G. D. Liu, J. T. Ma, S. Nishimura, S. C. Chung, H. Kiuchi, Y. Harada, J. Kikkawa, Y. Kobayashi, M. Okubo, A. Yamada, *Nat Commun* **2016**, *7*, 11397; d) W. Zheng, Q. Liu, Z. Y. Wang, Z. B. Yi, Y. Z. Li, L. J. Cao, K. L. Zhang, Z. G. Lu, *J Power Sources* **2019**, *439*, 227086; e) X. Bai, M. Sathiya, B. Mendoza-Sanchez, A. Iadecola, J. Vergnet, R. Dedryvere, M. Saubanere, A. M. Abakumov, P. Rozier, J. M. Tarascon, *Adv Energy Mater*

2018, *8*, 1802379 ; f) C. Z. Ma, J. Alvarado, J. Xu, R. J. Clement, M. Kodur, W. Tong, C. P. Grey, Y. S. Meng, *J Am Chem Soc* **2017**, *139*, 4835-4845; g) B. M. de Boisse, M. Reynaud, J. T. Ma, J. Kikkawa, S. I. Nishimura, M. Casas-Cabanas, C. Delmas, M. Okubo, A. Yamada, *Nat Commun* **2019**, *10*, 2185.

[6] W. E. Gent, K. Lim, Y. F. Liang, Q. H. Li, T. Barnes, S. J. Ahn, K. H. Stone, M. McIntire, J. Y. Hong, J. H. Song, Y. Y. Li, A. Mehta, S. Ermon, T. Tyliszczak, D. Kilcoyne, D. Vine, J. H. Park, S. K. Doo, M. F. Toney, W. L. Yang, D. Prendergast, W. C. Chueh, *Nat Commun* **2017**, *8*, 2091.

[7] G. Assat, S. L. Glazier, C. Delacourt, J. M. Tarascon, *Nat Energy* **2019**, *4*, 647-656.

[8] R. A. House, U. Maitra, M. A. P?rez-Osorio, J. G. Lozano, L. Jin, J. W. Somerville, L. C. Duda, A. Nag, A. Walters, K. J. Zhou, M. R. Roberts, P. G. Bruce, *Nature* **2020**, *577*, 502-508.

[9] J. H. Song, G. Yoon, B. Kim, D. Eum, H. Park, D. H. Kim, K. Kang, *Adv Energy Mater* **2020**, *10*, 2001207.

[10] J. Hong, W. E. Gent, P. Xiao, K. Lim, D. H. Seo, J. Wu, P. M. Csernica, C. J. Takacs, D. Nordlund, C. J. Sun, K. H. Stone, D. Passarello, W. L. Yang, D. Prendergast, G. Ceder, M. F. Toney, W. C. Chueh, *Nat Mater* **2019**, *18*, 256-265.

[11] a) D. H. Seo, J. Lee, A. Urban, R. Malik, S. Kang, G. Ceder, *Nat Chem* **2016**, *8*, 692-697; b) G. Assat, J. M. Tarascon, *Nat Energy* **2018**, *3*, 373-386; c) U. Maitra, R. A. House, J. Somerville, N. Tapia-Ruiz, J. G. Lozano, N. Guerrini, R. Hao, K. Luo, L. Y. Jin, M. A. Perez-Osorio, F. Massel, D. M. Pickup, S. Ramos, X. Y. Lu, D. E. McNally, A. V. Chadwick, F. Giustino, T. Schmitt, L. C. Duda, M. R. Roberts, P. G. Bruce, *Nat Chem* **2018**, *10*, 288-295; d) B. M. de Boisse, S. Nishimura, E. Watanabe, L. Lander, A. Tsuchimoto, J. Kikkawa, E. Kobayashi, D. Asakura, M. Okubo, A. Yamada, *Adv Energy Mater* **2018**, *8*, 1800409; e) K. H. Dai, J. P. Wu, Z. Q. Zhuo, Q. H. Li, S. Sallis, J. Mao, G. Ai, C. H. Sun, Z. Y. Li, W. E. Gent, W. C. Chueh, Y. D. Chuang, R. Zeng, Z. X. Shen, F. Pan, S. S. Yan, L. F. J. Piper, Z. Hussain, G. Liu, W. L. Yang, *Joule* **2019**, *3*, 518-541.

[12] a) P. Juhas, T. Davis, C. L. Farrow, S. J. L. Billinge, *J Appl Crystallogr* **2013**, *46*, 560-566; b) C. L. Farrow, P. Juhas, J. W. Liu, D. Bryndin, E. S. Bozin, J. Bloch, T. Proffen, S. J. L. Billinge, *J Phys-Condens Mat* **2007**, *19*, 335219.

[13] a) J. R. Croy, J. C. Garcia, H. Iddir, S. E. Trask, M. Balasubramanian, *J Power Sources* **2020**, *471*, 228335; b) F. Dogan, B. R. Long, J. R. Croy, K. G. Gallagher, H. Iddir, J. T. Russell, M. Balasubramanian, B. Key, *J Am Chem Soc* **2015**, *137*, 2328-2335.

[14] a) J. W. Somerville, R. A. House, N. Tapia-Ruiz, A. Sobkowiak, S. Ramos, A. V. Chadwick, M. R. Roberts, U. Maitra, P. G. Bruce, *J Mater Chem A* **2018**, *6*, 5271-5275; b) C. F. Petersburg, Z. Li, N. A. Chernova, M. S. Whittingham, F. M. Alamgir, *J Mater Chem* **2012**, *22*, 19993-20000.

[15] a) J. Xu, M. L. Sun, R. M. Qiao, S. E. Renfrew, L. Ma, T. P. Wu, S. Hwang, D. Nordlund, D. Su, K. Amine, J. Lu, B. D. McCloskey, W. L. Yang, W. Tong, *Nat Commun* **2018**, *9*, 947; b) W. Yang, T. P. Devereaux, *J Power Sources* **2018**, *389*, 188-197; c) J. P. Wu, Q. H. Li, S. Sallis, Z. Q. Q. Zhuo, W. E. Gent, W. C. Chueh, S. S. Yan, Y. D. Chuang, W. L. Yang, *Condens Matter* **2019**, *4*, 5.

[16] S. Roychoudhury, R. Qiao, Z. Zhuo, Q. Li, Y. Lyu, J. Kim, J. Liu, E. Lee, B. J. Polzin, J. Guo, S. Yan, Y. Hu, H. Li, D. Prendergast, W. Yang, ChemRxiv. Preprint. https://doi.org/10.26434/chemrxiv.11416374.v3..

[17] a) Z. Q. Zhuo, C. Das Pemmaraju, J. Vinson, C. J. Jia, B. Moritz, I. Lee, S. Sallies, Q. H. Li, J. P. Wu, K. H. Dai, Y. D. Chuang, Z. Hussain, F. Pan, T. P. Devereaux, W. L. Yang, *J Phys Chem Lett* **2018**, *9*, 6378-6384; b) Z. Q. Zhuo, Y. S. Liu, J. H. Guo, Y. D. Chuang, F. Pan, W. L. Yang, *J Phys Chem Lett* **2020**, *11*, 2618-2623.

[18] a) H. R. Chen, M. S. Islam, *Chem Mater* **2016**, *28*, 6656-6663; b) M. Ben Yahia, J. Vergnet, M. Saubanere, M. L. Doublet, *Nat Mater* **2019**, *18*, 496.

[19] Z. L. Chen, J. Li, X. C. Zeng, *J Am Chem Soc* **2019**, *141*, 10751-10759.

[20] A. Urban, I. Matts, A. Abdellahi, G. Ceder, *Adv Energy Mater* **2016**, *6*, 1600488.

[21] J. K. Norskov, J. Rossmeisl, A. Logadottir, L. Lindqvist, J. R. Kitchin, T. Bligaard, H. Jonsson, *J Phys Chem B* **2004**, *108*, 17886-17892.

[22] X. S. Hu, L. Xu, X. K. Lin, M. Pecht, *Joule* **2020**, *4*, 310-346.

[23] a) Y. N. Zhang, S. Kim, G. Y. Feng, Y. Wang, L. Liu, G. Ceder, X. Li, *J Electrochem Soc* **2018**, *165*, A1184-A1192; b) X. Chen, S. Hwang, R. Chisnell, Y. C. Wang, F. Wu, S. Kim, J. W. Lynn, D. Su, X. Li, *Adv Funct Mater* **2018**, *28*, 1803896; c) S. Kim, X. H. Ma, S. P. Ong, G. Ceder, *Phys Chem Chem Phys* **2012**, *14*, 15571-15578; d) Y. Takeda, K. Nakahara, M. Nishijima, N. Imanishi, O. Yamamoto, M. Takano, R. Kanno, *Mater Res Bull* **1994**, *29*, 659-666.

[24] Y. J. Li, Y. R. Gao, X. F. Wang, X. Shen, Q. Y. Kong, R. C. Yu, G. Lu, Z. X. Wang, L. Q. Chen, *Nano Energy* **2018**, *47*, 519-526.

[25] X. F. Wang, G. D. Liu, T. Iwao, M. Okubo, A. Yamada, *J Phys Chem C* **2014**, *118*, 2970-2976.

Chapter 5

Reversible Oxygen Redox in $Na_2Mn_3O_7$ by Coulombically-Stabilized Oxygen Hole Polarons

5.1 Introduction

Stable and reversible high-valent redox couples are foundational to electrochemical and catalytic transformations. A prominent application of such redox couples is intercalation battery electrodes.[1] In particular, the phenomenon of anion redox in lithium- and sodium-ion positive electrodes has the potential to significantly improve cell energy density by providing additional high voltage capacity beyond that of most transition metal (TM) redox couples.[2–4] Two major hypotheses have guided the search for intercalation layered oxides with stable and reversible oxygen redox. First, short covalent bonding between oxygen atoms (e.g., ~ 1.5 Å O-O peroxo, vs. 2.8 Å in a typical TMO_6 octahedron)[4,5] and between TM and oxygen atoms (e.g., ~ 1.8 Å metal-oxo vs. 2.0 Å typical)[6] can stabilize oxidized oxide species against oxygen release. Second, the energetic penalty associated with the local distortion induced by such major bonding rearrangements can be mitigated by in-plane[7] and out-of-plane metal vacancy/antisite disorder[5,6,8,9] (i.e., so called cation migration), leading to overall energy savings. The convergence of these two ideas has led to the current paradigm that oxygen redox and cation disordering come hand-in-hand to achieve stable but hysteretic redox in battery electrodes, typically involving hysteresis of several hundred mV.[9–11] As such, efforts have been directed at minimizing the hysteresis associated with transition metal hopping,[11] as well as identifying new structures that can accommodate local distortions induced by anion redox without disorder.[1] An alternative approach is to avoid such restructuring all together and therefore mitigate hysteresis.[3]

Recently, several groups reported an anion redox active material, $Na_{2-x}Mn_3O_7$, with a very small voltage hysteresis (~ 60 mV).[12–15] The negligible hysteresis is maintained even upon deep deintercalation unlike other materials where the magnitude of voltage hysteresis scales with the extent of deintercalation.[16] However, the mechanism that allowed such remarkable performance is still unclear. For example, Yamada and colleagues observed the emergence of a new absorption feature at ~531 eV upon anion redox in X-ray absorption spectroscopy (XAS) measurements,[12] which was also resulted from an oxygen-redox mechanism in typical oxygen redox active electrodes exhibiting large voltage hysteresis, such as $Li_{1+x}Ni_{1-y-z}Mn_yCo_zO_3$ (NMC),[9] $Li_{2-x}Ir_{1-y}Sn_yO_3$,[6] and $Na_{0.75}Li_{0.25}Mn_{0.75}O_2$.[8] However, since $Na_{2-x}Mn_3O_7$ and the other electrode materials exhibit differing hysteresis, distinctive redox mechanism and therefore XAS features would be expected. Therefore, an understanding of the redox mechanism in NMO could inform us ways to achieve similar exceptional behavior in other Na and Li based oxide positive electrode materials.

In this Chapter, we report unambiguous experimental and computational spectroscopic confirmation of redox mechanism in NMO that is different from anion redox positive electrode materials with high voltage hysteresis. We discover oxygen hole polaron formation and its electrochemical redox stability upon charging. The persistent ordered Mn vacancies in this electrode material provides the basis for calculating and understanding redox energetics in the absence of metal cation disordering. A clear picture for oxygen redox emerges: electrostatic interactions between oxygen hole polarons and Na vacancies compete with covalent bonding and transition metal disorder to determine the redox pathway. Through this understanding, we demonstrate that coulombic interactions can stabilize the otherwise unstable oxygen holes and provide energy saving as much as O-O covalent bonding, achieving exceptionally low, ~ 40 mV voltage hysteresis over electrochemical cycling with negligible voltage fade. Beyond batteries, stabilizing unusual polaronic states has many implications for defect engineering in condensed matter systems.

5.2 Experimental Details

5.2.1 Materials Synthesis

$Na_2Mn_3O_7$ powder was prepared by a solid-state method. A stoichiometric mixture of $NaNO_3$ (J. T. Baker, A.C.S. Reagent) and $MnCO_3$ (Aldrich, ≥ 99.9%) powder was ball-milled at 250 rpm for 1 h. The collected mixture powder was then heated at 600 °C (5 °C/min) for 12 h under an oxygen (99.5 %) flow and naturally cooled down to room temperature (RT). The as prepared powder sample transferred directly to an argon filled glovebox (MBraun, O_2 and $H_2O \leq 0.1$ ppm) without exposure to the air.

5.2.2 X-ray diffraction

High-resolution powder XRD patterns for Rietveld refinement were measured at beamline 2-1 at the Stanford Synchrotron Radiation Lightsource (SSRL, SLAC National Accelerator Laboratory) at 17 keV (0.7293 Å) beam energy. The size of the X-ray beam was 500 × 1500 μm^2 and the distance between sample and the Pilatus-100K detector was 700 mm. All of the samples were contained in capillaries to avoid possible preferred orientation of the particles. All of the samples were measured using transmission and $\theta - 2\theta$ geometry.

5.2.3 Electrochemistry

Positive electrodes were prepared inside an argon filled glovebox (O_2 and $H_2O < 1$ ppm) to avoid air contamination. $Na_2Mn_3O_7$ powder was mixed with 10 wt% Super P carbon and 10 wt% polyvinylidene fluoride (PVDF) (Aldrich average Mw ≈ 534 000) and suspended in N-methyl-2-pyrrolidinone (Sigma-Aldrich, 99.5%). The slurry was cast on aluminum foil with an active material loading of 5 - 7 $mg \cdot cm^{-2}$. The electrodes were punched to a 1 cm^2 geometric area and dried in a vacuum oven at 120 °C overnight. The electrochemical studies were carried out in 2325 coin-type half cells

with Na metal-disk as the counter electrode. The electrolyte was comprised of 1M $NaPF_6$ (Alfa Aesar, ≥ 99.0%) dissolved in a mixture of ethylene carbonate (BASF, 99.98%), propylene carbonate (BASF, 99.98%) and 4-fluoro-1,3-dioxolan-2-one (Sigma-Aldrich, 99%) with a volume ratio of 49:49:2. Glass fiber (Merck Millipore) was employed as a separator. Galvanostatic cycling was performed using a multi-channel battery tester (Model 4000, Maccor Inc.) at room temperature with a current density of C/20.

5.3 Result and Discussion

5.3.1 Structural stability upon charge

Structurally, one out of every seven Mn sites are vacant in the TM layer of $Na_{2-x}Mn_3O_7$ ($Na_{4/7-x}Mn_{6/7}\square_{1/7}O_2$, where $\square$ = vacant sites in the TM layer) (**Figure 5.1A**). This results in two oxygen sublattices: oxygen anions with two Mn neighbors (O-Mn2, termed "O1") and oxygen anions with three Mn neighbors (O-Mn3, termed "O2"). Normally, in Na layered TM oxide materials, the substantial difference in ionic radii between octahedral Mn^{4+} (0.53 Å) and Na^+ (1.02 Å) and the large interlayer spacing further increases the penalty for antisite defects which induces voltage hysteresis. Previous studies on $Na_{2-x}Mn_3O_7$ showed low voltage-hysteresis by charging up to 4.7 V and reversible structural evolution.[12–14] However, despite the stable structure, voltage and capacity fading were still observed when the electrode was charged to > 4.4 V (**Figure 5.1B**) possibly due to side reactions and electrolyte decomposition as the preserved local structure confirmed by extended X-ray absorption fine structure (EXAFS) results (**Figure 5.1C**). Since we are interested in determining the exact anion redox mechanism, we cycled the material in the voltage region of 3.5 - 4.3 V where electrolyte decomposition

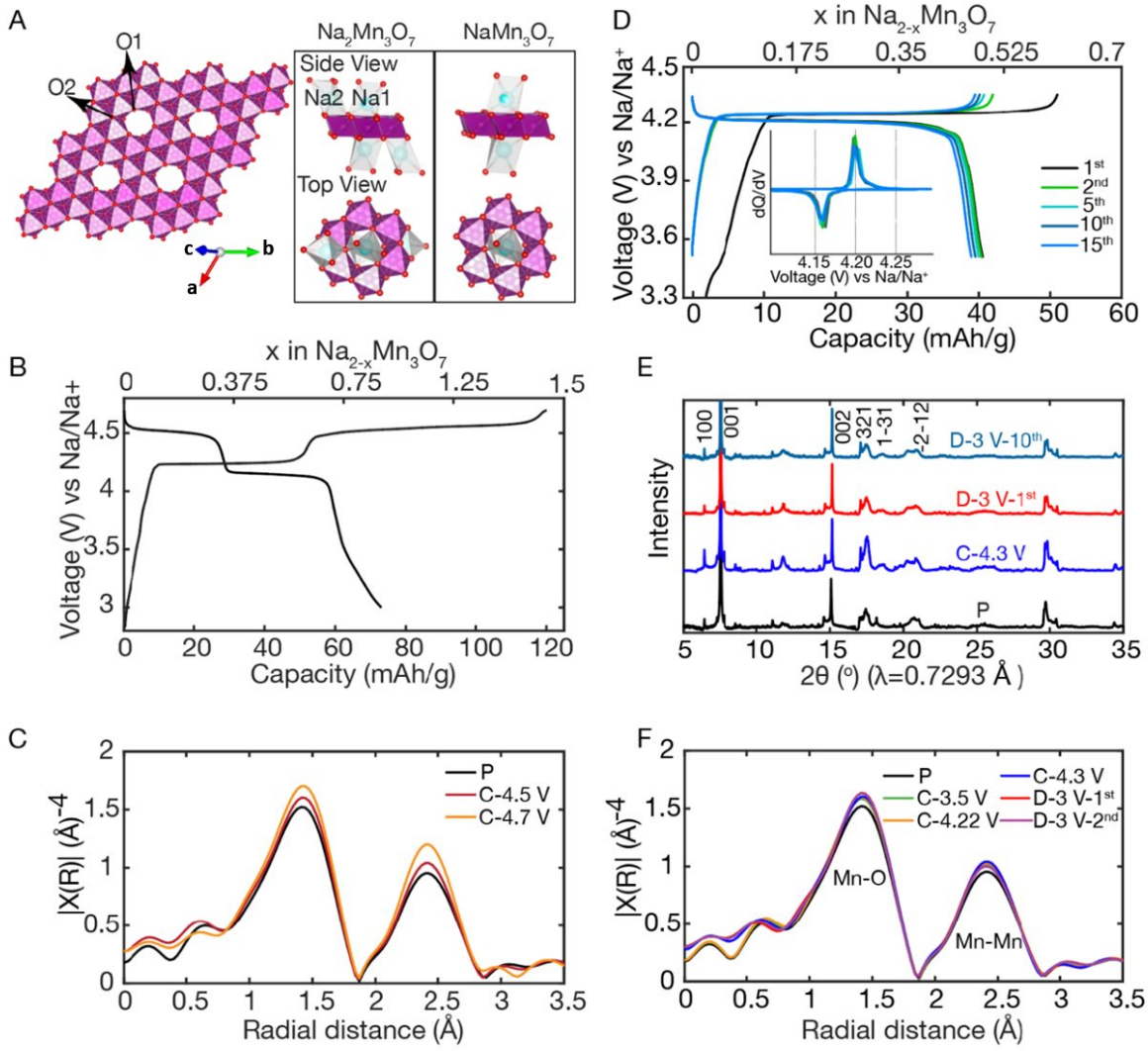

Figure 5.1 Reversible electrochemistry and stable structure. (A) Structure of the Mn-O layer in $Na_2Mn_3O_7$ (Mn atoms shown in magenta and O atoms in red). One out of seven Mn sites are vacant, which creates two unique O environments: O–Mn2 (O1) in the ring surrounding the Mn vacancy; and O–Mn3 (O2). Top and side view of pristine and charged state. There are two sodium sites: Na2 (distorted octahedral) and Na1 (prismatic). (B) Voltage versus specific capacity at C/20 between 2.7 V and 4.7 V. (C) Fourier transform of the ex-situ EXAFS spectra taken at the same voltage conditions. The negligible change in the EXAFS profile indicates preservation of the local structure upon deep desodiation. (D) Voltage profile up to the 15th cycle at C/20 (1 C is equivalent to 166 mAh/g) between 3.5 V - 4.3 V vs Na/Na^+, with very low voltage hysteresis (~ 40 mV). Inset: differential capacity as a function of voltage (dQ/dV vs V). (E) Fourier transform of the ex-situ EXAFS spectra of the pristine material (P) and electrodes charged to 3.5 V, 4.22 V, and 4.3 V in the 1st cycle and discharged to 3 V in the 1st and 2nd cycle (D-3V-1st and D-3V-2nd), respectively. The first peak corresponds to Mn-O

bonds and the second to Mn-Mn bonds. The negligible change in the EXAFS profile indicates preservation of the local structure upon cycling. (F) Synchrotron powder X-ray diffraction of the pristine material; electrodes were charged to 4.3 V in the 1st cycle and discharged to 3 V at the 1st and 10th cycle (D-3V-1st and D-3V-10th). The XRD patterns exhibit negligible changes that indicate minimal structural modification upon cycling (low angle XRD is shown in **Figure 5.4**).

and surface Mn oxidation are minimal (**Figure 5.2**). **Figure 5.1D** shows the reversible electrochemistry of $Na_{2-x}Mn_3O_7$ between X = 0 and ~ 0.5 (25% desodiation) over 30 cycles at a C/20 rate between 3.5 V and 4.3 V vs Na/Na^+, where C is 166 $mAh{\cdot}g^{-1}$. The symmetric and overlapping profiles of the differential capacity curve (**Figure 5.1D** inset) further confirms reversibility of the redox process and absence of voltage fade in the voltage plateau region. This plateau has been attributed to de/intercalation of the octahedrally coordinated Na2 ions (**Figure 5.1A**).[13]

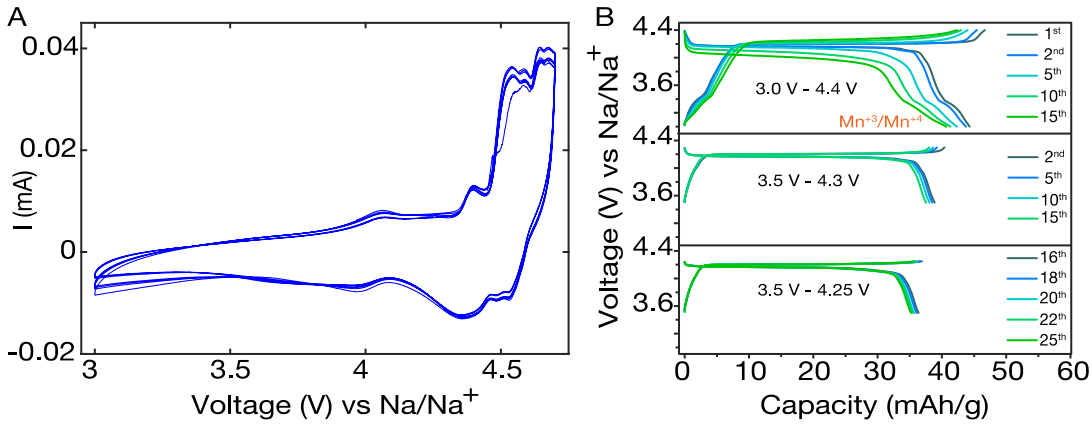

Figure 5.2 Determination of the optimum voltage window for cycling. (A) Cyclic voltammetry study in a coin cell (Na metal as anode, 1M $NaClO_4$ in PC as electrolyte and stainless steel as the counter electrode), showing that the electrolyte significantly degraded above 4.3 V due to side reactions. These reactions are avoided by using 4.3 V as the upper limit; (B) Investigation of reversibility with different voltage cut-off limits. As $Mn^{3+/4+}$ contributes to the capacity below 4.2 V (details are discussed in **Figure 5.7**), an increase in the lower cut off from 3V to 3.5 V enhances performance.

The Na1 ions that occupy trigonal prismatic sites in the layers above and below the Mn vacancies are retained in this process. Importantly, the electrode exhibits a low voltage hysteresis of ~40 mV between charge and discharge, smaller by several factors than that reported in other known Li and Na based anion redox active electrodes.[8–10] The voltage hysteresis remains significantly constant over the Na cell cycling (**Figure 5.3**) indicating that the crystal structure is stable up to 4.3 V with < 0.5 Na remaining in the interlayer gap, unlike other Na layered TM oxides employing high-valent redox, such as α-$NaFeO_2$.[17] Structural stability over repeated redox cycles was further confirmed by synchrotron powder XRD (**Figure 5.1E**) and Mn K-edge EXAFS (**Figure 5.1F**). Especially, the Fourier-transformed EXAFS spectra of Mn reveals a slight increase in the Mn-O bond length (< 2%) upon charge to 4.3 V indicating that the bond order does not change significantly upon desodiation. Likewise, there is negligible change in the pre-edge feature of Mn K-edge X-ray absorption spectrum proving the absence of Mn migration to tetrahedral sites and the stability of the local structure (**Figure 5.4D**). The invariant XRD patterns shown through the 10th cycle in **Figure 5.1E** and **Figure 5.4C** further indicate structural stability that is consistent with previous reports.[12–14]

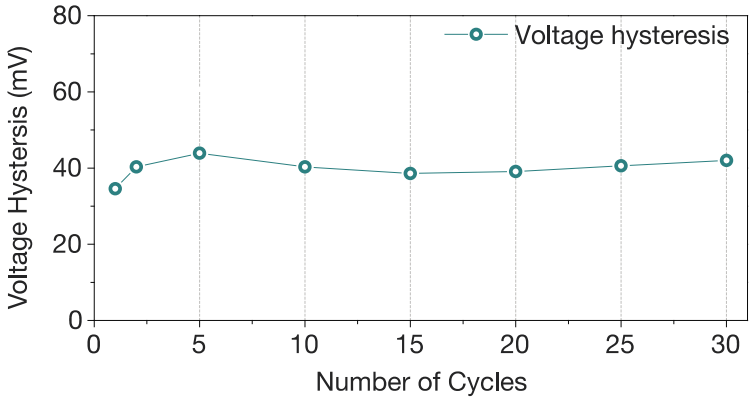

Figure 5.3 Invariant low voltage hysteresis of ~40 mV between charge and discharge over cycling.

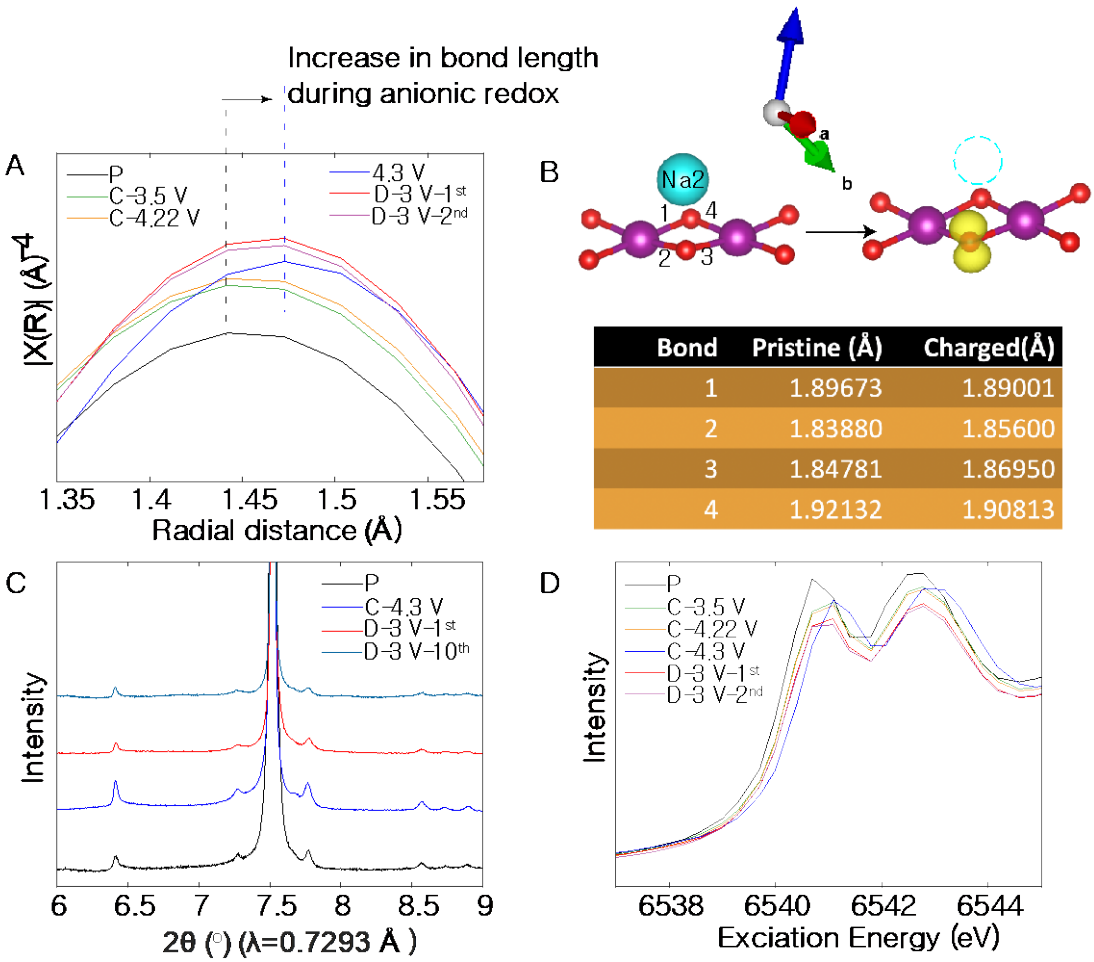

Bond	Pristine (Å)	Charged(Å)
1	1.89673	1.89001
2	1.83880	1.85600
3	1.84781	1.86950
4	1.92132	1.90813

Figure 5.4 Structural stability during anion redox. (A) Zoomed in Fourier transform of the ex-situ EXAFS the pristine material (P) and electrodes charged to 3.5 V, 4.22 V, and 4.3 V in the 1st cycle and discharged to 3 V in the 1st and 2nd cycle (D-3V-1st and D-3V-210th), respectively. The negligible change in the EXAFS profile indicates local stability upon cycling. The bond length of Mn-O increases by only < 2% increase upon charging to 4.3 V. (B) Bond length changes in DFT are consistent with EXAFS. Upon the removal of sodium atoms during charging, the Mn-O bond length near the oxidized oxygen increases. The yellow dumbbells show the localized hole polaron on the oxidized oxygen which are discussed in detail in Figure 5.9. (C) Synchrotron powder X-ray diffraction at low angle (pristine, charged to 4.3 V and discharged to 3 V at 1st and 10th cycle). XRD patterns exhibit negligible changes indicating no structural modification. (D) Pre-edge from Mn-K edge XANES. The pre-edge has negligible changes which indicate local structural stability and lack of Mn migration to tetrahedral site.

5.3.2 Spectroscopic signature of reversible oxygen redox without O-O dimerization

To elucidate the nature of this highly reversible redox couple in $Na_{2-x}Mn_3O_7$, we performed X-ray absorption spectroscopy (XAS) at the O K-edge (**Figure 5.5**) and at the Mn L- and K-edges (**Figure 5.6 and 5.7**). From total electron yield XAS, we confirmed a slight oxidation on the surface where we estimated the Mn oxidation state to change from ~ +3.9 in the pristine state to ~ +4.0 upon charging, **Figure 5.6**. This minimal oxidation contributes to the capacity only up to ~ 4.2 V (in the sloping region of the voltage curve). Both Mn K and L-edge spectra do not change during the voltage plateau. Rather, the plateau capacity at ~ 4.2 V arises from the oxidation of oxygen anions. The O K-edge resonant inelastic x-ray scattering (RIXS) map, **Figure 5.5A**, shows the emergence of a new feature at an excitation energy of ~ 527.5 eV upon charging, which disappears on discharge. This new feature also appears in the XAS at the same energy as shown in **Figure 5.5B**. The lack of change in the Mn K-edge (**Figure 5.7**) indicates that bulk Mn redox does not contribute to the capacity. Crucially, the oxygen redox feature remains largely constant in magnitude and reproducible between 1st and 10th cycle (**Figure 5.5C**), directly confirming the reversibility of this oxygen redox couple. Upon deep desodiation up to 4.7V (50% desodiation) (**Figure 5.5D**), we observed increase in the intensity of the ~527.5 eV peak, unlike previous reports.[14]

The spectroscopic signature of oxygen redox in $Na_{2-x}Mn_3O_7$ is distinct from a vast majority of known anion-redox-active electrodes. For example, Li-rich NMC,[9] $Li_{2-x}Ir_{1-y}Sn_yO_3$,[6] and $Na_{0.75}Li_{0.25}Mn_{0.75}O_2$ [8] share the same spectroscopic signature in XAS or RIXS (~531 eV feature in XAS or a sharp feature at 531 eV excitation energy and 523 eV emission energy in RIXS, **Figure 5.5A** for NMC). As can be seen in **Figure 5.5D and E**, such a feature is absent in $Na_{2-x}Mn_3O_7$. In electrodes with a 523 eV emission energy feature, the substantial structural disorder and large voltage hysteresis upon anion redox has been linked to the formation of ~ 1.5 Å O-O dimers, which was proposed

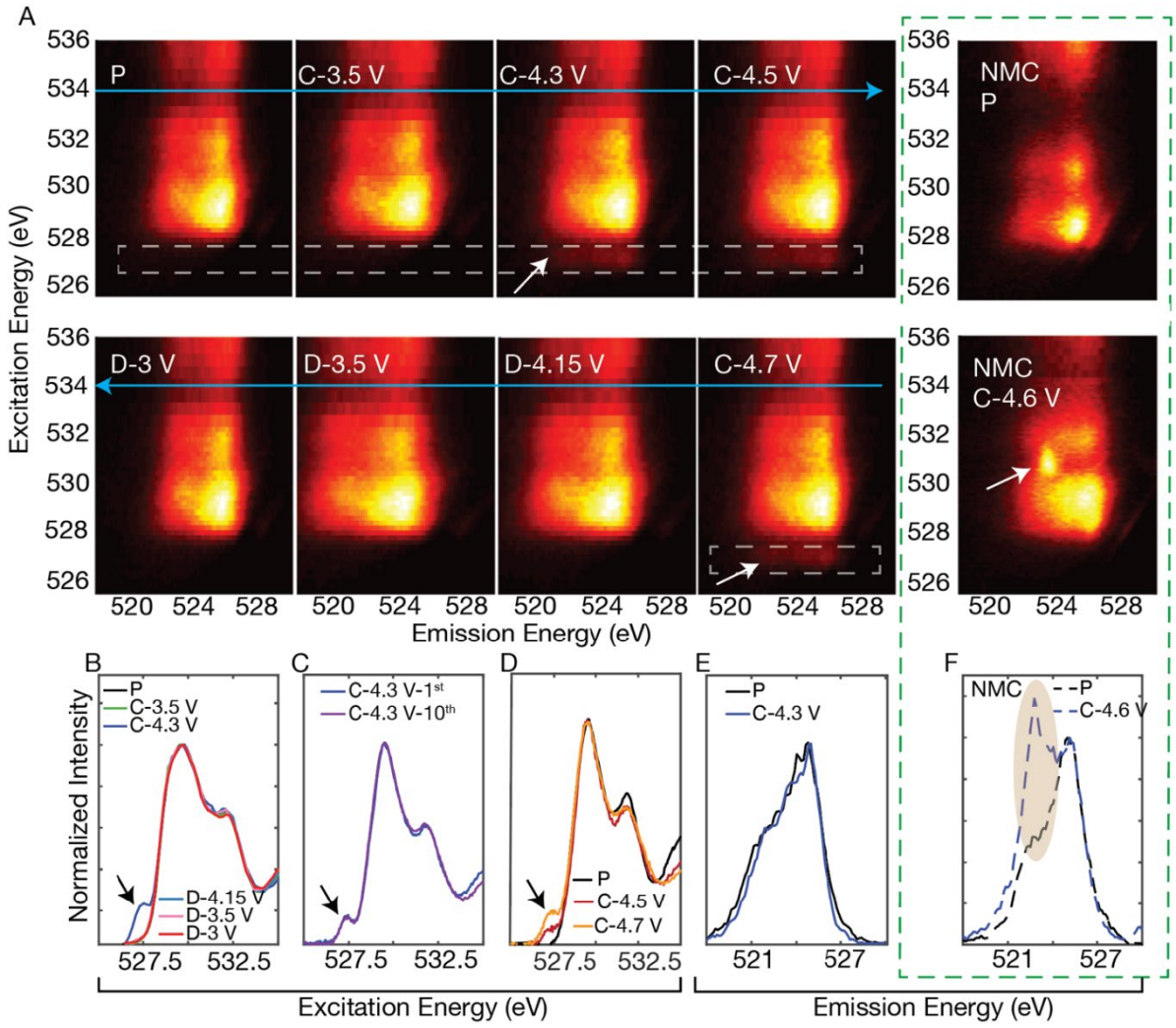

Figure 5.5 Oxygen-redox in $Na_{2-x}Mn_3O_7$. (A) O K-edge RIXS maps of $Na_{2-x}Mn_3O_7$ from pristine to 4.7 V during charging (P to C-4.7 V) and from 4.15 V to 3 V during discharging in the bottom panel (D-4.15 V to D-3 V). The anion-redox feature emerges at an excitation energy of ~527.5 eV upon charging (4.3-4.7V) as indicated by the white arrow. O K-edge RIXS maps of pristine and charged LR-NMC are also shown for comparison (NMC-P and NMC-4.6 V). The anion-redox feature emerges at an excitation energy of ~531 eV upon charging (4.6 V) as indicated by the white arrow. All maps are taken during the first cycle. (B) O K-edge XAS spectra of $Na_{2-x}Mn_3O_7$, taken at the same voltage conditions as in panel A, showing the emergence of the peak at ~ 527.5 eV. (C) Comparison of the O K-edge XAS after charging (4.3 V) for the 1st and the 10th cycle. The normalized intensity of the ~527.5 eV feature is equivalent for the two spectra, indicating the stability of the anion redox mechanism. (D) O K-edge XAS of $Na_{2-x}Mn_3O_7$ from pristine to 4.7 V during charging (P to C-4.7 V). The increase in the intensity of the 527.5 eV peak when charging between 4.5 V and 4.7 V indicates that anion redox with similar mechanism takes place on the ~ 4.3 V and ~ 4.5 V plateau. Emission spectra obtained by integrating

the RIXS maps along a cut at ~531 eV excitation energy to investigate the presence of O-O dimers in $Na_{2-x}Mn_3O_7$ (E) & NMC (F). A peak at 523 eV (shaded region) from such a line cut has been assigned previously to O-O dimer formation.[6,9] The absence of this peak in $Na_{2-x}Mn_3O_7$ indicates a lack of dimer formation.

through comparison with a library of peroxide reference compounds using RIXS[1] and Raman spectroscopy though the precise speciation is still under debate.[18–20] The absence of a peak at ~ 800 cm^{-1} [1] in the Raman spectrum of $Na_{2-x}Mn_3O_7$ (**Figure 5.8**) indeed shows that 1.5 Å O-O peroxo moieties do not form.[18] It should be noted that $Na_{0.6}Li_{0.2}Mn_{0.8}O_2$ [8] exhibits both the RIXS feature corresponding to O-O as well as the feature at an excitation energy of 527.5 eV observed in this work. However, as it would be expected in an electrode material exhibiting oxygen dimerization, the material exhibits a large voltage hysteresis and significant voltage fade over the Na cell cycling.

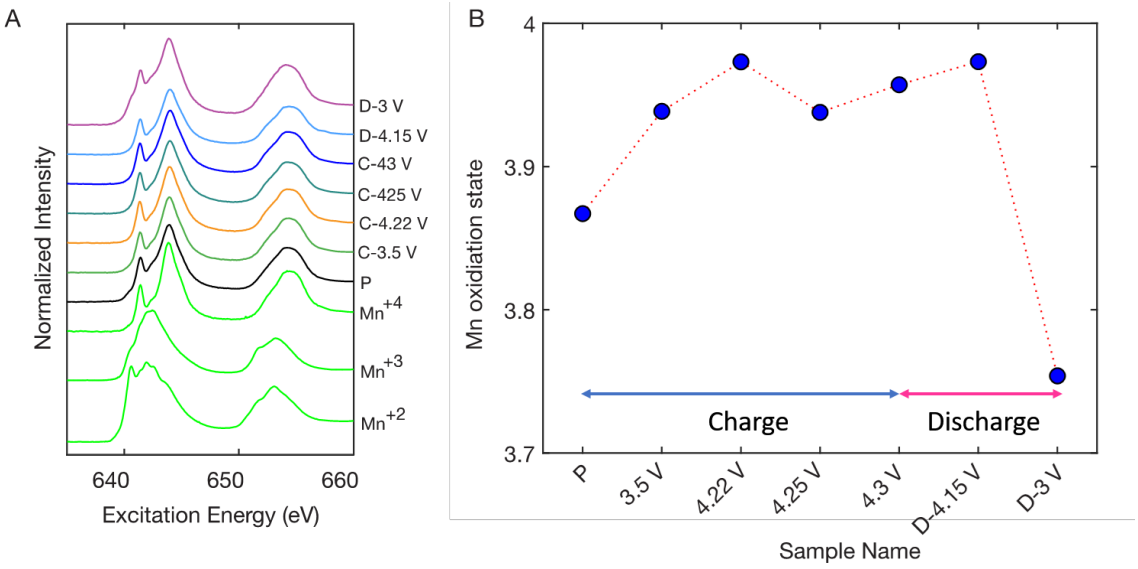

Figure 5.6 Surface oxidation of Mn < 4.2 V. (A) Mn L-edge XAS data measured by total electron yield mode. The green spectra are for reference compounds with Mn^{2+} (MnO), Mn^{3+} (Mn_3O_4) and Mn^{4+} ($Li_{1.17}Ni_{0.21}Co_{0.08}Mn_{0.54}O_2$). By linear combination fitting we estimated the Mn oxidiation state in

pristine $Na_2Mn_3O_7$ and changes upon charging (B). Mn oxidized mostly from pristine to ~ 4.2 V upon charging.

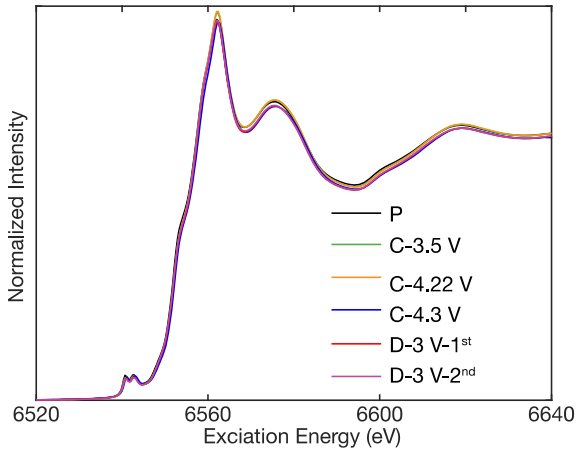

Figure 5.7 Mn-K edge of $Na_2Mn_3O_7$. Upon cycling, the shift in the Mn K-edge is negligible indicating that bulk Mn redox does not contribute to capacity.

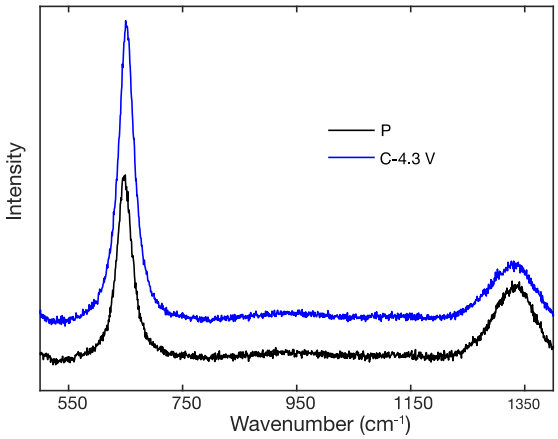

Figure 5.8 Raman spectroscopy and absence of O-O dimer formation. A Raman peak at ~800 cm^{-1} has been assigned to the formation of O-O dimer.[1, 21]. The absence of this peak in $Na_2Mn_3O_7$ confirms O-O dimer formation does not occur.

Next, we performed *ab-inito* calculations using density-functional theory (DFT) with a Heyd–Scuseria–Ernzerhof (HSE) functional, the most accurate functional for the ground state, and the Bethe-Salpeter Equation (BSE), a state-of-the art method for the excited state to understand the spectroscopic signature and energetic stability of oxidized oxide species. While it is challenging to employ first-principles calculations to identify the lowest energy structure of disordered materials (especially in the oxidized state), $Na_{2-x}Mn_3O_7$'s structural robustness against disordering makes it ideal for accurate first-principles analysis. **Figure 5.9A** shows a schematic top view of the pristine structure (sodium atoms colored cyan), with the corresponding density-of-states (DOS) shown in **Figure 5.9B**. The two oxygen sublattices, "O1" and "O2" (**Figure 5.1A**) exhibit a very different contribution to the DOS. Close to the Fermi level, the relative atomic contribution to the density-of-states follows the order O1 > Mn > O2 indicating that desodiation involves the preferential participation of the O1 species for anion redox.

We simulated desodiated $NaMn_3O_7$ in the ground state by removing Na from the octahedral sites, and examined multiple configurations with holes localized on O1 and O2. Localized holes on O2 sites could not be realized following DFT self-consistent field iterations, suggesting that such a configuration is not a metastable state of the desodiated system. Instead, we find holes are localized on the under-coordinated O1 sites that surround the structural Mn vacancy (**Figure 5.9D**). The local environment of O1 satisfies the condition for oxygen redox proposed by D. H. Seo et al.[23] First, we present results on the oxidation of two O1 located on opposite ends of the oxygen network surrounding a Mn vacancy (we term this the third-nearest neighbor, 3NN, configuration). Projected density of states indicates that oxidation localizes and upshifts the O 2p state at the top of the valence state by 1.4 eV (**Figure 5.9E and 5.9F**), confirming that state corresponds to a oxygen hole polaron (O^-). Therefore, we attribute the peak appearing at ~527.5 eV in the O K-edge XAS and RIXS to this localized hole polaron. Further confirmation is provided in the next section. We note that previous studies on this

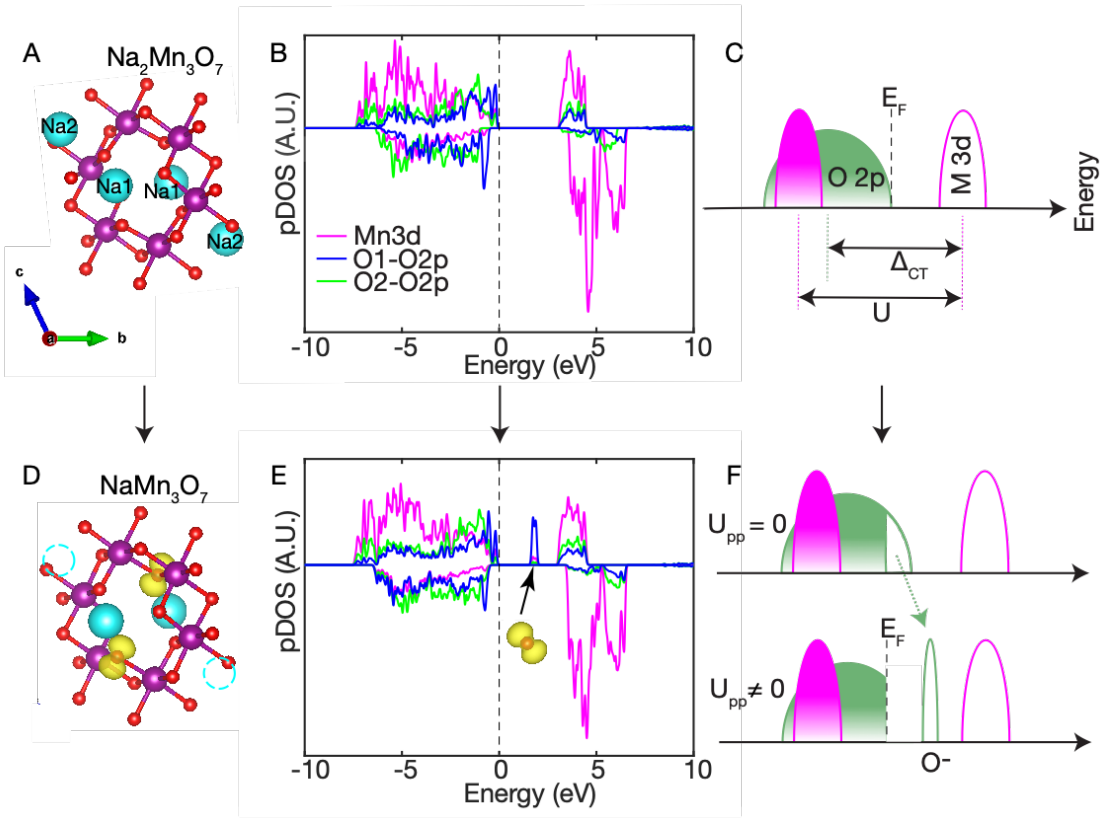

Figure 5.9 Density of states (DOS) of $Na_{2-x}Mn_3O_7$ from DFT. (A) Structure in the pristine state (Na atoms in cyan). (B) Local DOS showing that O-2p states dominate the band near the Fermi level, with O1 oxygen (blue) having a larger contribution to the DOS near the Fermi level than O_2 oxygen (green). (C) Based on the Zaanen–Sawatzky–Allen (ZSA)[22] classification, $Na_{2-x}Mn_3O_7$ is a charge transfer insulator with the oxygen 2p band closer to the Fermi level than the metal (Mn) 3d band. Here, U > ΔCT, where U is the coulomb interaction energy for the Mn 3d electrons and ΔCT is the charge transfer energy. (D) Structure after charging (desodiation, $NaMn_3O_7$), with hole polarons on oxygen (spin density shown in yellow dumbbells), which form on the O1 species near the Na2 vacancy. In this work, the spin density of the hole polarons depicted is calculated over an energy range spanning the single particle level in the band gap associated with the species. (E) Local DOS in the charged (desodiated) state, where hole polarons localize on O1 atoms to form in-gap states. (F) DOS schematic of charged state ($NaMn_3O_7$). Localized hole states form mid-gap states.

electrode material attributed the stability of O holes to hybridization between localized O 2p and Mn "t_{2g}" orbitals, but did not compare the relative energetics of O hole configurations and covalent bonded species.[12]

In order to address the energetic preference of O hole configurations in the charged electrode, for the first step, we theoretically model the O K-edge XAS spectra using BSE method.[24, 25] As shown in **Figure 5.10A** and **5.10B**, the experimentally observed spectra in **Figure 5.5** are well reproduced allowing us to assign the spectral features to O1 and O2. In the pristine material (**Figure 5.10A**), the main XAS peak at 529.5 eV is attributed to equal contributions from O1 (blue) and O2 (green), corresponding to the O1s → (Mn 3d–O 2p*) transitions. However, in the desodiated state (**Figure 5.10B**), the peak ~ 527.0 eV arises from localized hole polarons (O^-) that formed almost exclusively on O1 oxygen sites as shown by the further comparison between **Figure 5.11** and the inset of **Figure 5.10B** at 25% and 50% of desodiation, respectively. In general, these calculation results are in excellent agreement with the experimental XAS and RIXS results, as well as the projected DOS obtained from DFT. We note that holes on oxygen have been proposed in many systems.[8, 12, 23, 26, 27] Intensity changes in the ~531 eV region of the O K edge XAS (i.e. considerably above the absorption onset) are often claimed as evidence of such species, due to presumed large shifts in core level energies arising from the reduced electron density around oxidized O1 anions compared to O^{2-}. However, we have ruled out the presence of major chemical shifts (**Figure 5.12**), and show that localized hole polarons in fact manifest spectroscopically as an intensity at ~ 527.5 eV. X-ray photoemission spectroscopy (XPS) simulation of charged state of $Na_{2-x}Mn_3O_7$ is further performed to estimate the possible chemical shift energy. Based on the simulation, the relative chemical shift of the O-1s core-level on O^- sites is estimated to be approximately 2 eV (**Figure 5.12B**).

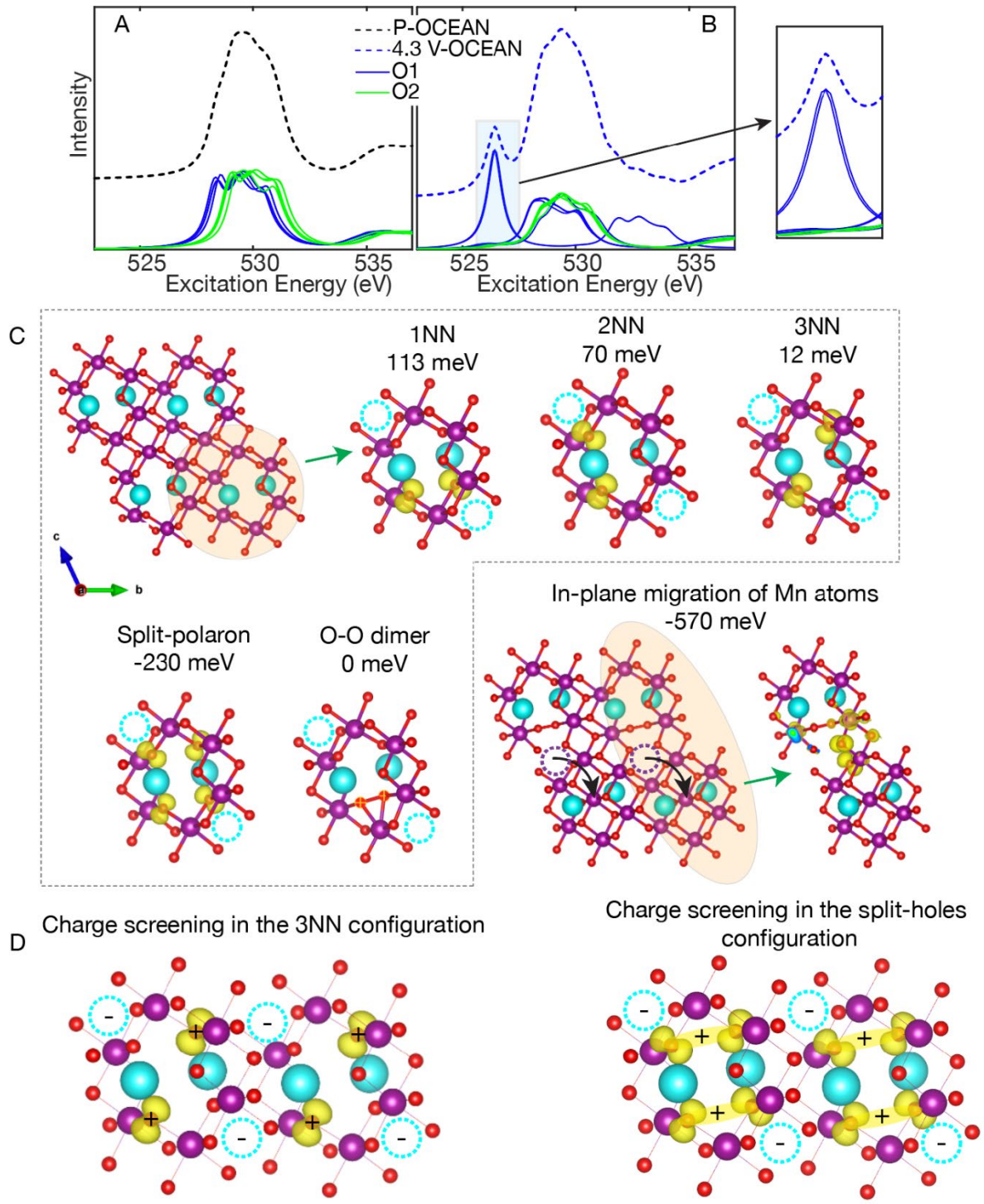

Figure 5.10 Confirmation via XAS simulation of O^{-} species stabilization mechanism. (A) & (B) Simulated O K-edge XAS for pristine and charged samples (50% desodiation, $Na_1Mn_3O_7$), respectively. The dominant peak ~529.5 eV is from both O1 and O2 species; however, the O1 atoms have an out-

weighted contribution to the localized hole polaron which gives rise to the peak at ~527.5 eV. (C) Comparing the energy (per Na atom removed) of different oxygen hole configurations. The split-polaron configuration (where a hole is shared among two O1 atoms) is the most stable configuration compared to first, third nearest neighbor (1NN & 3NN) and peroxo configurations when there is no inplane Mn atom migration. However, the structure with in-plane migration (dotted circles in magenta and black arrow) is the most stable configuration. (D) The mechanism for the hole polarons. The split-polaron configuration provides a stronger screening for the long-range electrostatics between the Na vacancy sites (dotted circles in cyan) compared to the other configuration.

Given that the O^- hole mid-gap state has a single-particle energy that is roughly 1 eV below the conduction band (CB) minimum (**Figure 5.9E**), and taking into account an additional core-excitonic interaction of roughly 1-1.5 eV in XAS, the O^- 1s → 2p (hole) XAS transition is expected to appear as a pre-edge peak near ~527.5 eV while the O^{2-} 1s → CB XAS transitions form the main edge at 529.5 eV. Our results highlight the importance of corroborating ground state DFT calculations with explicit spectroscopic simulation.

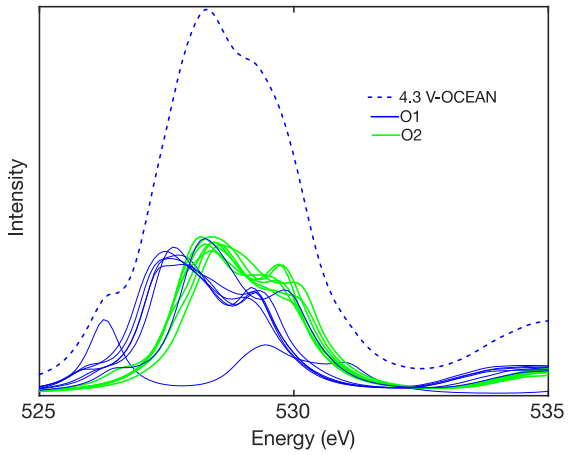

Figure 5.11 Simulated O K-edge XAS of 25% desodiated material ($Na_{1.5}Mn_3O_7$). The simulated XAS spectra of both 25% and 50% (**Figure 5.10B**) desodiated samples have the peak at ~ 527.0 eV (localized hole polarons are formed on both cases).

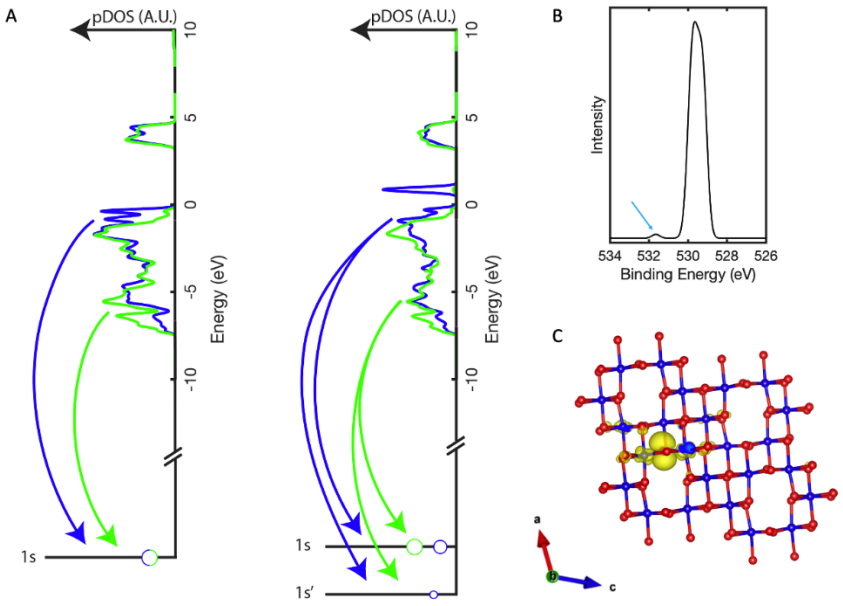

Figure 5.12 Estimating the chemical shift of the core hole. (A) Schematic showing the emission process from the valence band. The chemical shift of 1s electrons on O^- ions to lower 1s' energies relative to O^{2-} is also indicated schematically. (B) X-ray photoemission spectroscopy (XPS) simulation of charged state of $Na_1Mn_3O_7$. The relative chemical shift of the O-1s core-level on O^- sites is estimated to be approximately 2 eV. Given that the O^- hole mid-gap state has a single-particle energy that is roughly 1 eV below the conduction band (CB) minimum, and taking into account an additional core-excitonic interaction of roughly 1-1.5 eV in XAS, the O^- 1s - 2p (hole) XAS transition is expected to appear as a pre-edge at ~527.5 eV near to the O^{2-} 1s CB XAS transitions that form the main edge at ~ 529 eV. (C) Hole polaron formed in the charged state.

Driven by the significant covalent energy, oxygen hole polarons generally form O-O dimers.[4, 5] Previous direct detection of O^- species in metal oxides by electron paramagnetic resonance has been reported only at liquid-helium temperatures after irradiation or chemical doping.[28] Some even argued O^- ions with negligible covalence cannot exist as bulk oxidized species,[29] and indeed there have been incorrect assignments of spectroscopic signals.[8, 12, 26, 27] However, in $Na_{2-x}Mn_3O_7$, we observe the hole polaron XAS signal in the desodiated state for at least after 10 cycles (**Figure 5.5C**). To understand the hole polaron stabilization mechanism, we systematically explored different arrangements involving two

oxygen holes and two Na vacancies. In addition to the 3NN arrangement already considered, we now examine the oxidation of first and second nearest neighbor O1 (1NN and 2NN, respectively). Energetic stability is referenced to the peroxo dimer configuration of 0 eV (**Figure 5.10C**), though more oxidized oxygen could be more stable (which will be discussed later). For the 1NN configuration, it is 0.1 eV (per Na removed) less stable than the peroxo dimer. On the other hand, the 3NN configuration, wherein the two holes are maximally separated facing across the vacancy center, is essentially as stable as the peroxo dimer. Given the highly localized nature of the oxygen holes, the stability of the 3NN relative to 1NN and peroxo dimer is dominated by coulombic interactions. Specifically, the 3NN configuration has a higher degree of symmetry, with the positively-charged oxygen holes providing better charge screening for the negatively-charged Na vacancies (**Figure 5.10D**).

In our calculations, we also identified an unusual split-hole polaron configuration, where a hole is shared among two O1 atoms via a very weak covalent bond (evidenced by the long O-O distance ~ 2.6 Å, as well as by the DOS (**Figure 5.10D and 5.13**). This species can be loosely regarded as O_2^{3-}. This is unusual because cation vacancy bound deep acceptor states in wide gap oxides typically tend to form small polarons with spin density localized on a single O^- site.[30] We found that the split-hole configuration is the most stable: 0.23 eV (per Na removed) more stable than peroxo dimers and 3NN when no in-plane migration is considered. The explanation for this surprising stability lies in the selective removal of Na ions at the Na2 octahedral sites. Recall that Na ions at Na1 are not extracted during the 4.25 V plateau.[13] The positively charged holes are bound by coulombic forces to the negatively charged Na2 vacancy site. In the case of the split-hole polaron, a hole density is shared among two oxygen atoms and the oxidized O1 comes closer to the Na vacancy than in the 3NN configuration (**Figure 5.10D**).

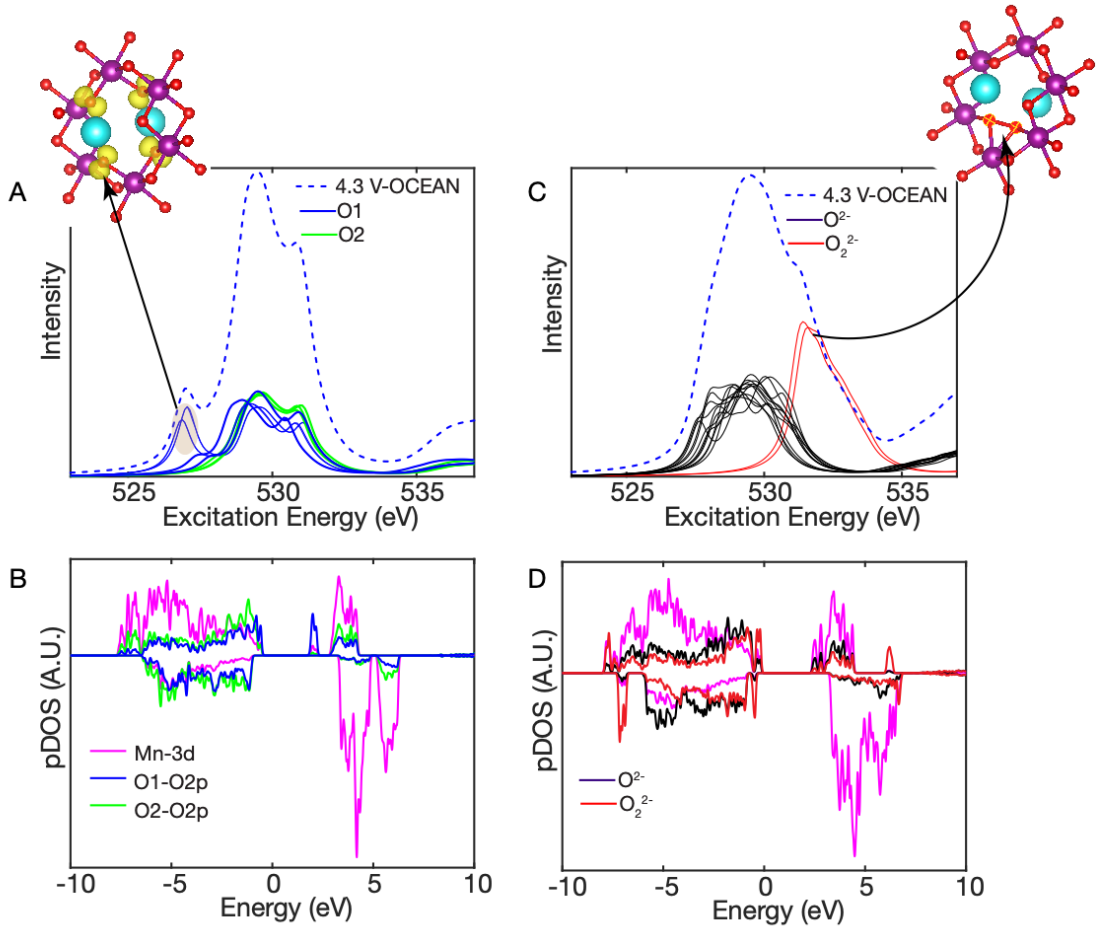

Figure 5.13 XAS simulation and density of states of different hole configurations ($NaMn_3O_7$). XAS simulation (A) and DFT DOS calculations (B) of the split-hole polaron configuration. The four O1 sites holes reside on have overlapping XAS contributions that give rise to the 527.5 eV peak as indicated by the shaded region in (A). XAS simulations for the 3NN (**Figure 5.10B**) and split-hole polaron configurations give similar spectroscopic signatures (peak near 527.5 eV). XAS simulation (C) and DFT DOS calculations (D) of a peroxo bi-polaron with 1.44 Å O-O distance. The peroxo oxygens (marked with yellow crosshair on the desodiated structure) exhibit large spectral weight peaked at 531 eV confirming the experimentally observed[1, 6, 9] at 531 eV feature in RIXS and XAS is indeed from the peroxo dimer.

The energy lowering via coulombic attraction in this state comes at the cost of some electron-lattice strain energy and exchange energy which tends to favor localization on an O1 site as in the 3NN case. We note that the XAS simulation for 3NN and split oxygen-hole polarons give similar spectroscopic signatures (peak ~ 527.5 eV). Therefore, we cannot distinguish the two types of polarons within our spectroscopy simulation accuracy limits. Nonetheless, both configurations are predicted to be as or more stable than the peroxo dimer, which likely explains the complete absence of the latter and the minimal hysteresis. To confirm the crucial role of coulombic interaction in stabilizing the oxygen hole polaron, we investigated several other extent and configuration of desodiation. Even at 25% desodiation, for an ordered Na2 vacancy arrangement, the split-hole polaron is predicted to be more stable than the localized hole by 0.3 eV. The situation is different, however, in the case of desodiating prismatic Na1 sites that sit on top of the Mn vacancy (**Figure 5.14**). In this case, no split-hole polaron is predicted and a 3NN configuration wherein each hole localizes on an O1 site closest to one of the Na1 vacancies is stabilized. While Na1 desodiation is overall energetically unfavorable, the hole density distribution is consistent with an electrostatically driven mechanism (**Figure 5.14**).

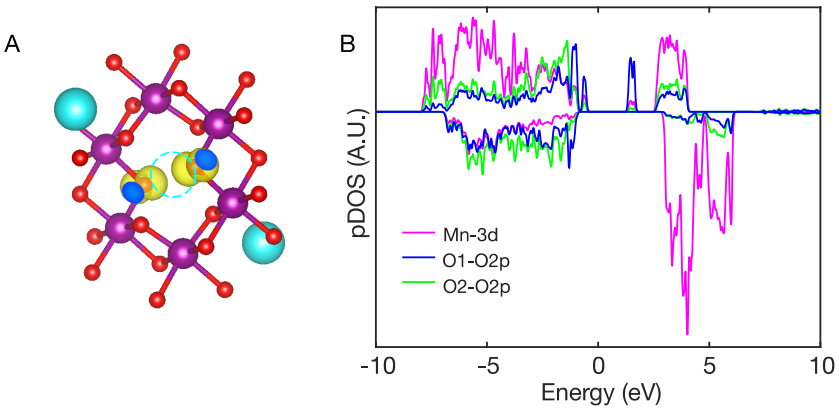

Figure 5.14 Structure and density of states after removing Na ions in prismatic sites (Na1) up on charging ($NaMn_3O_7$). The 3NN configuration is the most stable configuration (A) and its density of state is shown in (B).

At different states of desodiation, the Na2 vacancies can be disordered in the material and different Mn vacancy sites can locally experience variations in sodium vacancy ordering. Nevertheless, since electrostatic forces in this material favor keeping hole densities separated, the O-O dimer configuration will continue to be relatively disfavored. Even in the presence of Na2 vacancy inhomogeneity, we expect Mn vacancy sites overall to support a distribution of the split-hole and localized O^{-} hole configurations.

Recently, Bruce and colleagues suggested a new redox mechanism to describe anion redox materials with high voltage hysteresis.[7, 8] The mechanism involves in-plane TM migration and formation of O-O dimer with a bond length of ~ 1.2 Å. We explored this possibility in 50% desodiation of $Na_{2-x}Mn_3O_7$ as shown in **Figure 5.10C** and found that such configuration is more stable than split-hole polaron. Our observation of disappeared hole polaron XAS feature after more than 2 days from electrode harvesting also supports the calculation result indicating the formation of O-O dimer (**Figure 5.15**).

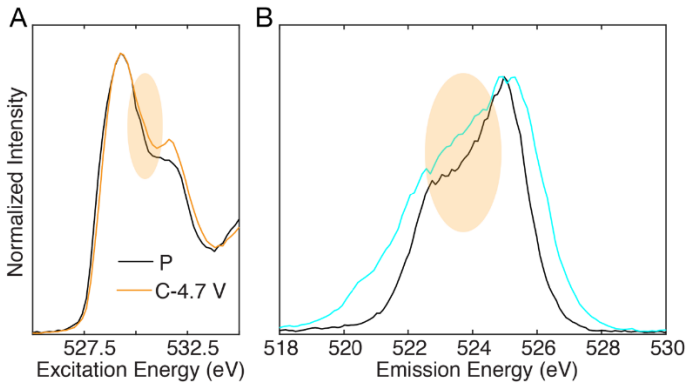

Figure 5.15 O-O dimer formation after 2 days of electrode harvesting. (A) The XAS hole polaron feature disappears after 2 days of electrode harvesting and a new peak emerges ~531 eV (shaded region). (B) RIXS spectra at 531 eV excitation energy. A new peak ~523 eV emission energy. These features in XAS and RIXS indicate formation of O-O dimer 2 days after electrode harvesting

A previous EPR study showed that hyperfine lines, which are related to the oxidized oxygen species in charged $Na_{2-x}Mn_3O_7$, disappeared after 7 days, also suggesting that the paramagnetic hole polarons ultimately form a diamagnetic O-O dimer.[13] These observations indicate that hole polarons in this material could have a substantial, but finite lifetime, potentially explaining why previous XAS reports on $Na_{2-x}Mn_3O_7$ did not observe the peak at 527.5 eV. However, here we have shown that holes can reversibly dis/appear during dis/charge for several cycles (**Figure 5.5B and C**), as fresh hole polarons, created every cycle, do not dimerize on the time scale of our cycling condition (C/20), which is less than 48 hrs per cycle. Therefore, redox-structure decoupling and the exceptional reversibility remain possible in $Na_{2-x}Mn_3O_7$, since O-O dimers do not form during cycling, unlike other anion redox active materials, possibly because of the effective polaron trapping and high migration barrier. Future work will investigate the stability of the hole polaron in the desodiated state.

5.4 Conclusions

Design rules for high-valent redox in intercalation electrode materials have evolved by tuning (1) covalent bonding and (2) local structural distortion. Our combined experimental and theoretical investigation on $Na_{2-x}Mn_3O_7$ shows that coulombic interaction is a crucial third contributor to the overall redox energetics. In this system, significant coulombic interaction between oxygen hole polarons and the adjacent negatively charged Na vacancy, which occurs over several atomic distances, is sufficiently large to disfavor O-O dimerization within individual Mn vacancy sites. These species likely dominate systems where cation migration is inhibited during high-valent redox. Coulombic interaction also rationalize previous hypotheses and computational predictions of partially oxidized, long (> 2 Å) O-O dimers with negligible TM hybridization forming during oxygen redox.[4] We suggest that tuning the in-plane cation-vacancy ordering, residual alkali content, and stacking order are means to control such coulombic effects and offer the possibility to accommodate a higher hole polaron

participation. This eventually tunes the redox chemistry and oxidized species in layered positive electrode materials to give rise to low voltage hysteresis where cation disorder/migration is suppressed. The general concept of employing coulombic interactions to tune high valent redox chemistry can be extended to other structural motifs such as twists[31] and gating.[32] This approach could lead to new compositions and structures with improved stability in a highly oxidized state, which has applications in energy storage and beyond.

References

1. W. E. Gent, I. I. Abate, W. L. Yang, L. F. Nazar and W. C. Chueh, *Joule*, 2020, **4**, 1369-1397.
2. M. Sathiya, G. Rousse, K. Ramesha, C. P. Laisa, H. Vezin, M. T. Sougrati, M. L. Doublet, D. Foix, D. Gonbeau, W. Walker, A. S. Prakash, M. Ben Hassine, L. Dupont and J. M. Tarascon, *Nat Mater*, 2013, **12**, 827-835.
3. G. Assat and J. M. Tarascon, *Nat Energy*, 2018, **3**, 373-386.
4. M. Ben Yahia, J. Vergnet, M. Saubanere and M. L. Doublet, *Nat Mater*, 2019, **18**, 496-502.
5. H. R. Chen and M. S. Islam, *Chem Mater*, 2016, **28**, 6656-6663.
6. J. Hong, W. E. Gent, P. Xiao, K. Lim, D. H. Seo, J. Wu, P. M. Csernica, C. J. Takacs, D. Nordlund, C. J. Sun, K. H. Stone, D. Passarello, W. L. Yang, D. Prendergast, G. Ceder, M. F. Toney and W. C. Chueh, *Nat Mater*, 2019, **18**, 256-265.
7. R. A. House, G. J. Rees, M. A. Perez-Osorio, J. J. Marie, E. Boivin, A. W. Robertson, A. Nag, M. Garcia-Fernandez, K. J. Zhou and P. G. Bruce, *Nat Energy*, 2020, **5**, 777-785.
8. R. A. House, U. Maitra, M. A. P?rez-Osorio, J. G. Lozano, L. Jin, J. W. Somerville, L. C. Duda, A. Nag, A. Walters, K. J. Zhou, M. R. Roberts and P. G. Bruce, *Nature*, 2020, **577**, 502-508.
9. W. E. Gent, K. Lim, Y. F. Liang, Q. H. Li, T. Barnes, S. J. Ahn, K. H. Stone, M. McIntire, J. Y. Hong, J. H. Song, Y. Y. Li, A. Mehta, S. Ermon, T. Tyliszczak, D. Kilcoyne, D. Vine, J. H. Park, S. K. Doo, M. F. Toney, W. L. Yang, D. Prendergast and W. C. Chueh, *Nat Commun*, 2017, **8**, 2091.
10. G. Assat, S. L. Glazier, C. Delacourt and J. M. Tarascon, *Nat Energy*, 2019, **4**, 647-656.
11. D. Eum, B. Kim, S. J. Kim, H. Park, J. P. Wu, S. P. Cho, G. Yoon, M. H. Lee, S. K. Jung, W. L. Yang, W. M. Seong, K. Ku, O. Tamwattana, S. K. Park, I. Hwang and K. Kang, *Nat Mater*, 2020, **19**, 419.
12. B. M. de Boisse, S. Nishimura, E. Watanabe, L. Lander, A. Tsuchimoto, J. Kikkawa, E. Kobayashi, D. Asakura, M. Okubo and A. Yamada, *Adv Energy Mater*, 2018, **8**, 1800409.
13. B. H. Song, M. X. Tang, E. Y. Hu, O. J. Borkiewicz, K. M. Wiaderek, Y. M. Zhang, N. D. Phillip, X. M. Liu, Z. Shadike, C. Li, L. K. Song, Y. Y. Hu, M. F. Chi, G. M. Veith, X. Q. Yang, J. Liu, J. Nanda, K. Page and A. Huq, *Chem Mater*, 2019, **31**, 3756-3765.
14. Y. J. Li, X. F. Wang, Y. R. Gao, Q. H. Zhang, G. Q. Tan, Q. Y. Kong, S. M. Bak, G. Lu, X. Q. Yang, L. Gu, J. Lu, K. Amine, Z. X. Wang and L. Q. Chen, *Adv Energy Mater*, 2019, **9**, 1803087.
15. E. Adamczyk and V. Pralong, *Chem Mater*, 2017, **29**, 4645-4648.

16. G. Assat, C. Delacourt, D. A. Dalla Corte and J. M. Tarascon, *J Electrochem Soc*, 2016, **163**, A2965-A2976.
17. N. Yabuuchi, H. Yoshida and S. Komaba, *Electrochemistry*, 2012, **80**, 716-719.
18. Y. Qiao, S. H. Guo, K. Zhu, P. Liu, X. Li, K. Z. Jiang, C. J. Sun, M. W. Chen and H. S. Zhou, *Energ Environ Sci*, 2018, **11**, 299-305.
19. X. Li, Y. Qiao, S. H. Guo, Z. M. Xu, H. Zhu, X. Y. Zhang, Y. Yuan, P. He, M. Ishida and H. S. Zhou, *Adv Mater*, 2018, **30**, 1705197.
20. Z. Q. Zhuo, Y. S. Liu, J. H. Guo, Y. D. Chuang, F. Pan and W. L. Yang, *J Phys Chem Lett*, 2020, **11**, 2618-2623.
21. P. Mori-Sanchez, A. J. Cohen and W. T. Yang, *Phys Rev Lett*, 2008, **100**, 146401.
22. J. Zaanen, G. A. Sawatzky and J. W. Allen, *Phys Rev Lett*, 1985, **55**, 418-421.
23. D. H. Seo, J. Lee, A. Urban, R. Malik, S. Kang and G. Ceder, *Nat Chem*, 2016, **8**, 692-697.
24. E. L. Shirley, *J Electron Spectrosc*, 2000, **110**, 305-321.
25. J. Vinson, T. Jach, M. Muller, R. Unterumsberger and B. Beckhoff, *Phys Rev B*, 2016, **94**, 035163.
26. U. Maitra, R. A. House, J. Somerville, N. Tapia-Ruiz, J. G. Lozano, N. Guerrini, R. Hao, K. Luo, L. Y. Jin, M. A. Perez-Osorio, F. Massel, D. M. Pickup, S. Ramos, X. Y. Lu, D. E. McNally, A. V. Chadwick, F. Giustino, T. Schmitt, L. C. Duda, M. R. Roberts and P. G. Bruce, *Nat Chem*, 2018, **10**, 288-295.
27. K. Luo, M. R. Roberts, R. Hao, N. Guerrini, D. M. Pickup, Y. S. Liu, K. Edstrom, J. H. Guo, A. V. Chadwick, L. C. Duda and P. G. Bruce, *Nat Chem*, 2016, **8**, 684-691.
28. O. F. Schirmer, *J Phys-Condens Mat*, 2006, **18**, R667-R704.
29. M. D. Radin, J. Vinckeviciute, R. Seshadri and A. Vander Ven, *Nat Energy*, 2019, **4**, 639-646.
30. S. Lany and A. Zunger, *Phys Rev B*, 2009, **80**, 085202.
31. S. Y. Yang, D. Prendergast and J. B. Neaton, *Nano Lett*, 2012, **12**, 383-388.
32. T. Ohta, J. T. Robinson, P. J. Feibelman, A. Bostwick, E. Rotenberg and T. E. Beechem, *Phys Rev Lett*, 2012, **109**, 186807.

Chapter 6

A 4 V class Polyanion-type Na ion Intercalation Cathode Material for Na-Ion Batteries

6.1 Introduction

The need for high performance electrochemical energy storage devices is growing overwhelmingly every year. This demand has propelled intense research efforts to build better battery systems and has revived some previously neglected chemistries such as sodium-ion batteries (NIBs).[1–3] Lithium ion batteries (LIBs) are ubiquitous in applications constrained by mass and volume, i.e., portable electronic devices and electric vehicles.[4–7] For stationary energy storage, however, earth abundant and low cost NIBs offer important sustainability and cost-effectiveness.[8–10] While sodium is heavier than lithium (which renders the cathode a slightly lower gravimetric capacity), it lends itself to different chemistries. In this regard, NIBs can be advantageous over their LIB counterparts.[11,12] Moreover, since the redox potential of sodium (- 2.73 V vs the standard hydrogen electrode) is only 0.3 V higher than lithium, the energy penalty to pay is small. The voltage and capacity of the positive host (cathode) material is the major determinant of the specific energy. Therefore, in parallel to LIBs, a large thrust in NIB research has been in identifying and developing new cathode hosts. Many different Na-ion analogues of classic Li-ion hosts have been explored. Distinct structural and electrochemical differences have emerged that are largely attributable to the larger size of the Na^+ ion.[13,14] Advances in Na-ion intercalation host materials based on oxides including $NaNi_{1/3}Mn_{1/3}Co_{1/3}O_2$, P2-$Na_{0.67}Mn_{0.5}Fe_{0.5}O_2$, and β-$NaMnO_2$ have been realized.[12,15,16] Breakthroughs have been reported with novel polyanionic materials such as $Na_{1.5}VPO_{4.8}F_{0.7}$ and $Na_2Fe_2(SO_4)_3$.[17,18] These latter two materials

exhibit a remarkably high redox potential of 3.8 V versus Na for $V^{5+}/V^{3.8+}$ and Fe^{3+}/Fe^{2+} redox, respectively. In fact, compared to layered oxides, polyanionic materials often present better structural and thermal stability, a flatter voltage response upon Na-(de) intercalation and better capacity retention.[19] In the pursuit of high capacity and high voltage cathodes, studies have focused on transition metals capable of multiple electron redox. Their redox potential can be tuned by altering the polyanionic group - for example, replacing PO_4^{3-} with the more electron withdrawing SO_4^{2-} moitié raises the voltage. The latter approach has been heavily exploited for the Fe^{2+}/Fe^{3+} redox couple. It has not been typically utilized for the $Co^{2+/3+}$ or $Ni^{2+/4+}$ couples, however, because their redox voltages already lie above the upper stability window of liquid organic electrolytes (≈ 4.3 V vs Na/Na^+ with a passivated cathode). For example, the $Co^{2+/3+}$ redox couple is close to 5 V for PO_4^{3-} based polyanion cathodes.[19–25] As a result, low discharge capacities are exhibited (< 50 $mA{\cdot}g^{-1}$). While cobalt is not an ideal choice for the redox center for NIBs because of its high cost, this metal has been explored in combination with a variety of polyanions - including the less withdrawing $[SiO_4]^{4-}$ moitié - in an attempt to find a compromise between voltage and electrolyte stability. For example, Na_2CoSiO_4 exhibits a high reversible capacity of 100 $mA{\cdot}g^{-1}$, but at a moderate voltage of 3.3 V versus Na/Na^+.[23] Alternatively, $NaCo(PO_3)_3$ and $NaCoP_2O_7$ show higher redox potentials between 3.5 and 3.7 V, but exhibit low discharge capacities of only 35 and 38 mA $h{\cdot}g^{-1}$, respectively.[21,24] In $Na_4Co_3(PO_4)_2P_2O_7$, the $Co^{2+/3+}$ redox couple is reported to be over 4.75 V (with an initial discharge capacity of ≈ 90 $mA{\cdot}g^{-1}$) but this high redox potential induces electrolyte decomposition.[20]

6.2 Experimental Details

6.2.1 Materials Synthesis

Nanostructured $Na_2Co_2(SeO_3)_3$ and the $Na_2Co_2(SeO_3)_3$–GO composites were prepared by employing a rapid and scalable microwave hydrothermal method. Water interacts strongly with

microwave irradiation through a dipole-microwave interaction, which leads to local superheated regions in the reaction media. While typical hydrothermal methods involve slow heating via a convection mechanism, microwave irradiation of the entire reaction media triggers rapid nucleation leading to more homogeneous particles. For the synthesis of $Na_2Co_2(SeO_3)_3$, a stoichiometric mixture of Na_2SeO_3 (99.8%, Sigma Aldrich) and anhydrous $CoCl_2$ (Purum p.a., ≥ 98.0% (KT), Sigma Aldrich) was dissolved in deionized (DI) water to give a total material concentration of 1 mol/L. An over-stoichiometric amount of Na_2SeO_3 was used to yield a pH of ≈10, and an equal volume of acetonitrile was added to this solution. The resultant mixture was placed in Teflon vessels, which were fitted to a rotor equipped with temperature and pressure sensors and placed in an Anton Parr microwave synthesis system (Synthos 3000). The system temperature was raised to 150 °C in 15 min and maintained for 30 min while the reaction mixture was magnetically stirred. The as-synthesized product was thoroughly washed with DI water, followed by a small volume of ethanol, and dried at 100 °C for 24 h. The same protocol was applied for the synthesis of the $Na_2Co_2(SeO_3)_3$-GO composite, where a 5 wt% GO suspension (prepared by the Hummers method) in water was used as the GO source.[26]

6.2.2 Operando X-ray Diffraction

Operando X-Ray Diffraction (XRD): Operando XRD experiments were conducted using a homemade cell mounted on a PANalytical Empyrean diffractometer. The diffraction patterns were collected in Bragg–Brentano geometry using Cu-Kα radiation and a PIXcel detector with a Ni Kβ filter. The operando cell was cycled at a rate of C/20 with an XRD pattern collection time of ≈ 30 min. The evolution of lattice parameters during charge/discharge was determined by means of Le Bail fitting of the patterns.

6.2.3 Electrochemistry

Electrochemical properties of the materials were evaluated in 2325 coin cells using Na metal as the counter electrode. Coin cell assembly was performed inside a glove box under argon (O_2 and H_2O < 0.1 ppm). For electrode fabrication, the $Na_2Co_2(SeO_3)_3$-GO composite was mixed with carbon black and polyvinylidene fluoride (average Mw ≈ 534 000, Sigma Aldrich) to achieve a final weight ratio of active material: carbon: binder in the cathode of 70:25:5. The weight of GO in the composite was taken into account for this formulation. The mixture was suspended in N-methyl-2-pyrrolidinone (99.5%, Sigma Aldrich) to obtain a viscous slurry, which was cast on aluminum foil with a typical loading of 4 - 5 mg·cm^{-2}. Electrodes of 1 cm^2 geometric area were punched and dried at 120 °C in a vacuum oven. A mixture of 1 m sodium hexafluorophosphate (≥ 98%, Alfa Aesar; dried for 24 h at 120 °C in a glass oven under dynamic vacuum) in propylene carbonate (BASF, 99.98%), and ethylene carbonate (BASF, 99.98%) in a ratio of 1:1 (by volume) was used as the electrolyte. The electrodes were separated by glass fiber separators (Merck Millipore), which were dried at 300 °C for 24 h under dynamic vacuum prior to use. Galvanostatic cycling and cyclovoltammetry tests were conducted at room temperature within a potential window of 1.0 - 4.5 V (vs Na/Na$^+$) using an MPG-2 (Bio-Logic) battery tester.

6.2.4 Electrochemical Impedance Spectroscopy (EIS) and Ionic Conductivity

The $Na_2Co_2(SeO_3)_3$ powder was pressed into a pellet of 0.92 mm in thickness and 11.27 mm in diameter using an uniaxial Carver press under a pressure of 6 ton·cm^{-2}. A silver conductive paste was applied to both sides of the pellet before mounting it in a symmetric Swagelok-type cell. The bulk resistance of the pellet was measured using two-probe ac impedance spectroscopy (VMP3, Bio-Logic) in a frequency range of 1 MHz to 10 mHz using a potentiostatic signal perturbation of 200 mV. Impedance spectroscopy data were recorded in a temperature range of 25 to 170 °C. Bulk ionic conductivities at different temperatures were obtained by fitting the Nyquist plot using EC-lab Z-fit

analysis software. The E_a for Na-ion migration was obtained by linear fitting of the ionic conductivity values at different temperatures by applying the Arrhenius equation, modified to include a temperature dependent pre-exponential: $\sigma T = \sigma_0 \exp(-E_a/k_bT)$, where σ is the temperature dependent ionic conductivity, σ_0 is the ionic conductivity at absolute zero temperature, E_a is the activation energy of ion migration, and k_b and T have their usual meanings.

6.3 Result and Discussion

6.3.1 Synthesis and Physiochemical Characterization

Even though transition metal selenites (SeO_3^{2-} containing compounds) are less prone to thermal decomposition than sulfates, they are not as stable as transition metal oxides or polyanionic compounds containing PO_4^{3-} or SiO_4^{4-} anions.[27,28] Therefore, selenites are normally synthesized via low temperature hydro-/solvothermal routes, which require prolonged heat treatment and a mineralizer for better phase purity and crystallinity.[29–32] Here, by employing a microwave heat treatment, we achieved an ultrafast (30 min) and scalable hydrothermal approach for the synthesis of crystalline-nanosized $Na_2Co_2(SeO_3)_3$. Similar to other polyanionic materials, this compound is an electrical insulator. In order to fabricate an electrically conductive composite material, a $Na_2Co_2(SeO_3)_3$-GO composite material was also prepared by employing the microwave hydrothermal route. The pristine material was confirmed to be $Na_2Co_2(SeO_3)_3$ by powder XRD. Rietveld refinement led to the fit in the Cmcm space group shown in **Figure 6.1a**, corresponding to lattice parameters of *a* = 11.1449 (1), *b* = 7.5591 (3), and *c* = 10.2655 (1) Å. More information on the refinement is provided in **Table 6.1**. A small amount of unidentified impurity was detected in the diffraction pattern (inset, Figure 1a) which was also visible under high-resolution transmission electron microscopy (HRTEM) imaging (see below). The 3D open framework structure of orthorhombic $Na_2Co_2(SeO_3)_3$ has been previously reported (Figure 1b).[33] It consists of 2D $CoSeO_3$ layers that are cross linked by SeO_3 units

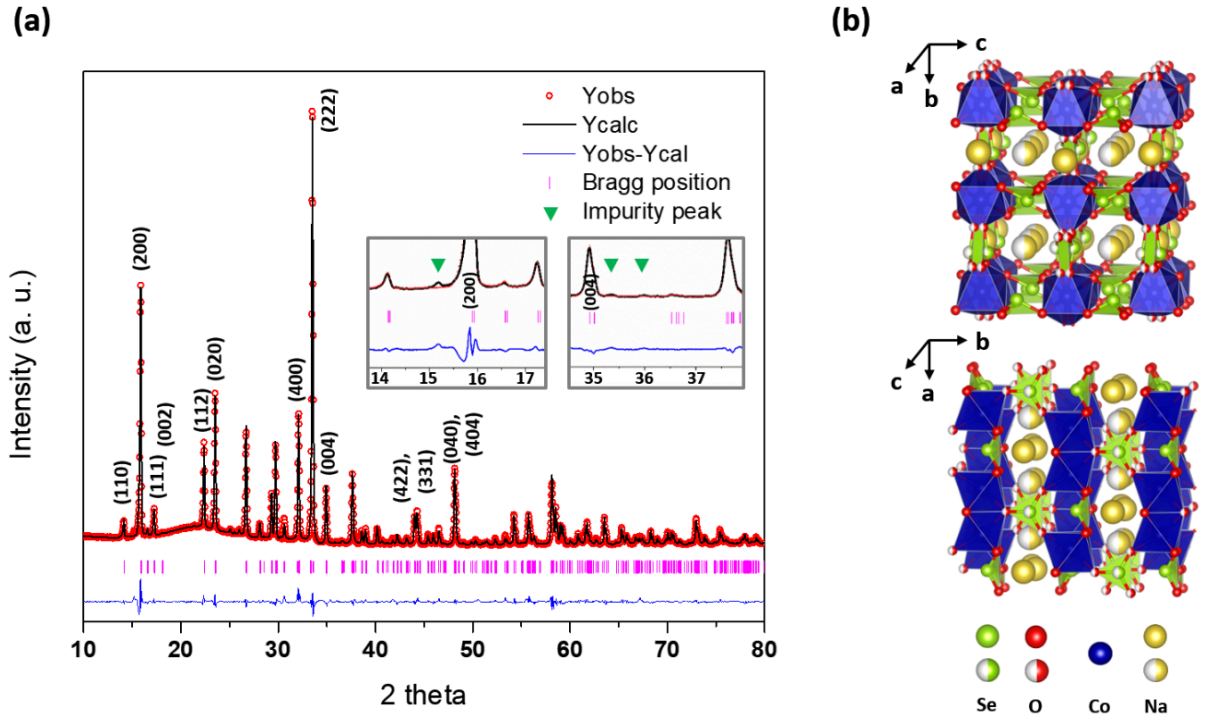

Figure 6.1 (a) Rietveld refinement of the powder XRD pattern of the pristine $Na_2Co_2(SeO_3)_3$. The experimental data are shown in red circles, the calculated pattern is shown in black, the difference curve is shown in blue, and the Bragg positions are shown in magenta. (b) Crystal structure of $Na_2Co_2(SeO_3)_3$ viewed along the [100] and [001] directions, showing the Na^+ migration channels in a 3D open framework built by CoO_6 and SeO_3 polyhedra. Color code: blue, CoO_6 octahedra; green, trigonal planar SeO_3; red spheres, O; yellow (or yellow/white representing partial occupancy of the second Na site) spheres, Na.

into a pillared architecture, leading to intersecting large channels for 2D Na^+ migration parallel to the *a* and *c* crystallographic axes. There are two crystallographically distinct Na sites in this structure. We note that the site occupying the channel along *a* is only half filled, and vacancies at the intersection of conduction pathways allow multidimensional diffusion. The Rietveld refinement of the XRD pattern of the as-synthesized $Na_2Co_2(SeO_3)_3$-GO composite (**Figure 6.2a**) is the same as that of the pristine material (**Figure 6.2b**).

Table 6.1 Atomic parameters of $Na_2Co_2(SeO_3)_3$ Calculated from Rietveld Refinement of X-ray Powder Diffraction Data (Space group: *Cmcm*, a = 11.1449 (1) Å, b = 7.5591 (3) Å, c = 10.2655 (1) Å, Cell Volume = 864.821(2) $Å^3$, R_{exp} = 5.16, R_{Bragg} [%] = 6.39, R_f [%] = 6.35, χ^2 = 4.65)

Site	Wycko.	x	y	z	$U_{iso}(Å^2)$	Occ.
Se1	8*f*	0	0.2336(1)	0.5303(1)	0.012(2)	1
Se2	8*f*	1/2	- 0.0141(2)	0.8044(2)	0.017(2)	0.5
Co1	8*g*	0.1906(1)	0.2409(2)	1/4	0.005(1)	1
O1	8*f*	0	0.1765(4)	0.3800(4)	0.017(2)	1
O2	8*f*	1/2	0.1240(7)	0.7198(10)	0.017(2)	0.5
O3	16*h*	0.1824(5)	0.1730(2)	0.6031(3)	0.018(2)	1
O4	16*h*	0.6824(1)	-0.0658(4)	0.7257(7)	0.019(5)	0.5
Na1	4*c*	0	- 0.0220(5)	1/4	0.024(1)	1
Na2	8*e*	0.2564(9)	0	1/2	0.031(1)	0.5

Thermogravimetric (TG) analyses of the pristine and the composite material (**Figure 6.3**) were performed to determine that the fraction of GO in the composite was 15 wt%. Thermal analysis also showed that both the pristine and the composite materials are stable up to 500 °C in air, which indicates good oxidative stability that is crucial for a high voltage cathode. Scanning electron microscopy (SEM) images of the pristine and GO composite materials are shown in **Figure 6.4a, b**, respectively. The pristine material is a mixture of plate and rod-shaped particles with thicknesses ranging from 300 nm to 1 μm. These particles are composed of thin crystalline plates with a smooth surface (**Figure 6.4a**, inset). The GO composite material consists of ≈ 1 μm cubic particles dispersed on graphene sheets, where the cubes are also composed of multiple thin plates (**Figure 6.4b**, inset). Low magnification TEM images shown in the inset of **Figure 6.4c, d** further confirm the rod and cube like morphology of the pristine and the composite material, respectively. Two perpendicular set of lattice fringes are visible - (002) and (020) - corresponding to d-spacings of 0.378 and 0.525 nm, respectively; (002) planes runs along the length and (020) planes run along the width of the crystallites. We conclude that the particles

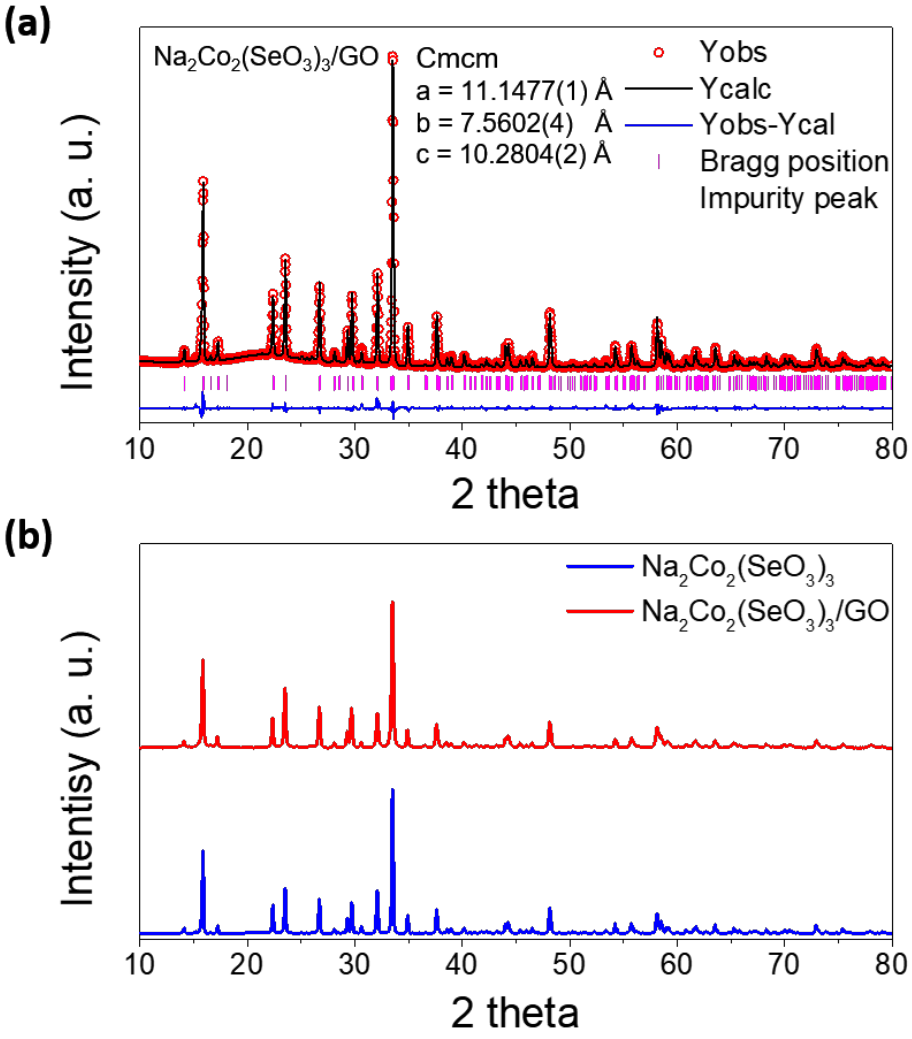

Figure 6.2 (a) Rietveld refinement of the powder XRD pattern of the $Na_2Co_2(SeO_3)_3$/GO composite. The experimental data is shown in red circles, the calculated pattern is shown in black, the difference curve is shown in blue, and the Bragg positions are shown in magenta. (b) X-ray diffraction patterns of the pristine $Na_2Co_2(SeO_3)_3$ (blue) $Na_2Co_2(SeO_3)_3$-GO composite (red), for comparison.

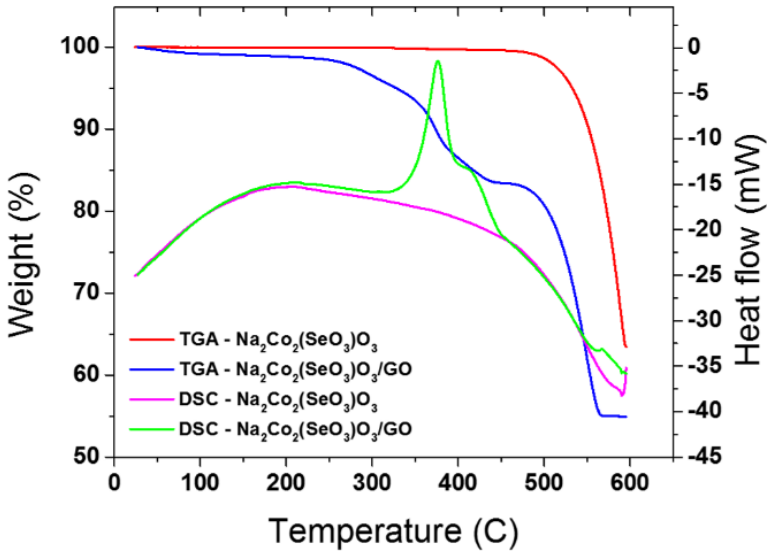

Figure 6.3 Thermogravimetric analysis (TGA, air) and differential thermal analysis (DTA) curves of the pristine $Na_2Co_2(SeO_3)_3$ and the $Na_2Co_2(SeO_3)_3$-GO composite materials.

terminate at the (200) surface with the *a* axis as the reduced growth direction. This feature is expected to assist Na^+-ion mobility since the *a* direction has open pathways for Na^+ migration. HRTEM studies also revealed a thin layer of an unknown phase (denoted as α) on the surface of the particles. This 5 nm impurity layer, which most likely corresponds to the unidentified impurity observed in the XRD pattern, can be seen in **Figure 6.4c, d**.

The activation energy (E_a) for Na ion migration and the corresponding Na^+ ionic conductivity were determined by performing electrochemical impedance spectroscopy (EIS) measurements on a pressed $Na_2Co_2(SeO_3)$ powder pellet. **Figure 6.5** shows the impedance plots obtained at different temperatures ranging from 25 to 170 °C and the Arrhenius plot obtained by fitting the bulk conductivity values. The ionic conductivity of 1.51×10^{-8} S·cm^{-1} at 298 K is comparable to values for other polyanion materials such as NASICON type $Na_3V_2(PO_4)_3$ or cubic $Na_3TiP_3O_9N$ (both ≈ 10^{-7} S·cm^{-1}).[34,35] The observed E_a of 0.6 eV·atom^{-1} is similar to that reported for either

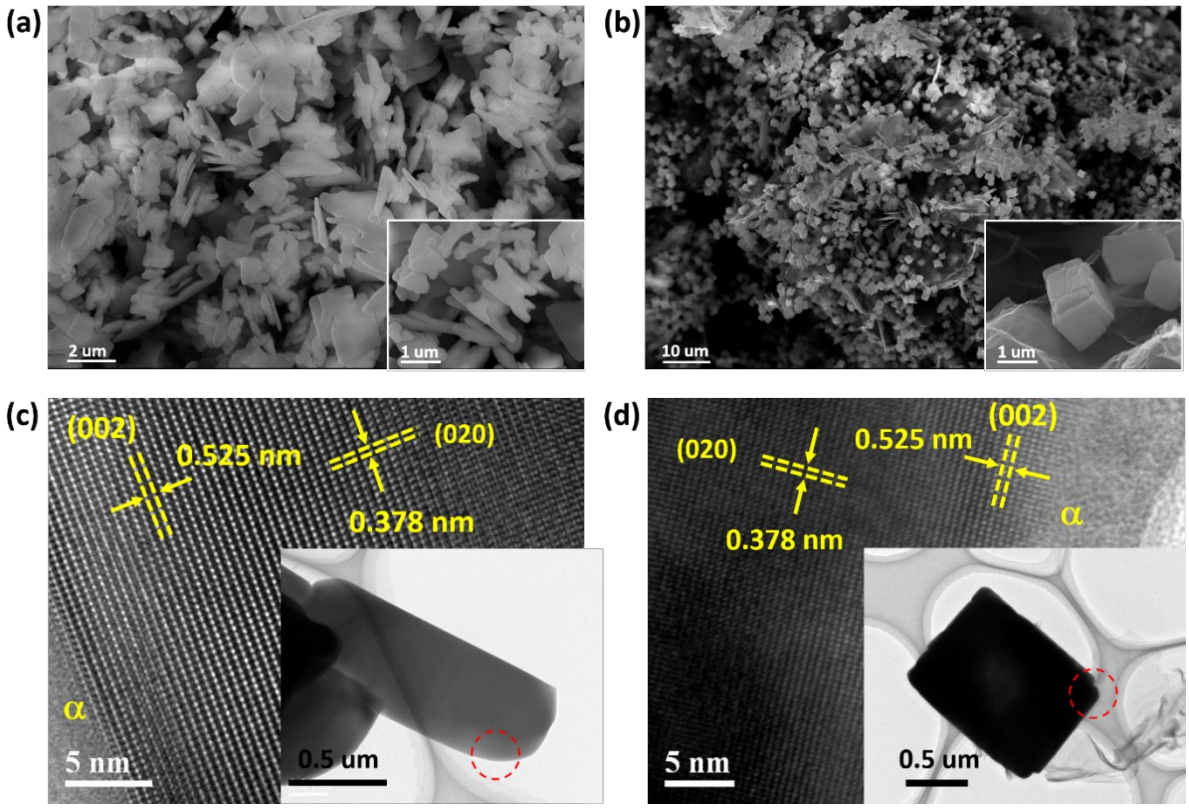

Figure 6.4 SEM images of (a) pristine $Na_2Co_2(SeO_3)_3$ and (b) $Na_2Co_2(SeO_3)_3$-GO composite materials. HRTEM images show the lattice fringes in the (c) pristine $Na_2Co_2(SeO_3)_3$ and (d) $Na_2Co_2(SeO_3)_3$-GO composite crystallites indicative of a high degree of crystallinity.

$Na_3TiP_3O_9N$ or P2 type layered $Na_2Co_2TeO_6$.[36] While the pristine material showed poor electrical conductivity ($\approx 10^{-10}$ S·cm^{-1}), as do most polyanion materials,[36] the electrical conductivity of the $Na_2Co_2(SeO_3)$-GO composite increased by nine orders of magnitude to 65 mS·cm^{-1}. This increase is key to electrochemical performance as we show below.

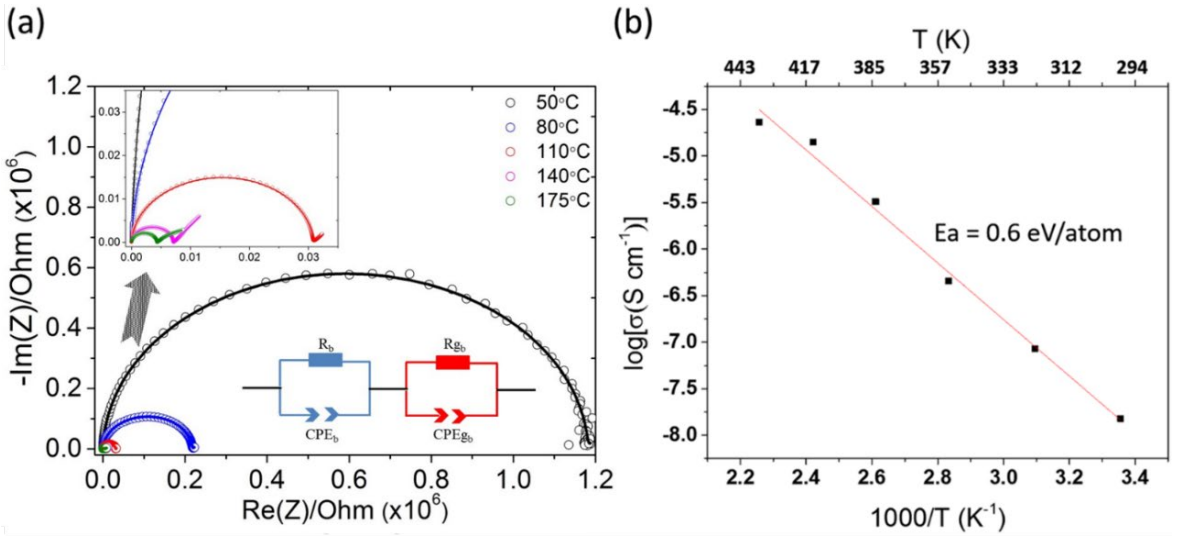

Figure 6.5 (a) AC impedance spectra (empty circles) of pristine $Na_2Co_2(SeO_3)_3$ along with fitted curves (solid line) at various temperatures. The inset shows the expansion of the high frequency region. Equivalent circuit used to fit the impedance data is shown in the inset; here, the subscripts b and gb denote bulk and grain boundary components, respectively. The impedance plane semicircles are depressed due to the distribution of the relaxation times and hence, a non-ideal capacitor or CPE is used to represent the depressed semicircle. Generally, the high frequency semicircle is attributed to bulk processes, and the low frequency semicircle arises from grain boundary contributions. (b) Arrhenius plot of ionic conductivity. The experimental data is shown in black dots and the activation energy for Na^+ ion migration is calculated from the slope of the fitted line (red).

6.3.2 Structural Changes upon Electrochemical Cycling

The evolution of the diffraction pattern obtained by an operando XRD study during the first charge/discharge cycle is shown in **Figure 6.6a** and **Figure 6.7**. A continuous shift of peak positions on cycling is evident, with the trend during Na^+ extraction being reversed on reinsertion. Further analysis reveals an underlying complex process. Upon Na^+ extraction beyond $x \approx 0.35$ in $Na_{2-x}Co_2(SeO_3)_3$, the XRD peaks broaden and the peak intensity decreases, a trend which continues until $x \approx 0.7$. This point is accompanied by a potential jump to 4.2 V in the galvanostatic profile. We ascribe the peak broadening to microstrain generation resulting from electrostatic repulsion between

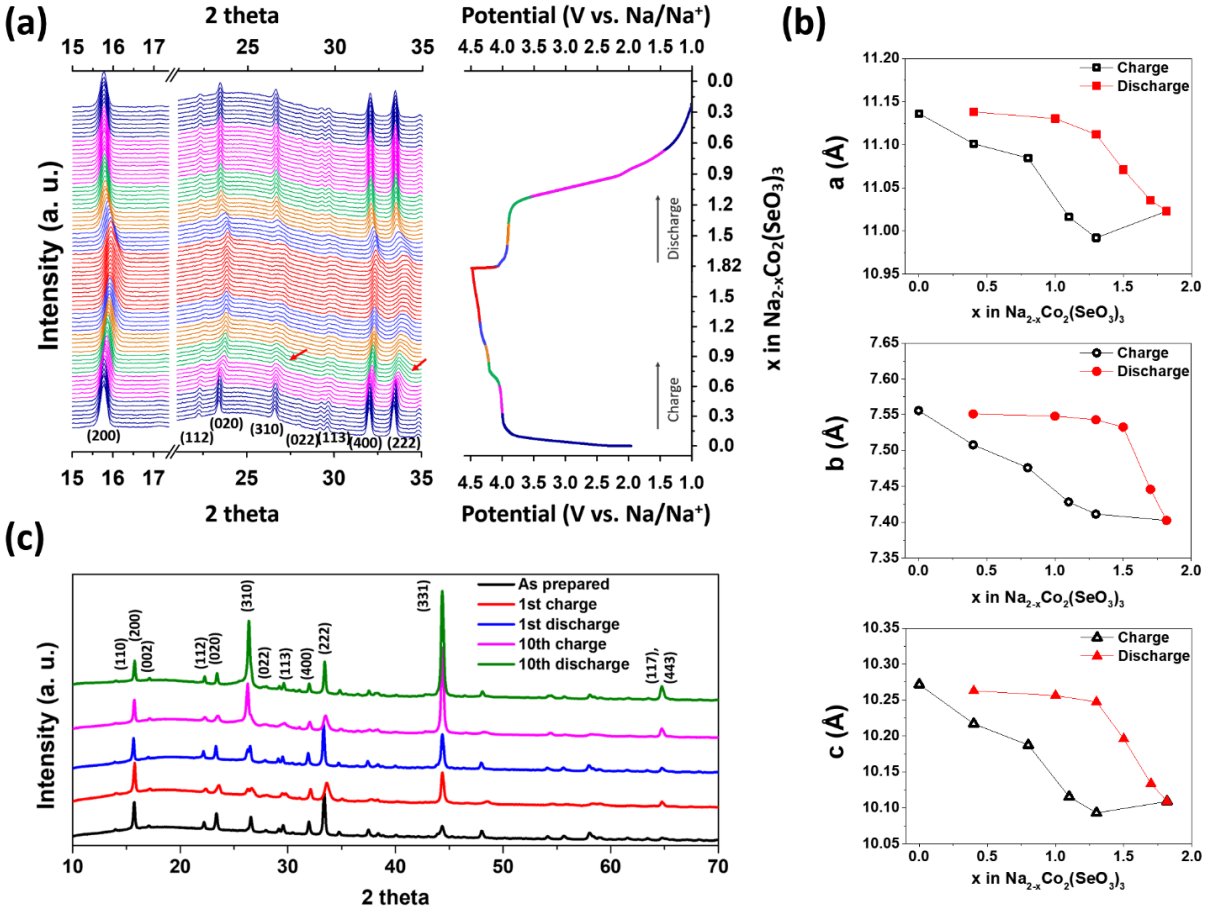

Figure 6.6 (a) Operando XRD data of $Na_2Co_2(SeO_3)_3$-GO electrode during the first charge/discharge cycle at 0.05C (5 mA·g^{-1}) in the potential range of 1.0 - 4.5 V (vs. Na/Na$^+$) (left) as a function of intercalated Na$^+$ concentration (right). (b) Evolution of lattice parameters of $Na_{2-x}Co_2(SeO_3)_3$ calculated from operando X-ray diffraction patterns as a function of Na$^+$ composition during the first cycle. (c) Ex situ XRD patterns collected from as-prepared, 1st charged/discharged and 10th charged/discharged electrodes.

adjacent $CoSeO_3$ layers that accompanies Na$^+$ extraction. Subsequent desodiation leads to an apparent biphasic process as demonstrated by the appearance of new peaks at 2θ = 26.77° and 34.07°, which evolve in the XRD pattern up until x ≈ 1.6. The deintercalation limit corresponds to a composition of $Na_{0.4}Co_2(SeO_3)_3$. The chemical composition of the electrochemically charged material was also probed by energy dispersive X-ray spectroscopy (EDX) and compared to that of the starting phase (**Figure**

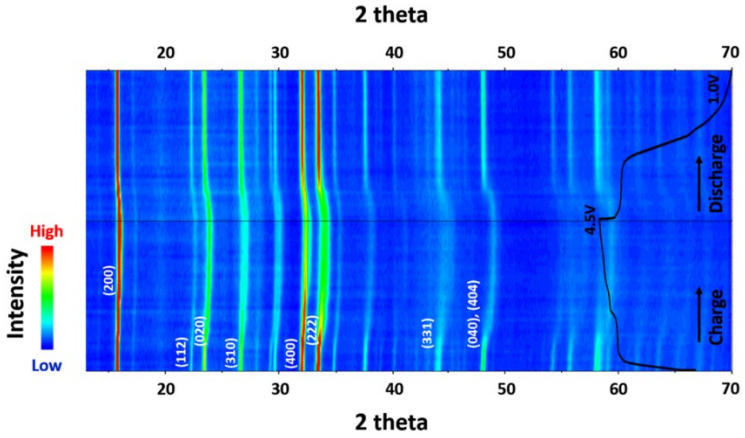

Figure 6.7 Contour plot of Operando XRD patterns of the $Na_2Co_2(SeO_3)_3$-GO electrode recorded over the first charge/discharge cycle at a rate of 0.05 C in the voltage window of 1.0 - 4.5 V (vs. Na/Na^+), along with voltage profile of the cell.

6.8a and b). While EDX does not provide a rigorous quantitative analysis, nonetheless the data show that after the first charge, the Na content of the charged compound is ≈ 0.4 mol per formula unit (i.e., $Na_{0.4}Co_2(SeO_3)_3$). This value - 80% of theoretical - is in excellent agreement with the electrochemical results. On charging above 4.4 V, the electrochemistry is dominated by electrolyte degradation. Interestingly, structural evolution during discharge does not mirror charge. The biphasic-like process on discharge occurs in a smaller compositional window of $1.8 \geq x \geq 1.45$, followed by an extended solid solution region until $x \approx 0.4$. Nonetheless, following a complete cycle, the XRD pattern is very similar to the pristine pattern, suggesting good structural reversibility. It is noteworthy that during the charge/discharge process, all the peaks upshift/downshift slightly, indicating an underlying solid solution mechanism. The appearance of two new peaks (red arrows, **Figure 6.6a**) suggests a two-phase reaction in the composition range, but these peaks also shift continuously which is typical of a solid solution reaction. The evolution of the lattice parameters of $Na_{2-x}Co_2(SeO_3)_3$ phases during Na^+ (de)intercalation was derived from full-pattern matching (**Figure 6.6b**). For most of the charge process, all three lattice parameters (*a*, *b*, and *c*) of the orthorhombic system continuously decrease with

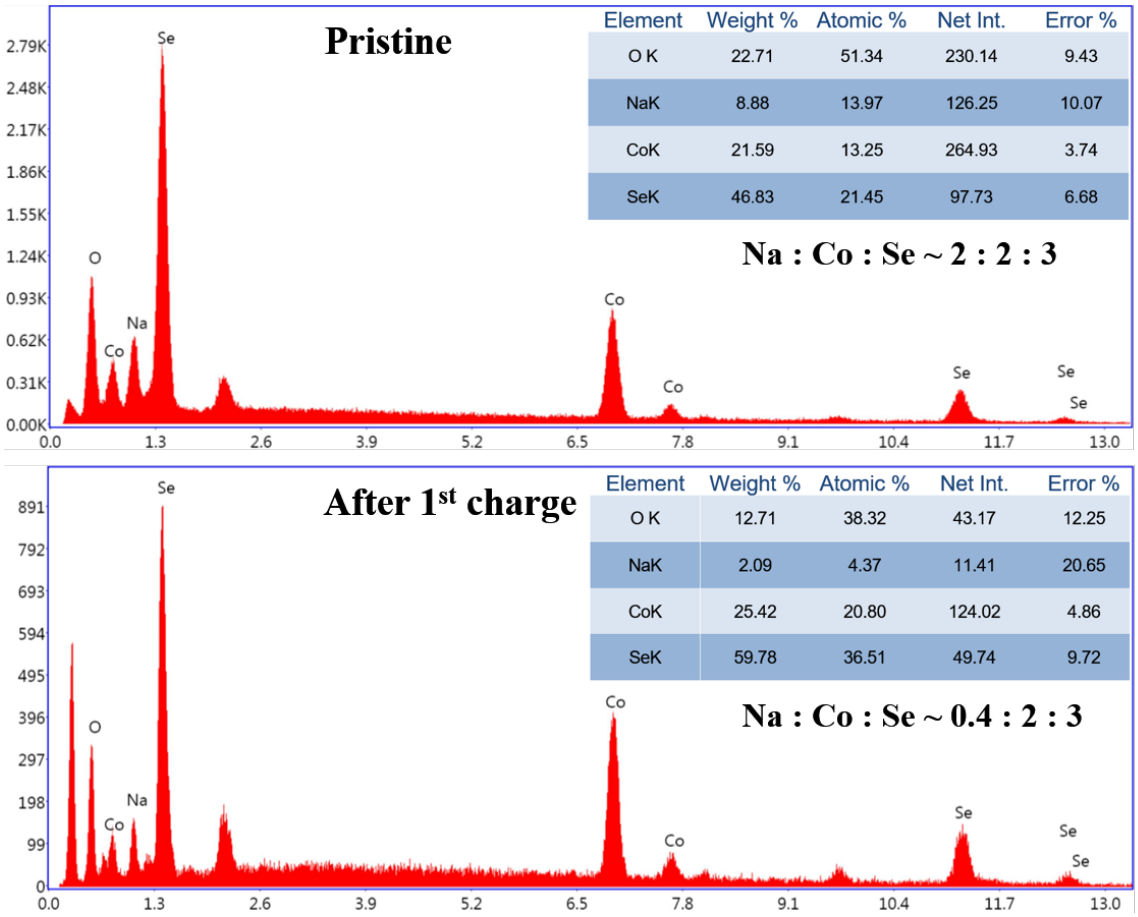

Figure 6.8 EDX spectra of a) as-prepared $Na_2Co_2(SeO_3)_3$ and b) the electrochemically charged material, $Na_{2-x}Co_2(SeO_3)_3$. The corresponding elemental analyses from the EDX data are shown in the inset tables and indicate that the composition of the pristine material ("$Na_{2.08}Co_2(SeO_3)_{3.2}$") is very close to $Na_2Co_2(SeO_3)_3$ in accord with that expected, and that of the electrochemically oxidized material after the 1st charge is $Na_{0.4}Co_2(SeO_3)_3$. While EDX is not intended to be quantitative, the data clearly shows that significant Na^+ is deintercalated on charge, and the oxidized composition is in perfect accord with the electrochemical capacity on charge.

decreasing Na content. This can be attributed to the contraction of the cobalt octahedra upon Co^{2+} oxidation to Co^{3+}. However, toward the end of charge, at x > 1.3, the *a* and *c* parameters increase slightly with Na removal. This is due to the increasing electrostatic repulsion between adjacent O^{2-} layers that are no longer screened by Na^+, because the layers are nearly empty. During discharge,

increasing Na^+ content leads to expansion of the lattice parameters, but again, the process follows a different trend than during charge. The lattice parameters increase sharply at the beginning of discharge with a small change in Na^+ content (*a*, *c*: until $x \leq 1.3$; *b*: until $x \leq 1.5$), beyond which they are almost constant until the end of discharge. After a full cycle, the lattice parameters return to their initial values. Typically polyanionic compounds undergo significant volume change, especially for Na^+ (de)intercalation due to the large size of the Na^+ cation, but $Na_{2-x}Co_2(SeO_3)_3$ ($2 < x < 0.2$) undergoes a relatively small volume change of $\approx$ 4.7%, which is beneficial. The structural stability upon electrochemical cycling was investigated by ex situ XRD analysis of the charged/discharged electrodes. **Figure 6.6c** shows the ex situ XRD patterns of the as prepared, 1st charged/discharged and 10th charged/discharged $Na_2Co_2(SeO_3)_3$ electrodes. The pattern of the material after the 10th cycle is very similar to that of the pristine, suggesting stability of the 3D structural framework. Closer examination reveals a change in the peak intensity ratios, whereby the intensity of the (310), (331), and (117, 443) reflections increase with cycling. Electrochemical grinding upon repeated cycling, leading to morphological degradation of the cubic particles of the GO composite as evident in the SEM image of electrode after 100 cycles (**Figure 6.9**) likely explains this. Structural modification induced by cation disordering cannot be ruled out, however. In-depth operando and ex situ synchrotron-XRD structural studies are required to probe the subtle details of the apparent biphasic and solid solution process, which will be the topic of future work.

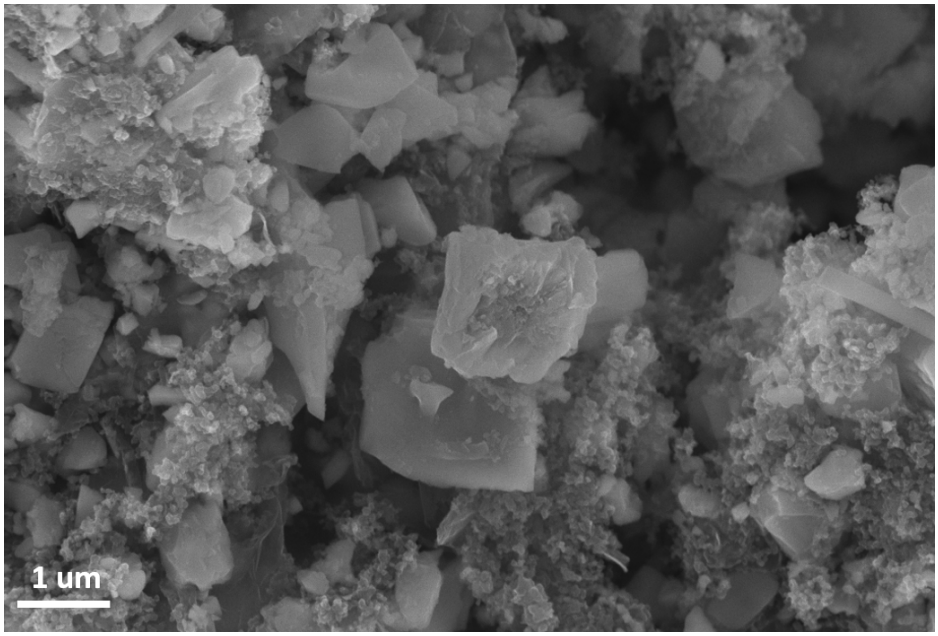

Figure 6.9 SEM images of $Na_2Co_2(SeO_3)_3$/GO composite materials after 100 cycles, indicating some fracturing of the active material. The Na cell was cycled at 0.05C within a voltage window of 1.0 - 4.5 V (vs. Na/Na^+).

6.3.3 Electrochemical Performance

Electrochemical properties of the pristine nanostructured $Na_2Co_2(SeO_3)_3$ and the $Na_2Co_2(SeO_3)_3$-GO composites were evaluated in Na half cells. The cathode materials were utilized without further modification such as carbon coating or particle downsizing. The GO composite material exhibited better performance than the pristine material due to its much higher electrical conductivity, and hence only it will be discussed here (the pristine material is described in **Figure 6.10**). **Figure 6.11a** shows the first three cyclic voltammograms of the GO composite. The cyclic voltammetry (CV) curves show two closely spaced reversible peaks, indicating two independent electrochemical processes. The first cycle differs a little from subsequent cycles. It shows an increasing current response at the end of the anodic sweep which primarily results from electrolyte oxidation, and the appearance of cathodic peaks

at slightly lower voltages relative to those in the subsequent cycles. In subsequent cycles, the reversible anodic/cathodic peaks are centered at 4 and 4.15 V. These potentials are very "moderate" for a cobalt-based sodium polyanionic compound,[21–26] although a similar potential was reported for $LiCoBO_3$.[38] Like trigonal BO_3^{3-}, the trigonal SeO_3^{2-} group (where Se^{4+} is the central cation) is a very weakly inductive polyanion compared to tetrahedral PO_4^{3-} or SO_4^{4-}. The two redox peaks arise due to the de/intercalation of sodium ions from two distinct lattice sites in the crystal structure and involve the $Co^{2+/3+}$ couple as confirmed by XPS and magnetic property studies (see below). **Figure 6.11b** shows the voltage-capacity profiles of the $Na_2Co_2(SeO_3)_3$-GO composite electrode for the first three cycles between 1.0 and 4.5 V at a C/20 rate, where 1 C corresponds to the theoretical $2e^-$ capacity of ≈ 98 mA $h \cdot g^{-1}$. After the first discharge, a capacity of 75 mA $h \cdot g^{-1}$ is recovered. Raising the lower cut-off voltage to 1.5 V results in a lower capacity (≈ 50 mA $h \cdot g^{-1}$; **Figure 6.12**) owing to increased polarization at high Na content, and therefore the wider window was utilized in this study.

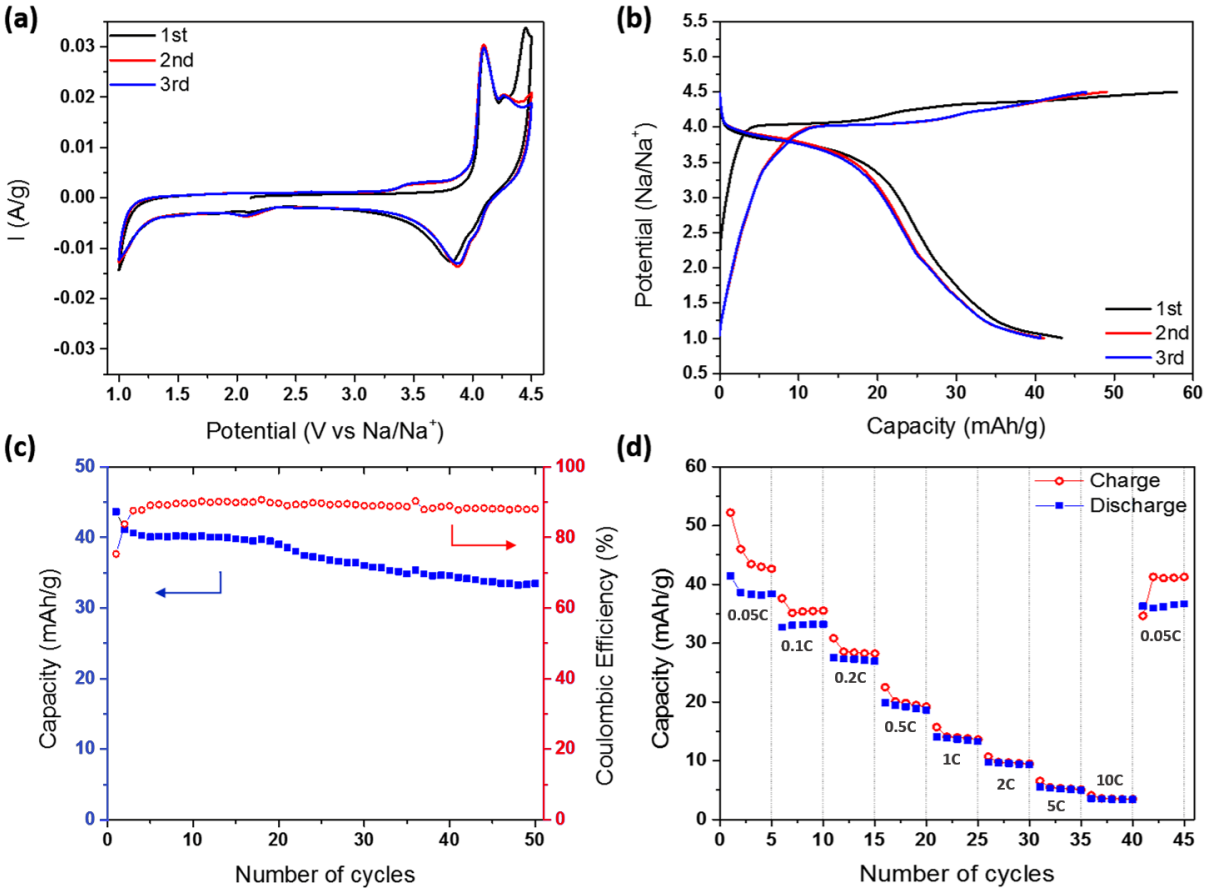

Figure 6.10 Electrochemical performance of the pristine $Na_2Co_2(SeO_3)_3$ electrode: (a) cyclic voltammograms during the first three cycles at a scan rate of 0.1 mV s-1; (b) voltage-capacity profiles for the first three cycles at a 0.05C rate (1C = 98.4 mA g-1) in a voltage window of 1.0 - 4.5 V vs. Na/Na^+; (c) cycling performance and corresponding Coulombic efficiency at a 0.05 C rate; (d) rate capability data at varying C rates and the corresponding Coulombic efficiencies.

The charge profile exhibit multiple plateau-like features along with sloping regions, indicating a rather complex phase evolution as demonstrated by the operando XRD studies. The discharge profile primarily consists of a 4 V plateau followed by a sloping region corresponding to a biphasic and a solid solution process, respectively. In the following cycles, the reversible capacity stabilizes at ≈ 70 mAh·g^{-1} (**Figure 6.11c**). Notably, the specific capacity slowly increases with cycling and reaches ≈ 75 mAh·g^{-1} after 15 cycles.

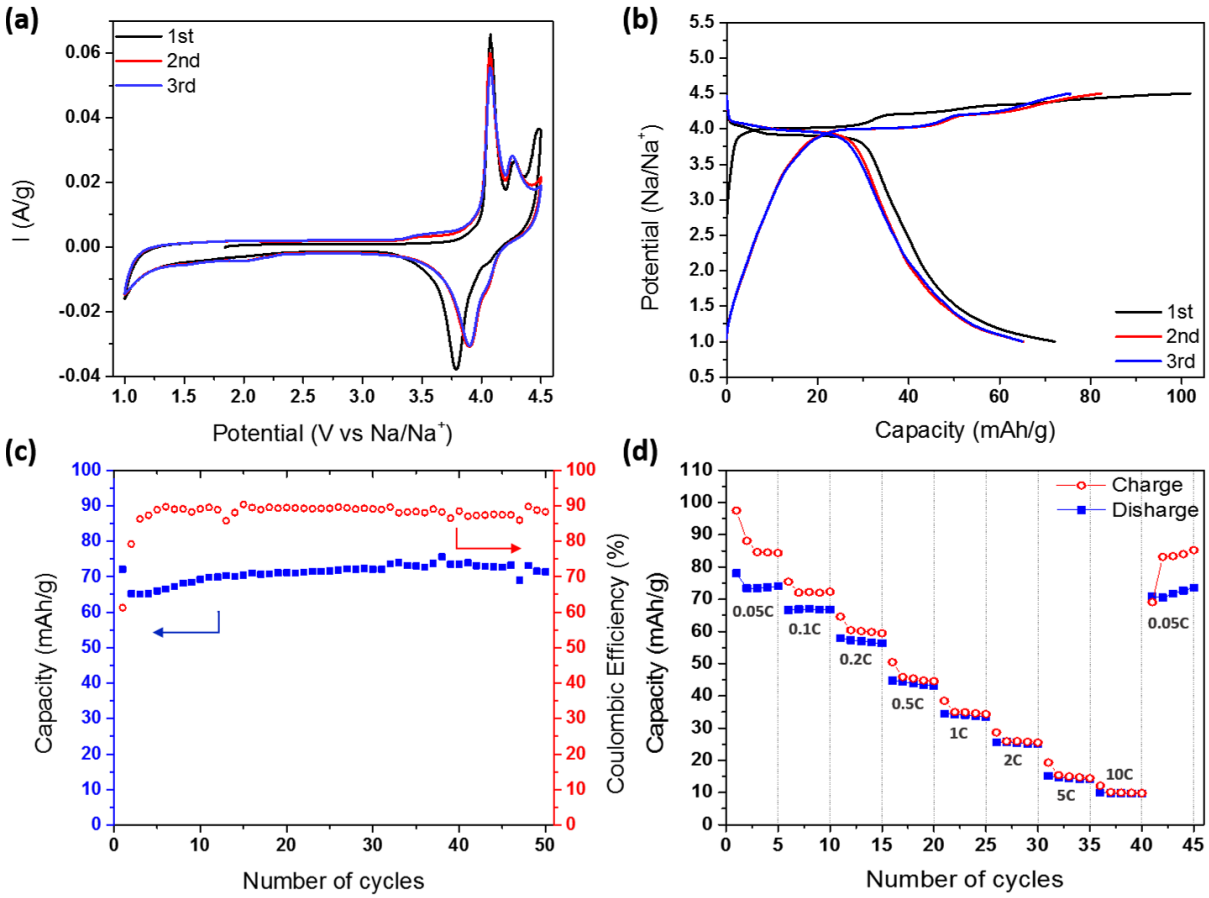

Figure 6.11 (a) Cyclic voltammograms of the $Na_2Co_2(SeO_3)_3$-GO electrode during the first three cycles at a scan rate of 0.1 $mV \cdot s^{-1}$. (b) Voltage-capacity profiles of the $Na_2Co_2(SeO_3)_3$-GO electrode for the first three cycles at a 0.05C rate (1C = 98.4 $mAh \cdot g^{-1}$) in a voltage window of 1.0 - 4.5 V vs. Na/Na^+. (c) Cyclability and corresponding coulombic efficiency of the $Na_2Co_2(SeO_3)_3$-GO electrode in a Na cell at a 0.05 C rate. (d) Rate capability of the $Na_2Co_2(SeO_3)_3$-GO electrode at varying C rates.

The discrepancy between the charge and discharge capacities originates from electrolyte decomposition during charge. This is apparent from a rate capability study (**Figure 6.11d**): upon increasing the current rate, the difference between the charge and discharge capacities slowly decreases as a 0.5 C rate is achieved. The difference disappears at 1 C and 2 C because of the sluggish kinetics of parasitic decomposition processes at higher current rates. The pristine material exhibited identical

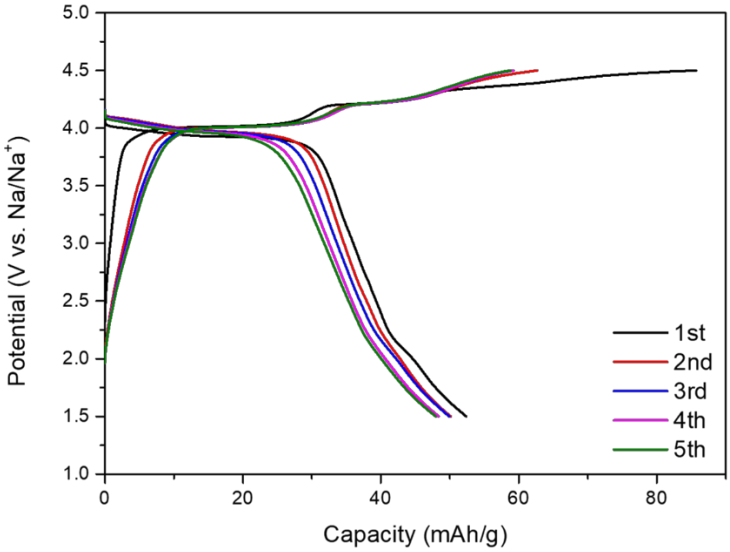

Figure 6.12 Voltage-capacity profiles of the $Na_2Co_2(SeO_3)_3$-GO electrode for the first five cycles at a 0.05C rate (1C = 98.4 $mAh \cdot g^{-1}$) in a voltage window of 1.5 – 4.5 V vs. Na/Na^+.

electrochemical characteristics, except lower specific capacity and inferior rate performance were observed (**Figure 6.10b, d**).

6.3.4 Redox Mechanism

The evolution of the chemical composition and the cobalt oxidation state of the pristine, charged, and discharged $Na_2Co_2(SeO_3)_3$ cells were examined by XPS analysis of the corresponding electrodes. In the as-prepared electrode (**Figure 6.13a**), the Co $2p_{3/2}$ region consists of primarily one component at 781.5 eV in accord with the Co^{2+} state of the pristine compound. The broad peak centered at ≈ 786 eV corresponds to the shakeup satellite, which is present for a paramagnetic metal state such as high spin (HS) Co^{2+}. For the sample charged to 4.5 V (**Figure 6.13b**), the Co $2p_{3/2}$ and $2p_{1/2}$ region was deconvoluted into two contributions, with both being necessary to achieve a good fit.

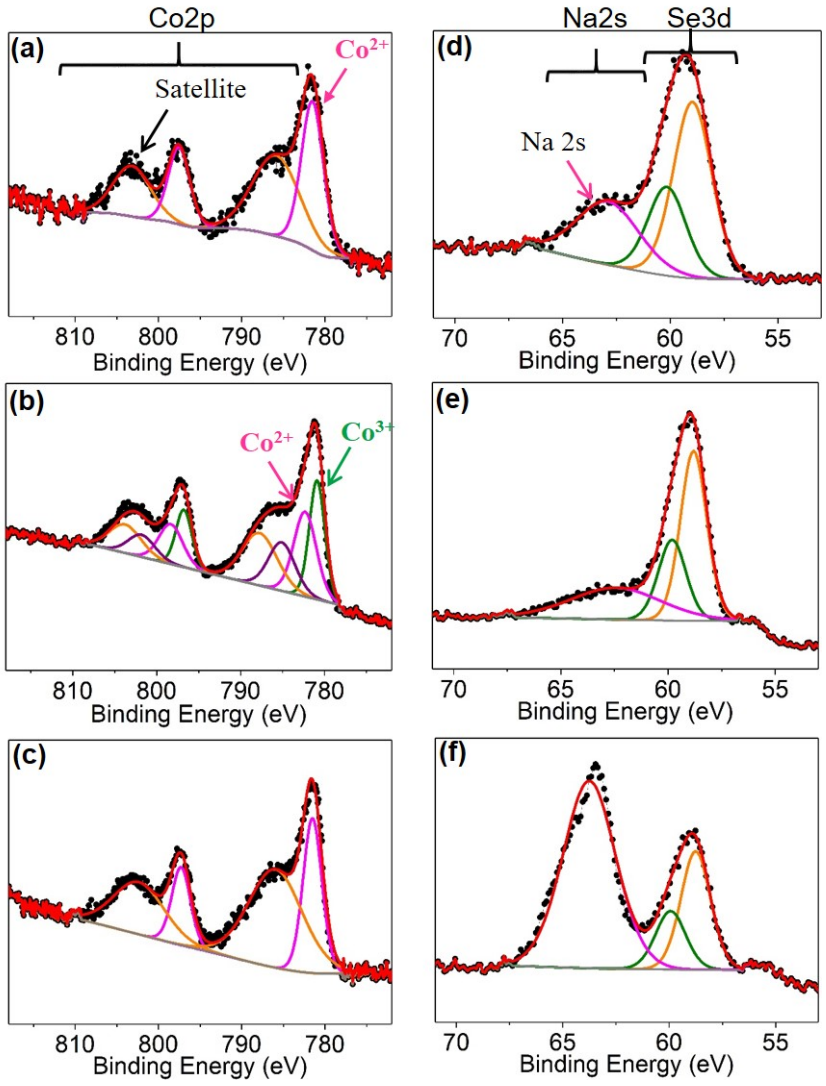

Figure 6.13 Co 2p XPS spectra of the $Na_2Co_2(SeO_3)$-GO electrodes: (a) as prepared; (b) after the first charge to 4.5 V; (c) after the first discharge to 1.0 V. Se 3d and Na 2s XPS spectra of $Na_2Co_2(SeO_3)_3$-GO electrodes: (a) as prepared; (b) after the first charge to 4.5 V; (c) after the first discharge to 1.0 V.

One peak is at slightly lower binding energy (780.6 eV) vis a vis Co^{2+}, consistent with the partial conversion of Co^{2+} to Co^{3+}.[39,40] The origin of the red shift is not well understood in the literature. The other peak arises from residual Co^{2+}, as the material does not fully oxidize on charge. The cobalt oxidation state is correlated to the amount of sodium that is deintercalated during charge (1.6 per

formula unit as indicated by the electrochemical studies, i.e., a little less than the theoretical $2e^-$ redox per formula unit). While the Co^{2+} feature in the charged material represents a higher fraction than expected from the electrochemistry, this is probably due to the fact that XPS probes the surface, not the bulk. Due to the subtlety (small shift of Co^{3+} w.r.t. Co^{2+}) and complexities (shake-up final states) involved, the fit in **Figure 6.13b** is an exemplary fit, not quantitative. Two satellite features are also observed beside the primary Co 2p contributions, which indicates the paramagnetic nature of both Co^{2+} (HS) and Co^{3+} (intermediate spin (IS): $t_{2g}^5e_g^1$) ions in the charged compound. Upon subsequent discharge (**Figure 6.13c**), the Co 2p spectrum returned to its initial state consisting of only the Co^{2+} component, implying a good reversibility of the cobalt redox process. Notably, no change in the selenium XPS component was observed for the charged/discharged materials (**Figure 6.13d-f**), which confirms the lack of selenium redox activity. The intensity of the Na 2s peak, which appears to the right of the Se 3d XPS feature, is not in agreement with the true sodium content of the charged (see EDX data, above) and discharged materials owing to residual surface Na^+ contamination from the electrolyte.

The magnetic properties of the pristine and the charged/discharged materials were probed to further investigate the change in the oxidation state of the cobalt ion. All those materials display Curie-Weiss paramagnetic behavior above 50 K as indicated by the linear fit of the reciprocal susceptibilities (**Figure 6.14a-c**) to the Curie–Weiss law

$$\chi_p = \frac{C}{T-\theta} \qquad \textbf{Equation 6.1}$$

where C is the molar curie constant, T is absolute temperature, and θ is the Curie-Weiss temperature (Weiss constant). The parameters obtained from the Curie-Weiss fitting are shown in **Table 6.2**, where the effective magnetic moment (μ_{eff}) values were calculated from: $\mu_{eff} = 2.84 \times C^{1/2}$. The magnetic moment obtained for pristine $Na_2Co_2(SeO_3)_3$ (4.23 $\mu_B \cdot mol^{-1}$ of Co) is consistent with typically observed values for Co^{2+} ions. These are higher than the spin-only value (3.87 μ_B) due to the spin-orbit

Table 6.2 Magnetic parameters of the as prepared, charged and discharged $Na_2Co_2(SeO_3)_3$.

Electrode	Θ (K)	C_M (emu·K/mol)	μ_{eff} (u_B)	$\mu_{eff/mole\ of\ Co}$ (μ_B)
Pristine	- 65.75	8.98	8.46	4.23
4.5V charged	- 40.01	4.23	5.80	2.90
1.5V discharged	- 52.45	7.71	7.84	3.92

contribution.[41] The charged material displays an effective moment (2.90 $\mu_B \cdot mol^{-1}$ of Co) that cannot be explained only by the magnetic moment of unoxidized Co^{2+} (high-spin (HS): $t_{2g}^5e_g^2$; 0.4 of 2 Co). Thus, we identify Co^{3+} as the source. Co^{3+} in both intermediate-spin (IS) ($t_{2g}^5e_g^1$ -spin-only μ_{eff}: 2.83 μ_B; 1.45 of 2 Co) and low spin (LS) ($t_{2g}^6e_g^0$-μ_{eff}: 0 μ_B; 0.15 of 2 Co) states are needed to explain the observed moment. An IS-state of Co^{3+} is often observed in oxides, particularly when Jahn-Teller distortion is significant due to the local distortion of CoO_6 octahedra.[42] In $Na_2Co_2(SeO_3)_3$, the Co-O bond lengths are shorter out-of-plane than in-plane, thus favoring Jahn–Teller distortion on oxidation and hence the IS state. Therefore, we speculate that upon Na^+ removal, HS Co^{2+} is initially oxidized to IS Co^{3+}, with a small fraction of LS Co^{3+} forming only at the very end of charge leading to $Na_{0.4}Co_{0.4(HS)}{}^{2+}Co_{1.45(IS)}{}^{3+}Co^{3+}{}_{0.15(LS)}(SeO_3)_3$. After discharge, the effective moment per cobalt ion closely resembles the pristine material, which confirms the reversibility of the cobalt redox upon electrochemical cycling. Furthermore, nearly superimposable magnetic susceptibility plots (**Figure 6.14d**) of the pristine and the discharged materials, where both display antiferromagnetic coupling below ≈ 14 K, provide substantial confirmation for the electrochemical reversibility of the system.

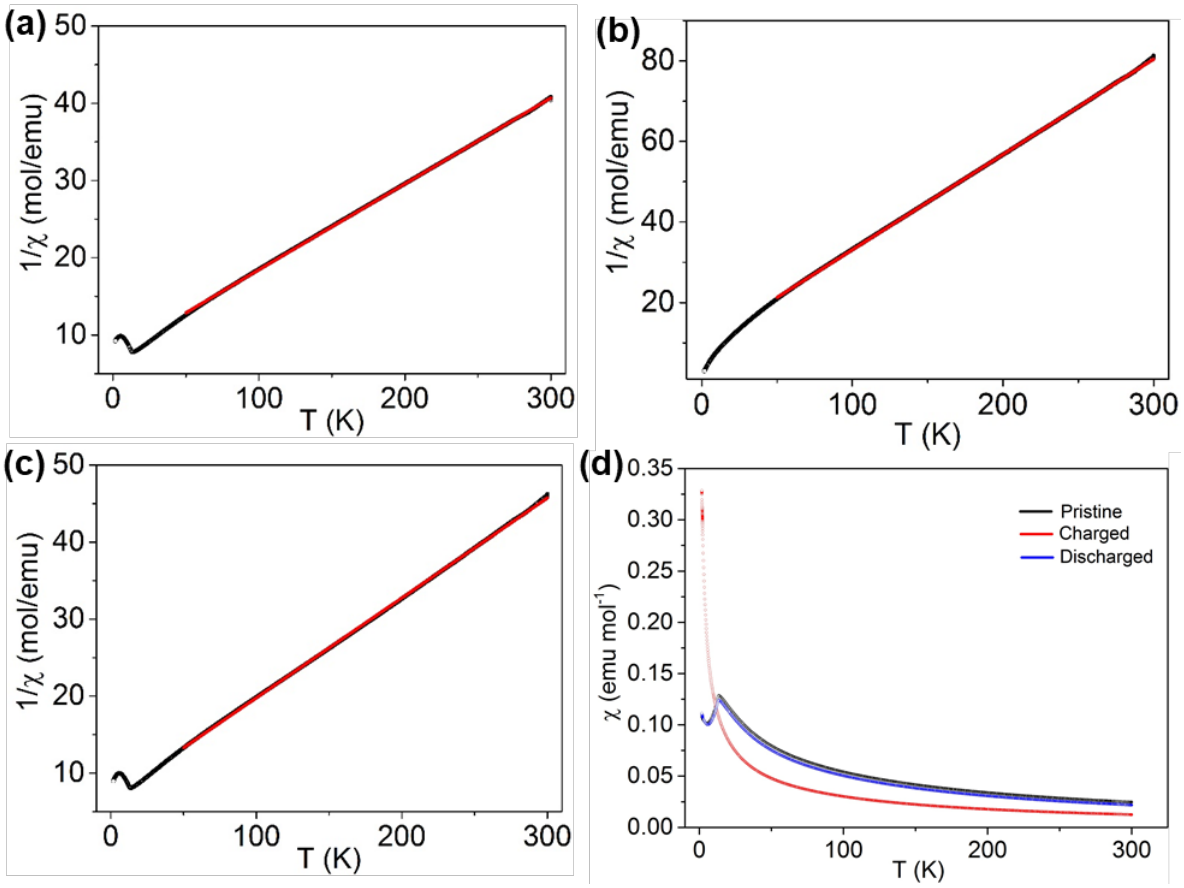

Figure 6.14 Variation of the inverse of the magnetic susceptibilities with temperature (black) and their fit to the Curie-Weiss (red) law above 50 K for the (a) as prepared, (b) charged, and the (c) discharged $Na_2Co_2(SeO_3)_3$-GO electrodes. (d) Variation of the magnetic susceptibilities with temperature for the as prepared (black), charged (red), and the discharged (blue) $Na_2Co_2(SeO_3)_3$.

6.4 Conclusions

In a search for novel polyanionic NIB cathode host materials in the transition metal selenite system, we developed a rapid and versatile microwave solvothermal synthesis route for nanostructured $Na_2Co_2(SeO_3)_3$ and its GO composite. In a NIB, the material delivers a reversible capacity of ≈ 75 mAh $\cdot g^{-1}$ at a potential of ≈ 4 V. Among high voltage NIB cathodes, this is the second highest $Co^{2+/3+}$ redox

potential after $Na_4Co_3(PO_4)_2P_2O_7$ (≈ 90 $mAh \cdot g^{-1}$ and 4.5 V)[20] and is more compatible with organic electrolytes. Furthermore, $Na_2Co_2(SeO_3)_3$ is stable to air and moisture unlike higher voltage cathode materials. While operando XRD investigation revealed a good structural reversibility during electrochemical cycling - with a predominantly solid solution mechanism and a relatively small volume change (4.7%) between the Na^+ intercalated and deintercalated members - XPS and magnetic susceptibility studies provided evidence for good chemical reversibility. The electrochemical process is based on the $Co^{2+/3+}$ redox couple, which is difficult to access in cobalt based polyanionic compounds. This is the first example of a Na^+ insertion compound based on a selenite polyanionic system. While our findings are not directed toward a commercially viable system, we hope that the fundamental understanding achieved in this work will pave the way for further discovery efforts to find new host materials for Na-ion battery applications.

References

[1] N. Yabuuchi, K. Kubota, M. Dahbi, S. Komaba, *Chem. Soc. Rev.* **2014**, *114*, 11636.

[2] D. Kundu, E. Talaie, V. Duffort, L. F. Nazar, *Angew. Chem.* **2015**, *127*, 3495; *Angew. Chem. Int. Ed. Engl.* **2015**, *54*, 3431.

[3] B. L. Ellis, L. F. Nazar, *Curr. Opin. Solid State Mater. Sci.* **2012**, *16*, 168.

[4] M. Armand, J. M. Tarascon, *Nature* **2008**, *451*, 652.

[5] B. Scrosati, J. Hassoun, Y. K. Sun, *Energy Environ. Sci.* **2011**, *4*, 3287.

[6] B. Scrosati, J. Garche, *J. Power Sources* **2010**, *195*, 2419.

[7] T. Kodama, H. Sakaebe, *J. Power Sources* **1999**, *81*, 144.

[8] V. Palomares, P. Serras, I. Villaluenga, K. B. Hueso, J. Carretero-Gonzalez, T. Rojo, *Energy Environ. Sci.* **2012**, *5*, 5884.

[9] M. D. Slater, D. Kim, E. Lee, C. S. Johnson, *Adv. Funct. Mater.* **2013**, *23*, 947.

[10] V. Etacheri, R. Marom, R. Elazari, G. Salitra, D. Aurbach, *Energy Environ. Sci.* **2011**, *4*, 3243.

[11] S. W. Kim, D. H. Seo, X. H. Ma, G. Ceder, K. Kang, *Adv. Energy Mater*. **2012**, *2*, 710.

[12] N. Yabuuchi, M. Kajiyama, J. Iwatate, H. Nishikawa, S. Hitomi, R. Okuyama, R. Usui, Y. Yamada, S. Komaba, *Nat. Mater.* **2012**, *11*, 512.

[13] S. Komaba, C. Takei, T. Nakayama, A. Ogata, N. Yabuuchi, *Electrochem. Commun*. **2010**, *12*, 355.

[14] S. P. Ong, V. L. Chevrier, G. Hautier, A. Jain, C. Moore, S. Kim, X. H. Ma, G. Ceder, *Energy Environ. Sci.* **2011**, *4*, 3680.

[15] M. Sathiya, K. Hemalatha, K. Ramesha, J. M. Tarascon, A. S. Prakash, *Chem. Mater.* **2012**, *24*, 1846.

[16] J. Billaud, R. J. Clement, A. R. Armstrong, J. Canales-Vazquez, P. Rozier, C. P. Grey, P. G. Bruce, *J. Am. Chem. Soc.* **2014**, *136*, 17243.

[17] Y. U. Park, D. H. Seo, H. S. Kwon, B. Kim, J. Kim, H. Kim, I. Kim, H. I. Yoo, K. Kang, *J. Am. Chem. Soc.* **2013**, *135*, 13870.

[18] P. Barpanda, G. Oyama, S. Nishimura, S. C. Chung, A. Yamada, *Nat. Commun.* **2014**, *5*, 4358.

[19] C. Masquelier, L. Croguennec, *Chem. Rev*. **2013**, *113*, 6552.

[20] M. Nose, H. Nakayama, K. Nobuhara, H. Yamaguchi, S. Nakanishi, H. Iba, *J. Power Sources* **2013**, *234*, 175.

[21] P. Barpanda, J. C. Lu, T. Ye, M. Kajiyama, S. C. Chung, N. Yabuuchi, S. Komaba, A. Yamada, *RSC Adv* **2013**, *3*, 3857.

[22] P. Barpanda, G. D. Liu, C. D. Ling, M. Tamaru, M. Avdeev, S. C. Chung, Y. Yamada, A. Yamada, *Chem Mater* **2013**, *25*, 3480.

[23] J. C. Treacher, S. M. Wood, M. S. Islam, E. Kendrick, *Phys Chem Chem Phys* **2016**, 18, 32744.

[24] X. H. Lin, Y. Z. Dong, Q. Kuang, D. L. Yan, X. D. Liu, W. Han, Y. M. Zhao, *J Solid State Electrochemistry* **2016**, *20*, 1241.

[25] A. Gutierrez, S. Kim, T. T. Fister, C. S. Johnson, *ACS Appl Mater Inter* **2017**, *9*, 4391.

[26] W. S. Hummers, R. E. Offeman, *J. Am. Chem. Soc.***1958**, *80*, 1339.
[27] H. L. Pan, Y. S. Hu, L. Q. Chen, *Energy Environ. Sci.* **2013**, *6*, 2338.
[28] Z. L. Gong, Y. Yang, *Energy Environ. Sci.* **2011**, *4*, 3223.
[29] M. Wildner, *J. Solid State Chem.* **1993**, *103*, 341.
[30] R. E. Morris, A. K. Cheetham, *Chem. Mater.* **1994**, *6*, 67.
[31] M. Wildner, *J. Alloys Compd.* **1995**, *217*, 209.
[32] M. Wildner, *Acta Crystallogr., Sect. C: Struct. Chem.* **1994**, *50*, 336.
[33] X. Q. Yuan, M. L. Feng, J. R. Li, X. Y. Huang, *J. Solid State Chem.* **2010**, *183*, 1955.
[34] W. X. Song, X. B. Ji, C. C. Pan, Y. R. Zhu, Q. Y. Chen, C. E. Banks, *Phys. Chem. Chem. Phys.* **2013**, *15*, 14357.
[35] J. Liu, D. H. Chang, P. Whitfield, Y. Janssen, X. Q. Yu, Y. N. Zhou, J. M. Bai, J. Ko, K. W. Nam, L. J. Wu, Y. M. Zhu, M. Feygenson, G. Amatucci, A. Van der Ven, X. Q. Yang, P. Khalifah, *Chem. Mater.* **2014**, *26*, 3295.
[36] M. A. Evstigneeva, V. B. Nalbandyan, A. A. Petrenko, B. S. Medvedev, A. A. Kataev, *Chem. Mater.* **2011**, *23*, 1174.
[37] Y. J. Zhu, Y. H. Xu, Y. H. Liu, C. Luo, C. S. Wang, *Nanoscale* **2013**, *5*, 780.
[38] Y. Yamashita, P. Barpanda, Y. Yamada, A. Yamada, *ECS Electrochem. Lett.* **2013**, *2*, A75.
[39] L. Daheron, R. Dedryvere, H. Martinez, M. Menetrier, C. Denage, C. Delmas, D. Gonbeau, *Chem. Mater.* **2008**, *20*, 583.
[40] D. H. Ge, J. J. Wu, G. L. Qu, Y. Y. Deng, H. B. Geng, J. W. Zheng, Y. Pan, H. W. Gu, *Dalton Trans.* **2016**, *45*, 13509.
[41] L. Tao, J. R. Neilson, B. C. Melot, T. M. McQueen, C. Masquelier, G. Rousse, *Inorg. Chem.* **2013**, *52*, 11966.
[42] C. Zobel, M. Kriener, D. Bruns, J. Baier, M. Gruninger, T. Lorenz, P. Reutler, A. Revcolevschi, *Phys. Rev. B: Condens. Matter Mater. Phys.* **2002**, *66*, 020402(R).

Chapter 7
Lithium Ytterbium Based Halide Solid Electrolytes for High Voltage All-Solid-State Li-Ion Batteries

7.1 Introduction

Increasing demand for electric vehicles has inspired the development of energy storage systems that can provide higher energy density and improved safety over current Li-ion battery systems.[1, 2] Commercial Li-ion batteries employ organic liquid electrolytes and additives which enable a high working voltage (~ 3.8 V vs. Li/Li^+) by forming a protective interphase (CEI) on the cathode active material during initial cell cycling, thereby somewhat suppressing electrolyte degradation.[3-8] Nonetheless, organic liquid electrolytes cause serious safety concerns originating from their flammability, and are subject to thermal run-away.[9-11] In order to enhance energy density and overcome these concerns, all-solid-state batteries (ASSBs) that employ inorganic solid electrolytes have been highlighted as a breakthrough technology that can also benefit from the effective integration of bipolar stacked cells.[12, 13]

Sulfide solid electrolytes have been the focus of much recent research due to their superior ionic conductivity and mechanical softness compared to their oxide counterparts. Good ductility of the electrolyte is essential to construct an effective ionic pathway in the ASSB composite cathodes or "catholyte".[14-16] In this context, several promising sulfide solid electrolytes exhibiting superionic conductivity in the range of ~ 10^{-2} $S \cdot cm^{-1}$ were reported.[17-21] However, the poor electrochemical oxidation stability of sulfide anions prevents the direct use of sulfide solid electrolytes with 4 V-class $LiMO_2$ (M = Co, Ni, Mn) cathode materials due to the growth of impedance layers on the surface caused by the decomposition of sulfide electrolytes upon repeated cycling.[22-26] Although electronically insulating coatings such as $LiNbO_3$,[27] $LiNb_{0.5}Ta_{0.5}O_3$,[28] and $Li_{3-x}B_{1-x}C_xO_3$,[29] have been employed on

cathode materials in an effort to mitigate sulfide oxidation, the anodic instability of sulfides still critically limits practical electrode design. This owes to decomposition of the electrolyte at any interface where it meets electrically conductive carbon (that is part of the catholyte composite) and the current collector. Hence, the development of new solid electrolytes with improved electrochemical stability at high potential is of paramount importance.

Materials in the Li_3MCl_6 family (M = Sc, In, Ho, Er, Y, Yb, Lu, etc.) were reported a few decades ago. Initial reports suggested very low ionic conductivities for Li_3InCl_6 (~ 10^{-5} S·cm^{-1} at 25 °C),[30] Li_3YCl_6 (~ 6.0×10^{-7} S·cm^{-1} at 110 °C) and Li_3YbCl_6 (2.5×10^{-7} S·cm^{-1} at 110 °C).[31] However, recent revisitation of some chlorides has revealed rather different results, with room temperature conductivity in the 0.1 - 1 mS·cm^{-1} range (Li_3InCl_6: 1.49×10^{-3} S·cm^{-1},[32] Li_3ErCl_6: 3.3×10^{-4} S·cm^{-1},[33] Li_2ZrCl_6: 5.0×10^{-4} S·cm^{-1},[34] and Li_3YCl_6: 5.1×10^{-4} S·cm^{-1}).[35] Aliovalent ion substitution in Li_3MCl_6 (M = Y, Er) results in materials that display even higher ionic conductivities ($Li_{2.5}Y_{0.5}Zr_{0.5}Cl_6$: 1.4×10^{-3} S·cm^{-1}; $Li_{2.633}Er_{0.633}Zr_{0.333}Cl_6$: 1.1×10^{-3} S·cm^{-1} at 25 °C) than their pristine counterparts.[36] Along with high ionic conductivity, the very good electrochemical stability of these solid electrolytes with 4 V-class cathode materials suggests the feasibility of practical electrode designs for ASSBs without any coating layers.

Among the trivalent lanthanide chlorides, Yb^{3+} (r = 87 pm) has a similar ionic radius to Er^{3+} (r = 89 pm) and Y^{3+} (r = 90 pm). However, Li_3YbCl_6 is known to crystallize in an orthorhombic phase (space group: *Pnma*), whereas Li_3ErCl_6 and Li_3YCl_6 adopt a trigonal phase (space group: P-3m1).[31] Although Li_3YbCl_6 structure was previously studied, it has not been explored as a superionic conductor for Li-ion ASSBs in spite of the relatively low cost of Yb (~ 17.1 USD/kg) compared to In (~ 178.0 USD/kg), Y (~ 30.0 USD/kg, 2020), and Er (~ 26.4 USD/kg).[37] Herein, we report the discovery of metastable Li_3YbCl_6 that crystallizes in a trigonal phase with space group P-3m1 at 350 °C, and exhibits a room temperature ionic conductivity of 1.02×10^{-4} S·cm^{-1}. This value jumps by an order of magnitude

to 1.11 × 10^{-3} S·cm^{-1} by substitution of Yb^{3+} with Zr^{4+} to form $Li_{3-x}Yb_{1-x}Zr_xCl_6$, which induces a trigonal-to-orthorhombic phase transition. The combination of our structural study (neutron powder diffraction and single-crystal X-ray diffraction) and evaluation of bond valence site energies reveals that enhancement of the ionic conductivity is due to the introduction of additional Li^+ ion migration pathways in the orthorhombic phase with relatively low activation energy. Importantly, the Zr-substituted lithium ytterbium chloride solid electrolyte enables excellent cycling performance of ASSBs with uncoated 4 V-class lithium transition metal oxide cathodes.

7.2 Experimental Details

7.2.1 Materials preparation

$Li_{3-x}Yb_{1-x}Zr_xCl_6$ ($0 \leq x \leq 0.8$) microcrystalline powders were prepared by solid-state reactions. Stoichiometric mixtures of LiCl (Sigma-Aldrich, 99 %), $YbCl_3$ (Sigma-Aldrich, 99.9 %) and $ZrCl_4$ (Sigma-Aldrich, 99.99 %) were prepared in an Ar-filled glove box and sealed in a quartz ampoule under vacuum, then heat treated at 350 ~ 650 °C for 36 h followed by cooling at a rate of 2 °C min^{-1}. For the single crystal X-ray diffraction (XRD) study, $Li_{3-x}Yb_{0.7}Zr_{0.3}Cl_6$ crystals were prepared by heating the stoichiometric mixture at 350 °C for 36 h and subsequent slow cooling (0.058 °C min^{-1}). To prepare the Li_3PS_4 glass (g-LPS) powders, Li_2S (SigmaAldrich, 99.98%) and P_2S_5 (SigmaAldrich, 99%) powders were mixed targeting the molar ratio of $75Li_2S$-$25P_2S_5$ and placed into 45 mL Si_3N_4 jars with Si_3N_4 balls (diameter: 5 mm) and milled for 10 hours at 500 rpm using a high energy planetary ball mill (Fritsch Pulverisette 7 Premium). $Li_{6.7}Si_{0.7}Sb_{0.3}S_5I$ was synthesized following our previously reported procedure.[38]

7.2.2 Single-crystal X-ray Diffraction and Structure Resolution

Several plate-shaped single crystals of Li_3YbCl_6 with dimensions of 0.01 × 0.02 × 0.04 mm^3 were scanned to determine their quality. The data were collected on BRUKER KAPPA diffractometer

equipped with SMART APEX II CCD, utilizing graphite monochromated Mo-Kα radiation. Since the crystals were moisture and air sensitive, they were protected by Paratone-N oil and liquid nitrogen flow using an OXFORD Cryostream controller 700 at 273 K. The data were collected by scanning ω and φ of 0.3° in couple of groups of frames using APEX2 strategy collection for complete data with an exposure time of 30 seconds per frame. The data were corrected for Lorentz and polarization effects. A multi-scan absorption correction were carried out using the program SADABS part of Bruker suite (since the crystal did not exhibit well defined facets). The unit cell was indexed using the Bruker APEX II suite, and reciprocal space was checked for any potential supercell since the crystal were twins. The structure was solved using direct methods and refined anisotropically using the least squares method incorporated in the SHELXTL package. The program Tidy was used to standardize the atomic positions.

7.2.3 Neutron Powder Diffraction

The powder neutron diffraction pattern of Li_3YbCl_6 and $Li_{2.7}Yb_{0.7}Zr_{0.3}Cl_6$ powder was measured on POWGEN at the Spallation Neutron Source (SNS) at the Oak Ridge National Laboratory. The samples were loaded into a vanadium can with a 3 mm inner diameter to reduce the absorption and gain more diffraction intensity, and was sealed under an argon atmosphere with a copper gasket and aluminum lid. The data were collected at 280 K with neutrons of central wavelengths 1.5 Å, covering the d-spacing range of 0.48 -10 Å in the orange cryostat. The neutron diffraction data were analyzed using the Rietveld refinement program suite FULLPROF.[39]

7.2.4 Pair Distribution Function simulation

The pair distribution function simulation was conducted by adopting the Li_3YbCl_6 and $Li_{2.7}Yb_{0.7}Zr_{0.3}Cl_6$ structures from PND Rietveld refinement. From the refined structures, lithium and chlorine atoms were removed and only ytterbium and zirconium atoms were considered to simulate pair distribution function. The real space data were obtained using PDFgui.[40]

7.2.5 Bond Valence Site Energy (BVSE) Calculation

BVSE calculations were conducted with the softBV program. The structural model obtained from single crystal diffraction and the softBV bond valence parameter set developed by S. Adams were used as input.[41,42] Lithium site energies were calculated for a dense grid of points with a resolution of 0.1 Å covering the crystal structure using the transferable Mores-type softBV force field. Li^+ ion conduction pathways were identified by regions of low bond valence site energy. BVSE maps with a constant isosurface energy of $E_{BVSE(Li)}$ over the global minimum indicate Li-ion diffusion pathways.

7.2.6 X-ray photoelectron Spectroscopy (XPS)

XPS analysis was performed on a Thermo ESCALAB 250 instrument configured with monochromatic Mg Kα (1253.6 eV) radiation. The air-sensitive electrode samples were transported to the spectrometer under an Ar atmosphere and transferred into the chamber without exposure to air. All spectra were fitted with Gaussian– Lorentzian functions and a Shirley-type background using CasaXPS software. The binding energy values were calibrated using the C 1s peak at 284.8 eV.

7.2.7 Electrochemical Characterization

Ionic conductivities of $Li_{3-x}Yb_{1-x}Zr_xCl_6$ ($0 \leq x \leq 0.8$) samples were measured by the AC impedance technique with Ti|$Li_{3-x}Yb_{1-x}Zr_xCl_6$ |Ti cells utilizing ionically blocking electrodes. A poly(aryl-ether-ether-ketone) (PEEK) mold (inner diameter: 10 mm) is used as a cell body with two Ti rods as the current collectors In order to fabricate the cell for activation energy measurement, the solid electrolyte (SE) powder (~ 70 mg) was pressed into 10 mm diameter pellet by a hydraulic press at 3 tons from an Ar-filled glovebox. Nyquist plots were recorded with 100 mV constant voltage at a frequency range of 35 MHz - 1 Hz using a MTZ-35 impedance analyzer (Bio-logic) at temperatures ranging from 30 to 100 °C. For cyclic voltammetry (CV) measurement, ~ 70 mg of $Li_{2.7}Yb_{0.7}Zr_{0.3}Cl_6$ powder was pressed into 10 mm diameter pellet at 3 tons and ~ 10 mg of SE-carbon (super P) mixture

(95:5 wt%) was placed on one side of the SE pellet to serve as a working electrode followed by another press at 2 tons. On the other side of the pellet, a thin indium foil (10 mm diameter, Alfa Aesar, 99.99%, 0.125 mm thickness) was attached with ~0.3 mg of Li plate (SigmaAldrich, 99.9%) and place on the pellet. The cell was then placed into a stainless steel casing with a constant applied pressure of ~1.5 tons. The CV measurement was performed with a can rate of 1 $mV \cdot s^{-1}$. The galvanostatic cycling tests was performed with working electrodes which were prepared by mixing $LiCoO_2$ (Wellcos corporation) or $LiNi_{0.6}Mn_{0.2}Co_{0.2}O_2$ (NMC622, BASF) active materials with $Li_{2.7}Yb_{0.7}Zr_{0.3}Cl_6$ in a weight ratio of 80:20. The separator layer (~ 70 mg) is first pelletized followed by an additional palletization of halide solid electrolyte layer (~ 30 mg) at 1 ton. The as-prepared working electrode powder mixture (7 ~ 8 mg) was then spread on the halide SE side of pellet and pressed at 3 tons again to secure the contact between active material and SE. A Li-In alloy was used as a counter electrode. Galvanostatic cycling of the cell was carried out in the voltage range of 3 - 4.3 V vs Li/Li^+ for the LCO cell (1C = 137 $mAh \cdot g^{-1}$) and 2.8 - 4.3 V vs Li/Li^+ for the NMC622 (1C = 180 $mAh \cdot g^{-1}$) cell using a VMP3 (Bio-Logic) cycler.

7.3 Result and Discussion

Figure 7.1 shows the powder X-ray diffraction (XRD) patterns that reveal the structural evolution of Li_3YbCl_6 synthesized at temperatures from 350 ℃ up to 650 ℃. The XRD pattern of Li_3YbCl_6 prepared at 350 ℃ (Li_3YbCl_6-350) was indexed to a trigonal structure (*P*-3*m*1 space group), representing the first report of this phase. On increasing the synthesis temperature 400 ℃, the emergence of new reflections indicates the evolution of the *Pnma* orthorhombic phase (isostructural to Li_3LuCl_6).[31] The process is fully complete at 650 ℃ (**Figure 7.1a**). Further investigation of the structural evolution was conducted for different samples by holding the temperature at 350 ℃ at times ranging from 36 → 50 → 100 hours, using the same cooling rate in all cases. The corresponding XRD patterns (**Figure 7.2**) demonstrate that the trigonal phase is a kinetically-preferred, metastable material

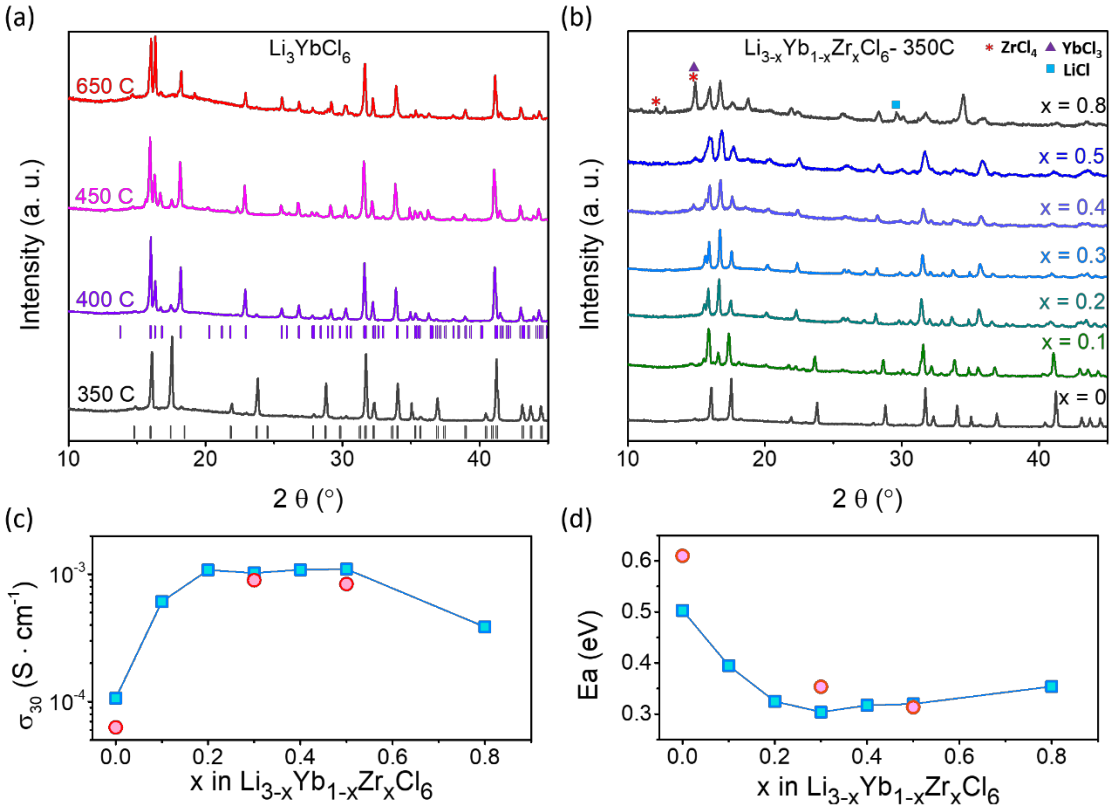

Figure 7.1 (a) XRD patterns of Li_3YbCl_6 prepared at 350, 400, 450, and 650 °C. Bragg positions of trigonal Li_3YbCl_6 (black markers) and orthorhombic Li_3YbCl_6 (purple markers) are indicated. (b) XRD patterns of $Li_{3-x}Yb_{1-x}Zr_xCl_6$ ($0 \leq x \leq 0.8$) synthesized at 350 °C. (c) Ionic conductivities measured at 30 °C and (d) corresponding activation energies for the $Li_{3-x}Yb_{1-x}Zr_xCl_6$-350 (blue squares) and -650 series (pink circles). The decrease in ion conductivity for x = 0.8 is attributed to the presence of insulating impurities apparent in the XRD pattern.

that converts to the more thermodynamically stable orthorhombic phase either through a long heat-treatment time or by employing high temperature. Its structure was determined by single-crystal X-ray diffraction at 273 K, refining in *P*-3*m*1 with lattice parameters of $a = 11.1110(19)$ Å and $c = 6.0014(10)$ Å (**Tables 7.1 - 7.3**). While the framework of trigonal Li_3YbCl_6-350 is isostructural to the thermodynamically stable form of Li_3ErCl_6,[31] the Li distribution in the lattice as determined by neutron diffraction is somewhat different (see below).

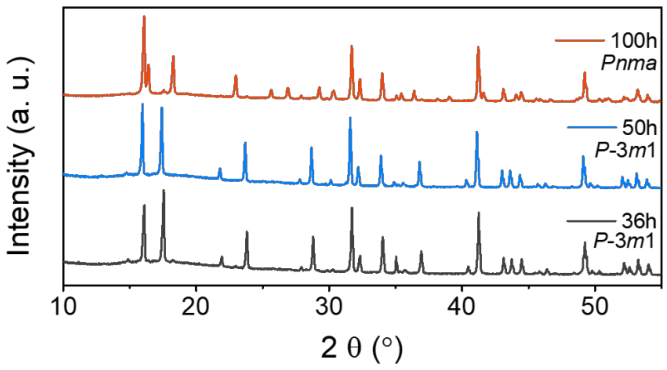

Figure 7.2 Powder XRD patterns of Li_3YbCl_6 samples heat treated at 350 C for 36 hours (bottom), 50 hours (middle) and 100 hours (top).

Aliovalent metal ion substitution to introduce vacancies in a mobile ion sublattice has been established as a strategy for improving the ionic conductivity of Li-ion conductors.[36, 43-46] **Figure 7.1b** shows the XRD patterns as a function of x for $Li_{3-x}Yb_{1-x}Zr_xCl_6$ synthesized at 350 °C ($0 \leq x \leq 0.8$; $Li_{3-x}Yb_{1-x}Zr_xCl_6$-350). Upon introducing even a small fraction of Zr^{4+} (i.e, x = 0.1) into the Li_3YbCl_6 lattice, growth of a new phase is signaled by the appearance of additional reflections in the XRD pattern. Rietveld refinement of powder neutron diffraction data (**Figure 7.9b** and **Table 7.6**) determine that for $x \geq 0.2$, $Li_{3-x}Yb_{1-x}Zr_xCl_6$-350 crystallizes in an orthorhombic structure (*Pnma* space group) which is different from orthorhombic Li_3YbCl_6 synthesized at 650 °C (**Figure 7.1a**). A solid solution exists in the range $0.2 \leq x \leq 0.5$, that exhibits a linear relationship in unit cell volume with variation in x (**Figure 7.3**). Traces of ex-solved impurities (LiCl, $ZrCl_4$, and $YbCl_3$) were observed for x = 0.6 and 0.7 compositions, which become significant for x = 0.8 shown in **Figure 7.1b**, indicating this composition lies beyond the solid solution regime. X-ray photoelectron spectroscopy (XPS) studies furthermore confirmed that the Yb^{3+} oxidation state is preserved up to x = 0.5 without any reduction of Yb^{3+} to Yb^{2+} by Zr^{4+} substitution (**Figure 7.4**). Since the XPS spectrum for Zr^{4+} 3d (175 ~ 190 eV)[47-49] and Cl^- 2p

Table 7.1 Atomic coordinates, occupation factor and equivalent isotropic displacement parameters of Li_3YbCl_6-350 collected from single crystal X-ray diffraction at 273 K

Crystal System			Trigonal			
Space Group			*P*-3*m*1 (no. 164)			
Lattice Parameter			*a* = 11.1110(19) Å *b* = 11.1110(19) Å *c* = 6.0014(10) Å			
Atom	Wyckoff position	x/a	y/b	z/c	Occ.	U_{equiv} (Å^2)
Li1	*6g*	0.339(5)	0	0	1	0.077(13)
Li2	*6h*	0.317(4)	0	1/2	0.5	0.015
Yb1	*1a*	0	0	0	1	0.0188(6)
Yb2	*2d*	1/3	2/3	0.5117(2)	0.967(3)	0.0183(4)
Yb3	*2d*	1/3	2/3	0.014(7)	0.033(3)	0.0183(4)
Cl1	*6i*	0.5551(2)	0.4449(2)	0.2433(6)	1	0.026(1)
Cl2	*6i*	0.2222(2)	0.7778(2)	0.2671(7)	1	0.026(1)
Cl3	*6i*	0.8867(2)	0.1133(2)	0.2316(6)	1	0.024(1)

Table 7.2 Anisotropic displacement parameters in Å^3 of Li_3YbCl_6-350 collected from single crystal X-ray diffraction at 273 K. Li sites are refined isotropically.

Atom	U_{11}	U_{22}	U_{33}	U_{23}	U_{13}	U_{12}
Yb1	0.0169(7)	0.0169(7)	0.0225(10)	0	0	0.0084(4)
Yb2	0.0170(5)	0.0170(5)	0.0209(7)	0	0	0.0085(3)
Yb3	0.0170(5)	0.0170(5)	0.0205(7)	0	0	0.0083(3)
Cl1	0.0326(19)	0.0326(19)	0.021(2)	0.0027(8)	-0.0027(8)	0.023(2)
Cl2	0.0295(18)	0.0295(18)	0.028(2)	0.0012(8)	-0.0012(8)	0.021(2)
Cl3	0.0230(16)	0.0230(16)	0.028(2)	-0.0027(8)	0.0027(8)	0.0130(18)

Table 7.3 Crystallographic data for Li_3YbCl_6-350 collected from single crystal X-ray diffraction at 273 K

Crystal data	
Formula	Li_3YbCl_6
Formula Weight	406.56
Crystal System	Trigonal
Space group	*P*-3*m*1
a, *b*, *c* (Å)	11.1110(19), 11.1110(19), 6.0014(10)
α, β, γ (°)	90, 90, 120
V (Å^3)	641.6(2)
Z	3
Calc. density (g/cm3)	3.157
Abs. coef. M (MoKa) (/mm)	12.706
F(000)	543
Crystal Size (mm)	0.01 x 0.02 x 0.04
Data Collection	
Temperature (K)	273(2)
Radiation (Å)	Mo-Kα, 0.71073
Theta range for data collection	2.1, 28.0
Index ranges	$-15 < h < 5$, $-7 < k < 15$, $-4 < l < 8$
Reflections collected	3126
Independent reflections	597 (R_{int}= 0.0650)
Completeness to θ = 25.242°	0.997%
Absorption correction	muli-scan (SADABS)
Max. and min transmission	0.7460, 0.6146
Refinement	
Refinement method	Full-matrix least squares on F2
Data / restraints / parameters	597 / 0 / 30
Goodness-of-fit on F2	0.93
Final R indices [I>2sigma(I)]	R1 = 0.0557, wR2 = 0.1089
R indices (all data)	R1 = 0.1019, wR2 = 0.1272
Extinction coefficient	n/a
Largest diff. peak and hole	2.16, -1.54

(195 ~ 210 eV)[47, 50] are overlapping with $Yb^{2+/3+}$ 4d peaks (170 ~ 225 eV),[51, 52] the XPS spectrum collected from the valence band region (0 ~ 20 eV) can better distinguish electron structure evolution for $Yb^{2+/3+}$.[53-55] In **Figure 7.4**, the XPS spectrum measured for $YbCl_3$ (top panel) and $Li_{3-x}Yb_{1-x}Zr_xCl_6$-350 series are shown with colored indicators corresponding to the different elements and their valence band peak positions. From the XPS spectra of $YbCl_3$ measured as a reference, the peaks centered at ~

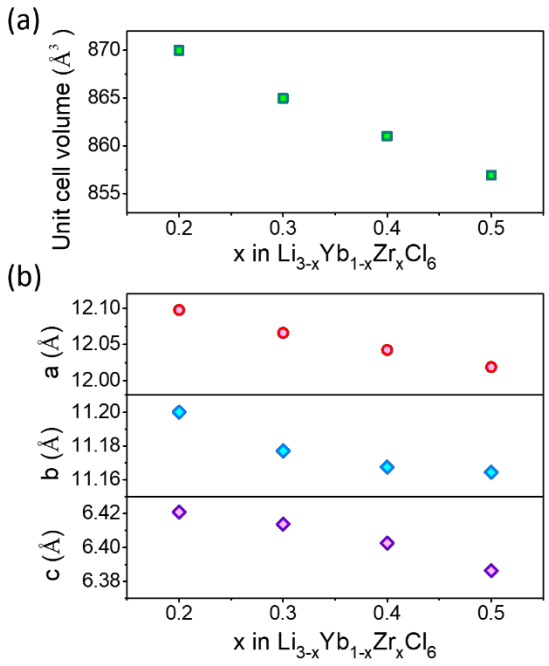

Figure 7.3 (a) The unit cell volumes of $Li_{3-x}Yb_{1-x}Zr_xCl_6$ ($0.2 \leq x \leq 0.5$). (b) The lattice parameters of $Li_{3-x}Yb_{1-x}Zr_xCl_6$ in the orthorhombic phase structure.

8 eV and ~ 13 eV stem from the valence band of Yb^{3+} 4f and the peak at ~ 16 eV is attributed to Cl^- 3s. The XPS spectra of Li_3YbCl_6-350 (x = 0) confirms that the oxidation state of Yb in Li_3YbCl_6-350 is 3+ as similar XPS peaks appear for $YbCl_3$. Comparing the XPS spectra of $Li_{3-x}Yb_{1-x}Zr_xCl_6$-350 series (x = 0.3, 0.5, and 0.8), the XPS peak at ~ 5 eV (shaded in orange) corresponds to overlapped Zr^{4+} 4d and Cl^- 3p peaks, which gradually increase up to x = 0.8, indicating the increased photoelectron attribution from the Zr^{4+} 4d band, whereas the XPS peak for Yb^{3+} 4f centered at ~ 13 eV (shaded in blue) decreased by Zr substitution. Meanwhile, there is no discernible XPS peak intensity change observed in the Yb^{2+} 4f region centered at ~ 2 eV (shaded in green) up to x = 0.5, while slight peak intensity increase observed for x = 0.8 indicating a possible Yb^{3+} reduction to Yb^{2+} from the compound. Although estimating the exact amount of Yb^{2+} from the materials is challenging due to the overlapping binding energy regions

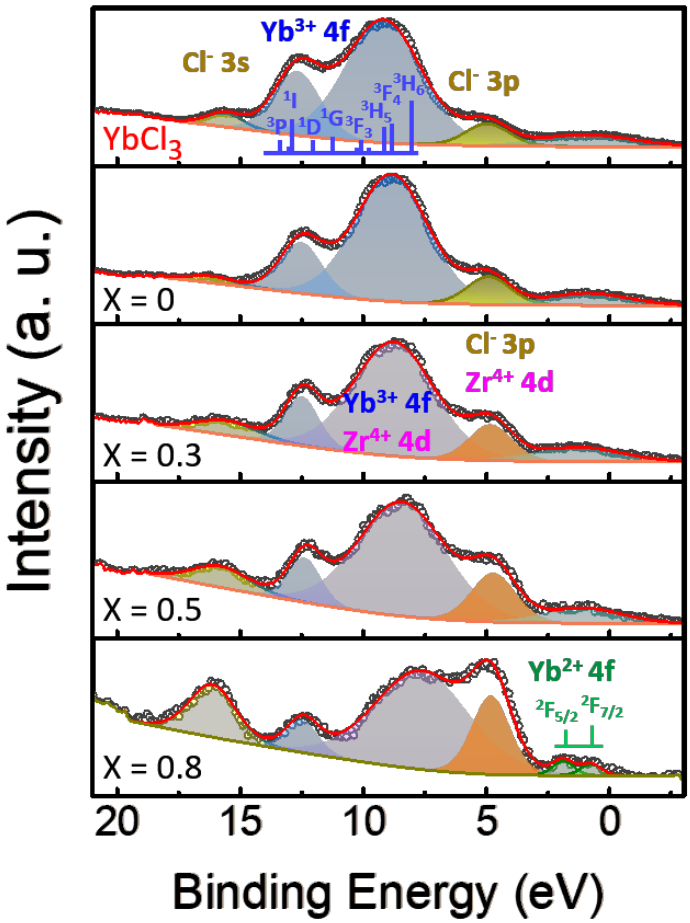

Figure 7.4 XPS in valence band region (- 3 ~ 21 eV) measured from $YbCl_3$ (top panel) and $Li_{3-x}Yb_{1-x}Zr_xCl_6$ - 350 series for x = 0, 0.3, 0.5, and 0.8 (from top down). The XPS spectra peaks shaded in different color indicates the XPS features from Cl 3s (yellow), Yb^{3+} 4f (blue), Zr^{4+} + Yb^{3+} 4f (pink), Cl^- 3p + Zr^{4+} 4d (orange) and Yb^{2+} 4f (green). It should be noted that the XPS peaks shaded in pink and orange area are not deconvoluted for the each corresponding elements.

of elements, the XPS results demonstrate that Yb^{3+} oxidation state is preserved upon Zr^{4+} substitution in the $Li_{3-x}Yb_{1-x}Zr_xCl_6$ series up to x = 0.5.

Structural evolution studies conducted for the $Li_{3-x}Yb_{1-x}Zr_xCl_6$ series synthesized at 650 °C ($Li_{3-x}Yb_{1-x}Zr_xCl_6$-650) (**Figure 7.5**) confirmed the same orthorhombic structure for x = 0.3 and 0.5 exhibited

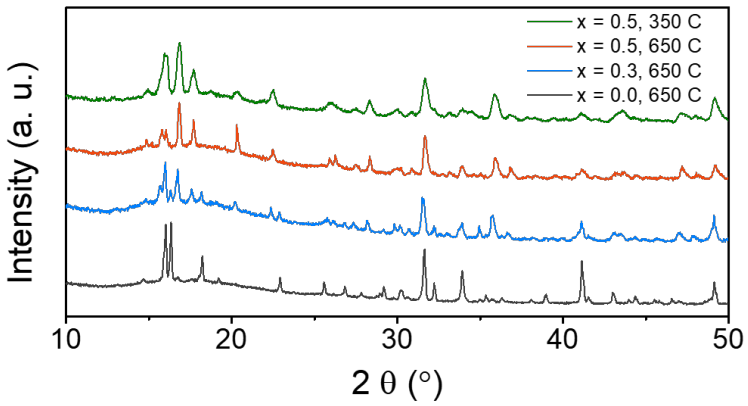

Figure 7.5 Powder XRD patterns of $Li_{3-x}Yb_{1-x}Z_xCl_6$ samples heat treated at 650 C for x = 0, x = 0.3 and x = 0.5. The broad background (2θ (°) = 12 ~ 23) is from kepton tape window from the sample holder.

by those compositions synthesized at 350 ℃. The XRD reflections exhibited a narrower linewidth, indicative of a greater crystalline coherence length owing to the higher synthesis temperature. Thus, the average transition metal ion radius in the $Li_{3-x}Yb_{1-x}Zr_xCl_6$ compounds determines the final crystal structure irrespective of the starting point.

The ionic conductivity of materials within the $Li_{3-x}Yb_{1-x}Zr_xCl_6$-350 and -650 series was measured by electrochemical impedance spectroscopy (EIS) at different temperatures.

Table 7.4 Summary of ionic conductivities and activation energies of $Li_{3-x}Yb_{1-x}Zr_xCl_6$-350 and $Li_{3-x}Yb_{1-x}Zr_xCl_6$-650 samples shown in Figure 1c and 1d

$Li_{3-x}Yb_{1-x}Zr_xCl_6$-350							
Zr content (x)	0	0.1	0.2	0.3	0.4	0.5	0.8
Ionic conductivity (mS·cm^{-1}, 30℃)	0.1	0.6	1.1	1.1	1.1	1.1	0.4
Activation Energy (eV)	0.5	0.39	0.32	0.30	0.31	0.31	0.35
$Li_{3-x}Yb_{1-x}Zr_xCl_6$-650							
Zr content (x)	0	0.1	0.2	0.3	0.4	0.5	0.8
Ionic conductivity (mS·cm^{-1}, 30℃)	0.06	-	-	0.9	-	0.8	-
Activation Energy (eV)	0.61	-	-	0.35	-	0.31	-

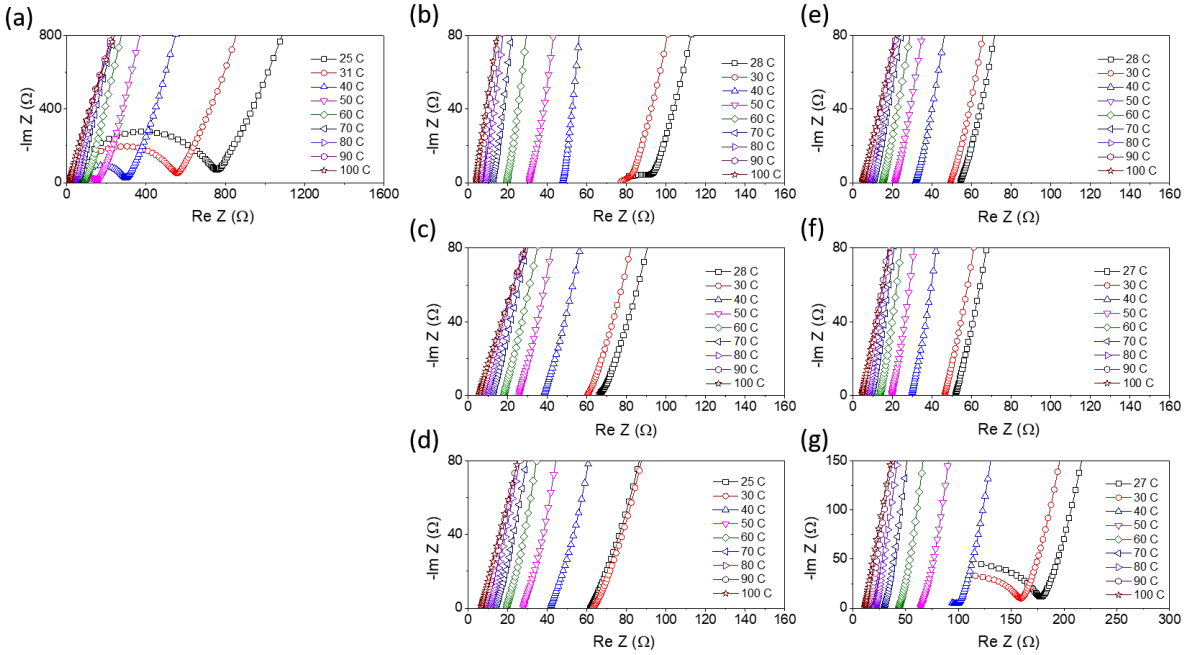

Figure 7.6 Nyquist plots of the $Li_{3-x}Yb_{1-x}Zr_xCl_6$ series synthesized at 350 °C for (a) x = 0 (b) x = 0.1 (c) x = 0.2 (d) x = 0.3 (e) x = 0.5 (f), and (g) x = 0.8.

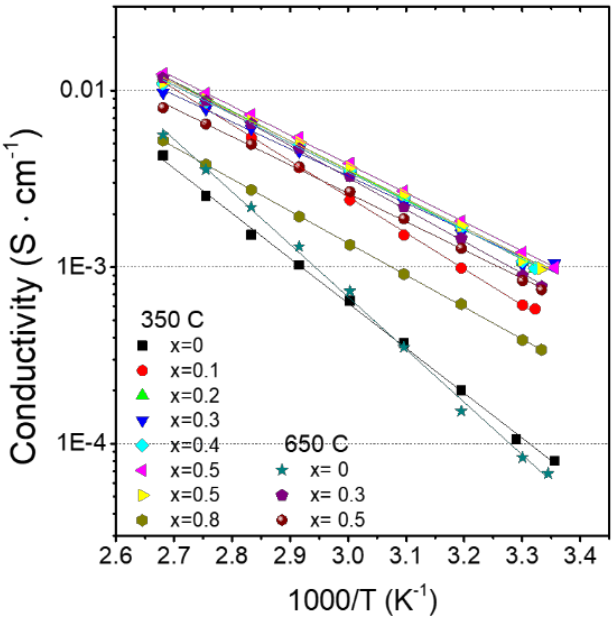

Figure 7.7 Arrhenius plots of the $Li_{3-x}Yb_{1-x}Zr_xCl_6$ series synthesized at 350 °C and 650 °C while Zr substitution for Yb in the compounds.

The data are plotted as a function of Zr content in **Figures 7.1c and 7.1d** and summarized in **Table 7.4**, and the corresponding Nyquist plots and Arrhenius plots to obtain activation energies are shown in **Figure 7.6 and 7.7**, respectively. The ionic conductivity of Li_3YbCl_6-650 shows two orders-of-magnitude higher conductivity (6.3×10^{-5} S·cm^{-1}, 30 °C) than that previously reported, which was measured at 110 °C (~ 1 x 10^{-7} S·cm^{-1}).[31] Trigonal Li_3YbCl_6-350 exhibits higher ionic conductivity (1.06×10^{-4} S·cm^{-1}, 30 °C) and lower activation energy (0.51 eV) than Li_3YbCl_6-650. Even more importantly, upon Zr-substitution, the conductivity of $Li_{3-x}Yb_{1-x}Zr_xCl_6$-350 increases to ~ 1.1 mS·cm^{-1} at x = 0.2, where only the orthorhombic phase is observed in the XRD pattern (**Figure 7.1b**). Such superionic behavior is maintained in the solid solution up to x = 0.5, and parallels the decrease in activation energy barrier from ~ 0.51 eV at x = 0 to ~ 0.30 eV at x = 0.2, and does not change significantly up to x = 0.5 (**Figure 7.1d**). The measured electronic conductivity at x = 0.3 is ~ 10^{-10} S cm^{-1}, which indicates a pure ionic conductor (**Figure 7.8**).

To gain insight into the improved ionic conductivity generated by Zr substitution, powder neutron diffraction (PND) studies were carried out on Li_3YbCl_6-350 and $Li_{2.7}Yb_{0.7}Zr_{0.3}Cl_6$-350 (x = 0.3), the latter being chosen due to its low activation energy.

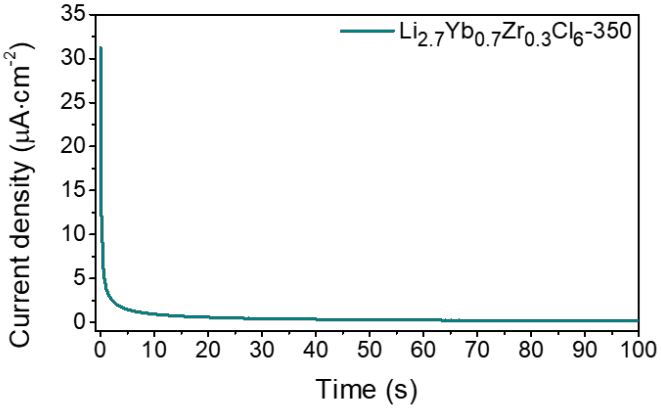

Figure 7.8 DC polarization result for the Ti|$Li_{2.7}Yb_{0.7}Zr_{0.3}Cl_6$|Ti cell with a voltage step of 1 V.

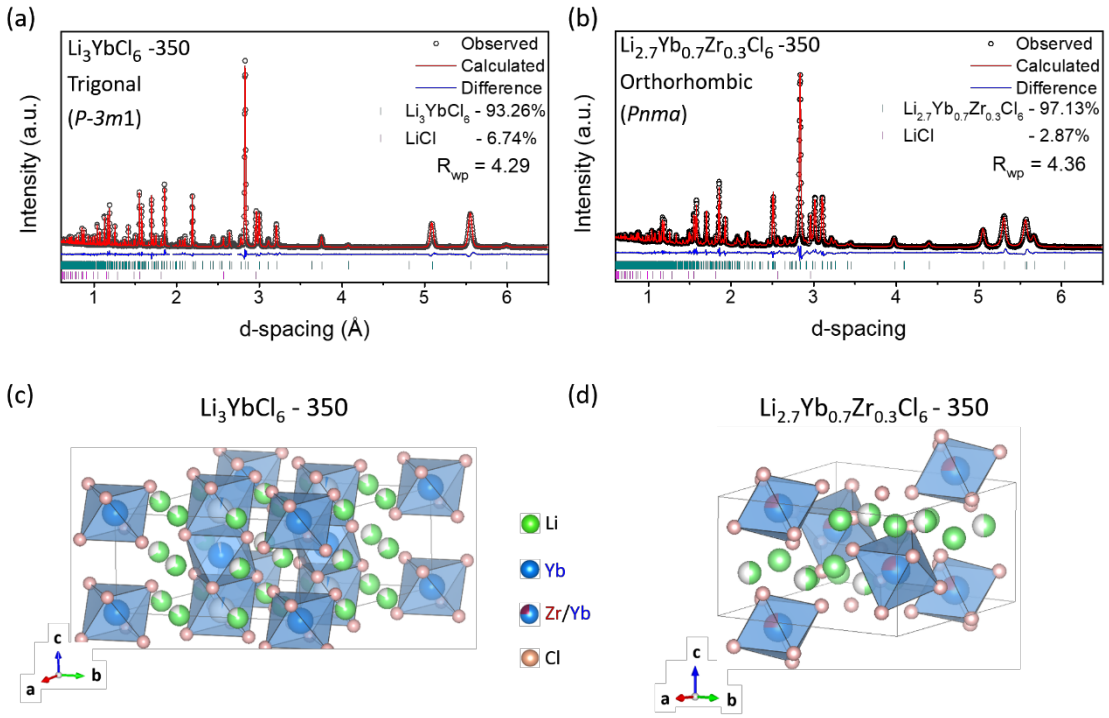

Figure 7.9 PND patterns and the corresponding Rietveld refinements for (a) Li_3YbCl_6-350 and (b) $Li_{2.7}Yb_{0.7}Zr_{0.3}Cl_6$-350 at 298 K. The experimental profile is shown in black empty circles; the red line denotes the calculated pattern; the difference profile is shown in blue, and calculated positions of the Bragg reflections are shown in green, and those of the minority impurity (LiCl) in pink. Crystal structures of (c) Li_3YbCl_6-350 and (d) $Li_{2.7}Yb_{0.7}Zr_{0.3}Cl_6$-350 based on the Rietveld refinements.

The lithium in the lattice is refinable by PND owing to its negative neutron scattering length (b = -1.9 pm) that provides clear contrast to the other elements that exhibit positive scattering lengths. Therefore, PND can locate the Li sites and identify their occupancies and atomic displacement parameters, along with determining the possibility of metal-Li anti-site disorder.

The PND patterns of the two compositions and their corresponding Rietveld fits and refinement results are displayed in **Figure 7.9a and 7.9b** and in **Table 7.5 and 7.6**, respectively. For Li_3YbCl_6-350, the data was fit by starting with the Yb-Cl framework of the model obtained from the single-crystal XRD study (where the Li occupancies were not refined), and freely refining all parameters with a fixed total Li occupancy of 1.5 to balance the charge. The resultant structure is shown in **Figure 7.9c**. The

Table 7.5 Atomic parameters of Li_3YbCl_6 obtained from refinement of powder neutron diffraction at 298K in *P*-3*m*1 (no. 164)[a]

Site	Wyck. Pos.	x	y	z	Occ	U_{iso} (Å^2)
Li1	*6g*	0.341(8)	0	0	0.83(6)	0.089(18)
Li2	*6h*	0.326(6)	0	1/2	0.67(6)	0.043(13)
Yb1	*1a*	0	0	0	1	0.012(2)
Yb2	*2d*	1/3	2/3	0.5096(9)	0.963(8)	0.011(1)
Yb3	*2d*	1/3	2/3	0.060(17)	0.037(8)	0.011(1)
Cl1	*6i*	0.5549(7)	0.4451(7)	0.2484(12)	1	0.026(2)
Cl2	*6i*	0.2208(4)	0.7792(4)	0.2732(11)	1	0.019(1)
Cl3	*6i*	0.8879(5)	0.1121(5)	0.2369(10)	1	0.014(1)

[a]Refinement lattice parameters: a = 11.1162(1) Å, b = 6.0005(1) Å, Refined composition: Li_3YbCl_6

Table 7.6 Atomic parameters of $Li_{2.7}Yb_{0.7}Zr_{0.3}Cl_6$ obtained from refinement of powder neutron diffraction at 298K in *Pnma* (no. 62)[b]

Site	Wyck. Pos.	x	y	z	Occ	U_{iso} (Å^2)
Li1	*8d*	0.128(3)	0.101(3)	0.124(5)	0.98(4)	0.041(8)
Li2	*8d*	0.376(7)	0.095(9)	0.161(12)	0.39(4)	0.041(8)
Yb	*4c*	0.3676(5)	1/4	0.5928(14)	0.74(2)	0.016(2)
Zr	*4c*	0.3676(5)	1/4	0.5928(14)	0.26(2)	0.016(2)
Cl1	*8d*	0.0114(5)	0.5834(8)	0.2451(10)	1	0.024(2)
Cl2	*8d*	0.2553(5)	0.0849(11)	0.4152(18)	1	0.021(1)
Cl3	*4c*	-0.0009(7)	1/4	0.2281(13)	1	0.013(2)
Cl4	*4c*	0.7470(8)	1/4	0.580(3)	1	0.019(2)

[b]Refinement lattice parameters: a = 12.0744(4) Å, b = 11.1577(6) Å, c = 6.4227(4) Å, Refined composition: $Li_{2.74}Yb_{0.74}Zr_{0.26}Cl_6$

PND refinement (**Table 7.5**) reveals that there are vacancies on the 6g site and a higher Li content in the 6h site than were originally fixed in the single–crystal XRD solution (1.0 and 0.5, respectively; **Table 7.1**). This gives rise to refined Li occupancies of 0.83(6) and 0.67(6) in the respective Li1 and Li2 sites in Li_3YbCl_6. The structure of $Li_{2.7}Yb_{0.7}Zr_{0.3}Cl_6$-350 (**Figure 7.9d, Table 7.6)** was refined (without constraints on Li occupancy) in the orthorhombic *Pnma* space group yielding a Li content of 2.74, very close to that targeted (2.7).

Figure 7.10a compares Li_3YbCl_6-350 and $Li_{2.7}Yb_{0.7}Zr_{0.3}Cl_6$-350 along three crystallographic directions, showing the structural changes created by aliovalent doping. Zr substitution triggers metal ion rearrangement and tilting of the $(Zr/Yb)Cl_6$ octahedra, similar to that observed in $Li_{3-x}(Er/Y)_{1-x}Zr_xCl_6$ ($0 \leq x \leq 0.6$) which also undergoes a phase transition from x = 0 (trigonal, *P*-3*m*1) to x = 0.6 (orthorhombic, *Pnma*).[36] The underlying factors responsible for improved ionic conductivity upon Zr substitution were determined by scrutinizing the activation energy barriers for the Li^+ ion pathways in Li_3YbCl_6-350 and $Li_{2.7}Yb_{0.7}Zr_{0.3}Cl_6$-350 using bond valence site energy (BVSE) calculations. This method reveals the paths that exist for the given structural model and allows for an approximate assessment of the *relative* heights of the barriers for transport, although the absolute values are typically higher than experiment.[41, 42] A 1D Li ion migration pathway in Li_3YbCl_6-350 passes through the face sharing Li1 and Li2 octahedral sites along the *c* axis (**Figure 7.10b**), with a modestly high activation energy barrier (**Figure 7.10e**); alternative pathways are of equivalently high energy. However, in $Li_{2.7}Yb_{0.7}Zr_{0.3}Cl_6$-350, the structural rearrangement afforded by Zr substitution generates an interstitial tetrahedral site between the Li1 and Li2 sites (denoted as □Tet, **Figure 7.10c**). The BVSE result (**Figure 7.10f**) shows it plays a key role in improving the ionic conductivity by providing an intermediate "stepstone" for Li^+ ion migration through the lattice. While our previous study on $Li_{2.5}Er_{0.5}Zr_{0.5}Cl_6$ - which has an analogous structure - showed that the corresponding tetrahedral site exhibits an occupancy of ~ 0.19 Li,[36] the PND refinement of $Li_{2.7}Yb_{0.7}Zr_{0.3}Cl_6$-350 (**Table 7.6**) suggests

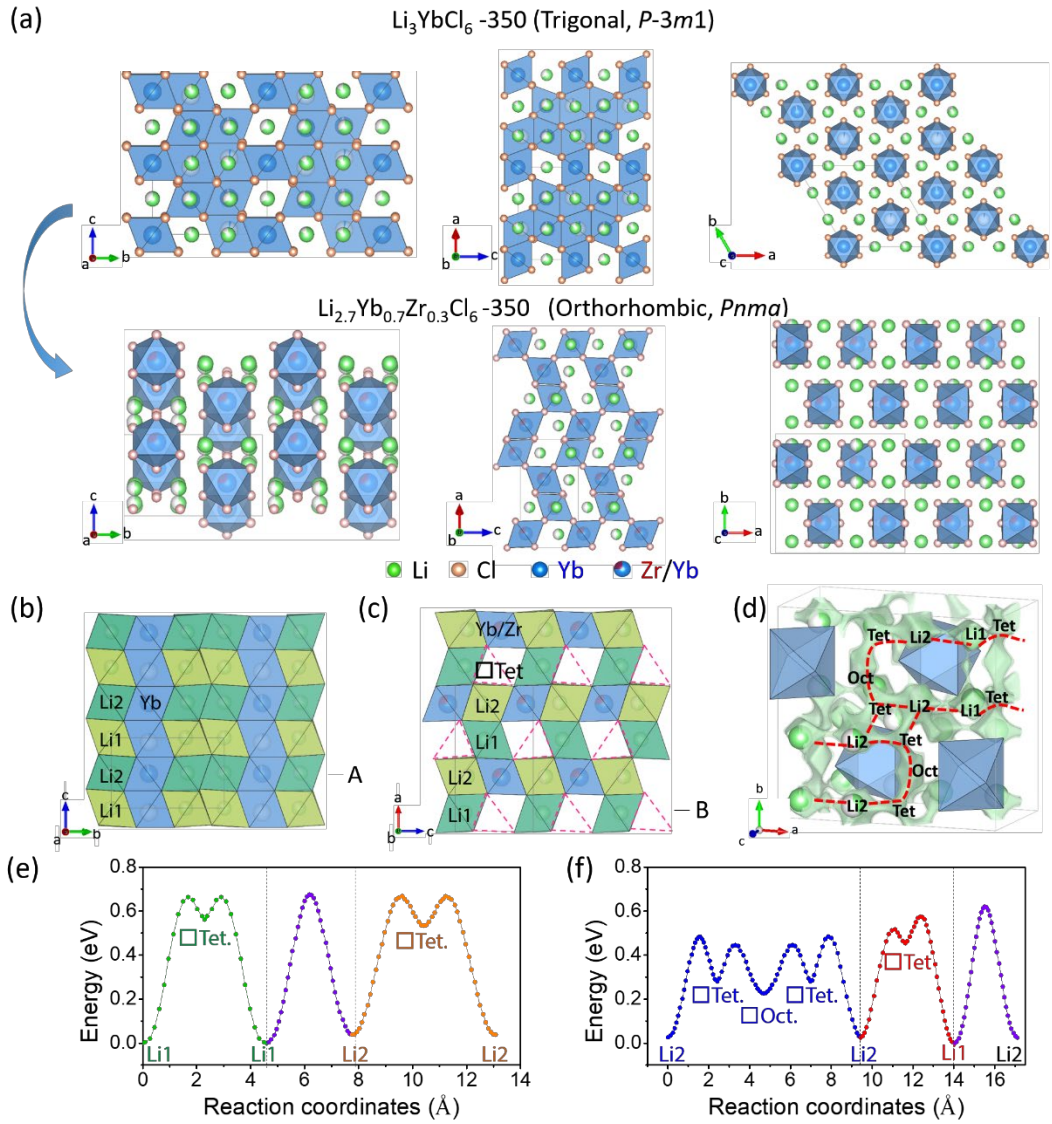

Figure 7.10 (a) Structural evolution of Li_3YbCl_6-350 to $Li_{2.7}Yb_{0.7}Zr_{0.3}Cl_6$-350 upon Zr substitution. Li site and □Tet site connectivity of (b) Li_3YbCl_6-350 along the [001] direction and (c) $Li_{2.7}Yb_{0.7}Zr_{0.3}Cl_6$-350 along the [100] direction. (d) Li^+ ion migration pathways in $Li_{2.7}Yb_{0.7}Zr_{0.3}Cl_6$-350 based on the bond valence site energy (BVSE) plot in panel (f). The green isosurface of constant $E_{BVSE(Li)}$ is superimposed on the crystal structure. BVSE model of migration energy barriers for (e) Li_3YbCl_6-350 and (f) $Li_{2.7}Yb_{0.7}Zr_{0.3}Cl_6$-350. The site energies are referenced to zero for the Li1 sites, which are the lowest energy. The direct path between the face-sharing Li1 and Li2 sites is delineated in purple in both structures. The portion in blue for $Li_{2.7}Yb_{0.7}Zr_{0.3}Cl_6$-350 is the lowest-energy Li^+ ion migration pathway along the [010] direction.

the tetrahedral site is unoccupied, and hence lies at a relatively higher energy. However, the occupation level may be too low to be readily detected. Furthermore, the BVSE study suggests that other metastable interstitial tetrahedral (□Tet) and octahedral (□Oct) sites also exist, which are shown in **Figure 7.10d**. These share trigonal faces (**Figure 7.11**) and form the [Li2-□Tet−□Oct.−□Tet−Li2] chain running along the [010] direction (blue curve, **Figure 7.10f**). Intersection of this 1D ion pathway with the [Li2−□Tet −Li1] path (red curve, **Figure 7.10f**) that runs along the [100] direction forms a 3D network.

The metastable sites also provide interconnected in-plane Li^+ migration pathways in the MCl_6 (M = Li, Yb, Zr) octahedral layers, evident by comparison of the (002) plane of Li_3YbCl_6-350 (the "A" layers in **Figure 7.10b**) with the (h00) planes of $Li_{2.7}Yb_{0.7}Zr_{0.3}Cl_6$-350 shown in **Figure 7.10c**. For reference, the MCl_6 layers in Li_3YbCl_6-350 and $Li_{2.7}Yb_{0.7}Zr_{0.3}Cl_6$-350 are represented as stacks of edge-sharing MCl_6 octahedral layers in **Figure 7.12a and 7.12b** respectively. In **Figure 7.13a,** the (002) plane of Li_3YbCl_6-350 and its corresponding isosurface of constant $E_{BVSE(Li)}$ for lithium indicate that the in-plane Li^+ ion pathway [Li2−□Tet−Li2] is restricted to the hexagonal space (red dotted line, **Figure 7.13a**) formed by six adjacent Li(2)Cl_6 octahedra that surround the □Oct site. Another Li^+ migration pathway (black arrow) is energetically unfavorable based on the BVSE landscape, likely because the electrostatic repulsive interaction between Li^+ and Yb^{3+} cations leads to a high Li^+ ion migration barrier. In contrast, in the (100) plane of $Li_{2.7}Yb_{0.7}Zr_{0.3}Cl_6$-350 shown in **Figure 7.13b** (i.e., the "B" layer in **Figure 7.10c**), the Li^+ ion migration pathway [Li1−□Tet –Li2] along the [001] direction connects the [Li2-□Tet−□Oct−□Tet−Li2] chains that form the 2D Li^+ ion migration network. While Li_3YbCl_6-350 exhibits restricted Li^+ ion migration, the 2D in-plane Li^+ migration pathways in all of the MCl_6 layers of $Li_{2.7}Yb_{0.7}Zr_{0.3}Cl_6$-350 contribute to enhanced Li^+ ion transport owing to a larger fraction of □Oct sites.

Overall, the comparison of the BVSE landscape between Li_3YbCl_6-350 and $Li_{2.7}Yb_{0.7}Zr_{0.3}Cl_6$-350 (**Figure 7.10e and 7.10f**) shows ~ 30 % lower activation energy barriers for Li^+ ion migration in

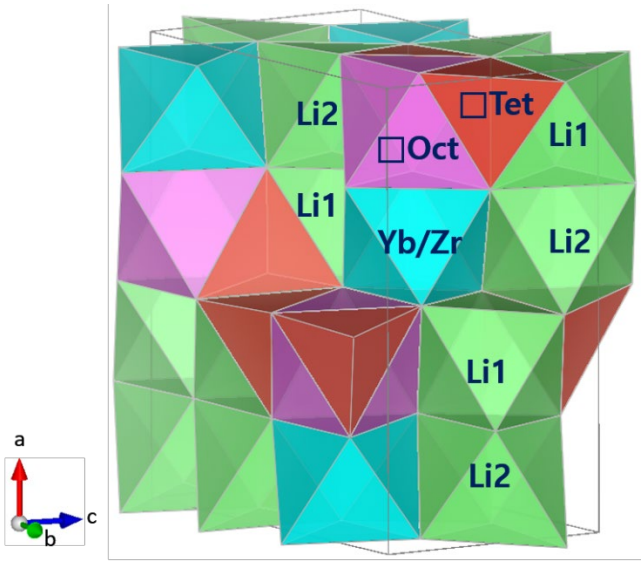

Figure 7.11 The unit cell of $Li_{2.7}Yb_{0.7}Zr_{0.3}Cl_6$-350 showing the arrangement of cation polyhedral and □ Oct and □ Tet vacancies in the crystal.

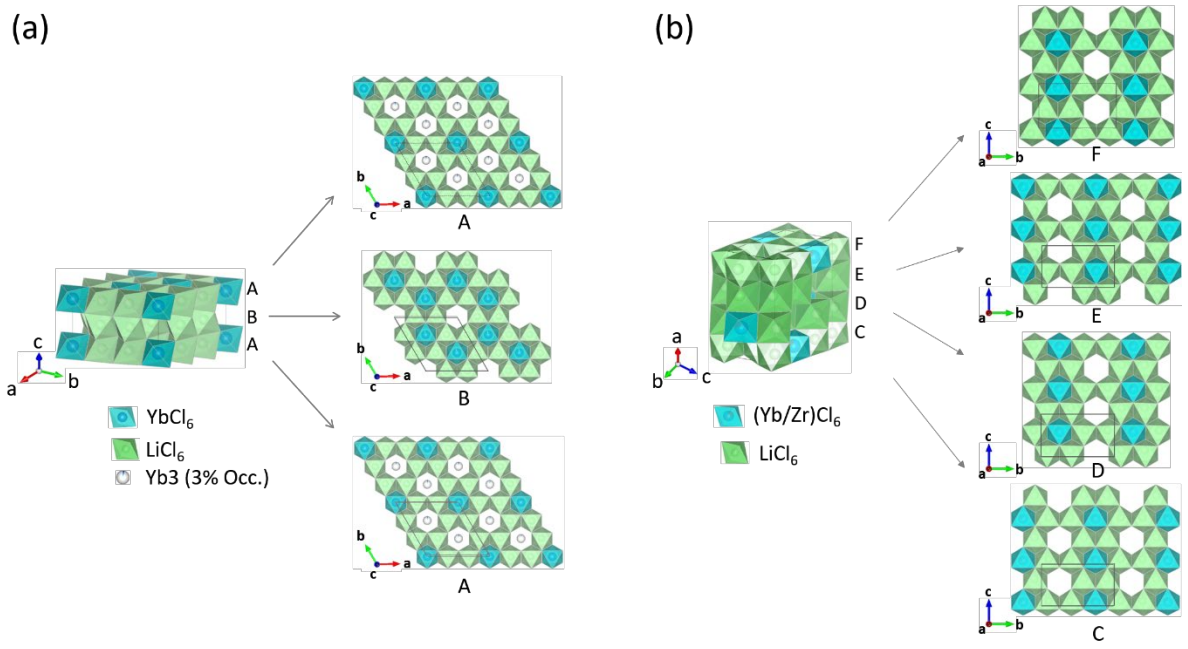

Figure 7.12 Schematic presentation of (a) Li_3YbCl_6-350 and (b) $Li_{2.7}Yb_{0.7}Zr_{0.3}Cl_6$-350 showing the layers consisting of the corresponding crystal structures. The Yb(3)-Cl octahedral in (a) Li_3YbCl_6-350 is omitted due to the low site occupancy (3 %).

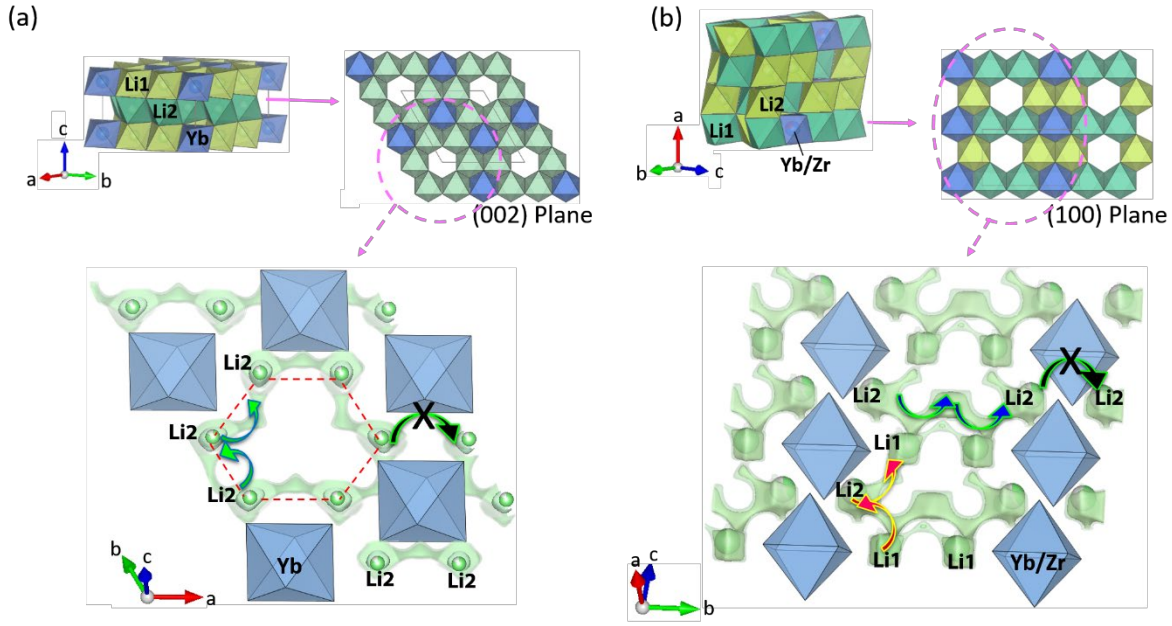

Figure 7.13 Comparison of the (a) (002) plane in the Li_3YbCl_6-350 and (b) (100) plane in $Li_{2.7}Yb_{0.7}Zr_{0.3}Cl_6$-350 structures and Li^+ ion migration pathways derived from BVSE calculations. The green isosurface of constant $E_{BVSE(Li)}$ is superimposed on the corresponding structure. Green and red arrows in the BVSE maps in (a) and (b) indicate the Li^+ migration pathways passing through the □Tet site. Green and red arrows in (a) and (b) indicate the Li1-□Tet-Li2 Li^+ migration pathway. Blue arrows in (b) indicate the [Li2-□Tet−□Oct.−□Tet−Li2] migration pathway running along the [010] direction in the *bc* plane of $Li_{2.7}Yb_{0.7}Zr_{0.3}Cl_6$-350. Black arrows indicate restricted Li^+ ion migration pathways.

the latter, indicating that the metastable tetrahedral and octahedral interstitial sites play a key role in flattening the energy landscape and improving ionic conductivity.

Liu et al. also recently reported first-principles calculations of metal chloride Li^+ ion conductors that suggest the concentration and configuration of the metal cations surrounding the Li sites affect the ionic conductivity.[56] These calculations confirmed our previous[36] and current experimental findings, namely that aliovalent cation (e.g. Zr^{4+}) substitution in $Li_3M'Cl_6$ (e.g., M' = Sc^{3+}, In^{3+}, Y^{3+}, Er^{3+}) can lower the Li^+ ion migration barrier by inducing structural changes that generate interstitial Li ion sites for hops (as described above in **Figure 7.10e and 7.10f**). Their computational study also indicated that

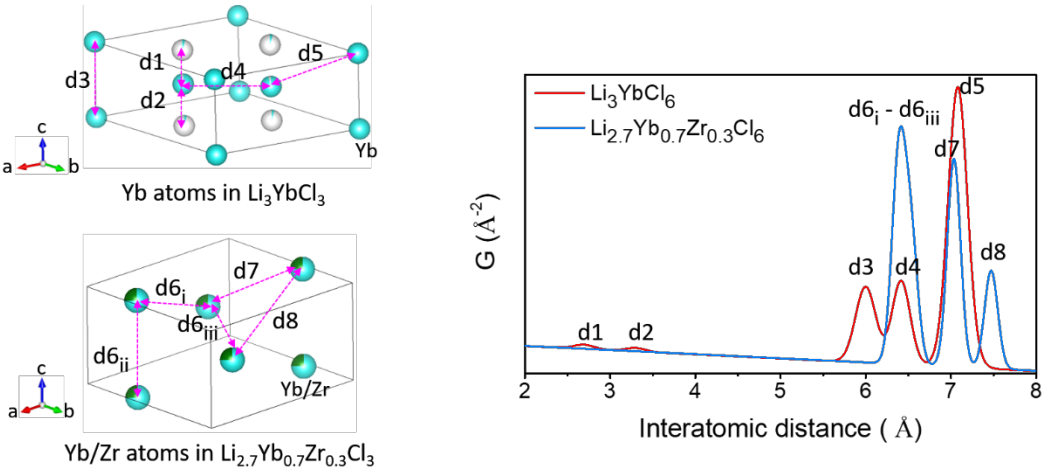

Figure 7.14 (Left) The Yb/Zr atoms in Li_3YbCl_6-350 and $Li_{2.7}Yb_{0.7}Zr_{0.3}Cl_6$-350 structures from PND refinement (**Tables 7.5 and 7.6**) and (Right) their simulated X-ray pair distribution function (PDF) profiles. The PDF profiles show the atomic distance distribution between Yb/Zr atoms in the materials. The relatively short interatomic distance between Yb atoms in Li_3YbCl_6-350, d1 (~ 2.7 Å), d2 (~ 3.3 Å), and d3 (~ 6.0 Å), are absent in $Li_{2.7}Yb_{0.7}Zr_{0.3}Cl_6$-350, indicating the more dispersed Yb/Zr atoms in the $Li_{2.7}Yb_{0.7}Zr_{0.3}Cl_6$-350 structure.

the migration barrier is lowered in the case of a sparse distribution of metal cations surrounding the Li^+ ions. Inspired by this finding, we compared the simulated pair distribution function (PDF) profiles for the Yb^{3+}/Zr^{4+} ions in Li_3YbCl_6-350 and $Li_{2.7}Yb_{0.7}Zr_{0.3}Cl_6$-350 (**Tables 7.5 and 7.6** and **Figure 7.14**). These show that the short distances of 2.7 Å, 3.3 Å, and 6.0 Å between the Yb^{3+} ions in Li_3YbCl_6-350 are absent for Yb/Zr contacts in $Li_{2.7}Yb_{0.7}Zr_{0.3}Cl_6$-350. The presence of statistically more dispersed non-Li metal atoms in the latter material may also play a role in increasing the conductivity.

Cyclic voltammetry (CV) studies were performed to assess the electrochemical stability of $Li_{2.7}Yb_{0.7}Zr_{0.3}Cl_6$-350. A cell consisting of ($Li_{2.7}Yb_{0.7}Zr_{0.3}Cl_6$-350 + Super P, 95:5 wt%)|glassy (g)-Li_3PS_4|Li-In was assembled and cycled between 2.8 V ~ 5.0 V (V vs. Li/Li^+) at a 1 $mV{\cdot}s^{-1}$ scan rate. The CV curve in **Figure 7.15a** shows an anodic current onset potential of ~ 4.3 V. This electrochemical

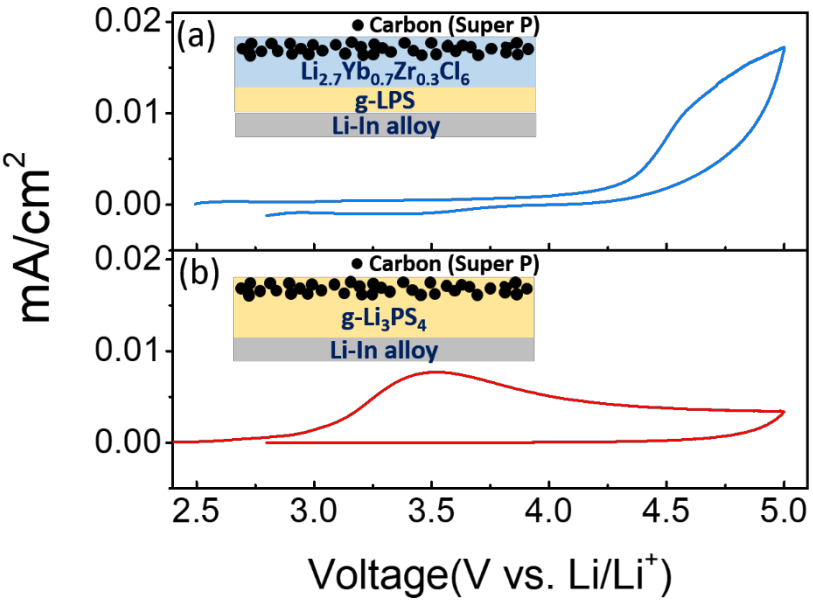

Figure 7.15 Evaluation of electrochemical oxidative stability. The first cyclic voltammetry results for (a) $Li_{2.7}Yb_{0.7}Zr_{0.3}Cl_6$+carbon (Super P)|g-LPS|Li-In cell and (b) g-LPS+carbon (Super P)|g-LPS|Li-In cell with a scan rate 1mV·s^{-1}. A solid electrolyte and carbon (super P) mixture (95:5 wt%) is used as a working electrode. The schematic used cell configurations and materials are described as insets.

stability limit is much higher than in sulfide solid electrolytes (typically about 2.7 V (**Figure 7.15b**)). The consecutive cathodic scan to 2.8 V shows no discernible reduction current peak as expected, since reduction of Yb^{3+} to Yb^{2+} would occur near ~ 1.9 V (V vs. Li/Li$^+$).[57] Therefore, $Li_{2.7}Yb_{0.7}Zr_{0.3}Cl_6$-350 is electrochemically stable within the potential range of 2.8 V - 4.3 V and the material can be paired with > 4 V-class cathode materials for ASSB applications.

The electrochemical performance of $Li_{2.7}Yb_{0.7}Zr_{0.3}Cl_6$-350 in ASSBs was examined at room-temperature employing either bare, non-coated $LiCoO_2$ (LCO) or $LiNi_{0.6}Mn_{0.2}Co_{0.2}O_2$ (NMC622) as the cathode active material (CAM). The CAM was mixed with $Li_{2.7}Yb_{0.7}Zr_{0.3}Cl_6$-350 solid electrolyte in a 8:2 weight ratio to form the catholyte, and the composite positive electrodes were paired with Li-

In alloy as the anode and a sulfide solid electrolyte separator (see **Figure 7.16a and 7.16c**). In **Figure 7.16a**, the first and second charge/discharge profiles of an LCO ASSB employing a conventional glassy-Li_3PS_4 separator (a-LPS, σ = ~ 0.5 mS·cm^{-2}) are displayed. The cell was cycled at a current density of 0.1 C within a voltage window of 3.0 V ~ 4.3 V at room-temperature and exhibits stable electrochemical performance with a discharge capacity of ~ 125 mAh·g^{-1}. Cell cycling at 0.5 C (0.55 mA·g-1) performed after the rate capability test (**Figure 7.16b**) shows very good capacity retention of ~ 90 % over 200 cycles with high coulombic efficiency (> 99.7 %).

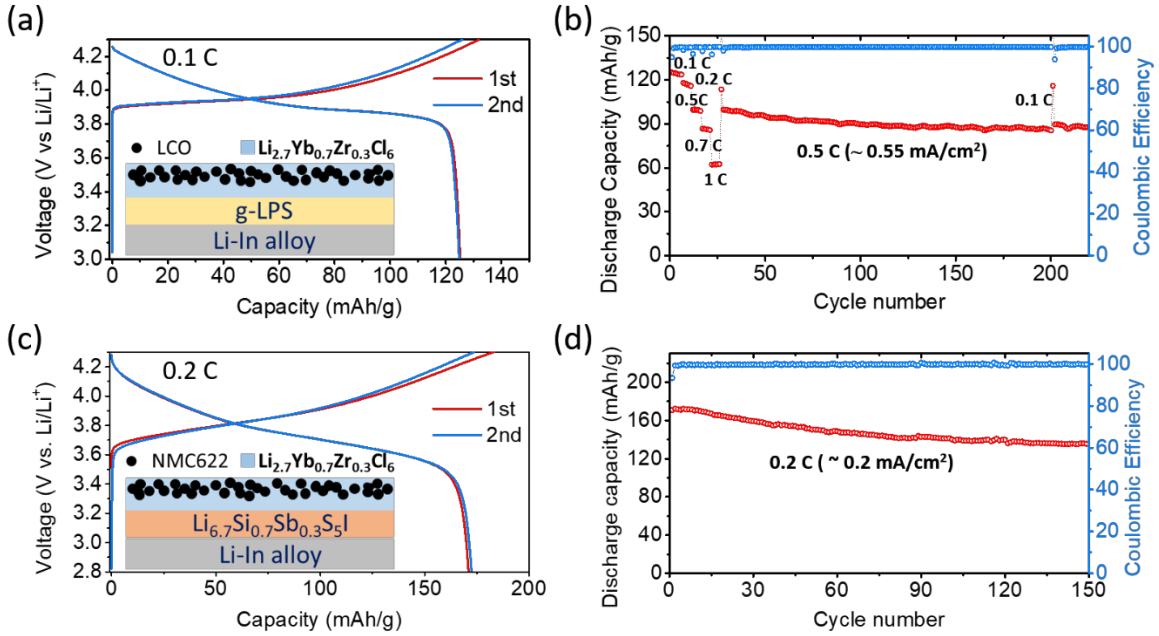

Figure 7.16 Electrochemical performance of (a), (b) LCO and (c), (d) NMC622 ASSBs using $Li_{2.7}Yb_{0.7}Zr_{0.3}Cl_6$-350 as the solid electrolyte cycled between 3.0 V ~ 4.3 V and 2.8 V ~ 4.3 V (V vs. Li/Li^+), respectively. Glassy g-LPS was used as a separator for the LCO ASSB, and a $Li_{6.7}Si_{0.7}Sb_{0.3}S_5I$ separator was used for NMC622 ASSB as shown in the diagrams. Charge/discharge profiles from the initial two cycles of (a) LCO ASSB at 0.1 C and (c) NMC622 ASSB at 0.2 C, and their corresponding charge/discharge capacity and coulombic efficiency as a function of cycle number for (b) LCO and (d) NMC 622 ASSBs.

The performance of a representative NMC622 cell cycled between 2.8 V ~ 4.3 V at a two-fold higher current density of 0.2 C (~ 0.2 $mA \cdot g^{-1}$) is shown in **Figure 7.16c** and **7.16d**. Here, to reduce the cell resistance, an ultra-high conductivity argyrodite ($Li_{6.7}Si_{0.7}Sb_{0.3}S_5I$; σ = ~ 10 $mS \cdot cm^{-1}$) solid electrolyte[38] separator was employed. The initial cycling profiles of the NMC622 cell in **Figure 5c** shows an initial charge/discharge performance with discharge capacity of ~ 170 $mAh \cdot g^{-1}$ and good capacity retention of ~ 80 % with columbic efficiency of > 99.6 % over 150 cycles. The capacity fading of the NMC622 ASSB may be partly attributed to the volume expansion of polycrystalline NMC622 particles which increases the overall impedance upon cell cycling due to particle cracking and contact loss between NMC622 and solid electrolyte.[58-60] Using binders or suppressing the volume change of cathode material through doping could improve the performance.

7.4 Conclusions

We report a new metastable trigonal polymorph of Li_3YbCl_6 and the Zr substituted orthorhombic solid solution phase, $Li_{3-x}Yb_{1-x}Zr_xCl_6$ ($0.2 \leq x < 0.8$), that are synthesized at a relatively low temperature of 350 °C. The materials are promising solid electrolytes, which exhibit superionic conductivity up to 1.1 $mS \cdot cm^{-1}$ at room temperature. Zr-substitution lowers the Li^+ ion migration energy barrier in the crystal structure by introducing additional interstitial sites for Li^+ ion migration and sparsely distributing non-Li metal cations in the vicinity of the Li sites. The $Li_{2.7}Yb_{0.7}Zr_{0.3}Cl_6$ solid electrolyte enables the use of uncoated, bare 4 V-class cathode materials (LCO and NMC622) as demonstrated by the good cycling performance of the corresponding ASSBs due to the excellent electrochemical oxidation stability of the electrolyte, and relative chemical compatibility with the oxide cathode active materials. We believe these findings can be applied to other metal chloride systems and further provide important advances for designing practical ASSBs.

References

(1) Kwade, A.; Haselrieder, W.; Leithoff, R.; Modlinger, A.; Dietrich, F.; Droeder, K. Current status and challenges for automotive battery production technologies. Nat Energy 2018, 3 (4), 290-300.

(2) Turcheniuk, K.; Bondarev, D.; Singhal, V.; Yushin, G. Ten years left to redesign lithium-ion batteries Reserves of rare metals used in electric-vehicle cells are dwindling, so boost research on iron and silicon alternatives, urge Kostiantyn Turcheniuk and colleagues. Nature 2018, 559 (7715), 467-470.

(3) Aurbach, D. Review of selected electrode-solution interactions which determine the performance of Li and Li ion batteries. J Power Sources 2000, 89 (2), 206-218.

(4) Etacheri, V.; Marom, R.; Elazari, R.; Salitra, G.; Aurbach, D. Challenges in the development of advanced Li-ion batteries: a review. Energ Environ Sci 2011, 4 (9), 3243-3262.

(5) Yu, X. W.; Manthiram, A. Electrode-electrolyte interfaces in lithium-based batteries. Energ Environ Sci 2018, 11 (3), 527-543.

(6) Xu, K. Electrolytes and Interphases in Li-Ion Batteries and Beyond. Chem Rev 2014, 114 (23), 11503-11618.

(7) Li, W. D.; Song, B. H.; Manthiram, A. High-voltage positive electrode materials for lithium-ion batteries. Chem Soc Rev 2017, 46 (10), 3006-3059.

(8) Li, W. D.; Dolocan, A.; Oh, P.; Celio, H.; Park, S.; Cho, J.; Manthiram, A. Dynamic behaviour of interphases and its implication on high-energy-density cathode materials in lithium-ion batteries. Nat Commun 2017, 8.

(9) Arbizzani, C.; Gabrielli, G.; Mastragostino, M. Thermal stability and flammability of electrolytes for lithium-ion batteries. J Power Sources 2011, 196 (10), 4801-4805.

(10) Murmann, P.; Schmitz, R.; Nowak, S.; Ignatiev, N.; Sartori, P.; Celdc-Laskovic, I.; Winter, M. Electrochemical Performance and Thermal Stability Studies of Two Lithium Sulfonyl Methide Salts in Lithium-Ion Battery Electrolytes. J Electrochem Soc 2015, 162 (9), A1738-A1744.

(11) Cao, X.; Ren, X. D.; Zou, L. F.; Engelhard, M. H.; Huang, W.; Wang, H. S.; Matthews, B. E.; Lee, H.; Niu, C. J.; Arey, B. W.; Cui, Y.; Wang, C. M.; Xiao, J.; Liu, J.; Xu, W.; Zhang, J. G. Monolithic solid-electrolyte interphases formed in fluorinated orthoformate-based electrolytes minimize Li depletion and pulverization. Nat Energy 2019, 4 (9), 796-805.

(12) Janek, J.; Zeier, W. G. A solid future for battery development. Nat Energy 2016, 1.

(13) Famprikis, T.; Canepa, P.; Dawson, J. A.; Islam, M. S.; Masquelier, C. Fundamentals of inorganic solid-state electrolytes for batteries. Nat Mater 2019, 18 (12), 1278-1291.

(14) Sakuda, A.; Hayashi, A.; Tatsumisago, M. Sulfide Solid Electrolyte with Favorable Mechanical Property for All-Solid-State Lithium Battery. Sci Rep-Uk 2013, 3.

(15) Hayashi, A.; Sakuda, A.; Tatsumisago, M. Development of Sulfide Solid Electrolytes and Interface Formation Processes for Bulk-Type All-Solid-State Li and Na Batteries. Front Energy Res 2016, 4.

(16) Kato, A.; Nose, M.; Yamamoto, M.; Sakuda, A.; Hayashi, A.; Tatsumisago, M. Mechanical properties of sulfide glasses in all-solid-state batteries. J Ceram Soc Jpn 2018, 126 (9), 719-727.

(17) Kamaya, N.; Homma, K.; Yamakawa, Y.; Hirayama, M.; Kanno, R.; Yonemura, M.; Kamiyama, T.; Kato, Y.; Hama, S.; Kawamoto, K.; Mitsui, A. A lithium superionic conductor. Nat Mater 2011, 10 (9), 682-686.

(18) Kato, Y.; Hori, S.; Saito, T.; Suzuki, K.; Hirayama, M.; Mitsui, A.; Yonemura, M.; Iba, H.; Kanno, R. High-power all-solid-state batteries using sulfide superionic conductors. Nat Energy 2016, 1.

(19) de Klerk, N. J. J.; Roslon, T.; Wagemaker, M. Diffusion Mechanism of Li Argyrodite Solid Electrolytes for Li-Ion Batteries and Prediction of Optimized Halogen Doping: The Effect of Li Vacancies, Halogens, and Halogen Disorder. Chem Mater 2016, 28 (21), 7955-7963.

(20) Kraft, M. A.; Culver, S. P.; Calderon, M.; Bocher, F.; Krauskopf, T.; Senyshyn, A.; Dietrich, C.; Zevalkink, A.; Janek, J.; Zeier, W. G. Influence of Lattice Polarizability on the Ionic Conductivity in the Lithium Superionic Argyrodites Li6PS5X (X = Cl, Br, I). J Am Chem Soc 2017, 139 (31), 10909-10918.

(21) Adeli, P.; Bazak, J. D.; Park, K. H.; Kochetkov, I.; Huq, A.; Goward, G. R.; Nazar, L. F. Boosting Solid-State Diffusivity and Conductivity in Lithium Superionic Argyrodites by Halide Substitution. Angew Chem Int Edit 2019, 58 (26), 8681-8686.

(22) Richards, W. D.; Miara, L. J.; Wang, Y.; Kim, J. C.; Ceder, G. Interface Stability in Solid-State Batteries. Chem Mater 2016, 28 (1), 266-273.

(23) Zhu, Y. Z.; He, X. F.; Mo, Y. F. First principles study on electrochemical and chemical stability of solid electrolyte-electrode interfaces in all-solid-state Li-ion batteries. J Mater Chem A 2016, 4 (9), 3253-3266.

(24) Banerjee, A.; Tang, H. M.; Wang, X. F.; Cheng, J. H.; Nguyen, H.; Zhang, M. H.; Tang, D. H. S.; Wynn, T. A.; Wu, E. A.; Doux, J. M.; Wu, T. P.; Ma, L.; Sterbinsky, G. E.; D'Souza, M. S.; Ong, S. P.; Meng, Y. S. Revealing Nanoscale Solid-Solid Interfacial Phenomena for Long-Life and High-Energy All-Solid-State Batteries. Acs Appl Mater Inter 2019, 11 (46), 43138-43145.

(25) Swamy, T.; Chen, X. W.; Chiang, Y. M. Electrochemical Redox Behavior of Li Ion Conducting Sulfide Solid Electrolytes. Chem Mater 2019, 31 (3), 707-713.

(26) Dewald, G. F.; Ohno, S.; Kraft, M. A.; Koerver, R.; Till, P.; Vargas-Barbosa, N. M.; Janek, J.; Zeier, W. G. Experimental Assessment of the Practical Oxidative Stability of Lithium Thiophosphate Solid Electrolytes. Chem Mater 2019, 31 (20), 8328-8337.

(27) Ohta, N.; Takada, K.; Sakaguchi, I.; Zhang, L. Q.; Ma, R. Z.; Fukuda, K.; Osada, M.; Sasaki, T. LiNbO3-coated LiCoO2 as cathode material for all solid-state lithium secondary batteries. Electrochem Commun 2007, 9 (7), 1486-1490.

(28) Zhang, W. B.; Weber, D. A.; Weigand, H.; Arlt, T.; Manke, I.; Schroder, D.; Koerver, R.; Leichtweiss, T.; Hartmann, P.; Zeier, W. G.; Janek, J. Interfacial Processes and Influence of Composite Cathode Microstructure Controlling the Performance of All-Solid-State Lithium Batteries. Acs Appl Mater Inter 2017, 9 (21), 17835-17845.

(29) Jung, S. H.; Oh, K.; Nam, Y. J.; Oh, D. Y.; Bruner, P.; Kang, K.; Jung, Y. S. Li3BO3-Li2CO3: Rationally Designed Buffering Phase for Sulfide All Solid-State Li-Ion Batteries. Chem Mater 2018, 30 (22), 8190-8200.

(30) Steiner, H. J.; Lutz, H. D. Novel Fast Ion Conductors of the Type M(I)3m(Iii)Cl6 (M(I) = Li, Na, Ag, M(Iii) = in, Y). Z Anorg Allg Chem 1992, 613 (7), 26-30.

(31) Bohnsack, A.; Stenzel, F.; Zajonc, A.; Balzer, G.; Wickleder, M. S.; Meyer, G. Ternary halides of the A(3)MX(6) type .6. Ternary chlorides of the rare-earth elements with lithium, Li3MCl6 (M=Tb-Lu, Y, Sc): Synthesis, crystal structures, and ionic motion. Z Anorg Allg Chem 1997, 623 (7), 1067-1073.

(32) Li, X. N.; Liang, J. W.; Luo, J.; Banis, M. N.; Wang, C. H.; Li, W. H.; Deng, S. X.; Yu, C.; Zhao, F. P.; Hu, Y. F.; Sham, T. K.; Zhang, L.; Zhao, S. Q.; Lu, S. G.; Huang, H.; Li, R. Y.; Adair, K. R.; Sun, X. L. Air-stable Li3InCl6 electrolyte with high voltage compatibility for all-solid-state batteries. Energ Environ Sci 2019, 12 (9), 2665-2671.

(33) Muy, S.; Voss, J.; Schlem, R.; Koerver, R.; Sedlmaier, S. J.; Maglia, F.; Lamp, P.; Zeier, W. G.; Shao-Horn, Y. High-Throughput Screening of Solid-State Li-Ion Conductors Using Lattice-Dynamics Descriptors. Iscience 2019, 16, 270-+.

(34) Kwak, H.; Han, D.; Lyoo, J.; Park, J.; Jung, S. H.; Han, Y.; Kwon, G.; Kim, H.; Hong, S. T.; Nam, K. W.; Jung, Y. S. New Cost-Effective Halide Solid Electrolytes for All-Solid-State Batteries: Mechanochemically Prepared Fe3+-Substituted Li2ZrCl6. Adv Energy Mater 2021, DOI:ARTN 2003190 10.1002/aenm.202003190.

(35) Asano, T.; Sakai, A.; Ouchi, S.; Sakaida, M.; Miyazaki, A.; Hasegawa, S. Solid Halide Electrolytes with High Lithium-Ion Conductivity for Application in 4 V Class Bulk-Type All-Solid-State Batteries. Adv Mater 2018, 30 (44).

(36) Park, K. H.; Kaup, K.; Assoud, A.; Zhang, Q.; Wu, X. H.; Nazar, L. F. High-Voltage Superionic Halide Solid Electrolytes for All-Solid-State Li-Ion Batteries. Acs Energy Lett 2020, 5 (2), 533-539.

(37) Rare earth prices in 2020, Institute of Rare Earths and Metals, 2020.

(38) Zhou, L. D.; Assoud, A.; Zhang, Q.; Wu, X. H.; Nazar, L. F. New Family of Argyrodite Thioantimonate Lithium Superionic Conductors. J Am Chem Soc 2019, 141 (48), 19002-19013.

(39) Rodriguezcarvajal, J. Recent Advances in Magnetic-Structure Determination by Neutron Powder Diffraction. Physica B 1993, 192 (1-2), 55-69.

(40) Farrow, C. L.; Juhas, P.; Liu, J. W.; Bryndin, D.; Bozin, E. S.; Bloch, J.; Proffen, T.; Billinge, S. J. L. PDFfit2 and PDFgui: computer programs for studying nanostructure in crystals. J Phys-Condens Mat 2007, 19 (33).

(41) Chen, H. M.; Wong, L. L.; Adams, S. SoftBV - a software tool for screening the materials genome of inorganic fast ion conductors. Acta Crystallogr B 2019, 75, 18-33.

(42) Chen, H. M.; Adams, S. Bond softness sensitive bond-valence parameters for crystal structure plausibility tests. Iucrj 2017, 4, 614-625.

(43) Murayama, M.; Kanno, R.; Irie, M.; Ito, S.; Hata, T.; Sonoyama, N.; Kawamoto, Y. Synthesis of new lithium ionic conductor thio-LISICON - Lithium silicon sulfides system. J Solid State Chem 2002, 168 (1), 140-148.

(44) Stegmaier, S.; Voss, J.; Reuter, K.; Luntz, A. C. Li+ Defects in a Solid-State Li Ion Battery: Theoretical Insights with a Li3OCl Electrolyte. Chem Mater 2017, 29 (10), 4330-4340.

(45) Minafra, N.; Culver, S. P.; Krauskopf, T.; Senyshyn, A.; Zeier, W. G. Effect of Si substitution on the structural and transport properties of superionic Li-argyrodites. J Mater Chem A 2018, 6 (2), 645-651.

(46) Ohno, S.; Helm, B.; Fuchs, T.; Dewald, G.; Kraft, M. A.; Culver, S. P.; Senyshyn, A.; Zeier, W. G. Further Evidence for Energy Landscape Flattening in the Superionic Argyrodites Li6-xP1-xMxS5I (M = Si, Ge, Sn). Chem Mater 2019, 31 (13), 4936-4944.

(47) J. F. Moulder, and J.Chastain, Handbook of X-Ray Photoelectron Spectroscopy: A Reference Book of Standard Spectra for Identification and Interpretation of XPS Data, Eden Prairie, Minn: Physical Electronics Division, Perkin-Elmer Corp, 1992.

(48) Li, Y. T.; Zhou, W. D.; Chen, X.; Lu, X. J.; Cui, Z. M.; Xin, S.; Xue, L. G.; Jia, Q. X.; Goodenough, J. B. Mastering the interface for advanced all-solid-state lithium rechargeable batteries. P Natl Acad Sci USA 2016, 113 (47), 13313-13317.

(49) Lackner, P.; Zou, Z. Y.; Mayr, S.; Diebold, U.; Schmid, M. Using photoelectron spectroscopy to observe oxygen spillover to zirconia. Phys Chem Chem Phys 2019, 21 (32), 17613-17620.

(50) Zhang, X.; Schiros, T.; Nordlund, D.; Shin, Y. C.; Kong, J.; Dresselhaus, M.; Palacios, T. X-Ray Spectroscopic Investigation of Chlorinated Graphene: Surface Structure and Electronic Effects. Adv Funct Mater 2015, 25 (26), 4163-4169.

(51) Ohno, Y. XPS studies of the intermediate valence state of Yb in (YbS)(1.25)CrS2. J Electron Spectrosc 2008, 165 (1-3), 1-4.

(52) Schmidt, S.; Hufner, S.; Reinert, F.; Assmus, W. X-ray photoemission of YbInCu4. Phys Rev B 2005, 71 (19).

(53) Utsumi, Y.; Sato, H.; Kurihara, H.; Maso, H.; Hiraoka, K.; Kojima, K.; Tobimatsu, K.; Ohkochi, T.; Fujimori, S.; Takeda, Y.; Saitoh, Y.; Mimura, K.; Ueda, S.; Yamashita, Y.; Yoshikawa, H.; Kobayashi, K.; Oguchi, T.; Shimada, K.; Namatame, H.; Taniguchi, M. Conduction-band electronic states of YbInCu4 studied by photoemission and soft x-ray absorption spectroscopies. Phys Rev B 2011, 84 (11).

(54) Kimura, S.; Kwon, Y. S.; Suzuki, T. Mixed valence of Yb3S4. Physica B 1997, 230, 301-303.

(55) Pollini, I. Photoemission-Study of the Electronic-Structure of Crcl3 and Rucl3 Compounds. Phys Rev B 1994, 50 (4), 2095-2103.

(56) Liu, Y. S.; Wang, S.; Nolan, A. M.; Ling, C.; Mo, Y. F. Tailoring the Cation Lattice for Chloride Lithium-Ion Conductors. Adv Energy Mater 2020, 10 (40).

(57) "Electrochemical series", in CRC Handbook of Chemistry and Physics 101th edition, David R. Lide, ed., CRC Press, Boca Raton, FL, 2005.

(58) Jung, S. H.; Kim, U. H.; Kim, J. H.; Jun, S. G.; Yoon, C. S.; Jung, Y. S.; Sun, Y. K. Ni-Rich Layered Cathode Materials with Electrochemo-Mechanically Compliant Microstructures for All-Solid-State Li Batteries. Adv Energy Mater 2020, 10 (6).

(59) de Biasi, L.; Kondrakov, A. O.; Gesswein, H.; Brezesinski, T.; Hartmann, P.; Janek, J. Between Scylla and Charybdis: Balancing Among Structural Stability and Energy Density of Layered NCM Cathode Materials for Advanced Lithium-Ion Batteries. J Phys Chem C 2017, 121 (47), 26163-26171.

(60) Qian, G. N.; Zhang, Y. T.; Li, L. S.; Zhang, R. X.; Xu, J. M.; Cheng, Z. J.; Xie, S. J.; Wang, H.; Rao, Q. L.; He, Y. S.; Shen, Y. B.; Chen, L. W.; Tang, M.; Ma, Z. F. Single-crystal nickel-rich layered-oxide battery cathode materials: synthesis, electrochemistry, and intra-granular fracture. Energy Storage Mater 2020, 27, 140-149.

Chapter 8

Summary and Future Perspectives

This thesis presents strategies to improve the energy density of positive electrode materials for Li/Na ion batteries and all-solid-state batteries by stabilizing high-valent cation/anion redox in layered oxide positive electrode materials and improving electrochemical stability of lithium halide solid electrolyte, respectively. In general, the anion redox in Li/Na layered transition metal oxides accompanies local structural distortion for multiple reasons such as lattice oxygen dimerization, oxygen loss by O_2 release, and transition metal migration, that eventually degrade the electrochemical performance of Li/Na ion batteries. In addition, the low oxidative stability of halide solid electrolytes hinders the application of high voltage cathode materials to all-solid-state batteries. Therefore, a deep understanding of a link between structural evolution and cation/anion redox in cathode materials and electrochemical properties of solid electrolytes are required to design high energy density lithium/sodium ion batteries.

Chapter 3 presents the effect of a polydopamine (PDA) coating on a Li-rich NCM (LRLO) cathode, which is able to improve electrochemical performance by scavenging oxygen radicals evolved from the LRLO. The impregnation method of self-polymerizing PDA coating successfully covers the porous spherical secondary agglomerates of nanoscale primary LRLO particles. By combining XPS, HRTEM and ToF-SIMS techniques, the controlled thickness of the PDA coating layer and the PDA infiltration into the interior of the porous LRLO secondary particle is confirmed. The oxygen radical scavenging effect of PDA is demonstrated by a combination of surface chemistry and electrochemical studies. XPS characterization conducted for the first charged and discharged electrodes confirms that the PDA coating on LRLO suppresses the formation of undesirable cathode electrolyte interphase (CEI) layer compared to a bare LRLO electrode indicating the suppressed side reactions between LRLO and

electrolyte. Raman spectroscopy conducted on PDA coated LRLO electrodes and chemically oxidized PDA powder confirm the reactivity of PDA to reactive oxygen species (ROS, e.g. $^1O_2$, $O_2^{\bullet-}$, and O^{n-}) by showing the cyclization of dopamine group to 5,6-dihydroxyindole in PDA. OEMS result shows the suppressed CO_2 and O_2 gas evolution after the first charge. These results demonstrate that PDA coating reacts with the ROS evolved from the LRLO surface during the first charge, thus suppressing the side reaction between electrolyte and LRLO and preventing surface lattice oxygen loss from LRLO. The retained surface lattice oxygen by PDA coating is confirmed by the HRTEM study that shows the suppressed layered to spinel/rocksalt phase transition from the coated LRLO after 100 cycles. Importantly, the electrochemical performance comparison between bare and PDA coated LRLO (cycling performance, derivative plots, and EIS) demonstrates that conformal PDA coating improves the capacity retention (from 70 % to 82 % after 200 cycles) and rate capability due to the suppressed continuous side reaction between ROS and electrolyte, thereby preserved anion redox active oxygen (O_2) in the bulk. Therefore, the PDA coating effectively improves the structural stability of LRLO by retaining surface oxygen from reactive oxygen release, leading to enhanced capacity retention and rate capability of LRLO involving reversible oxygen redox.

Like LRLO, improving capacity by accessing cation and anion redox has also been demonstrated in several sodium layered transition metal oxides. To understand the anion redox mechanism in sodium layered transition metal oxides, the presence of the non-bonded O 2p band in A-O-A' (where A stands for an alkali metal and A' stands for species with no covalent bonding interaction with the oxygen; e.g., Na-O-Li/Mg/Zn or Na-O-Vacancy) local configurations have been studied and suggested as a requirement for transition metal oxides. However, this suggestion is only based on DOS calculations from Li_2TMO_3 (TM = transition metal) systems; more local structures that enable anion redox and its stabilization mechanism in the electrode materials require further investigation. In **Chapter 4**, I present the study of anion redox in P2-type sodium layered transition metal oxides without

A-O-A' configuration by employing P2-type $Na_{0.67-x}[Mn_{0.5}Fe_{0.5}]O_2$ (NMF) and its analogous materials synthesized by substituting Fe with Cu ($Na_{0.67-x}[Mn_{0.66}Fe_{0.20}Cu_{0.14}]O_2$, NMFC) and Ni ($Na_{0.67-x}[Mn_{0.65}Fe_{0.20}Ni_{0.15}]O_2$, NMFN). In this study, the effect of Cu and Ni substitution on NMF reveals the complex interplay of the factors that control redox behavior and local structural evolution in this material. By combining experimental (RIXS, XANES, electrochemistry, and PDF analysis) and theoretical (DOS calculations) studies, the link between the extent of oxygen redox activity and transition metal antisite defect formation that accompanies the voltage hysteresis from high valent state NMF, NMFC, and NMFN electrodes is demonstrated. In particular, although NMF shows a higher degree of antisite–vacancy defects (AVDF) formation and voltage hysteresis than NMFC, the estimated extent of oxygen redox of NMFC is higher than NMF, indicating that the degree of AVDF and the extent of anion redox are not 1:1 correlation. In short, the trend in the degree of AVDF is NMF > NMFC > NMFN, whereas the trend in the extent of anion redox is NMFC ≥ NMF >> NMFN. This is due to the significant structural disorder triggered by the Jahn-Teller nature of Fe^{4+}, which has a higher concentration in NMF than NMFC. More importantly, the NMF and NMFC electrode materials do not have a local configuration of A-O-A' that was previously proposed as a structural requirement of anion redox. The causality of the different extent of anion redox from the electrodes is further investigated by DOS calculations of simplified compounds: $Na_{2/3}Mn_{1/2}Fe_{1/2}O_2$ (NMF), $Na_{2/3}Mn_{1/2}Cu_{1/2}O_2$ (NMC), and $Na_{2/3}Mn_{1/2}Ni_{1/2}O_2$ (NMN). This DOS calculation result demonstrates that anion redox is possible if the oxygen 2p band dominates the energy band near the Fermi level in the TM-O bond. Namely, as the oxygen 2p states are closer to the Fermi level, the more oxygen 2p contributes to charge compensation (extent of anion redox) at a high valent charge state. Consequently, the extent of anion redox follows an order based on how much the oxygen band dominates near the Fermi level, i.e. $O_{NMC} > O_{NMF} > O_{NMN}$. In addition, reducing the concentration of Fe^{4+} ions in the charged state via their partial substitution is necessary to alter the composition in order to tune anion redox and affect structural

stability-redox coupling. Consequently, this chapter suggests two approaches for designing iron-based P2-type sodium layered transition metal oxides: 1) choosing a TM substituent which minimizes AVDF but optimizes anion redox (e.g. Cu); 2) choosing a TM substituent whose band is closer to the Fermi level than the oxygen band to suppress anion redox and AVDF formation (e.g. Ni). Therefore, understanding the cation and anion redox chemistry and applying the design principles outlined in this study will help develop layered sodium electrode materials exhibiting low voltage hysteresis with a stable structure for sodium-ion batteries.

To better understand the oxygen redox stabilization mechanism and utilize the reversible oxygen redox without voltage hysteresis in sodium layered oxides, **Chapter 5** reports a study of coulombically-stabilized reversible oxygen redox in $Na_{2-x}Mn_3O_7$. From previously reported oxygen anion redox in layered transition metal oxide materials, local structural distortion, e.g., O-O dimerization, has been considered a stabilization mechanism for oxygen redox that induces voltage hysteresis for the Li/Na cell cycling. In this chapter, the combined experimental (electrochemistry, XRD, and various spectroscopy techniques) and theoretical (DFT calculation) study reveals that $Na_{2-x}Mn_3O_7$ ($0 \leq x \leq 1$) electrodes exhibit reversible oxygen redox showing negligible voltage hysteresis evolution (~ 40 mV) without O-O dimerization and Mn migration upon charge. The theoretical investigation conducted by the DOS calculation and O K-edge XAS spectra modeling for the partially desodiated electrode ($NaMn_3O_7$) shows the evolution of O hole polarons in Mn vacancy sites, which is indicative of oxygen redox. More importantly, the DFT ground state energy for $NaMn_3O_7$ demonstrates that there is significant coulombic interactions between O hole polarons and interlayer Na vacancies. The calculation further shows that the interaction is large enough to restrict the O-O dimerization of lattice oxygens. Moreover, if two O hole polarons are separated maximally within the Mn vacancy center, this coulombically-stabilized O hole polaron formation result in low $NaMn_3O_7$ system energy that is comparable to the O-O dimerization case. We also found that an unusual split-hole polaron

configuration can provide even lower system energy than O-O dimerization while stabilizing oxygen redox in the partially desodiated $Na_{1-x}Mn_3O_7$ electrode. Therefore, the coulombic interaction is crucial to the overall redox energetics in electrode materials employing anion redox. For the first time, this study reveals the role of coulombic interaction in stabilizing oxygen anion redox in sodium layered oxide materials. In addition, this study suggests a new design rule for high energy density layered oxide materials, which take into account stable oxygen redox without voltage hysteresis and local structure distortion. By tuning cation-vacancy ordering and layer stacking order through material synthesis modifications, we would be able to utilize the coulombic interaction effect between the O hole polaron and negatively charged alkali metal vacancy couple from the material.

In **Chapter 6**, a different approach is taken to enhance the energy density of cathode materials for NIBs by synthesizing 4 V class polyanionic sodium transition metal oxide-graphene oxide composite. In this study, a novel nanostructured $Na_2Co_2(SeO_3)_3$ and its GO composite were synthesized using a rapid and versatile microwave-assisted solvothermal synthesis route. The synthesized $Na_2Co_2(SeO_3)_3$ crystalized in a 1 um^3 cubic particle, which is stable to air and moisture, unlike other higher voltage cathode materials. From the electrochemical performance tests in sodium-ion batteries, the material delivers a reversible capacity of ≈ 75 mA·h g^{-1} at a potential of ≈ 4 V utilizing the $Co^{2+/3+}$ redox couple. The $Co^{2+/3+}$ redox couple is typically difficult to access and utilize in cobalt-based polyanionic compounds. Among high voltage NIB cathodes, this is the second-highest $Co^{2+/3+}$ redox potential after $Na_4Co_3(PO_4)_2P_2O_7$ (≈ 90 mA·g^{-1} and 4.5 V) and is more compatible with organic electrolytes. An operando XRD investigation shows good structural reversibility of the electrode material with a solid solution mechanism during electrochemical cycling. The XRD study further revealed that the material experiences a relatively small volume change (4.7%) over the sodium (de)intercalation. The combined XPS and magnetic susceptibility analysis confirm the $Co^{2+/3+}$ redox couple based electrochemical reaction mechanism with good chemical reversibility over the sodium

cell cycling. To the best of my knowledge, $Na_2Co_2(SeO_3)_3$ is the first Na^+ insertion material based on a selenite polyanionic system. Although the findings here are not directed toward commercializing the selenite system, the fundamental understanding of selenite polyanionic family achieved in this study will help discover new sodium (de)intercalation materials for Na-ion batteries.

Chapter 7 presents a strategy to improve the energy density of all solid state batteries. A new metastable trigonal structure of Li_3YbCl_6 is discovered from this work, while conventionally Li_3YbCl_6 is known to crystalize into orthorhombic structure. The Zr substituted phases, $Li_{3-x}Yb_{1-x}Zr_xCl_6$ ($0 \leq x \leq 0.8$), synthesized at a relatively low temperature of 350 °C are explored in terms of their structure evolution and electrochemical properties. The Zr substituted compounds exhibit high ionic conductivity up to 1.1 $mS \cdot cm^{-1}$ at 30 °C due to the decreased Li^+ ion migration energy barrier by introducing additional Li^+ ion hopping sites and sparsely distributing non-Li metal cations surrounding Li sites. Importantly, the excellent electrochemical oxidation stabilities of the $Li_{2.7}Yb_{0.7}Zr_{0.3}Cl_6$ solid electrolyte is demonstrated by the cycling performance of ASSBs adopting the uncoated 4 V-class cathode materials ($LiCoO_2$ and $LiNi_{0.6}Mn_{0.2}Co_{0.2}O_2$).

This thesis suggests various approaches to improve the specific energy density of Li/Na ion batteries and all-solid-state batteries, such as surface coating, stabilizing/suppressing oxygen redox by covalency tuning in TM-O bond or O-O bonds, tuning cation redox potential by polyanion ligand, and developing a new solid electrolyte that exhibits a wide electrochemical stability window. Although these approaches showed the enhanced electrochemical performance of the Li/Na battery cycling, intrinsic problems of the electrode materials, such as structural instability caused by phase transitions, surface densification by cation mixing, and limited operation voltage range due to the electrolyte stability window, are yet to be overcome. To address these issues, a deeper understanding of the chemical and electrochemical reactivity of electrode surface to electrolytes and coating layer is required. As proposed from this thesis, the functional organic polymer coating materials can provide a

chemical protection layer that prevents side reactions between the organic electrolyte and electrode surface by scavenging oxygen radicals at high voltage. However, organic materials are vulnerable to hydrofluoric acid (HF), typically generated by the decomposition of the fluorine-based lithium salt in electrolytes. Therefore, developing multifunctional lithium ion conductive coating materials that can protect the electrode surface from HF attack and oxygen loss by oxygen radical formation is required to improve the electrochemical performance of high voltage positive electrode materials. Second, in addition to the current study on transition metal substituents that can stabilize the anion redox and suppress the cation mixing, exploring an anion substituent with stronger electronegativity than oxygen (e.g., fluorine) is necessary to enhance the structural stability of Li/Na layered metal oxides while utilizing anion redox. These strategies have not been explored much and deserve further investigation. Lastly, the anion substitution strategy is also applicable to lithium metal halide solid electrolytes to enhance their electrochemical and chemical stability to high voltage metal oxide positive electrode materials for all solid state batteries. The improving oxidative stability of solid electrolyte will open a chance to raise the charge cut-off voltage for 4 V-class positive electrode materials, thus ASSBs can achieve a high specific energy density comparable to current commercialized Li/Na ion batteries. Certainly, all the strategies have to be integrated and optimized to develop high energy density Li/Na ion batteries that exhibit negligible voltage hysteresis and high capacity retention over the long term battery cycling.

References

Chapter 1. References

1. M. S. Whittingham, *Chem Rev*, 2004, **104**, 4271-4301.
2. M. Li, J. Lu, Z. W. Chen and K. Amine, *Adv Mater*, 2018, **30**, 1800561.
3. "Global direct primary energy consumption". Our World in Data. Retrieved 8 November 2020.
4. R. H. Han, J. E. Lee, S. H. Yoon and G. B. Kim, *Arch Microbiol*, 2020, **202**, 727-732.
5. M. Sufyan, N. A. Rahim, M. M. Aman, C. K. Tan and S. R. S. Raihan, *J Renew Sustain Ener*, 2019, **11**, 014105.
6. N. Nitta, F. X. Wu, J. T. Lee and G. Yushin, *Mater Today*, 2015, **18**, 252-264.
7. G. O. Adam, G. B. Kim, S. J. Lee, H. Lee, S. J. Kim, J. S. Kim and H. S. Kang, *Indian J Biochem Bio*, 2019, **56**, 445-454.
8. M. S. Whittingham, *Science*, 1976, **192**, 1126-1127.
9. K. Mizushima, P. C. Jones, P. J. Wiseman and J. B. Goodenough, *Mater Res Bull*, 1980, **15**, 783-789.
10. R. Fong, U. Vonsacken and J. R. Dahn, *J Electrochem Soc*, 1990, **137**, 2009-2013.
11. D. Guyomard and J. M. Tarascon, *J Electrochem Soc*, 1993, **140**, 3071-3081.
12. H. Y. Li, T. Yamaguchi, S. Matsumoto, H. Hoshikawa, T. Kumagai, N. L. Okamoto and T. Ichitsubo, *Nat Commun*, 2020, **11**, 1584.
13. J. N. Reimers and J. R. Dahn, *J Electrochem Soc*, 1992, **139**, 2091-2097.
14. M. Yoon, Y. Dong, Y. Yoo, S. Myeong, J. Hwang, J. Kim, S. H. Choi, J. Sung, S. J. Kang, J. Li and J. Cho, *Adv Funct Mater*, 2020, **30**, 1907903.
15. Y. C. Lyu, X. Wu, K. Wang, Z. J. Feng, T. Cheng, Y. Liu, M. Wang, R. M. Chen, L. M. Xu, J. J. Zhou, Y. H. Lu and B. K. Guo, *Adv Energy Mater*, 2020, **11**, 2000982.
16. R. Hausbrand, G. Cherkashinin, H. Ehrenberg, M. Groting, K. Albe, C. Hess and W. Jaegermann, *Mater Sci Eng B-Adv*, 2015, **192**, 3-25.
17. G. L. Xu, X. Liu, A. Daali, R. Amine, Z. H. Chen and K. Amine, *Adv Funct Mater*, 2020, **30**, 2004748.
18. A. Manthiram, *Nat Commun*, 2020, **11**, 1550.
19. C. P. Liang, F. T. Kong, R. C. Longo, S. Kc, J. S. Kim, S. Jeon, S. Choi and K. Cho, *J Phys Chem C*, 2016, **120**, 6383-6393.

20. W. Liu, P. Oh, X. Liu, M. J. Lee, W. Cho, S. Chae, Y. Kim and J. Cho, *Angew Chem Int Edit*, 2015, **54**, 4440-4457.
21. A. Manthiram and J. B. Goodenough, *J Solid State Chem*, 1987, **71**, 349-360.
22. A. K. Padhi, K. S. Nanjundaswamy and J. B. Goodenough, *J Electrochem Soc*, 1997, **144**, 1188-1194.
23. C. Masquelier and L. Croguennec, *Chem Rev*, 2013, **113**, 6552-6591.
24. P. Barpanda, L. Lander, S. Nishimura and A. Yamada, *Adv Energy Mater*, 2018, **8**, 1703055.
25. Z. Y. Bi, X. D. Zhang, W. He, D. D. Min and W. S. Zhang, *Rsc Adv*, 2013, **3**, 19744-19751.
26. A. Yamada, S. C. Chung and K. Hinokuma, *J Electrochem Soc*, 2001, **148**, A224-A229.
27. M. S. Islam, D. J. Driscoll, C. A. J. Fisher and P. R. Slater, *Chem Mater*, 2005, **17**, 5085-5092.
28. J. H. Park, B. Choi, Y. S. Kang, S. Y. Park, D. J. Yun, I. Park, J. Ha Shim, J. H. Park, H. N. Han and K. Park, *Energy Technol-Ger*, 2018, **6**, 1361-1369.
29. R. Jung, R. Morasch, P. Karayaylali, K. Phillips, F. Maglia, C. Stinner, Y. Shao-Horn and H. A. Gasteiger, *J Electrochem Soc*, 2018, **165**, A132-A141.
30. H. H. Ryu, K. J. Park, C. S. Yoon and Y. K. Sun, *Chem Mater*, 2018, **30**, 1155-1163.
31. M. H. Rossouw and M. M. Thackeray, *Mater Res Bull*, 1991, **26**, 463-473.
32. M. H. Rossouw, D. C. Liles and M. M. Thackeray, *J Solid State Chem*, 1993, **104**, 464-466.
33. K. Numata, C. Sakaki and S. Yamanaka, *Chem Lett*, 1997, DOI: DOI 10.1246/cl.1997.725, 725-726.
34. Z. H. Lu, D. D. MacNeil and J. R. Dahn, *Electrochem Solid St*, 2001, **4**, A191-A194.
35. Z. H. Lu and J. R. Dahn, *J Electrochem Soc*, 2002, **149**, A815-A822.
36. J. S. Kim, C. S. Johnson, J. T. Vaughey, M. M. Thackeray and S. A. Hackney, *Chem Mater*, 2004, **16**, 1996-2006.
37. M. M. Thackeray, S. H. Kang, C. S. Johnson, J. T. Vaughey, R. Benedek and S. A. Hackney, *J Mater Chem*, 2007, **17**, 3112-3125.
38. Z. H. Lu, L. Y. Beaulieu, R. A. Donaberger, C. L. Thomas and J. R. Dahn, *J Electrochem Soc*, 2002, **149**, A778-A791.
39. Z. H. Lu, Z. H. Chen and J. R. Dahn, *Chem Mater*, 2003, **15**, 3214-3220.
40. J. R. Croy, M. Balasubramanian, K. G. Gallagher and A. K. Burrell, *Accounts Chem Res*, 2015, **48**, 2813-2821.
41. G. Assat and J. M. Tarascon, *Nat Energy*, 2018, **3**, 373-386.

42. H. J. Yu, Y. G. So, Y. Ren, T. H. Wu, G. C. Guo, R. J. Xiao, J. Lu, H. Li, Y. B. Yang, H. S. Zhou, R. Z. Wang, K. Amine and Y. Ikuhara, *J Am Chem Soc*, 2018, **140**, 15279-15289.
43. W. E. Gent, K. Lim, Y. F. Liang, Q. H. Li, T. Barnes, S. J. Ahn, K. H. Stone, M. McIntire, J. Y. Hong, J. H. Song, Y. Y. Li, A. Mehta, S. Ermon, T. Tyliszczak, D. Kilcoyne, D. Vine, J. H. Park, S. K. Doo, M. F. Toney, W. L. Yang, D. Prendergast and W. C. Chueh, *Nat Commun*, 2017, **8**, 2091.
44. R. A. House, U. Maitra, L. Y. Jin, J. G. Lozano, J. W. Somerville, N. H. Rees, A. J. Naylor, L. C. Duda, F. Massel, A. V. Chadwick, S. Ramos, D. M. Pickup, D. E. McNally, X. Y. Lu, T. Schmitt, M. R. Roberts and P. G. Bruce, *Chem Mater*, 2019, **31**, 3293-3300.
45. R. A. House, G. J. Rees, M. A. Perez-Osorio, J. J. Marie, E. Boivin, A. W. Robertson, A. Nag, M. Garcia-Fernandez, K. J. Zhou and P. G. Bruce, *Nat Energy*, 2020, **5**, 777-785.
46. J. Wang, X. He, E. Paillard, N. Laszczynski, J. Li and S. Passerini, *Adv Energy Mater*, 2016, **6**, 1600906.
47. J. Wandt, A. T. S. Freiberg, A. Ogrodnik and H. A. Gasteiger, *Mater Today*, 2018, **21**, 825-833.
48. N. Yabuuchi, K. Yoshii, S. T. Myung, I. Nakai and S. Komaba, *J Am Chem Soc*, 2011, **133**, 4404-4419.
49. E. Castel, E. J. Berg, M. El Kazzi, P. Novak and C. Villevieille, *Chem Mater*, 2014, **26**, 5051-5057.
50. R. Schmuch, R. Wagner, G. Horpel, T. Placke and M. Winter, *Nat Energy*, 2018, **3**, 267-278.
51. G. Patry, A. Romagny, S. Martinet and D. Froelich, *Energy Sci Eng*, 2015, **3**, 71-82.
52. G. H. Newman and L. P. Klemann, *J Electrochem Soc*, 1980, **127**, 2097-2099.
53. C. Delmas, J. J. Braconnier, C. Fouassier and P. Hagenmuller, *Solid State Ionics*, 1981, **3-4**, 165-169.
54. R. Berthelot, D. Carlier and C. Delmas, *Nat Mater*, 2011, **10**, 74-U73.
55. N. Yabuuchi and S. Komaba, *Sci Technol Adv Mat*, 2014, **15**, 043501.
56. A. Mendiboure, C. Delmas and P. Hagenmuller, *J Solid State Chem*, 1985, **57**, 323-331.
57. Y. Takeda, K. Nakahara, M. Nishijima, N. Imanishi, O. Yamamoto, M. Takano and R. Kanno, *Mater Res Bull*, 1994, **29**, 659-666.
58. S. Komaba, C. Takei, T. Nakayama, A. Ogata and N. Yabuuchi, *Electrochem Commun*, 2010, **12**, 355-358.
59. D. Kundu, E. Talaie, V. Duffort and L. F. Nazar, *Angew Chem Int Edit*, 2015, **54**, 3431-3448.

60. T. Jin, H. X. Li, K. J. Zhu, P. F. Wang, P. Liu and L. F. Jiao, *Chem Soc Rev*, 2020, **49**, 2342-2377.
61. N. Zhao, T. Zhang, H. L. Zhao and Y. L. Hou, *Mater Today Nano*, 2020, **10**, 100072.
62. S. P. Ong, V. L. Chevrier, G. Hautier, A. Jain, C. Moore, S. Kim, X. H. Ma and G. Ceder, *Energ Environ Sci*, 2011, **4**, 3680-3688.
63. K. Kuratani, N. Uemura, H. Senoh, H. T. Takeshita and T. Kiyobayashi, *J Power Sources*, 2013, **223**, 175-182.
64. N. Yabuuchi, K. Kubota, M. Dahbi and S. Komaba, *Chem Rev*, 2014, **114**, 11636-11682.
65. S. Komaba, T. Ishikawa, N. Yabuuchi, W. Murata, A. Ito and Y. Ohsawa, *Acs Appl Mater Inter*, 2011, **3**, 4165-4168.
66. L. Li, Y. Zheng, S. L. Zhang, J. P. Yang, Z. P. Shao and Z. P. Guo, *Energ Environ Sci*, 2018, **11**, 2310-2340.
67. S. Komaba, W. Murata, T. Ishikawa, N. Yabuuchi, T. Ozeki, T. Nakayama, A. Ogata, K. Gotoh and K. Fujiwara, *Adv Funct Mater*, 2011, **21**, 3859-3867.
68. X. W. Dou, I. Hasa, D. Saurel, C. Vaalma, L. M. Wu, D. Buchholz, D. Bresser, S. Komaba and S. Passerini, *Mater Today*, 2019, **23**, 87-104.
69. C. Bommier, T. W. Surta, M. Dolgos and X. L. Ji, *Nano Lett*, 2015, **15**, 5888-5892.
70. C. Delmas, C. Fouassier and P. Hagenmuller, *Physica B & C*, 1980, **99**, 81-85.
71. B. M. de Boisse, D. Carlier, M. Guignard, L. Bourgeois and C. Delmas, *Inorg Chem*, 2014, **53**, 11197-11205.
72. R. Stoyanova, D. Carlier, M. Sendova-Vassileva, M. Yoncheva, E. Zhecheva, D. Nihtianova and C. Delmas, J Solid State Chem, 2010, 183, 1372-1379.
73. R. D. Shannon, *Acta Crystallogr A*, 1976, **32**, 751-767.
74. Y. C. Lei, X. Li, L. Liu and G. Ceder, *Chem Mater*, 2014, **26**, 5288-5296.
75. R. Fielden and M. N. Obrovac, *J Electrochem Soc*, 2015, **162**, A453-A459.
76. X. Li, D. Wu, Y. N. Zhou, L. Liu, X. Q. Yang and G. Ceder, *Electrochem Commun*, 2014, **49**, 51-54.
77. Z. H. Lu and J. R. Dahn, *J Electrochem Soc*, 2001, **148**, A1225-A1229.
78. N. Yabuuchi, M. Kajiyama, J. Iwatate, H. Nishikawa, S. Hitomi, R. Okuyama, R. Usui, Y. Yamada and S. Komaba, *Nat Mater*, 2012, **11**, 512-517.
79. E. Talaie, V. Duffort, H. L. Smith, B. Fultz and L. F. Nazar, *Energ Environ Sci*, 2015, **8**, 2512-2523.

80. C. Delmas, A. Maazaz, C. Fouassier, J. M. Reau and P. Hagenmuller, *Mater Res Bull*, 1979, **14**, 329-335.
81. D. H. Lee, J. Xu and Y. S. Meng, *Phys Chem Chem Phys*, 2013, **15**, 3304-3312.
82. J. M. Paulsen and J. R. Dahn, *Solid State Ionics*, 1999, **126**, 3-24.
83. Z. H. Lu and J. R. Dahn, *J Electrochem Soc*, 2001, **148**, A710-A715.
84. D. H. Seo, J. Lee, A. Urban, R. Malik, S. Kang and G. Ceder, *Nat Chem*, 2016, **8**, 692-697.
85. K. Luo, M. R. Roberts, R. Hao, N. Guerrini, D. M. Pickup, Y. S. Liu, K. Edstrom, J. H. Guo, A. V. Chadwick, L. C. Duda and P. G. Bruce, *Nat Chem*, 2016, **8**, 684-691.
86. D. D. Yuan, X. H. Hu, J. F. Qian, F. Pei, F. Y. Wu, R. J. Mao, X. P. Ai, H. X. Yang and Y. L. Cao, *Electrochim Acta*, 2014, **116**, 300-305.
87. I. Hasa, D. Buchholz, S. Passerini, B. Scrosati and J. Hassoun, *Adv Energy Mater*, 2014, **4**, 1400083.
88. J. Xu, D. H. Lee, R. J. Clement, X. Q. Yu, M. Leskes, A. J. Pell, G. Pintacuda, X. Q. Yang, C. P. Grey and Y. S. Meng, *Chem Mater*, 2014, **26**, 1260-1269.
89. N. Yabuuchi, R. Hara, K. Kubota, J. Paulsen, S. Kumakura and S. Komaba, *J Mater Chem A*, 2014, **2**, 16851-16855.
90. N. Yabuuchi, R. Hara, M. Kajiyama, K. Kubota, T. Ishigaki, A. Hoshikawa and S. Komaba, *Adv Energy Mater*, 2014, **4**, 1301453.
91. D. P. Wang, I. Belharouak, G. W. Zhou and K. Amine, *Adv Funct Mater*, 2013, **23**, 1070-1075.
92. D. Mohanty, A. Huq, E. A. Payzant, A. S. Sefat, J. L. Li, D. P. Abraham, D. L. Wood and C. Daniel, *Chem Mater*, 2013, **25**, 4064-4070.
93. J. Billaud, G. Singh, A. R. Armstrong, E. Gonzalo, V. Roddatis, M. Armand, T. Rojob and P. G. Bruce, *Energ Environ Sci*, 2014, **7**, 1387-1391.
94. U. Maitra, R. A. House, J. Somerville, N. Tapia-Ruiz, J. G. Lozano, N. Guerrini, R. Hao, K. Luo, L. Y. Jin, M. A. Perez-Osorio, F. Massel, D. M. Pickup, S. Ramos, X. Y. Lu, D. E. McNally, A. V. Chadwick, F. Giustino, T. Schmitt, L. C. Duda, M. R. Roberts and P. G. Bruce, *Nat Chem*, 2018, **10**, 288-295.
95. S. H. Guo, P. Liu, H. J. Yu, Y. B. Zhu, M. W. Chen, M. Ishida and H. S. Zhou, *Angew Chem Int Edit*, 2015, **54**, 5894-5899.
96. M. Keller, D. Buchholz and S. Passerini, *Adv Energy Mater*, 2016, **6**, 1501555.
97. M. Bianchini, E. Gonzalo, N. E. Drewett, N. Ortiz-Vitoriano, J. M. L. del Amo, F. J. Bonilla, B. Acebedo and T. Rojo, *J Mater Chem A*, 2018, **6**, 3552-3559.

98. G. K. Veerasubramani, Y. Subramanian, M. S. Park, B. Senthilkumar, A. Eftekhari, S. J. Kim and D. W. Kim, *Electrochim Acta*, 2019, **296**, 1027-1034.
99. L. T. Yang, J. M. L. del Amo, Z. Shadike, S. M. Bak, F. Bonilla, M. Galceran, P. K. Nayak, J. R. Buchheim, X. Q. Yang, T. Rojo and P. Adelhelm, *Adv Funct Mater*, 2020, **30**, 2003364.
100. R. R. Li, Y. Y. Liu, Z. Wang and J. L. Li, *Electrochim Acta*, 2019, **318**, 14-22.
101. P. Moreau, G. Ouvrard, P. Gressier, P. Ganal and J. Rouxel, *J Phys Chem Solids*, 1996, **57**, 1117-1122.
102. Z. Y. Wu, G. Ouvrard, S. Lemaux, P. Moreau, P. Gressier, F. Lemoigno and J. Rouxel, *Phys Rev Lett*, 1996, **77**, 2101-2104.
103. J. Rouxel, *Chem-Eur J*, 1996, **2**, 1053-1059.
104. J. Rouxel, *Curr Sci India*, 1997, **73**, 31-39.
105. J. M. Tarascon, G. Vaughan, Y. Chabre, L. Seguin, M. Anne, P. Strobel and G. Amatucci, *J Solid State Chem*, 1999, **147**, 410-420.
106. M. H. Lindic, H. Martinez, A. Benayad, B. Pecquenard, P. Vinatier, A. Levasseur and D. Gonbeau, *Solid State Ionics*, 2005, **176**, 1529-1537.
107. H. Koga, L. Croguennec, M. Menetrier, K. Douhil, S. Belin, L. Bourgeois, E. Suard, F. Weill and C. Delmas, *J Electrochem Soc*, 2013, **160**, A786-A792.
108. H. Koga, L. Croguennec, M. Menetrier, P. Mannessiez, F. Weill, C. Delmas and S. Belin, *J Phys Chem C*, 2014, **118**, 5700-5709.
109. M. Sathiya, G. Rousse, K. Ramesha, C. P. Laisa, H. Vezin, M. T. Sougrati, M. L. Doublet, D. Foix, D. Gonbeau, W. Walker, A. S. Prakash, M. Ben Hassine, L. Dupont and J. M. Tarascon, *Nat Mater*, 2013, **12**, 827-835.
110. E. McCalla, A. M. Abakumov, M. Saubanere, D. Foix, E. J. Berg, G. Rousse, M. L. Doublet, D. Gonbeau, P. Novak, G. Van Tendeloo, R. Dominko and J. M. Tarascon, *Science*, 2015, **350**, 1516-1521.
111. R. A. House, U. Maitra, M. A. P?rez-Osorio, J. G. Lozano, L. Jin, J. W. Somerville, L. C. Duda, A. Nag, A. Walters, K. J. Zhou, M. R. Roberts and P. G. Bruce, *Nature*, 2020, **577**, 502-508.
112. W. S. Yoon, K. B. Kim, M. G. Kim, M. K. Lee, H. J. Shin, J. M. Lee, J. S. Lee and C. H. Yo, J Phys Chem B, 2002, **106**, 2526-2532.
113. Y. Xie, M. Saubanere and M. L. Doublet, Energ Environ Sci, 2017, 10, 266-274.
114. J. H. Song, G. Yoon, B. Kim, D. Eum, H. Park, D. H. Kim and K. Kang, *Adv Energy Mater*, 2020, **10**, 2001207.

115. L. F. Yang, X. Li, J. Liu, S. Xiong, X. T. Ma, P. Liu, J. M. Bai, W. Q. Xu, Y. Z. Tang, Y. Y. Hu, M. L. Liu and H. Chen, *J Am Chem Soc*, 2019, **141**, 6680-6689.
116. P. F. Wang, Y. Xiao, N. Piao, Q. C. Wang, X. Ji, T. Jin, Y. J. Guo, S. F. Liu, T. Deng, C. Y. Cui, L. Chen, Y. G. Guo, X. Q. Yang and C. S. Wang, *Nano Energy*, 2020, **69**, 104474.
117. M. Jia, Y. Qiao, X. Li, F. L. Qiu, X. Cao, P. He and H. S. Zhou, *Acs Appl Mater Inter*, 2020, **12**, 851-857.
118. C. Hakim, N. Sabi, L. A. Ma, M. Dahbi, D. Brandell, K. Edstrom, L. C. Duda, I. Saadoune and R. Younesi, *Commun Chem*, 2020, **3**, 9.
119. K. H. Dai, J. Mao, Z. Q. Zhuo, Y. Feng, W. F. Mao, G. Ai, F. Pan, Y. D. Chuang, G. Liu and W. L. Yang, *Nano Energy*, 2020, **74**, 104831.
120. Y. S. Jung, D. Y. Oh, Y. J. Nam and K. H. Park, *Isr J Chem*, 2015, **55**, 472-485.
121. J. Schnell, F. Tietz, C. Singer, A. Hofer, N. Billot and G. Reinhart, *Energ Environ Sci*, 2019, **12**, 1818-1833.
122. L. D. Zhou, C. Y. Kwok, A. Shyamsunder, Q. Zhang, X. H. Wu and L. F. Nazar, *Energ Environ Sci*, 2020, **13**, 2056-2063.
123. K. H. Park, K. Kaup, A. Assoud, Q. Zhang, X. H. Wu and L. F. Nazar, *Acs Energy Lett*, 2020, **5**, 533-539.
124. N. Ohta, K. Takada, I. Sakaguchi, L. Q. Zhang, R. Z. Ma, K. Fukuda, M. Osada and T. Sasaki, *Electrochem Commun*, 2007, **9**, 1486-1490.
125. W. D. Richards, L. J. Miara, Y. Wang, J. C. Kim and G. Ceder, *Chem Mater*, 2016, **28**, 266-273.
126. R. S. Chen, Q. H. Li, X. Q. Yu, L. Q. Chen and H. Li, *Chem Rev*, 2020, **120**, 6820-6877.
127. M. Kotobuki, H. Munakata, K. Kanamura, Y. Sato and T. Yoshida, *J Electrochem Soc*, 2010, **157**, A1076-A1079.
128. K. H. Kim, Y. Iriyama, K. Yamamoto, S. Kumazaki, T. Asaka, K. Tanabe, C. A. J. Fisher, T. Hirayama, R. Murugan and Z. Ogumi, *J Power Sources*, 2011, **196**, 764-767.
129. H. Zhang, F. F. Chen, O. Lakuntza, U. Oteo, L. X. Qiao, M. Martinez-Ibanez, H. J. Zhu, J. Carrasco, M. Forsyth and M. Armand, *Angew Chem Int Edit*, 2019, **58**, 12070-12075.
130. G. Homann, L. Stolz, J. Nair, I. C. Laskovic, M. Winter and J. Kasnatscheew, *Sci Rep-Uk*, 2020, **10**, 4390.
131. A. Manthiram, X. W. Yu and S. F. Wang, *Nat Rev Mater*, 2017, **2**, 16103.

132. M. A. Kraft, S. P. Culver, M. Calderon, F. Bocher, T. Krauskopf, A. Senyshyn, C. Dietrich, A. Zevalkink, J. Janek and W. G. Zeier, *J Am Chem Soc*, 2017, **139**, 10909-10918.
133. X. N. Li, J. W. Liang, X. F. Yang, K. R. Adair, C. H. Wang, F. P. Zhao and X. L. Sun, *Energ Environ Sci*, 2020, **13**, 1429-1461.
134. S. Wang, Q. Bai, A. M. Nolan, Y. S. Liu, S. Gong, Q. Sun and Y. F. Mo, *Angew Chem Int Edit*, 2019, **58**, 8039-8043.
135. T. Asano, A. Sakai, S. Ouchi, M. Sakaida, A. Miyazaki and S. Hasegawa, *Adv Mater*, 2018, **30**, 1803075.
136. A. D. Sendek, E. D. Cubuk, E. R. Antoniuk, G. Cheon, Y. Cui and E. J. Reed, *Chem Mater*, 2019, **31**, 342-352.
137. S. Muy, J. Voss, R. Schlem, R. Koerver, S. J. Sedlmaier, F. Maglia, P. Lamp, W. G. Zeier and Y. Shao-Horn, *Iscience*, 2019, **16**, 270-282.
138. A. Bohnsack, F. Stenzel, A. Zajonc, G. Balzer, M. S. Wickleder and G. Meyer, *Z Anorg Allg Chem*, 1997, **623**, 1067-1073.
139. H. J. Steiner and H. D. Lutz, *Z Anorg Allg Chem*, 1992, **613**, 26-30.
140. A. D. Sendek, Q. Yang, E. D. Cubuk, K. A. N. Duerloo, Y. Cui and E. J. Reed, *Energ Environ Sci*, 2017, **10**, 306-320.
141. R. Schlem, S. Muy, N. Prinz, A. Banik, Y. Shao-Horn, M. Zobel and W. G. Zeier, *Adv Energy Mater*, 2020, **10**, 1903719.
142. H. Kwak, D. Han, J. Lyoo, J. Park, S. H. Jung, Y. Han, G. Kwon, H. Kim, S. T. Hong, K. W. Nam and Y. S. Jung, *Adv Energy Mater*, 2021, 2003190.

Chapter 2. References

1. N. Tsiouvaras, S. Meini, I. Buchberger and H. A. Gasteiger, *Journal of The Electrochemical Society*, 2013, **160**, A471-A477.
2. P. Sigmund, *Physical Review*, 1969, **184**, 383-416.
3. E. Talaie, P. Bonnick, X. Sun, Q. Pang, X. Liang and L. F. Nazar, *Chemistry of Materials*, 2016, **29**, 90-105.
4. L. J. P. Ament, M. van Veenendaal, T. P. Devereaux, J. P. Hill and J. van den Brink, *Reviews of Modern Physics*, 2011, **83**, 705-767.
5. I. Simbotin, M. J. Jamieson and A. Dalgarno, J Geophys Res-Atmos, 2004, 109.

6. R. S. Das and Y. K. Agrawal, Vib Spectrosc, 2011, 57, 163-176.
7. K. Periyapperuma, T. T. Tran, S. Trussler, D. Ioboni and M. N. Obrovac, Journal of the Electrochemical Society, 2014, 161, A2182-A2187.